LONG-TERM PERFORMANCE EVALUATION OF SAND-BENTONITE BUFFER MATERIALS TO CONTAIN HAZARDOUS WASTE

A THESIS

Submitted by

SURYA, S. S.

for the award of the degree
of

DOCTOR OF PHILOSOPHY

DEPARTMENT OF CIVIL ENGINEERING
INDIAN INSTITUTE OF TECHNOLOGY MADRAS
CHENNAI-600 036

July 2018

Dedicated to Family

Thesis Certificate

This is to certify that the thesis entitled **Long-term Performance Evaluation of Sand-bentonite Buffer Materials to Contain Hazardous Waste**, submitted by **Surya, S. S.** to the **Indian Institute of Technology Madras**, **Chennai**, for the award of the degree of **Doctor of Philosophy** is a bona fide record of the research work done by her under my supervision. The contents of this thesis, in full or in parts, have not been submitted to any other Institute or University for the award of any degree or diploma.

Place: Chennai
Date : 05 July 2018

Dr. D. N. Arnepalli
(Thesis Supervisor)
Department of Civil Engineering
Indian Institute of Technology Madras
Chennai, India

Acknowledgements

I thank the real researcher- the formless, shapeless and endless Almighty- for his blessings which enabled me to accomplish my research work successfully, for the strength that keep us believing that this affiliation would be possible.

I would like to express my insightful gratitude to my thesis supervisor Dr. D. N. Arnepalli, for his patient guidance, and encouragement throughout my research work. I extent my deep gratitude to the family of Dr. D. N. Arnepalli, for their immense care and providing a family feel during my days at IIT Madras.

I am highly thankful to Dr. K. Ramamurthy, Head, Department of Civil Engineering, and to the Doctoral Committee members, Dr. G. Appa Rao, Dr. Ligy Philip, Dr. K. Srinivasa Reddy and Dr. Abhijith Choudhury for their valuable and constructive suggestions during my thesis work. I would like to thank Dr. S. R. Gandhi, Dr. K. Rajagopal, Dr. A. Boominathan, Dr. G. R. Dodagoudar, Dr. R. G. Robinson, Dr. T. Thyagaraj, Dr. Subhadeep Banerjee, and Dr. V. B. Maji, faculty members of Geotechnical Engineering Division, Department of Civil Engineering, for their critical comments and suggestions at various stages of the research work. I would also like to express my gratitude to the family of Dr. Subhadeep Banerjee, for their kindness to provide a temporary accommodation for my family.

I wish to acknowledge the employees of HoD office and stores & purchase, Department of Civil Engineering, for their prompt help in procuring the equipment and consumables required for research work. I am grateful to Mr. Thiruppathi, Mr. Earnest, Mr. Murali, Mr. Om Prakash, Mr. Suresh, Mr. Soundara Pandian, and Mrs. Malarvizhi, for their sincere cooperation and technical assistance during my experimental work.

Completing this work would have been far more difficult without the support of my friends and colleagues, Chinchu, Saranya, Rejoice, Vineetha, Julina, Siva, Tamizharasi, Bijly, Surabhi Jain, Nikhil John, Sandeep Bandipally, Anjana R. Kadni, Arsha Lekshmi, Jayalekshmi, and Biju. My association with Nihar, Ros Ann Joseph, Anusha, Reshma, Leeban Joseph, Partha Narayan Misra, Vinay Kumar Gadi, Abinesh, Muthuraj, Priyusha, and Christina is quite memorable and would like to thank them for their inevitable help for my thesis. I am strongly indebted to Malavika, Amal, and Fathima for the timely support for my stay in the institute campus during

the thesis correction. I sincerely express my words of appreciation to all other research scholars and graduate students of the Department of Civil Engineering, IIT Madras for their help at various stages of my research work. I would like to thank Mr. Shekhar, Mr. Anil, and Mr. Selvaganapathi, Department of Chemical Engineering, and Mr. Vinod, Agilent Technologies for their help and support during the tough time of my experimental work.

This journey would not have been successful without the unraveling support from my family to whom all my achievements are dedicated. I am obliged to my husband, Mr. Vimal, who ungrudgingly tolerated my persistent absence from his life while I was away for research; for his love, patience, inspiration, sacrifice and unremitting cooperation throughout this study. I am beholden to my parents Mr. Surendran Nair and Mrs. Sathee Devi, and my sister Ms. Arya, who supported me in all my endeavors including my research. A big thank you to my grand mother-in-law Santha Kumari amma, mother-in-law Valsala amma, brother-in-law Mr. Vijesh, sister-in-law Mrs. Anitha, nephew Sreehari, and niece Sahasra for their affection, moral support and encouragement.

Surya, S. S.

Abstract

The use of sand-bentonite mixtures as a part of engineered multi barrier systems to ensure long-term confinement and isolation of radioactive waste contained canisters from the geoenvironment is common in deep geological repositories (DGR). The efficacy of DGR to contain these canisters highly depends on the long-term performance of the buffer materials under combined influence of physical, chemical and thermal loadings. In this study, the fundamental behavior of sand-bentonite buffer material over wide range of environmental conditions were analyzed and simulated for several years to evaluate the long-term performance of DGR.

First of all, the selected materials (sand and bentonite) were characterized for their physico-chemico-mineralogical and geotechnical properties. The thermal characteristics of sand-bentonite buffer materials were quantified in terms of their thermal conductivity by employing an in-house fabricated thermal probe. As the buffer materials need to endure the varying environmental conditions including temperature and moisture imbalance, a generalized model was developed based on the experimental studies for the estimation of thermal conductivity.

From the realization of alteration in the moisture regime due to the imposed thermal loads, state-of-the-art coupled flow studies were developed by simulating a real life DGR model. The canister was represented by a line heat source and the spatial and temporal variations of temperature, relative humidity, and volumetric moisture contents were recorded using data logger. The vapor flow along the radial distance from the line heat source was quantified from the above measured data by employing experimentally obtained isothermal vapor diffusivity value.

Further, the buffer material was characterized for their contaminant transport properties especially gas transport characteristics as the most prominent waste form in high temperature canister is gaseous in nature. The gas permeability characteristics of the sand-bentonite buffer materials were ascertained from the pressure decay method, and the role of molding moisture content and temperature on the gas permeability characteristics of buffer materials were established by performing gas permeability experiments at varying test conditions. A generalized relationship for gas permeability determination was developed by considering the synergetic effect of volumetric air content (estimated from soil air characteristic curve) and temperature variation. Similarly, the buffer materials were characterized for their gas diffusion properties in terms of the gas diffusion coefficient and the effect of molding moisture content on gas diffusion was verified.

The contaminant transport properties of sand-bentonite buffer materials were also estimated, in terms of their sorption coefficient. The effect of temperature on the sorption characteristics of buffer materials was recognized by conducting batch sorption tests at varying temperatures. In addition, the realistic contaminant buffer material interaction was simulated by estimation of sorption coefficients from column flow through experiments. Finally, the long-term performance of sand-bentonite buffer materials was ascertained from the numerical analysis using finite element based numerical tools for heat flow as well as contaminant migration.

From the analysis it could be inferred that sand-bentonite mixture with 30 % bentonite content exhibits favorable geotechnical, thermal, and contaminant transport properties. The long-term performance analysis of the buffer material for heat flow and contaminant transport properties also reveals the suitability of SB30 with a maximum elevated temperature of 95°C at the end of 9.5 years, when the initial canister temperature is 120 °C. Moreover, the effect of canister temperature was found to have no significant influence beyond a distance of 10 m from the canister surface. The analysis for safe placement distance between the canisters, resulted in a reasonable placement distance of 4 m between the canisters.

Keywords: *Buffer material*, *Thermal conductivity*, *Coupled flow*, *Water vapor diffusion*, *Gas permeability and diffusion*, *Soil water characteristic curve*, *Sorption*, *Long-term performance*.

Table of Contents

List of Tables

List of Figures

Nomenclature

English Symbols

$\Delta P_{t=0}$	initial pressure difference
$\Delta P_{t>0}$	pressure difference between the reservoirs
$\Delta P_t/\Delta P_o$	normalized pressure variation
Δq	quantity of flow for given time
Δt	time interval
ΔT	temperature rise
A	cross sectional area
A_1	constant parameter
Ag-K	silver kaolinite
B	Skempton’s pore pressure parameter
B_1	constant parameter
B_i	basis function for i'th input variable
b_o	bias at the output layer
b_{hk}	bias at the k^{th} neuron of hidden layer
b_i	pore size distribution index
b	Langmuir sorption coefficient
C_1	constant parameter
C	concentration
C_p	specific heat capacity
C_0	source reservoir gas concentration
C_e	equilibrium solution concentration
$CaCl_2$	calcium chloride
Cd	cadmium
CH_4	methane
C_i	initial concentration of the solution
CO_2	carbon dioxide
C_p	specific heat capacity
Cr	chromium
C_s	mass of contaminant sorbed by the geomaterial
Cs	caesium
C_t	effluent gas concentration
C_t/C_0	normalized effluent concentration
Cu^{2+}	copper cation

C_v'	saturation vapor concentration
D	diffusion coefficient
D_h	longitudinal hydrodynamic dispersion coefficient
D_V	vapor diffusion coefficient
E	evaporation rate
f_K	fraction of kaolinite minerals
f_M	fraction of montmorillonite minerals
f_Q	fraction of quartz minerals
f_{sa}	fraction of sand-sized particles
f_{sc}	fraction of clay-sized particles
f_{si}	fraction of silt-sized particles
f_{sig}	sigmoid basis or transfer function
F	rate of transfer
F_x	rate of transfer through unit area of the corresponding plane though p
f_s	weighing factors for solid
f_a	weighing factors for air phase
G	specific gravity
h	hydraulic head
I	applied current
^{129}I	iodine isotopes
k	hydraulic conductivity
K	thermal conductivity
K_a	coefficient of gas permeability
K_a^*	benchmark gas permeability
K_d	distribution coefficient
K_{fr}	thermal conductivity for frozen soils
K_{fl}	thermal conductivity of fluid phase
K_{ru}	normalized thermal conductivity for unfrozen soils
K_{rf}	normalized thermal conductivity for frozen soils
K_{dry}	dry thermal conductivity of soil
K_r	Freundlich sorption constant
K_{sr}	saturated thermal conductivity of soil
K_r	normalized thermal conductivity of soils
K_L	Langmuir sorption coefficient
K_l	partition coefficient

K_{dry}	dry thermal conductivity of soil
K_s	thermal conductivity of solid phase
K_u	thermal conductivity for unfrozen soils
K_{up}	upper bound for thermal conductivity
K_{lw}	lower bound for thermal conductivity
L	length of sample
La	lanthanum
Li^+	lithium cation
Lu	lutetium
M_s	mass of soil specimen
Mg^{2+}	magnesium cation
MgO	magnesium oxide
Na	sodium
n	constant
Nd	neodymium
P	pressure
Pb	lead
P_{50}	50 % cumulative probability
Q	heat generated
Q_w	cumulative volume of water collected
q_v	rate of vapor flow
q_v^i	isothermal vapor flow rate
q_v^T	non-isothermal vapor flow rate
R_T	thermal resistivity
R	retardation coefficient
r	radial distance
h_r	fractional relative humidity
R^2	regression coefficient
S	slope
s	slope of the saturation vapor concentration function
Sc	scandium
Sm	samarium
S_r	degree of saturation
Sr	strontium
T	temperature
t	time

V	applied voltage
v_f	seepage velocity
$V_{receiver}$	volume of receiver reservoir
$V_{sourcce}$	volumes of source reservoir
V_s	volume of soil solids
w	gravimetric moisture content
W_i	weight for i'th input variable
w_{ik}	connection weight between ith input variable and kth neuron of hidden layer
w_k	connection weight between kth neuron of hidden layer and the single output neuron
w_L	liquid limit
x	linear distance
w_P	plastic limit
w_S	shrinkage limit
Y	yttrium
z	linear distance
Zn	zinc

Greek Symbols

ρ	density
ρ_l	density of the specimen
ρ_w	density of distilled water
α	coefficient of exponential function
α_D	thermal diffusivity
α_T	curve fitting parameter
β	compressibility factor
β_T	curve fitting parameter
λ	decay constant
ε	volumetric soil air content
ε^*	benchmark soil air content
ξ	electrical resistance per unit length
ψ	soil suction
χ_f	fraction of fluid
χ_s	fraction of solids
χ_a	fraction of air
γ	bulk unit weight

γ_d	dry unit weight
2θ	diffraction angle
θ	volumetric moisture content
θ_a	soil air porosity
η	porosity
ɳ	tortuosity
μ	dynamic viscosity
ν	permeability coefficient

Abbreviation

AAS	atomic absorption spectrophotometer
AEC	atomic energy commission
Ag-K	silver kaolinite
ANN	artificial neural network
BES	bentonite enhanced sand
BTCs	break through curves
BWRs	boiling water reactors
CEC	cation exchange capacity
CH	high compressible clay
DAS	data analysis software
DC	direct current
DDL	diffused double layer
DGR	deep geological repositories
EBS	engineered barrier system
ESEM	environmental scanning electron microscope
FAAS	flame atomic absorption spectroscopy
GC	gas chromatograph
GCL	geosynthetic clay liners
GMZ	Gaomiaozi
HLW	high-level wastes
IAEA	international atomic energy agency
ICDD	international center for diffraction data
ILW	intermediate level wastes
IR	infrared
KIRMAT	kinetic reactions and mass transport
LLW	low-level wastes

L/S	liquid to solid
MIP	mercury intrusion porosimetry
MLR	multiple linear regression
MSB	multi swellable bentonite
NEB	negative exponential basis
NMR	nuclear magnetic resonance
NSDFs	near-surface disposal facilities
OCR	over consolidation ratio
OMC	optimum moisture content
PI	plasticity index
PR	percentage removal
PVC	polyvinyl chloride
RH	relative humidity
RE	rare earth
RMSE	root mean square error
SACC	soil air characteristic curve
SB	sand-bentonite
SE	standard error
SEM	scanning electron microscope
SP	poorly graded sand
SSA	specific surface area
STANMOD	STudio of ANalytical MODels
SWCC	soil-water characteristic curve
TAPS	Tarapur atomic power station
TC	thermal conductivity
TC1	thermocouple 1
TCD	thermal conductivity detector
TDR	time domain reflectometer
THM	thermo-hydro-mechanical
USEPA	United States environmental protection agency
USCS	unified soil classification system
XRD	X-ray diffractometer
XRF	X-ray fluorescence
1D-ADE	one-dimensional advective dispersion equation
3D	three dimensional
2D	two dimensional

Chapter 1
INTRODUCTION

1.1 General

Ever since the mid-twentieth century, nuclear power generation, radioactive materials utilization in medicine and industry, and nuclear weapons production, etc. have produced a significant amount of radioactive wastes. The management of the radioactive wastes is very challenging as it causes or results in physical, chemical and radioactive hazard. In the present chapter, a brief outline of the role of nuclear power, classification and disposal strategies of radioactive wastes, etc. are discussed. Further, the need for the present study, objectives and scope of the study, as well as organization of the thesis are presented.

1.2 Role of Nuclear Power

Rapid urbanization and industrialization lead to a tremendous increase in demand for energy. India, the seventh largest country in the world is having a population of around 1.3 billion with an area of 3.3 million km^2 (www.indiaonlinepages.com). Even today, approximately 10 % of India's population faces a severe shortage of electricity and the remaining is deprived of access to the clean energy such as nuclear power (Load generation balance report 2016-17). Therefore, ensuring energy security for the future generations is one of the essential responsibilities the society needs to shoulder these days. Figure 1.1 depicts the present resources of country's energy mix for producing electricity. Even though hydro and coal-fired thermal power plants remain the mainstay of our electricity production, there is a large need to supplement our available energy resources with sizable alternative resources to ensure long-term energy security without compromising environmental impacts. Considering the waning non-renewable energy resources and inadequate technical advancement in the renewable energy sector, nuclear energy seems to be the most promising solution to the forthcoming energy crisis in India. It is an elegant alternative to both thermal and hydraulic energies. Moreover, the inimitable feature of getting rejuvenated while being spent also makes nuclear energy sustainable and eco-friendly (carbon-free). Therefore, the complete dependency of nuclear technology on the availability of fresh fuel materials gets reduced in a long run (Sengupta et al., 2013).

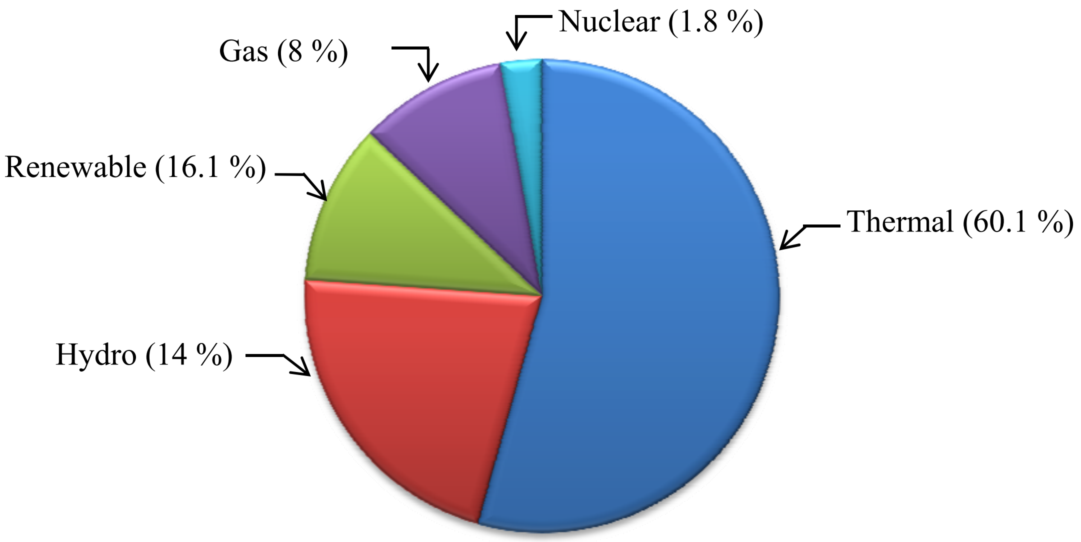

Figure 1.1Breakup of installed power capacity in India as on January 31, 2016 (modified from MNRE, CEA)

As on February 2018, nuclear power provides world over about 11 % of electricity through 450 nuclear power plants with a total installed capacity of 392 GW. At present, 128 nuclear power plants connected to the world energy grid are built in Asia (nuclear energy institute, www.nei.org).

1.3 History of Nuclear Power in India

Nearly forty years ago Homi Jehangir Bhabha formulated the strategy of Indian nuclear program. On 10th August 1948, the government of India has constituted the atomic energy commission (AEC), under the atomic energy act to launch the atomic energy program. Precisely, the Indian nuclear power program has commenced in 1969 with the building of the twin-reactor units of the Tarapur atomic power station (TAPS), employing boiling water reactors (BWRs), with the assistance of United States of America. Presently, there are 21 nuclear power reactors in operation with a capacity of 4.56 GW (Bhardwaj, 2013).

The Indian nuclear fuel cycle program primarily depends on uranium imports since the domestic nuclear fuel reserves of the nation are meager. Russia has been a major supplier of nuclear fuel to India from early 1990's (The Indian Express, 22 August 2010). In September 2008, India commenced international nuclear trade and has initiated bilateral agreements for the supply of civilian nuclear energy technology with countries including France, the United States of America, the United Kingdom, Canada, Mongolia, Kazakhstan, Argentina, Namibia, and South Korea. Incidentally, in March 2011 large deposits of natural uranium have been discovered in Tummalapalle belt in the Southern part of Kadapa basin in Andhra Pradesh, India (www.wikipedia.org).

1.4 Strategies for Disposal of Radioactive Waste

As of today, India has gained a commendable experience in operating the nuclear reactors with closed-fuel cycles and is gradually moving towards the amalgamation of the overall program. The closed-fuel cycle involves reprocessing of spent fuel and recycling of plutonium and uranium 233 which in turn beneficial in terms of volume of waste generated (Bhardwaj, 2013). Figure 1.2 presents the schematic of closed-fuel cycle adopted by Indian nuclear industry.

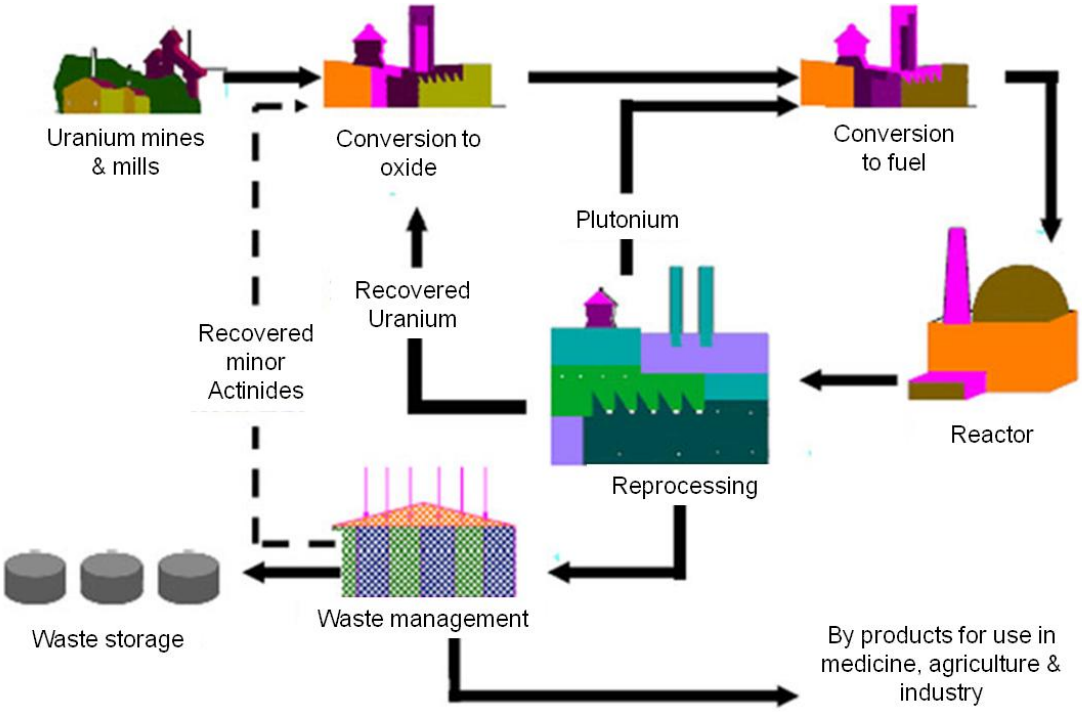

Figure 1.2 Schematic of fuel cycle of nuclear industry in India
(modified from Wattal, 2013)

However, this avenue has its own problems pertaining to safe disposal of waste generated, disposition of spent fuel and possible risks of nuclear weapons proliferation. The radioactive waste is being regulated by government agencies in order to prevent environmental degradation and to protect the eco-system as it is harmful to most forms of life. As per the International Atomic Energy Agency (IAEA) guidelines, radioactive wastes can be categorized into three kinds based on the time elapsed for radioactivity to die down, and exposure risk to the environment and people. They are low-level wastes, intermediate level wastes, and high-level wastes denoted as LLW, ILW, and HLW respectively. As a waste management doctrine, the paramount importance is given to the minimization of waste generation at all stages of design, operation, and maintenance.

In general, radioactive waste management involves three principles: (a) dilute and disperse; (b) concentrate and contain and (c) delay and decay applicable to LLW, ILW, and HLW, respectively (IAEA, 1994; AERB, 2001). The waste management strategies for treatment and disposal of LLW and ILW are well established and being practiced for several decades in an impeccable fashion. These strategies involve categorization and incineration of the combustible waste, interim storage, treatment, conditioning, and ultimate disposal in concrete trenches at shallow depths (< 30 m) called near-surface disposal facilities, NSDFs. Prior to disposal, the solid and liquid wastes are concentrated, immobilized in cement-based polymer matrices and stored in interim storage facilities. The gaseous wastes consisting of the exhaust from ventilation of plant buildings are filtered through high-efficiency particulate scrubbers and discharged through a high stack (Raj et al., 2006). It has been observed that the metallic melter technology was established for efficient waste management; nevertheless, the continuous ceramic-based technology is being pursued for HLW management and the same is being set up at Tarapur (Raj et al., 2006).

Due to the presence of long-lasting radioactive transmutation reactions, HLWs cannot be subjected to the similar disposal practices. Because of the hazardous nature of the HLW, it is first calcinated to immobilize and then vitrified using borosilicate glass, sealed in stainless steel containers known as canisters, and disposed into deep geological formations (depth > 300 m) called deep geological repositories, DGR. This disposal practice is considered to be the best way to isolate radioactive waste from the surrounding geoenvironment for few thousands of years, as the half-life of major radionuclides present in these wastes is in the same order of magnitude. Such repositories involve multi-layer engineered barrier systems to ensure long-term confinement and isolation of these waste contained canisters from the surrounding environment. The engineered barrier system (EBS) comprises of either the natural intact rock mass or salt deposits, engineered buffer or backfill materials.

In view of developing Indian DGR, suitable sites were identified based on in-situ as well as laboratory investigations. For this purpose, mockup (heat migration) studies have been commenced in the early eighties at a depth of 1000 m in an abandoned gold mine. Based on the experimental studies, numerical codes were developed to model the heat migration phenomena (Raj et al., 2006). Geologically India is gifted with a number of suitable rock formations viz. granites, basalts, shales, etc. However, major studies were conducted on granitic formations since the continental crust in Indian region is covered by these formations with sound thermo-mechanical, geochemical and geohydrological properties (Mathur et al., 1998).

The pivotal component of the EBS is the buffer material which is made of either bentonite or a sand-bentonite mixture. Bentonite is a clayey soil with a high content of smectite clay mineral, having properties that are conducive for isolating radioactive waste canisters. It has a very low hydraulic conductivity and ion diffusion characteristics for positively charged radionuclide as well as anions. In addition, the high swelling potential of bentonite enables the self-sealing of microcracks within the EBS, interfaces between the EBS and host rock as well as the waste contained canister. Its thermal properties are adequate to conduct heat away from the canister. However, the application of bentonite alone as an EBS results in desiccation cracking upon exposure to moderate temperature emanating from the waste contained canister, owing to the high volume change behavior of the bentonite. In view of this, it is recommended to mix the bentonite with non-swelling soils such as quartz sand so that its volume change behavior is mitigated and hence the chances of desiccation cracking are minimized. Therefore, the application of sand-bentonite mixtures in place of natural clays as barriers are less susceptible to shrinkage (Dixon et al., 1985) and frost damage (Kraus et al., 1997).

During the serviceability of a DGR, the performance of the EBS is influenced by complex hydro-geological, thermo-mechanical, chemical and biological processes, due to the release of heat by radioactive decay, multiphase flow of contaminants, waste dissolution and chemical reactions. Consequently, the efficacy of DGR to contain the wastes highly depends on the long-term performance of sand-bentonite buffer under the combined influence of physical, chemical and thermal loadings. In view of this, the sand-bentonite buffer is expected to hold the containers in place. The plastic deformability of bentonite is essential to redistribute the stresses resulting from the excavation and creep of host rock, which in turn may damage the waste contained canisters. The buffer is also required to facilitate heat transfer from the canister to the near field host rock and hence to the far field surrounding geoenvironment. It should have low hydraulic conductivity to limit the entry of groundwater containing potentially corrosive substances into the repository, and at the same time prevent the escape of radionuclide through it.

Another important property of the compacted sand-bentonite mixture is the swell potential which should be reasonably high to warrant the sealing of any fractures that might have formed during the construction as well as the service life of DGR. Besides the mechanical and hydraulic barrier functions, buffer material must also exhibit low diffusion characteristics and sufficiently high sorption affinity towards contaminants. This will ensure the minimal escape of radionuclides via diffusion mechanism and optimal retardation towards radionuclides. In addition, the buffer material should maintain its physical and engineering integrity at elevated temperatures (up to 150 °C), particularly under a saline environment that may exist in a waste disposal facility (Dixon et al., 1985). Keeping in view of above-mentioned requisites, it is essential to understand the fundamental behavior of buffer material over a wide range of environmental conditions, to ascertain its long-term performance.

1.5 Objectives and Scope of the Study

Though many researchers have conducted studies on buffer materials pertaining to their thermo-mechanical behavior and sorption-desorption characteristics individually, majority of the studies lack a synergetic approach for characterization of these materials by considering the effect of thermal flux on the migration of moisture which in turn results in a change of thermal properties. This scenario creates the coupled transport of moisture and heat which is responsible for the changes of their fundamental behavior in terms of unsaturated hydraulic conductivity, sorption-desorption, gas diffusion and permeability characteristics. So, it is mandatory to characterize the buffer material considering the combined influence of above-mentioned factors.

In view of this, the primary objective of the present study was to understand the fundamental behavior of buffer materials under the synergetic effect of physical, chemical and thermal loadings. In order to achieve this, the study aimed to quantify the coupled flow of heat and moisture through buffer material. Further, the effects of temperature and moisture on liquid as well as gaseous contaminant migration properties of buffer material were evaluated. The secondary objective of the study was to ascertain the long-term performance of the buffer material by considering its contaminant, water vapor, and thermal transport properties variation with time using numerical tools. Ultimately, this study paves the way to develop a design methodology for identifying suitable buffer material to contain the hazardous waste in it.

In order to achieve these objectives, the scope of the study includes the following.

- Characterization of selected geomaterials (fine sand and sodium bentonite) for their physical, mineralogical and geotechnical properties.
- Fabrication of an experimental setup to obtain the thermal characteristics of geomaterials and loss of moisture under the given thermal flux in terms of water vapor diffusion.
- Quantification of coupled migration of heat and moisture properties of buffer material.
- Establishing the role of temperature and moisture on the diffusion and permeation characteristics of buffer material for gaseous contaminants.
- Evaluation of sorption parameters as a function of temperature (10 °C, 27 °C, and 50 °C) so as to incorporate the influence of temperature on retardation behavior of buffer materials.
- Assessment of the long-term performance of buffer material using numerical tools such as SVHeat and POLLUTE by considering the synergetic effect of environmental conditions that prevail in a DGR.

1.6 Organization of the Thesis

Chapter 1: Describes the introduction, scope, and objectives of the present study.

Chapter2: Presents the review of literature related to the buffer material characterization in terms of thermal characteristics and contaminant transport properties. Based on the reviewed literature, a critical appraisal of the same is also presented.

Chapter 3: Details the methodologies employed to obtain physical, mineralogical and geotechnical characteristics of the buffer materials. Methodologies pertaining to the determination of thermal characteristics, liquid and gaseous contaminant transport properties such as gas diffusion and permeation, sorption characteristics, and hydraulic conductivity of buffer materials are also presented in this chapter. Further, the methodology to assess the unsaturated soil properties of buffer materials is described.

Chapter 4: Illustrates the results and discussions pertaining to thermal characteristics, gaseous and liquid contaminant transport properties of buffer materials. The influence of various geotechnical properties and temperature on these characteristics is established and the details are reported in this chapter.

Chapter 5: Explains the numerical modeling for the estimation of long-term performance of the buffer materials in DGR. The long-term performance of buffer materials was assessed by considering the synergetic effect of environmental conditions that prevail in a DGR, and the details are illustrated in this chapter.

Chapter 6: Summarizes the findings and major conclusions of the study.

Chapter 2

LITERATURE REVIEW

2.1. General

This chapter presents an overview of literature pertaining to the characterization of buffer materials for containment of radioactive waste. It includes a brief account of studies highlighting the influence of various phenomena such as the coupled heat and moisture migration, gas permeability, gas diffusion, sorption etc. on the long-term performance of buffer materials. Further, both experimental and numerical methodologies reported in the literature for assessing these parameters are presented in this chapter.

In view of providing the comprehensive understanding of buffer materials, the reviewed literature was purposefully divided into subcategories and the same is presented in the following.

2.2. Studies on Buffer Material Characterization

As highlighted in the previous chapter, clay mineral based geomaterials are widely accepted as an efficient buffer material for the effective containment of radioactive waste. Therefore, majority of the literature pertaining to the studies on buffer material discusses the characterization of smectite clay mineral based geomaterials particularly bentonite, and mixtures of sand and bentonite. Though the studies pertaining to this area have been initiated in the early eighties, they are still in active evolution. The following paragraphs describe briefly about the attempts made by the previous researchers to characterize the buffer materials and thereby designing an efficient buffer material.

Dixon et al. (1985) described a study on the maximum attainable densities of candidate buffer materials comprised of mixtures of sand and sodium bentonite (Na-bentonite), and illite for their potential application in the nuclear waste disposal. The study reported the significant increase in compacted density of Na-bentonite based buffers with the addition of sand without altering their swelling potential. The presence of sand in the buffer material also decreased its shrinkage potential as well as effective soil porosity and thereby the rate of contaminant mass diffusion decreased. The study concluded that the presence of 50 % sand by weight in the buffer material resulted in optimal physical properties.

Guven (1990) have investigated the longevity of bentonite as a buffer material. It has been reported that the longevity of bentonite depends on the stability of the smectite mineral component as well as on its ability to retain the intended functional property for a long period of time. Hydrothermal stabilities of smectites considerably vary according to their chemical and crystal structure properties. Trioctahedral smectites with Mg^{2+} and Li^{+} as base cations are characterized with very high hydrothermal stabilities (up to 850 °C) whereas iron-rich smectites exhibit the least hydrothermal stability. The most common smectites in bentonite are montmorillonites which are found to be stable up to 400 °C. For extremely hot repository conditions (i.e., above 300 °C), trioctahedral smectites like saponite and hectorites are considered to be effective.

Madsen (1998) investigated the mineralogical and geotechnical characteristics of compacted bentonite in view of its plausible application as a buffer material. Authors conducted an elaborate study on the influence of steam on the swelling behavior of bentonite. It has been reported that steam lowered the swelling pressure of compacted bentonite to about 60 % of its swelling pressure in the presence of water. The compacted mixtures of bentonite and 20 % by weight of cement showed higher swelling pressure and lower swelling strain compared to that of compacted virgin bentonite. The properties of bentonite are influenced to an extent by heat, steam, and cement; however, the compacted virgin, as well as modified bentonite, are found to be efficacious.

Further, Studds et al. (1998) measured the swelling behavior and hydraulic conductivity of sodium bentonite and sand-bentonite mixtures with distilled water and various ionic salt solutions. The swelling behavior of a sand-bentonite mixture is a function of the pore fluid chemistry, the applied effective stresses, and the clay-size fraction. It is observed that in dilute solutions, the bentonite mixtures subjected to small confining stress swells sufficiently to segregate the sand particles from the mixture to attain the void ratio corresponding to bentonite alone. Whereas, at high confining pressure or interaction with strong ionic solutions, the bentonite in the mixture has inadequate swelling capacity to segregate the sand particles and swelling is confined to the pore volume created by the sand. The swelling nature of a sand-bentonite mixture upon interaction with various aqueous solutions is predicted based on the swelling properties of the bentonite and the load-deformation properties of sand. Similarly, the hydraulic conductivity of a sand-bentonite mixture depends on the void ratio of bentonite, porosity and the tortuosity of the bulk matrix.

Yong (1999) conducted a detailed study on the influence of clay microstructure and internal energy on transport phenomenon through partially saturated expansive soils. The study also attempted to identify the compatibility between conceptual and numerical models.

Stewart et al. (2003) conducted studies on swelling and hydraulic conductivity of bentonite enhanced sand (BES) mixtures for their performance as environmental barriers. Authors observed sufficient swelling of bentonite within BES mixture at low effective stresses and described a prediction model based on Archie's equation by considering the tortuosity for swelling and hydraulic conductivity of BES upon interaction with various pore solutions.

In the following year, Komine and Ogata (2004) proposed a new method for predicting swelling characteristics of buffer materials. The swelling characteristics were determined from two sets of experiments; the first test is dedicated for measurement of bentonite swelling pressure and the other is for estimating the rate of swelling. This study evaluated the applicability of the proposed model by comparing the experimental results of different bentonites with that of predicted values.

Ada (2007) assessed the performance of compacted sand-bentonite mixtures in terms of hydrological and mechanical properties. Based on the extensive laboratory testing, the dosage of 30 % bentonite resulted in optimal engineering properties.

Wersin et al. (2007) evaluated the stability of bentonite at elevated temperatures. The alteration of the mineralogical composition is attributed to cementation by precipitation of silica which in turn transformed the smectite mineral into non-swellable illite with low swelling and plasticity as well as high hydraulic conductivity and diffusivity. Under wet conditions hydraulic and mechanical properties of the bentonite were not subjected to significant change; however, under dry conditions, bentonite was stable even at high temperature of 350 °C.

In 2008, Rao et al. characterized bentonite samples collected from north-west regions of India for their index properties, compaction, hydraulic conductivity and swelling characteristics. The variation of liquid limit, swell potential, swell pressure, and hydraulic conductivity with exchangeable sodium percentage and effective montmorillonite dry density has been quantified.

Alba et al. (2009) investigated the transformation of argillaceous materials present in the engineered barrier system into rare earth disilicates upon exposure to elevated temperature conditions that may prevail in a typical DGR. For this purpose, the saponite mineral was hydrolyzed using different ionic concentrations of the rare earth elements (viz. Sc, Lu, Y, Sm, Nd, La) at temperatures of 175 °C and 150 °C. The transformation of the mineral was quantified using X-ray diffractometer (XRD), nuclear magnetic resonance (NMR) and electron microscopy. It has been observed that the mineral saponite was transformed permanently into rare earth silicates upon exposure to the simulated DGR environmental conditions.

Yong et al. (2009) investigated the effect of Cu^{2+} cations (plausibly aroused from corrosion of the copper-based canister) on smectite consolidation behavior and transmission characteristics with and without the addition of sodium carbonate in the clay. The experiments aimed to identify the effect of copper ions in variable concentration on buffering capacity, permeability and consolidation. Authors concluded that swelling forces and buffering capacity are the dominant factors in deciding the performance of the buffer materials, through the formation and restructuring of microstructures in the buffer materials.

Galunin et al. (2011) established the stability range of the rare earth (RE= Se, Lu, or Y) disilicate and examined whether this disilicate phase would permit RE leaching under DGR experimental conditions. The experimental results were analyzed for the leaching rate and transformation of the crystalline and amorphous phases of RE by powdered X-ray diffraction and nuclear magnetic resonance technique. It could be observed that the stability of RE is related to its hydrated ratio and is stable within a wide range of pH. The stability was found to be increasing with the ionic radius of RE and it was confirmed that the confinement of radioactive wastes in engineered buffers is contributed by the formation of disilicate phases.

Wilson et al. (2011) reviewed the key issues and processes influencing the performance of bentonite barriers in radioactive waste disposal facilities. The major aspects such as temperature, the effects of radiation, canister corrosion, effects of ground water, and waste compositions govern the performance of bentonite. It has been concluded that the mechanisms involved in the transformation of bentonite under DGR conditions is complex and are strongly coupled. It was observed that in order to ensure the homogeneous nature of buffer, a swelling pressure of at least 1 MPa should be developed within the buffer. Also, the hydraulic conductivity of a bentonite barrier is strongly related to the density of the buffer material as well as interlayer cation density, and ionic strength of the groundwater.

2.3. Studies on Thermal Characteristics

Estimation of thermal characteristics of geomaterials is imperative for the applications like design of cover systems for landfills, mine tailing ponds, buffer materials for deep geological repositories, thermal stabilization of fine-grained soils, thermal storage, performance of pavements in extreme climatic conditions, studies on shrinkage of soil, design and lying of underground power cables, oil and gas pipelines, etc. (King and Halfter, 1982; Thomas, 1985; Issa, 1996; Rao and Singh, 1999; Arnepalli and Singh, 2004a). Among the thermal properties, thermal conductivity is the most important soil property associated with the conductive heat flow. In view of this, many studies devoted to determine thermal conductivity of geomaterials.

One of the pioneers in the field of thermal characterization of geomaterials, Johansen (1975) made an effort to arrive at relations which can be used for indirect determination of thermal conductivity parameters which in many cases are ignored during geotechnical analysis. A significant portion of the report was devoted to investigate the relationship between accuracy and level of information from the mathematical model developed. The effects of uncertainties in thermal conductivity values on thermal computations were also discussed.

Galbraith et al. (1998) described investigations in which moisture flux experiments were carried out using small-scale soil models subjected to both humidity and temperature gradients. The significance of temperature-driven transport compared to concentration driven component was identified from the analysis of the results. The study reported the importance of experimental facilities which overcome the limitations of small sample measurements carried out to produce reliable non-isothermal data.

Tarnawski and Leong (2000) analyzed thermal conductivity of soils over a range of moderate temperatures and at very low moisture content. It has been reported that the thermal conductivity of soils has not varied significantly till the critical moisture content. The study proposed two simple models for estimating the critical moisture content based on permanent wilting point and clay mass fraction.

Cho et al. (2001) reviewed the thermal and mechanical properties of compacted bentonite and sand-bentonite mixtures reported in the literature. It was found that thermal conductivity is increasing almost linearly with increasing dry density and water content of the bentonite. The coefficient of thermal expansion was found to be independent of the dry density, however, the specific heat of soil exhibited a linear relationship with water content.

Lahoucine et al. (2002) developed a thermistor based thermal probe to determine the thermal conductivity of bentonite and mixtures of bentonite and variable amounts of silica sand in them over a range of densities and water contents. The thermal conductivity was determined by comparing the measured and simulated temperature-time histories. The simulated temperature-time history was obtained from numerical computations of the two-dimensional heat conduction model of a sample including a thermistor. The temperature of the sample could be known from the resistance of the inserted thermistor. It has been concluded that the thermistor probe method provides good thermal contact between sample and thermistor and demands a less quantity of sample than the line heat source method.

Nichol et al. (2003) characterized unsaturated moisture movement through mine waste rock using thermal conductivity sensors which provide an estimation of matric suction. Long-term performance and accuracy of thermal conductivity (TC) sensors were evaluated using two years of monitoring data. Thermal conductivity variation with temperature and volumetric moisture content were measured using eighteen thermal conductivity sensors. The matric suction for each sample was measured independently using jet-fill tensiometers. TC sensors and tensiometers were installed at different depth and radial distances. The tensiometers were installed within 0.5 m of the TC sensors. In order to improve the contact of the ceramic thimble of the tensiometer with the waste rock, its tip was coated with saturated silica flour paste. A correction method for the ambient temperature was derived and a comparison between the corrected and uncorrected field measurements indicated that the magnitude of these corrections could be similar. Comparison of corrected measurements to the tensiometer measurements showed that the response of the thermal conductivity sensor to the initial arrival of a wetting front lagged behind the tensiometer measurements by 1-3 days. When compared to the tensiometer data, the TC sensor data tend to overestimate matric suction in the waste rock.

In 2004, Arnepalli and Singh developed a generalized relationship for determining the thermal resistivity of various soils from their dry density, moisture content, and percent fraction of various particle sizes. The field thermal resistivity of soils has been investigated using a field thermal probe and validated the proposed generalized equations with the results available in the literature.

Later, Tien et al. (2005) discussed improved thermal probe method for thermal conductivity measurement of sand-bentonite based buffer material. The relationship for the estimation of thermal conductivity with clay dry density, water content, and sand/crushed granite was established.

Rochais et al. (2008) characterized the particle layers at microscopic scale using the photo-reflectance microscopy technique and proposed a model to estimate the effective conductivity of different layers in the soil pore system by considering the properties of the gases confined in the pores and simulating the conduction flux through the layers in relation to its microstructure. Infrared microscopic measurements of thermal diffusivity were used to validate this approach and the characterization of silicon carbide layers was also presented in their work.

Tang et al. (2008) measured the thermal conductivity of compacted bentonite specimens using a thermal probe based on the hot wire method. The influence of various factors such as dry unit weight, moisture content, hysteresis, the degree of saturation and volumetric fraction of soil components on thermal conductivity was assessed. Further, a linear correlation for thermal conductivity of compacted bentonite with a volumetric fraction of air was developed based on experimental data.

2.4. Studies on Thermo-Hydro-Mechanical Characteristics

The thermo-hydro-mechanical (THM) behavior of buffer materials plays a pivotal role in assessing the performance of deep geological repositories, oil & gas extraction, geothermal energy systems and carbon sequestration technologies (Vardon et al., 2011). The major thermo-hydro-mechanical properties associated with buffer materials are that related to the coupled flow of heat and moisture in the form of water vapor diffusion due to the imposition of moderate temperature from the canisters.

In view of this, Kanno et al. (1994) investigated the moisture movement through buffer materials in response to a temperature gradient for their role in deep geological repositories by a series of experiments and numerical simulations. Highly compacted blocks of Japanese sodium bentonite were used as the buffer materials. The study showcased the theory and numerical formulation for the measurement of temperature and water content distribution in compacted bentonites under a temperature gradient. The experiment was designed to have one-dimensional vertical movement of heat and moisture and the results could be reproduced by the proposed mechanistic model.

Selvadurai (1996) attempted to solve the governing differential equation for the coupled heat and moisture movement in clay buffer using Galerkin finite element technique. The study primarily focused on the axisymmetric modeling of the hygrothermal process encountered in the single borehole element configuration developed for laboratory simulation. The results indicated that the thermal integrity of buffer material was maintained even after considerable amount of moisture from the buffer has lost.

Yong et al. (1997) experimentally verified that the moisture moves from both ends of the horizontal soil column specimen headed for the mid part of the soil column owing to both thermal and hydraulic gradient from the respective ends. It was observed that apart from overall volume change, a volume change occurs locally in the system. The study estimated the diffusivity parameters using the moisture and temperature profiles measured experimentally as well as that combined with the finite difference method, which employed Powell's optimization algorithm.

Ikonen (2003) have calibrated the thermal flux obtained from a line heat source and extended the solution of a line heat source with homogeneous material to analyze the actual canister. The maximum design temperature on the canister surface was limited to 100 °C. Due to parameter uncertainties in thermal analysis, the maximum canister temperature was set to 90 °C causing a safety margin of 10 °C. The study indicated that the temperature in the DGR can be restricted to 90 °C with reasonable canister and tunnel spacing and an initial canister power of 1700 Watts.

Agus (2005) presented a study on the hydro-mechanical characterization of sand-bentonite mixtures. A series of experiments, including basic and physicochemical characterization, microstructure and fabric studies, suction and swelling pressure measurements, wetting and drying tests, one-dimensional compression rebound test, one-dimensional cyclic wetting-drying test under constant vertical stress and saturated permeability test, were conducted on mixtures of calcium bentonite and quartz sand.

Poltze et al. (2007) simulated the effect of heat-producing waste in a repository by embedding a heater element in compacted bentonite blocks saturated for 35 months and then subjected to a heating phase of 18 months. Minute modifications in bentonite and a weak change in layer charge density as well as smectite chemical composition were noticed. Moreover, the THM characteristics such as water intake, thermal characteristics and porosity changes were observed which is an indication of cementation process.

Gens et al. (2010) detailed a fully coupled THM formulation that has been incorporated as an integral part of numerical tool CODE_BRIGHT. This version of the CODE_BRIGHT is capable of analyzing THM processes as well as homogeneous and heterogeneous chemical reactions and migration of chemical species. A one-dimensional axisymmetric analysis was conducted for investigating the behavior of bentonite barrier and intermediate adjacent rock. The THM results were obtained from three locations in the buffer material viz. one near to the interface of buffer and canister (heater), second in the central region of the buffer, and the third close to the interface of buffer and surrounding rock. Variation of temperature and degree of saturation with time and distribution of ionic strength and distribution of chalcedony concentration over a period of time was presented. An example of the application was briefly described which simulate the conditions of a repository for high-level radioactive waste. The study showcased the application of the computational tool as a feasible option for the THM analysis of engineering problems.

Cui and Tang (2013) presented the recent findings of the thermo-hydro-mechanical behavior of geological and engineered barrier materials in the nuclear waste disposal. The study used the natural Boom clay and compacted bentonite-based materials. Volume change behavior and shear strength studies revealed the role of carbonate content on engineering behavior. Soil with higher carbonate content correspond to higher effective cohesion and was more compressible. The thermal volume change depends on the over consolidation ratio (OCR), as the low OCR leads to thermal contraction while dilation occurs for high OCR values. The volume change behavior was also found to be time depended and this behavior was governed by the stress level and temperature. High smectite content signifies the effect of pore water salinity on volume change behavior of materials. Thermal contraction also found to occur at low OCR values for bentonite-based materials, but this was suction dependent which promoted thermal dilation. Under constant volume conditions, hydraulic conductivity decreased as a result of wetting and then increased in relation to macro-pore size. Wetting induced a decrease of macro-pore size, followed by an increase due to aggregate fissuring.

Rao and Ravi (2013) characterized Barmer-1 bentonite for hydro-mechanical properties such as swell pressure, saturated permeability, soil-water characteristic curve (SWCC) and confined compression strength at different dry densities. The relationships between swell pressure and saturated permeability coefficients of bentonite buffers were obtained by comparing the properties of Barmer-1 bentonite with bentonite buffers reported in the literature.

2.5. Studies on Water Vapor Diffusion

Moisture migration in soil affects heat and solute transport through it. The moisture transport defines the rate of biological processes in soil and water supply to plants, governs transpiration and ground water replenishment, controls runoff and has many other important functions in the environment (Pachepsky et al., 2003). Transfer of moisture and chemicals dissolved therein plays the pivotal role in the durability of structures as well as health and comfort of occupants. The correct description of moisture flow phenomena and their transport potentials are the key aspects (Janssen, 2011).

Cary (1979) measured the flow of heat through silty loamy soil at 7 °C and 36 °C under matrix potential near -30 kPa. An empirical correlation was proposed for deVries' method and calculated the thermal vapor diffusion coefficient for the three soils considered. The values were compared with the experimental results from the calorimeter. The thermal water vapor flow was estimated from the thermal conductivity of saturated soil, quartz content, water content, bulk density, and temperature.

Dobchuk et al. (2004) studied the fundamental mechanisms of water vapor diffusion through waste rock. This was achieved by conducting column tests on glass marbles and waste rock and developing a numerical model. The numerical model considered the diffusion coefficient, porosity, dry density, and sorption while determining the water vapor diffusion in the waste rock. It has been observed that the transient vapor flux depends on the slope of the sorption isotherm. The comparison of measured and predicted water vapor flux validated the estimated diffusion coefficient.

Jabro (2009) proposed an experimental setup for determining the isothermal water vapor diffusion through soil over a range of temperature and porosity conditions. The experimental setup comprised of a plexiglass box partitioned into two compartments by a soil specimen. Movement of water vapor was achieved by creating a gradient in water vapor across the soil reservoir by placing calcium chloride ($CaCl_2$) drying agent in a container suspended by a spring in one compartment and water in a container suspended by spring in the other compartment. The controlled temperature was achieved by keeping the apparatus inside a percival environmental chamber. Aggregate sizes varied from 2.8-2 mm, 2-1mm, and 1-0.5 mm. Samples were air-dried and contained 0.3-0.35 % water at the beginning of each set of measurements. The porous medium reservoir consists of a ring plexiglass with an inside diameter of 50.8 mm and a 200 mesh screen mounted below it. The springs inside the compartments were calibrated and the amount of water evaporated was measured in terms of the change in lengths of the spring.

Cleall et al. (2011) have conducted extensive investigations on non-isothermal moisture movement through unsaturated kaolin by considering thermal gradient, thermal hydraulic gradient, and isothermal hydraulic gradients. In the thermal gradient tests, overall moisture movement showed significant drying in the hot regions and a corresponding wetting in the cold regions. The accumulation of conservative chloride ions in hot regions indicated the cycle of vapor and liquid movement. As a whole, the study improved the water vapor flux calculations.

Cleall et al. (2013) investigated the movement of vapor in unsaturated bentonite, quantified water vapor fluxes and compared with the existing mechanistic theories. Accumulation of soluble chloride ion near the heat source indicated a cycle of movement of moisture away from the warmer region in the vapor phase and a subsequent movement of liquid phase towards the warmer regions due to the hydraulic gradient. Further, an empirical correlation was proposed to calculate the water vapor fluxes by knowing the variation of soluble chloride ion concentration and moisture content with time.

Belleghem et al. (2014) presented a new coupled heat and moisture migration model through porous building materials. This model was capable of estimating vapor diffusion as well as capillary moisture transport, simultaneously. The better agreement between the simulated and measured water vapor flow has been achieved by altering the liquid permeability or retention properties of the porous material.

2.6. Studies on Sorption

Calvet (1989) investigated the adsorption of organic chemicals on geological sediments. The adsorption of gaseous and liquid phases was examined and the physical meaning of the shape of the sorption isotherms has been described. The findings did not exhibit a general rule that describes univocally the relationship between the shape of isotherms and the nature of the adsorbate-adsorbent system. The adsorption kinetics were discussed by considering factors like the structure and properties of adsorbents, and organic carbon content in the adsorbate.

Devulapalli and Reddy (1996) evaluated the influence of nonlinear adsorption behavior on contaminant transport through clay liners. Two types of contaminants like hexavalent chromium and pentachlorophenol were studied using batch sorption experiment. It has been observed that the contaminant transport models grossly over predict retardation of contaminants at high solute concentrations by assuming linear adsorption kinetics. Therefore, it is important to incorporate the nonlinear adsorption behavior for precise estimation of contaminant transport through the liners.

Tsai et al. (2001) studied the transport of radionuclides through bentonite based buffer materials by considering the sorption and diffusion processes. The sorption and diffusion behavior of Cs and Sr through Jih- Hsing bentonite were established. It has been observed that the retardation factor obtained from diffusion experiments is one order less than that obtained from the batch sorption experiments; though, the diffusion experiments represents the field scenario in a better fashion.

Itakura et al. (2003) compared the sorption coefficients of natural clayey soils obtained from various methods. The sorption coefficient obtained from batch sorption experiments were compared with that of predicted based on organic carbon content present in the soil. On the contrary, the sorption coefficients resulted from the diffusion test represents the intermediate range and hence it is essential to assess the sorption parameters by employing at least two methods.

Sezer and Turkmenoglu (2003) studied the mineralogical and sorption characteristics of Ankara clay for the purpose of its potential application as a liner. Mineralogical analyses were carried out by XRD (X-ray diffraction), morphological features by SEM (scanning electron microscopy) and CEC (cation exchange capacity) by FAAS (flame atomic absorption spectroscopy). The study demonstrated the efficacy of fluvial clays as a landfill liner.

Nakayama et al. (2004) measured the dissolution rates of montmorillonite and diffusivity of hydroxide ions through compacted sand-bentonite specimens under alkaline groundwater conditions. The dissolution rate of montmorillonite was quantified using a linear relationship over a range of pH and temperatures. The diffusivity of hydroxide ions through the bentonite has been assessed with the help of pore diffusion model. At low temperatures, the dissolution of bentonite is insignificant and hence, the variation in permeability of compacted sand-bentonite buffers was established based on the coupled mass transport as well as reaction kinetics.

Bellir et al. (2005) investigated the suitability of natural clay as landfill liners by considering the influence of physicochemical parameters on clay contaminant interaction. The experimental results were fitted using theoretical Langmuir and Freundlich sorption isotherms. The results showed that the natural clay has a great retention capacity for the contaminant copper and hence, clay barriers are efficacious in containing it.

Vejsada and Vokal (2006) compared the sorption characteristics of various bentonites for cesium by employing batch sorption and diffusion experiments. Though the batch sorption experiments lack to simulate the geomaterial contaminant interaction, these experiments were conducted using very high liquid to solid ratios. On the contrary, the diffusion experiments do not recognize the slow changes in solution chemistry which may occur due to the interaction of bentonite with ground water on sorption characteristics. In view of these limitations, the sorption coefficients were obtained using both the sorption and diffusion-based methods. The study shows that the diffusion and batch sorption methods yield interchangeable results for bentonites having high smectite contents; however, the sorption characteristics are primarily dependent on L/S ratio.

Knop and Gulok (2008) employed laboratory column flow-through experiments to analyze the contaminant transport of acidic leachate through the compacted artificially cemented soil. The result showed that the intense of cement content increases the solute pore volumes required for the occurrence of a breakthrough. It has been observed that the addition of cement slightly enhanced the hydraulic conductivity and reduced the acidity of the effluent. It has been concluded that the amendment of cement to the soil is primarily responsible for enhanced attenuation of cement treated soil towards the acidic contaminants.

Vinsova et al. (2008) investigated the effect of groundwater exposure at elevated temperatures on the sorption properties of bentonite that was used in Mock up Cz experiment. Vertical placement of a canister was simulated in accordance with Swedish KBS-3 for a period of three years. The study evaluated the chemical changes caused by the long-term exposure of bentonite to thermal and hydraulic gradients. The short-term exposure of bentonite to elevated temperatures higher than 1000 °C may transform the smectites to illite. Even, if the temperature exceeds 900 °C for a short period, the physicochemical properties such as CEC and SSA undergo substantial changes and hence, deteriorate the performance of the bentonite as a buffer. For instance, a drop in CEC by 50 % leads to a decrease of sorption affinity by 10 % towards cationic radionuclides.

Cuevas and Liguey (2009) studied the ability of compacted Spanish ceramic clays as landfill barriers using leaching experiments. The mineralogical, physicochemical and heavy metal ions adsorption properties were characterized upon interaction with synthetic leachate containing Zn, Pb, Cd and Cr ions in it. It has been observed that the upper portion of the liner, which is in contact with the synthetic leachate, has been coated with a bio-film which in turn reduced the specific surface area of the clay without altering the mineralogical composition. The clay mineralogy and the presence of carbonates and soluble salts greatly influenced the barrier performance. It is concluded that the diffusion of anions and alkaline cations was faster than predicted based on the advective flow.

Werner et al. (2011) assessed the efficacy of various theoretical sorption isotherms using results of batch sorption and column flow-through experiments. It has been reported that the Freundlich sorption model performed well when the concentration independent sorption coefficients are used. Further, the modeling of the fate of the contaminant in pervious aquifers, which contains low carbonaceous particles, require considering relatively high advective groundwater velocities, slow diffusion limited by low sorption kinetic rates.

Sivachidambaram and Rao (2012) attempted to enhance the retention ability of bentonite for iodide by mixing it with 10 and 20 % silver kaolinite (Ag-K) on the dry mass basis. The Ag-K has been produced by heating the mixture of silver nitrate and kaolinite at 400 °C. The desorption of iodide retained by Ag-K was found to be nominal under extreme acidic and alkaline environments. The mixing of Ag-K with bentonite did not alter the chemical properties of the bentonite and thereby its expansive nature.

Xie et al. (2012) investigated the diffusion coefficient of chemo-toxic elements through bentonite in view of its function as an engineered barrier material. Authors reported that the transport parameters like diffusion and sorption coefficients are crucial for the safety assessment of chemo-toxic contaminants. Bentonite is found to be widely used as engineered barrier material considering its properties like low permeability, self-sealing capacity, and long-term stability. The permeability of bentonite increased with the ionic strength of the solution.

2.7. Studies on Gas Diffusion

Lai and Mortland (1962) studied the diffusion of sodium, cesium and calcium ions in bentonite by solving Fick’s law. The study introduced radioactive tracer for measuring the interdiffusion of isotopes in an approach to determine self-diffusion. This technique also offers the advantage of measuring trace level concentration thus obtaining a diffusion coefficient by mitigating the effect of concentration on it. For each element, the corresponding isotope was allowed to diffuse into the clay plug for a specified time and the plug was then cut into slices and the radioactivity of each slice was measured. The graphical method at special boundary conditions solved the Fick’s law and evaluated the self-diffusion coefficients of the ions.

Cho et al. (1993) assessed the various techniques such as in-diffusion, through-diffusion, and time-lag diffusion for determining diffusion characteristics of barriers for Cesium (^{135}Cs) and Iodine (^{129}I). The diffusion characteristics of ^{135}Cs and ^{129}I merit close attention in long-term disposal of nuclear fuel waste because of their long half-lives of 1.6×10^7 years for ^{129}I and 2.3×10^6 years for ^{135}Cs. They can also serve as useful models for the behavior of anions and cations in densely saturated clays as the chemistry of I^- and Cs^+ is comparatively simple.

Lambert and Renken (1999) assessed the utilization of industrial by-products as a concrete admixture to reduce the porosity, air permeability, and transport of radionuclides through concrete. Among the tested industrial by-products (fly ash, bottom ash, slag, silica fume and crumb rubber), the fly ash and slag are found to be efficacious in minimizing the contaminant transport properties.

Higashihara et al. (2001) proposed a new experimental approach to determine the diffusion coefficient of hydrogen gas through water-saturated compacted montmorillonite. The study estimated the diffusion coefficients for hydrogen gas in the montmorillonite using diffusion coefficients of helium using transient diffusion technique. The estimates were based on the assumption that the geometric factors in the compacted montmorillonite are approximately the same for diffusion of helium and hydrogen since both the molecules are non-sorptive in nature.

Itakura et al. (2003) estimated the effective molecular diffusion coefficient and sorption coefficient for volatile organic compounds through natural clays using curve fitting method.

Montes et al. (2005) studied the properties of bentonite in view of its use as a barrier material for radioactive waste confinement. The objective of this study includes simulation of chemical transformations with the help of thermo-kinetic-hydro-chemical code (KIRMAT: Kinetic Reactions and Mass transport), and estimation of swelling capacity by volume balance method. The study considered a barrier system consisting of 1 m thick zone of the engineered barrier which was sandwiched between geological fluid on one side and source metallic iron on the other side so that the difusion of geological fluid will occur into the barrier. Based on the numerical simulations it was observed that the engineered barrier in contact with the geological fluid was transformed significantly after 10,000 years of interaction. It is reported that the illitization, cation exchange and saponization are the most significant chemical processes whereas neo-formation of silicates, anhydrite, laumonite, magnetite and chlorite in the system are of minor importance.

Snoddy (2005) attempted to measure permeability and diffusivity of concrete and correlated with its physical parameters such as mix design, porosity, surface finish etc. For the determination of diffusion coefficient, uranium mill tailings were used as a source for radon gas emission. It is found that both diffusivity and permeability primarily depends on water binder ratio. Considering the favorable pozzolanic properties of flyash it was used as the cementing agent along with the cement. The study indicated that small defects with high tortuosity in the concrete acted as channels for air flow, however, these defects did not alter the diffusivity of concrete.

Allaire et al. (2008) compared various laboratory-based methods for the determination of the diffusion coefficient (D_s/D_o) using loamy sand. The study included: (1) small repacked soil columns in a closed system, (2) long repacked soil columns in a closed system, (3) small repacked or intact soil columns in an open system, (4) large flat soil columns containing macropores in a closed system, and (5) large intact monoliths in a closed system. In the absence of macro-pores, all methods yielded similar diffusion coefficient. Whereas, near a macropore, the diffusion coefficient might be higher than the regions without macro-pores. It is showed that preferential paths are very important for the diffusion in soil. In view of mitigating the sampling difficulties in preserving the preferential paths, an in-situ method is considered to be attractive. It is also observed that in the case of small samples, installation of samples on pressure plates or tension tables modify the soil air porosity (θ_a) and it becomes harder to obtain uniform θ_a with an increase in length of the soil column especially when the column is installed vertically.

Mazzeiri et al. (2010) discussed chemically modified bentonite for ensuring low hydraulic conductivity for permeants containing potentially aggressive chemicals. The study considered a combined chemico-osmotic diffusion test in order to investigate solute diffusion and to evaluate the potential for membrane behavior of propylene carbonate treated multi swellable bentonite (MSB). Combined chemico-osmotic diffusion test was performed on the specimen using 5 mM $CaCl_2$ solution, and the diffusion stage was preceded by permeation with distilled water followed by permeation with 5 mM $CaCl_2$ solution.

Unatrakarn et al. (2011) performed a series of experiments to estimate diffusion coefficients from pressure profile as a function of time coupled with a semianalytical solution of the one-dimensional diffusion equation. The diffusion coefficient resulting from the best fit curve was taken as the average diffusion coefficient. The significance of this study was to have a better understanding of the molecular diffusion coefficient which is important in several oil recovery and carbon dioxide (CO_2) storage processes. The diffusion coefficients of CO_2 and CH_4 in heavy oil were determined experimentally and it is observed that CO_2 is having higher diffusivity compared to CH_4. It is also observed that due to the tortuosity of the porous medium diffusivity of CO_2 in porous media is less compared to that in bulk oil and the increase in temperature in both the systems seems to increase the diffusion coefficient.

2.8. Studies on Gas Permeability

Altena et al. (1983) studied the applicability of gas permeation methods to characterize microporous and asymmetric ultra-filtration or hyper-filtration membranes. In this study, a better method to handle the data was presented by modifying the basic governing equations. Mean radius of the membrane pores were determined in terms of mean pressure across the membrane, and coefficient of gas permeability through it. The study conducted experiments on microporous millipore membranes with a nominal pore radius of 50 nm and on ultra filtration membranes of poly (2, 6-dimethyl-1, 4) phenylene oxide with a sharp pore-size distribution around 2 nm. The calculated pore radius for the Millipore membrane depends on the type of the gas used in the experiment. It is not possible to determine permeability coefficient of ultra-filtration membranes accurately since the permeation involves viscous flow thereby the study reported some limitations of the gas permeation method.

Abaci et al. (1992) investigated the two-phase flow of the mixture of liquids and gases at different proportions. An experimental technique for the measurement of relative permeability under steady state dynamic conditions was developed. Results for the combination of nitrogen with de-aired water and air with de-aired water were reported in this study. Three different sand samples such as fine sand, heterogeneous sand, and coarse sand were tested.

Calogovic (1995) presented the theoretical approach for the determination of the coefficient of gas permeability through porous material based on the variation of gas pressure with time. Theoretical results obtained were verified experimentally by using modified laboratory equipment. The comparison of results obtained using the proposed method with the results of popular constant pressure method confirmed the efficacy of the present study.

Stormont (1997) conducted gas permeability measurements in bedded rock salt formation. Two types of tests were conducted: constant pressure flow tests for permeability values higher than 10^{-18} m^2, and pressure decay tests for smaller permeabilities. The details of the equipment and measurement technique used were discussed, elaborately. Further, different test conditions for each type of tests were explained.

Bouazza and Vangpaisal (2003) measured the gas permeability through geosynthetic clay liners (GCL) by measuring pressure difference across the GCL at different flow rates and the tests were repeated for different gravimetric moisture contents. It has been observed from the experiments that the intrinsic permeability decreases with increase in gravimetric moisture content and it is found to be affected by the hydration process.

Billiotte et al. (2008) conducted experimental studies on gas permeability of mudstones. Transient pulse method was employed to measure permeability. The study investigated the relationship between the permeability and state of stress between the rupture of the sample and the permeability. From experimental observations, it was concluded that gas permeability decreases with the increase of confining stresses due to the sealing of micro-fissures in the sample and this reduction is irreversible after loading-unloading cycle. Furthermore, it was found that at confining pressures equivalent to the lithological pressure at a depth of 467 m, the variability in the permeability was not observed.

2.9. Numerical Analysis of Buffer Materials

Rowe (1990) discussed about the various mathematical techniques for the contaminant transport modeling such as finite layer techniques, inversion of transforms, space and time discretization, sensitivity analyses etc. The manuscript mainly described the background for programs using POLLUTE and MIGRATE.

Franz and Rowe (1993) conducted numerical and analytical studies for groundwater flow and contaminant transport at a landfill site in Canada. Three models such as FLOWPATH, USGS MOC and POLLUTE were described in the manuscript.

Authors concluded that these models are successful in simulating groundwater flow and contaminant transport conditions at landfill sites.

Selvadurai (1996) used Galerkin finite element technique for solving the coupled heat and moisture movement through clay buffers. Main attention of the study was focused on the axisymmetric modeling of the hygrothermal process encountered in the single borehole element configuration developed for laboratory simulation. The results indicated that the buffer is able to maintain its thermal integrity even in situations where there is a significant loss of moisture from the buffer. Inspecting the condition of the buffer at the termination of the experiment, there was no evidence for shrinkage of the buffer as a result of the moisture depletion process.

2.10. Studies on Soil Suction and Hydraulic Conductivity

Dixon et al. (1985) developed a common relation for hydraulic conductivity in terms of dry density and showed that mineralogy is not governing the saturated hydraulic conductivity. Experiments were performed on Kunigel VI bentonite at different mineralogy and dry density.

Feng et al. (2002) proposed a mathematical approach from the experimental data by considering the effects of capillary hysteresis. Authors found that the main hysteresis loop and the primary scanning curves are stable and reproducible over a two-year testing period and therefore, the thermal conductivity matric suction sensor is suitable for long-term suction measurements.

Loiseau et al. (2002) observed that the permeability of compacted sand-bentonite mixtures depend on the hydraulic gradient when they are at the saturated condition. A significant interaction between the clay and water was found and therefore in the unsaturated case also the hydraulic conductivity governs the permeability.

Shuai et al. (2002) have studied the influences of the environmental factors (such as ambient temperature, pH value, freeze-thaw cycles and wetting-drying cycles) on the performance of the newly developed soil suction sensor. Authors proposed a technique for temperature correction in order to eliminate the effect of thermal influences. Tests were conducted in a freezing environment using a pressure plate apparatus with three thermal conductivity soil suction sensors placed inside. The test results indicate that the freeze-thaw cycles do not appear to influence the soil suction measurements after thawing. However, a drop in suction measurement was observed during freezing process which was attributed to the latent heat of fusion associated with water. As a result, the sensor readings are meaningless when the soil becomes frozen. Authors proposed a hysteresis model to account for hysteresis which can be used to modify the data obtained according to the wetting and drying history of the sensor.

Ye et al. (2009) determined the hydraulic conductivity of GMZ bentonite by simultaneous profile method through a specific infiltration cell with five relative humidity probes. The results of studies on water retention properties showed that the confining conditions do not govern the water retention capacity at high suctions above 4 MPa and at low suctions below 4 MPa, the confined condition reduced the water retention capacity. Mercury intrusion porosimetry (MIP) and environmental scanning electron microscope (ESEM) were used to find the microstructure at different states of compaction under constant volume condition. Authors concluded that the bentonite hydration in the infiltration test is a diffusion controlled process rather convection process.

2.11. Summary and Critical Appraisal

Based on the literature review reported above, many attempts have been made by the pioneer researchers to identify suitable buffer material to contain radioactive wastes. Majority of the studies focused on the maximum attainable density of the buffer material and its longevity in terms of geotechnical properties. In general, clay mineral based fine-grained geomaterial such as bentonite is preferred as buffer material of a typical deep geological repository to isolate and contain the radioactive waste contained canisters from the surrounding geoenvironment. This is primarily due to the favorable contaminant transport properties and self-healing ability associated with the bentonite. However, due to the substantial volume change behavior of the bentonite as a result of alteration in moisture regime when subjected to moderate temperature conditions and subsequent desiccation cracking, sand-bentonite mixtures are commonly considered as efficient buffer materials (Dixon et al., 1985; Ada, 2007; Rao et al., 2008). Optimum mixtures of buffer material are selected by assessing the performance of compacted sand-bentonite mixtures in terms of hydrological and mechanical properties by carrying out a variety of laboratory tests. Finally, previous researchers recommend an optimum sand-bentonite mixture with 30 percent bentonite by weight (Dixon et al., 1985; Ada, 2007; Rao et al., 2008).

Researchers have experimentally demonstrated the coupled heat and water flow in soil column and presented the numerical solution for differential equations governing coupled heat flow and moisture movement in buffer materials (Cary, 1979; Kanno et al., 1994; Selvadurai, 1996; Yong et al., 1997; Galbraith et al., 1998; Tarnawski and Leong, 2000; Cho et al., 2001). In order to demonstrate the heat flow characteristics, it is essential to quantify the thermal conductivity of the geomaterials. Many authors developed thermal probes to measure thermal conductivity of soils and have established relationship of thermal conductivity with dry density, water content, percent size fraction, degree of saturation, volumetric fraction of soil constituents, etc. (Lahoucine et al., 2002; Arnepalli and Singh, 2004b; Tien et al., 2005; Tang et al., 2008). In most of the studies, it is observed that at very low moisture content there is no significant variation in thermal conductivity of soils, and then begins to increase from a certain critical moisture content, the value of which tends to depend on clay mass fraction, dry density and water content of the buffer.

Contaminant transport properties are also critical in the characterization of buffer materials for effective and safe disposal of the radioactive waste. Many researchers have conducted batch sorption studies and laboratory column flow-through experiments to analyze the transport of contaminants through soils (Devulapalli and Reddy, 1996; Tsai et al., 2001; Bellir et al., 2005; Knop and Gulok, 2008). Authors concluded that the experimental results can be analyzed by fitting well-known theoretical sorption models such as Langmuir and Freundlich to understand the contaminant-geomaterial interaction.

Moreover, the high-level radioactive waste contained in the canister generates hazardous gases during the service life which may escape through the buffer material. However, the efficiency of the buffer material to contain these canisters highly depends on the fundamental interaction between the materials and hazardous gases under variable environmental conditions (Lambert and Renken, 1999; Snoddy, 2005; Higashihara et al., 2001; Unatrakarn et al., 2011). This interaction is quite complex in nature and may alter the physicochemical characteristics of the materials formed. To understand the above-mentioned phenomena from the fundamental point of view, it is very much essential to evaluate the gas permeability and diffusion characteristics of various materials under simulated DGR conditions.

Even though many researchers have conducted studies on buffer materials pertaining to their thermo-mechanical behavior and sorption and desorption characteristics individually, majority of the studies lack a synergetic approach for characterization of these materials by considering the effect of thermal flux on the migration of moisture which in turn results in a change of thermal properties. This scenario creates the coupled transport of moisture and heat which is responsible for the change of their fundamental behavior in terms of unsaturated hydraulic conductivity, sorption & desorption as well as gas diffusion and permeability characteristics. Hence it is mandatory to characterize the buffer material considering the combined influence of above-mentioned factors in a synergetic fashion.

Chapter 3

METHODOLOGY AND EXPERIMENTAL INVESTIGATIONS

3.1. General

This chapter presents the experimental investigations and methodologies employed for characterizing physical, chemical, geotechnical and mineralogical properties of buffer materials in view of assessing their efficacy to contain high-level radioactive waste canisters. The design details of a newly developed test setup for the determination of coupled heat and moisture transport properties of buffer materials are also reported. Further, the methodologies to evaluate liquid and gaseous contaminant transport properties and sorption characteristics of buffer materials are illustrated.

3.2. Materials Selection

Clay mineral based fine-grained geomaterial such as bentonite is considered as buffer material of a typical deep geological repository (DGR) due to its favorable contaminant transport properties and superior self-healing ability, as highlighted in the previous chapter. However, the substantial volume change behavior of bentonite upon the alteration in moisture content has enforced in considering sand-bentonite mixtures as an efficient buffer material (Dixon et al., 1985; Ada, 2007; Rao et al., 2008). Therefore, different sand-bentonite mixtures were synthesized using commercially available fine-sand and sodium bentonite with different weight fractions of bentonite in them viz. 30 %, 50 %, 70 % and 100 % denoted as SB30, SB50, SB70, and SB100, respectively. The physical, mineralogical, geotechnical, thermal and coupled flow properties, sorption characteristics, and contaminant transport characteristics of the selected geomaterials were obtained using various methodologies and the same is presented in the following.

3.3. Physical Characteristics

3.3.1. Specific gravity

The specific gravity (G) of the selected materials were determined with the help of a helium gas pycnometer (Quantachrome, USA) as shown in Figure 3.1, by following the guidelines in ASTM D5550 (2006).

Representative samples of the chosen materials were oven-dried and a known weight of the sample was transferred into the pycnometer sample holder to measure its solid volume. Prior to the measurement of solid volume, the sample was evacuated to expel the entrapped gas or vapor present in it. From the measured solid volume and weight of the sample, the specific gravity was determined using mass-volume relationships given in Equation 3.1. The specific gravity values of the geomaterials were then reported by averaging the values of five independent measurements.

$$G = \frac{(M_s/V_s)}{\rho_w} \tag{3.1}$$

where M_s is mass of soil specimen, V_s is volume of soil solids and ρ_w is density of distilled water at 4 °C.

Figure 3.1 Helium gas pycnometer

3.3.2. Particle size distribution characteristics

The particle size distribution characteristics of the selected materials were obtained by conducting both sieve- and sedimentation- analyses as per ASTM D6913 (2009) and ASTM D422 (2007), respectively. Approximately 500 g of air-dried sample was considered for this purpose and washed through sieve number 200 (i.e., 75 µm) using a jet of water. The material retained on 75 µm sieve was subjected to dry-sieve analysis and the material passed through 75 µm was utilized for sedimentation analysis. Results of sieve and sedimentation analyses were combined to obtain the complete particle size distribution characteristics of the selected materials.

3.3.3. Consistency limits

Consistency limits (known as Atterberg's limits) such as liquid limit (w_L), plastic limit (w_P), and shrinkage limit (w_S) were determined as per the guidelines in ASTM D4318 (2002) and ASTM D427 (2008).

3.4. Chemical and Mineralogical Characteristics

3.4.1. Chemical characteristics

The chemical composition of the geomaterials in the form of major oxides was determined using an X-ray fluorescence test setup, XRF (Phillips 1410, Holland). For this purpose, approximately 4 g of finely ground sample, 1 g of microcrystalline cellulose and isopropyl alcohol were mixed thoroughly using mortar and pestle and the mixture was kept below an infrared lamp for slow drying. A small aluminum dish of 33 mm inner diameter and 12 mm height was taken and two third of it was filled with a mixture of 70 percent methylcellulose and 30 percent paraffin wax, followed by the dried sample. In order to make sample pellet, the soil-filled aluminum dish was compressed with the help of a hydraulic jack by applying a load of approximately 5 tons. Further, the chemical composition of the material was determined by mounting the sample pellet in the sample holder of the XRF test setup.

3.4.2. Mineralogical characteristics

The mineralogical characteristics of the geomaterials were obtained using powder X-ray diffraction technique, XRD (PANanalytical X'pert Pro, Netherlands) with copper monochromated Cu-K_α as the source radiation. The X-ray diffractometer was set to a continuous scan mode with the range of scanning angle 2θ from 5 ° to 90 °. The powdered soil samples were air-dried and stored in a low relative humidity desiccator under controlled temperature to avoid the adsorption of water vapor. Further, the desiccated powder sample was transferred to the sample holder of the XRD machine and irradiated with the incident radiation within the focal plane of the source and detector (Goniometric circle). The scanning process was initiated from lower 2θ angle to the higher and the corresponding relative intensities of the diffracted radiations were filtered using a monochromator placed between the sample and the detector. Subsequently, the intensity of diffracted X-ray radiations was recorded in order to obtain the X-ray diffraction patterns of the sample. The minerals present in the sample were identified using the international center for diffraction data (ICDD, 2010).

3.5. Geotechnical Characteristics

3.5.1. Compaction characteristics

Standard Proctor compaction tests were performed on the selected geomaterials to assess their compaction characteristics as per the guidelines in ASTM D698 (2012). The compaction characteristic curves were established by plotting the variation of dry unit weight (γ_d) with the molding moisture content (w).

In order to minimize the amount of the sample and compaction energy required for establishing the compaction characteristics of the geomaterials, a miniature compaction apparatus developed by Sridharan and Sivapullaiah (2004) was employed (as depicted in Figure 3.2). The miniature compaction apparatus consisted of a cylindrical mold having an internal diameter of 38 mm and height of 100 mm. Based on the energy required per unit volume of the sample corresponding to the standard Proctor compaction test, the weight of miniature hammer was taken as 1 kg, and the drop height was limited to 160 mm. A detachable base plate and a collar of height 35 mm were attached to either side of the compaction mold to obtain a compacted specimen of 38 mm diameter and 100 mm height.

Air-dried samples of sand-bentonite mixtures such as SB10, SB20, SB30, SB40, SB50, SB70 and SB100 were synthesized. Approximately, 300 g of sample was mixed with predetermined moisture contents and stored in air-tight polyethylene bags in a humidity controlled desiccator for sample maturation. After 24 h of the maturation, the moist samples were taken out of desiccator and compacted in the miniature compaction mold in three layers by imparting thirty six blows per layer. Later, the collar was detached from the miniature compaction apparatus and the projected soil layer above the brim of compaction mold was trimmed using a wire knife. The compacted specimen was ejected from the cylindrical mold and its bulk unit weight was measured. Three representative samples were collected from the compacted specimen for measuring its mean gravimetric moisture content using the oven-drying method. Knowing the bulk unit weight and corresponding gravimetric moisture content, the compaction characteristic curve was established. By following the above methodology the compaction characteristics of the selected sand-bentonite mixtures were obtained.

Figure 3.2 Miniature compaction test setup

3.5.2. Hydraulic conductivity

The low hydraulic conductivity is one of the most demanding properties of a buffer material to limit the influx of groundwater containing potentially corrosive substances into the repository, and at the same time to prevent the migration of radionuclide from the waste into the surrounding geoenevironment. Further, the United States Environmental Protection Agency, USEPA, recommended that the hydraulic conductivity of compacted clay liners used for disposal of hazardous waste should not be more than 1×10^{-9} $m \cdot s^{-1}$ (USEPA, 1989).

With this in view, the hydraulic conductivity of the selected buffer materials was evaluated using flexible wall permeameter (Humbolt, USA) by following the guidelines presented in ASTM D5084 (2010). For this purpose, cylindrical samples of 38 mm diameter and 76 mm height were prepared in the split cylindrical mold, by compacting the geomaterial in three layers using the handheld hammer to achieve its maximum dry unit weight at OMC. In order to reduce the testing time required, the sample height was restricted to 25 mm, the minimum height recommended by standards. Before commencement of the test, the top and bottom drainage tubes leading to the permeameter cell were vented to remove the entrapped air. The bottom porous stone was placed over the bottom pedestal of the cell with a filter paper and then the soil sample was carefully placed over the filter paper. The top filter paper with the porous stone and top cap were placed above the sample. The rubber membrane was placed around the soil sample using a membrane stretcher, and the O' rings were placed at both top and bottom to seal the membrane to the base and top pedestal. The permeameter cell was placed in position on a bottom pedestal and the cell was fixed by bolting it to the bottom plate of the permeation cell. The top and bottom drainage were connected to a burette. The flexible wall permeameter setup is shown in Figure 3.3.

Figure 3.3 Flexible wall permeameter

Initially, the sample was pressurized to a minimum pressure of 35 kPa and later the soil sample was saturated by applying the back pressure till the Skempton’s pore pressure parameter B approaches unity. Further, a constant head test was performed to obtain the hydraulic conductivity. In order to achieve this, a pressure head difference of 50 kPa was maintained between the top and bottom of the soil specimen with the help of a pressure-volume control system. The amount of the permeant (q) passed through the soil sample was monitored and the hydraulic conductivity of the geomaterials was obtained by using the following relationship (ASTM D5084, 2010).

$$k=\frac{\Delta q\times L}{A\times h\times \Delta t} \tag{3.2}$$

where, k is hydraulic conductivity in $m \cdot s^{-1}$; Δq is quantity of flow for given time in m^3; L is height of the soil specimen in m; A is cross-sectional area of specimen m^2; h is hydraulic head causing flow in m, and Δt is time interval in seconds.

3.6. Thermal Properties

The long-term performance of the buffer material is governed by the hydrogeological, thermomechanical, and chemical processes. The buffer material is subjected to variable temperatures due to its spatial and temporal variation in thermal properties as well as the decay of radioactive compounds and associated exothermic reactions. Hence, it is mandatory to understand the variation in the buffer material properties with temperature. The existence of the temperature gradient across the buffer material results in moisture imbalance in the direction of heat migration which in turn imposes coupled migration of heat and moisture through it.

Among the thermal properties, thermal conductivity is the most important soil property associated with heat migration. The heat capacity of a soil is usually proportioned with fractions of water and soil solids present in it. With this in view, the present study evaluated the thermal conductivity of buffer materials using an in-house fabricated thermal probe. Experimental setup for assessing the thermal properties of buffer materials comprised of thermal probe, PVC molds, constant DC supply, and a data acquisition system.

3.6.1. Experimental setup

Thermal probe was designed and fabricated in-house using stainless steel tube of 7 mm internal diameter, 10 mm external diameter and 100 mm length, as shown in Figure 3.4. Nichrome wire was used as heating element provided at the center of the probe and the annular space around the heating element was filled with magnesium oxide (MgO) to act as an electrical insulator and to ensure uniform dissipation of heat generated by the heating element. To measure the temperature of the probe, two T-type thermocouples were provided each at one-third distance from both top and bottom ends. In order to minimize the heat loss from the top end of the probe, 25 mm distance from the top was made as non-heating portion referred as cold region. The probes were kept in position with the help of thermal insulating support system as depicted in Figure 3.4b. In Figure 3.4b, the wires in white color are the power supply leads to connect to the constant DC power supply unit and blue color wires are T-type thermocouples for temperature measurement. The Agilent make constant DC power supply unit, as depicted in Figure 3.5, was employed for supplying constant power to the probe and a Campbell scientific data logger (refer Figure 3.6) was employed for continuous monitoring of the temperature of the probe. Figure 3.7 depicts a closer view of the data logger terminals with thermocouples connected to it. PVC sample mold with an internal diameter 100 mm and height 210 mm was used for compacting the geomaterial. Figure 3.8 depicts the compacted soil specimens in PVC sample molds connected to constant DC power supply unit.

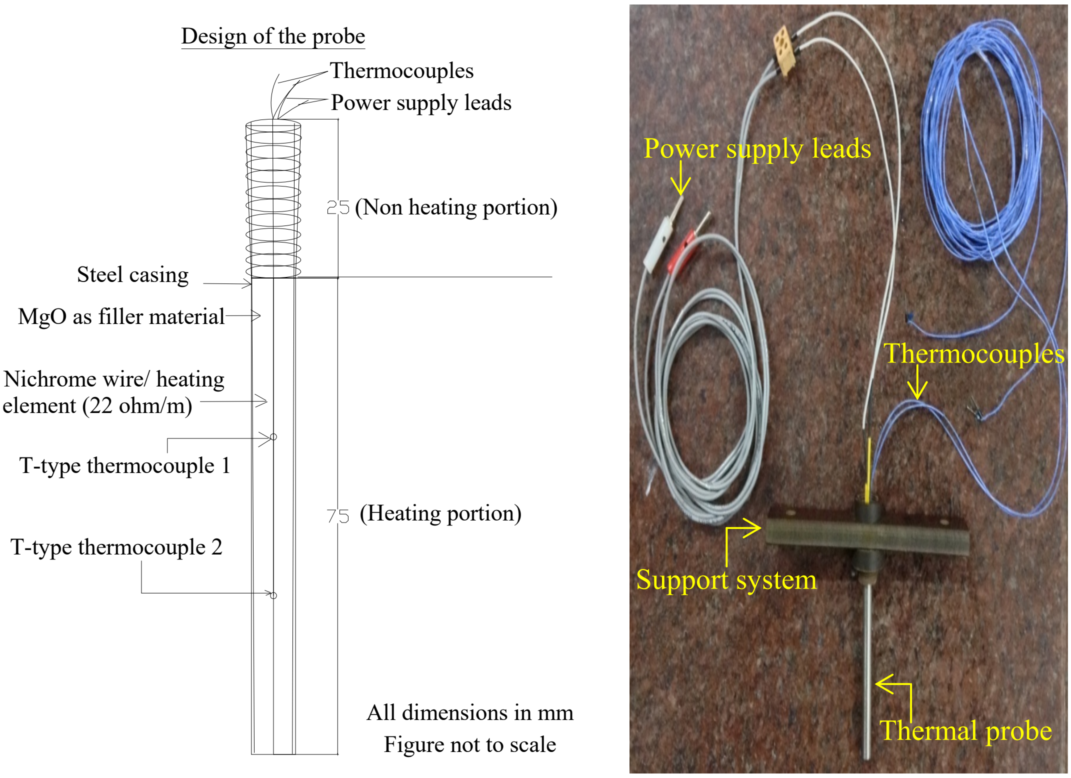

(a) Schematic view

(b) Photographic view

Figure 3.4 Thermal probe fabricated for assessing thermal properties

Figure 3.5 DC power supply unit used for constant power supply to the thermal probe

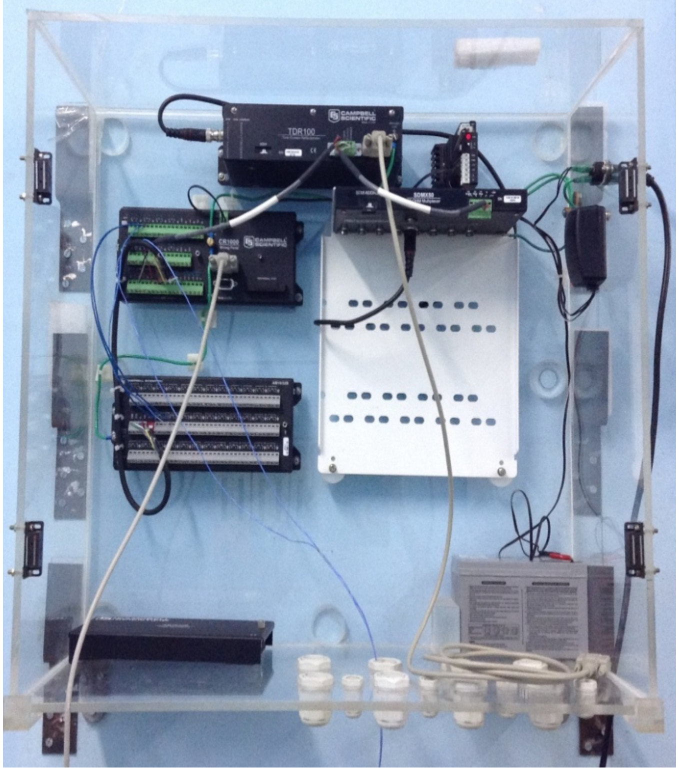

Figure 3.6 Thermocouples connected to the data logger

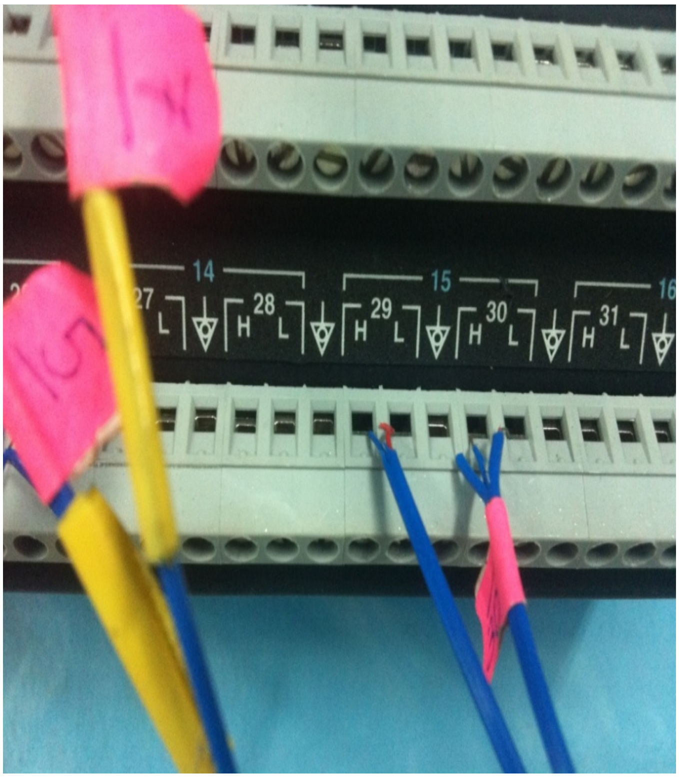

Figure 3.7 A closer view of thermocouples connected to the data logger

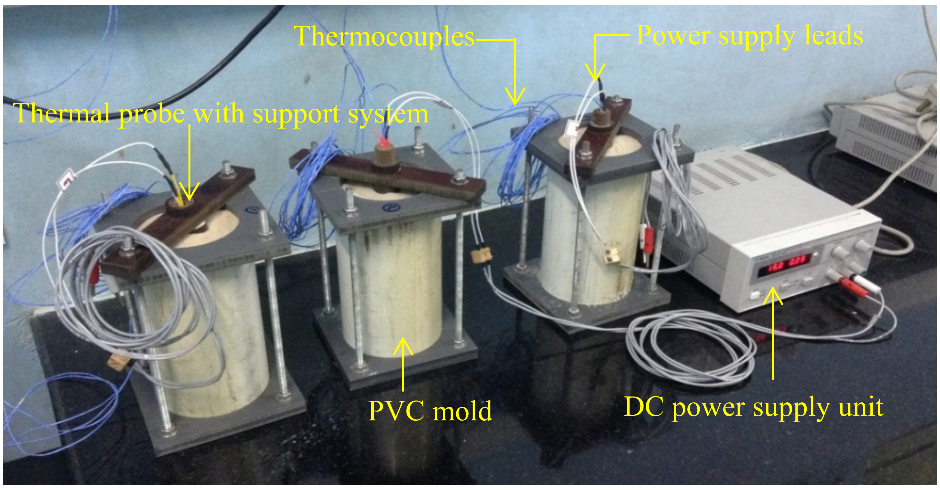

Figure 3.8 Apparatus used for determining thermal conductivity of buffer materials

3.6.2. Working principle of thermal probe

Working principle of the thermal probe was based on the transient heating technique of thermal conductivity measurement. The transient heating technique incorporates the fact that the rate of temperature increase of heat source when subjected to constant heat flux, depends on the thermal conductivity of the material in which it is embedded. In this method, the heat source was assumed to be a line of infinite length and infinitesimal diameter and the embedded material was assumed to be homogeneous, isotropic, and of infinite extent. Moreover, the temperature at any point in the medium in which the line heat source was embedded depends on the duration of heating and the thermal conductivity of the medium, and mathematically it can be represented by Equation 3.3 (Arnepalli et al., 2004; Joseph, 2014).

$$\frac{\partial T}{\partial t}=\alpha_D\left[\frac{\partial^2 T}{\partial r^2}+\frac{1}{r}\frac{\partial T}{\partial r}\right] \tag{3.3}$$

where T is temperature of the medium, t is time, α_D is thermal diffusivity [= $K/(\gamma\times C_p)$] and K is thermal conductivity (inverse of thermal resistivity, R_T) of the soil, γ is bulk unit weight of the soil, C_p is specific heat capacity of the soil and r is radial distance. The temperature rise ΔT between times t_1 and t_2 can be obtained using Equation 3.4 (Arnepalli et al., 2004; Joseph, 2014).

$$\Delta T=\frac{Q}{4\pi K}\log\left[\frac{t_2}{t_1}\right]=s\times\log\left[\frac{t_2}{t_1}\right] \tag{3.4}$$

From the above relationship, it is comprehensible that the variation of temperature with time in logarithmic scale yields a straight line and its slope, s can be related to thermal conductivity, K of the medium using the following relationships.

$$s=\frac{Q}{4\pi K} \tag{3.5}$$

$$Q=I^2\xi=\frac{V^2}{\xi} \tag{3.6}$$

where Q is heat generated, ξ is electrical resistance per unit length of the heating element (22.5 Ω·m), V is applied voltage and I is applied current (Arnepalli et al., 2004; Joseph, 2014; Surya et al., 2014). From Equations 3.4, 3.5 and 3.6, the thermal conductivity of the medium can be obtained as:

$$K=\frac{2.303\times I^2\times\xi}{4\pi s}=\frac{2.303\times V^2}{4\pi\xi s} \tag{3.7}$$

3.6.3. Calibration of thermal probe

The thermal probe was calibrated using glycerol whose thermal conductivity value is known. For this purpose, the PVC sample mold was filled with analytical grade glycerol (Merck made, ≥ 99.5 % purity, density 1.231 $g\cdot cm^{-3}$) and the probe was inserted in it. The thermal probe was allowed to attain thermal equilibrium with glycerol till both the thermocouples of the probe measured identical ambient temperature of glycerol. Further, power supply leads of the probe were connected to the constant DC supply unit and the leads of T-type thermocouples were connected to the data acquisition system. Calibration of the thermal probe was performed by applying different voltages viz. 15 V, 20 V, 25 V and 30 V with the help of a constant DC power supply. For each of these applied voltages, variation of probe temperature with time was recorded as shown in Figure 3.9.

The thermal conductivity value was determined from the slope of temperature versus logarithmic time response using Equation 3.7. The slope was precisely obtained from regression analysis of the linear portion of the temperature versus time response, as shown in Figures 3.9 and 3.10. For the sake of brevity, Figure 3.10 presents the regression results for an applied voltage of 20 V. From the slope value, the thermal conductivity of glycerol was determined and compared with the known thermal conductivity value of glycerol (0.287 $W\cdot m^{-1}\cdot K^{-1}$). The percent difference along with regression coefficient, R^2 between the experimentally measured and known values of thermal conductivity of glycerol was obtained and the same is reported in Table 3.1. Based on the percent difference as well as the regression coefficient, the optimal voltage to be applied for precise measurement of the thermal conductivity using the thermal probe was found to be 15 V. Therefore, the thermal conductivity of buffer materials was obtained experimentally by supplying the DC voltage of 15 V to the probe. To enhance the confidence regarding the optimal voltage to be applied, calibration efforts were extended using Ennore sand whose thermal conductivity is established as 0.225 $W \cdot m^{-1} \cdot K^{-1}$ (Joseph, 2004). The obtained results pertaining to the thermal conductivity of Ennore sand is also presented in Table 3.1. From the data presented in Table 3.1, it can be seen that the thermal conductivity values obtained with the applied voltage of 15 V yield satisfactory results with reasonable percent difference and R^2 value.

Table 3.1 Calibration results of the probe using glycerol and Ennore sand

Applied Voltage (V)	**Current (I)**	**Thermo couple**	**Slope**	R_T **($m \cdot K \cdot W^{-1}$)**	**K ($W \cdot m^{-1} \cdot K^{-1}$)**	**Percent difference (%)**	R^2
Glycerol							
15	0.05	1-TC1	4.36	3.17	0.32	9.94	0.997
		1-TC2	5.12	3.73	0.27	-6.50	0.970
		2-TC3	3.97	2.89	0.35	20.59	0.989
		2-TC4	3.63	2.64	0.38	32.11	0.995
		3-TC5	5.79	4.21	0.24	-17.24	0.983
		3-TC6	6.27	4.56	0.22	-23.67	0.984
20	0.06	1-TC1	12.36	5.62	0.18	-38.01	0.982
		1-TC2	13.95	6.34	0.16	-45.06	0.980
		2-TC3	9.61	4.37	0.23	-20.22	0.986
		2-TC4	9.72	4.42	0.23	-21.13	0.990
		3-TC5	13.65	6.21	0.16	-43.87	0.986
		3-TC6	16.11	7.33	0.14	-52.43	0.984
25	0.08	1-TC1	25.09	6.85	0.15	-49.10	0.981
		1-TC2	29.74	8.11	0.12	-57.05	0.969
		2-TC3	12.26	3.34	0.30	4.18	0.992
		2-TC4	12.09	3.30	0.30	5.65	0.990
		3-TC5	16.39	4.47	0.22	-22.07	0.985
		3-TC6	18.75	5.12	0.19	-31.89	0.984
30	0.10	1-TC1	22.55	4.10	0.24	-15.06	0.990
		1-TC2	24.58	4.47	0.22	-22.05	0.990
		2-TC3	22.23	4.04	0.25	-13.81	0.987
		2-TC4	22.05	4.01	0.25	-13.12	0.984
		3-TC5	25.57	4.65	0.22	-25.07	0.994
		3-TC6	27.44	4.99	0.20	-30.19	0.986
Ennore sand							
15	0.05	1-TC1	6.38	4.64	0.22	-4.25	0.989
		1-TC2	6.23	4.53	0.22	-1.94	0.987
		2-TC3	5.96	4.34	0.23	2.50	0.927
		2-TC4	5.72	4.16	0.24	6.80	0.994
		3-TC5	6.13	4.46	0.22	-0.34	0.972
		3-TC6	6.10	4.44	0.23	0.15	0.975

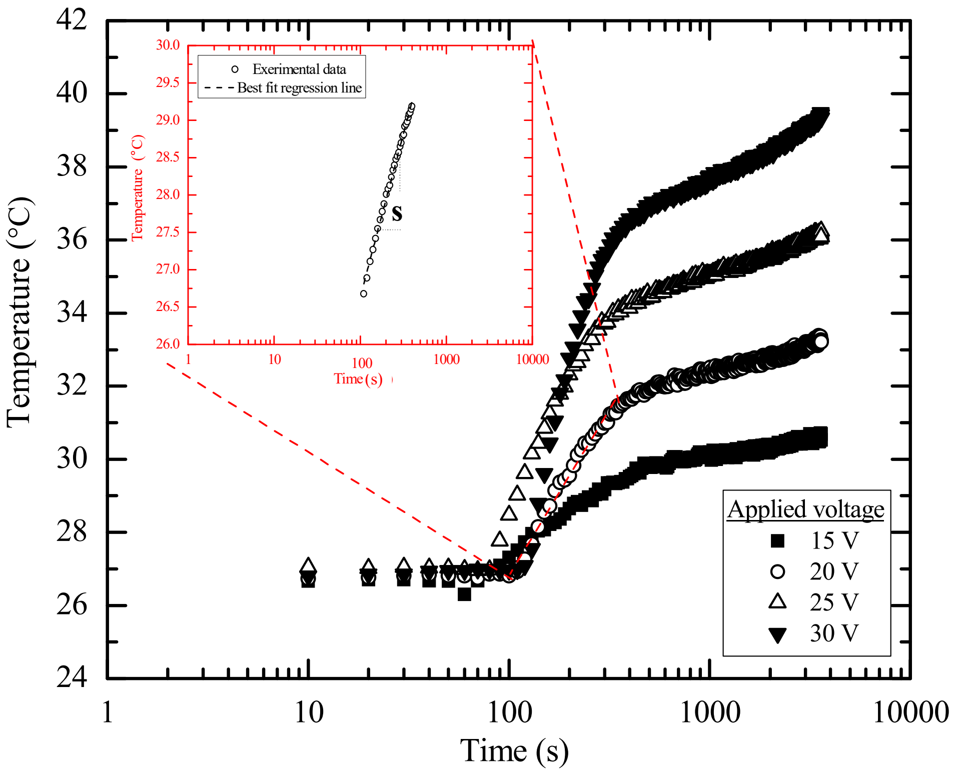

Figure 3.9 Variation of temperature with time for different applied voltages

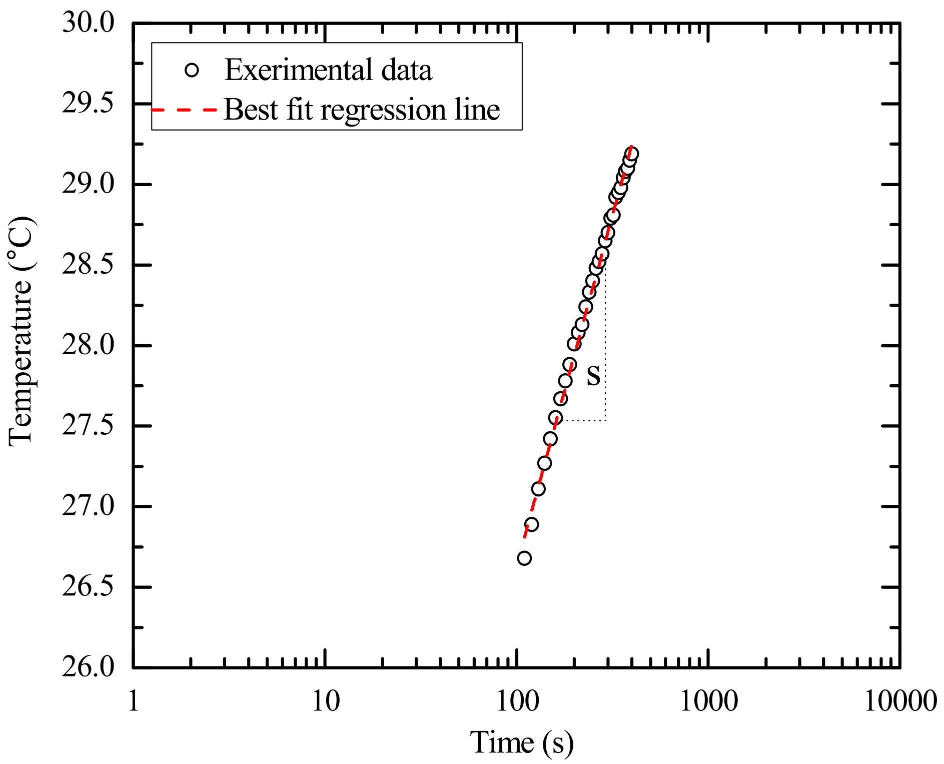

Figure 3.10 Regression analysis of experimental data for an applied voltage of 20 V

The calibration and corresponding regression coefficients obtained for three different probes over a range of applied voltages are shown in Table 3.1. The respective thermocouples in the probes are designated as probe number-thermocouple number viz. 1-TC1 to 3-TC6. In the table, R_T is thermal resistivity value; K thermal conductivity value and R^2 is regression coefficient.

3.6.4. Thermal conductivity of buffer materials

The thermal conductivity values of sand-bentonite mixtures were determined using the same experimental setup employed for calibration of thermal probe. The samples of sand-bentonite mixtures were synthesized and compacted to predetermined compaction states. A hole of diameter and length slightly smaller than that of thermal probe was precisely drilled through the center of compacted buffer material using a high precision drilling machine with a helical drill bit. The probe was carefully inserted into the predrilled hole ensuring intimate contact between the compacted material and the probe.

The power supply leads of the thermal probe were connected to the constant DC power supply unit and the T-type thermocouples were connected to the Campbell Scientific data logger, which enabled to monitor the variation of temperature with time. Subsequently, the thermal conductivity value of the buffer materials was obtained.

3.7. Coupled Flow Characteristics

The existence of thermal gradient results in the migration of heat and moisture in a coupled fashion (Villar et al., 2018). In view of this, efforts were made to investigate the migration of heat and moisture through various buffer materials. The coupled flow of heat and moisture studies involved the imposition of the constant heat source to simulate the conditions similar to that of radioactive waste disposal scenario in the real field.

Experimental setup for coupled flow studies consisted of two parts namely constant heat source and mold, which were indigenously fabricated. The mold was made up of PVC tube having an internal diameter 150 mm and length 285 mm. The PVC mold was provided with a bottom polypropylene plate. The constant heat source was made up of a copper heater having a length of 280 mm and 19 mm diameter with 25 mm cold regions at top and bottom. Nichrome wire was employed as the heating element with a resistance of $22.5\ \Omega\cdot m^{-1}$ and wattage of the heater was 120 W. Core of the heater was filled with magnesium oxide (MgO) to serve as thermal conductor and assist in achieving uniform distribution of temperature along the length of the heater.

At the same time, MgO also served as an electrical insulator and prevented the nichrome heating element from short-circuiting with the heater body.

Three T-type thermocouples were encapsulated in the constant heat source to measure the internal surface temperature of the heater. Though the 25 mm long cold regions do not have the heating element; however the conduction of heat takes place through the external surface of the heater body. In order to minimize the heat loss through these cold regions, two wooden sleeves were provided to insulate these regions from contact with the surrounding soil. Figure 3.11 illustrates the schematic of the experimental setup used for coupled flow studies. As shown in Figure 3.11, the constant heat source was placed at the center of the mold surrounded by the candidate buffer material which resembles the canister buffer assembly in the field. As the surface of the heater was at a higher temperature than its surroundings, the temperature gradient made the heat to migrate from the center of the experimental setup towards periphery which in turn caused moisture migration in the similar direction as the heat. In order to capture the spatial and temporal variation of temperature, relative humidity and volumetric moisture content, few thermocouples, relative humidity (RH) sensors (DHT-11 along with Arduino micro-chip board) and time domain reflectometer (TDR), respectively were provided along the radial distance from the center as well as the depth of the setup.

The sand-bentonite mixture SB30 was found to be optimal as buffer material in terms of its compaction characteristics and thermal conductivity properties. Hence, SB30 was considered as the candidate buffer material for coupled flow studies. Since the buffer material in the field is expected to be compacted at its maximum compaction densities, the compaction state of the candidate buffer material in the study was selected as that of optimum moisture content and maximum dry unit weight. A representative specimen of SB30 was prepared by compacting it in the PVC mold using standard Proctor compaction hammer. Prior to the compaction of buffer material, the heater was positioned at the center of the PVC mold, its verticality was maintained by fixing it to the polypropylene base plate with the help of wooden peg and silicon glue. While preparing the specimen, the thermocouples, TDR probes and RH sensors were placed at predetermined positions. Subsequently, the TDR probes and thermocouples were connected to the data logger and the power supply leads of the heater were connected to power supply unit through temperature controller, as shown in Figure 3.12. At the same time, RH sensors compatible to Arduino micro-chip board were also connected to a computer for recording the variation of relative humidity throughout the experiment. Thus, the variation of temperature, humidity and volumetric moisture content with respect to time was recorded when the buffer material subjected to a constant heat flux was at its center. Further, an isothermal vapor diffusion test was conducted to determine the isothermal vapor diffusion coefficient (i.e., moisture evaporation coefficient) and the rate of vapor flow was calculated by employing the relationship proposed by Bittelli et al. (2008).

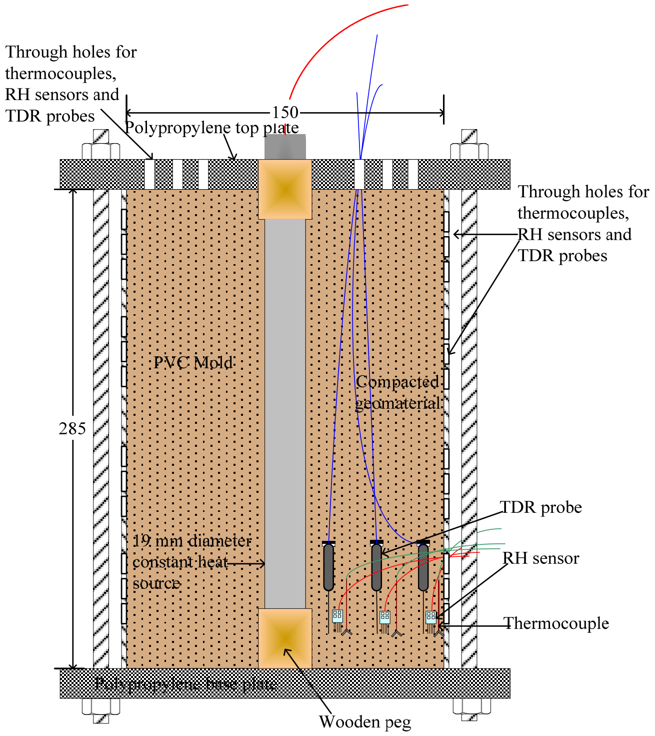

All dimensions in mm
Figure not to scale

Figure 3.11 Schematic view of experimental setup used for assessing coupled flow properties of buffer materials

The isothermal vapor diffusivity, D_v through sand-bentonite buffer materials was determined as per the methodology proposed by Evgin and Svec (1988). For this purpose, a PVC pipe of 15.6 mm diameter and 63.7 mm length was employed as the evaporation test setup, as depicted in Figure 3.13. A representative sand-bentonite buffer material was compacted at its optimum moisture content in the PVC pipe with an end cap. The specimen was placed horizontally throughout the evaporation process to minimize the effects of gravity on water vapor migration. The water vapor diffusion experiments were conducted in a temperature and humidity controlled chamber so as to maintain the boundary and physical conditions of the specimen constant and hence to achieve a controlled rate of drying and evaporation from the specimen. The rate of evaporation, in terms of weight loss of moisture from the specimen, was recorded as a function of time. At the end of the test, the moisture profile within the specimen was established by measuring the variation of gravimetric moisture content along with its length. Further, the D_v was obtained for the one-dimensional vapor flow condition under isothermal scenario using the mathematical relationship proposed by Evgin and Svec, 1988.

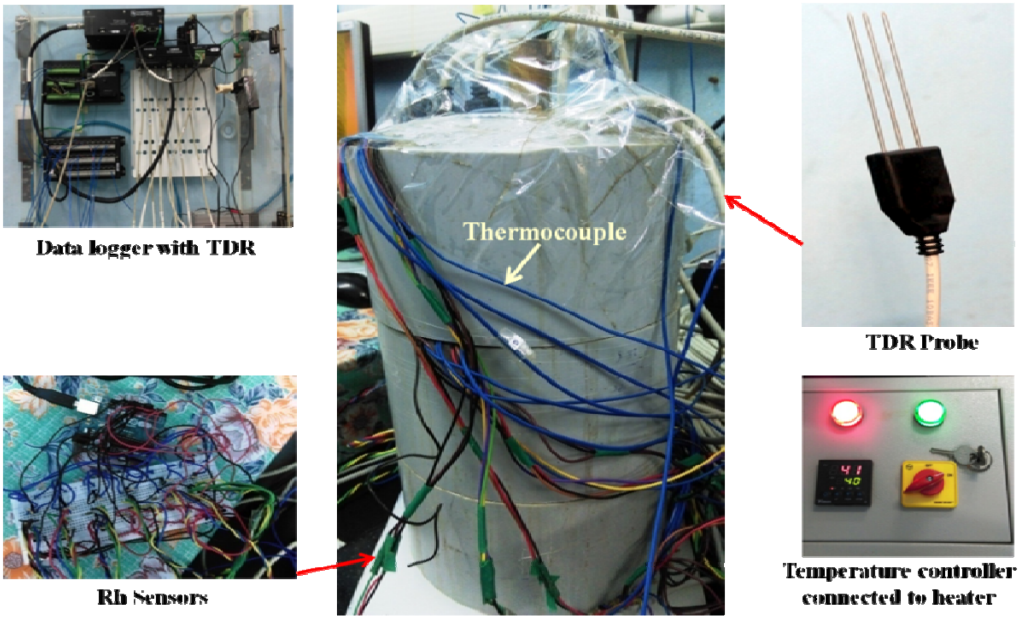

Figure 3.12 Experimental setup for assessing coupled flow properties

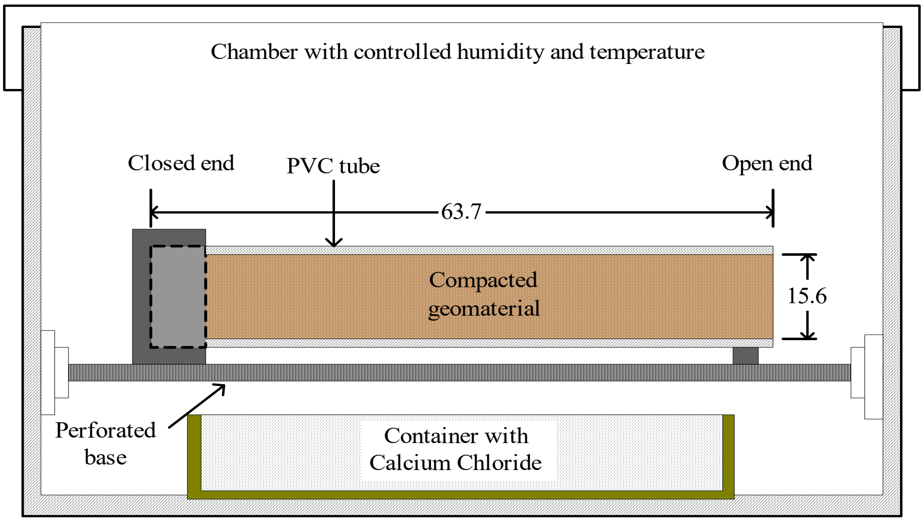

All dimensions in mm
Figure not to scale

Figure 3.13 Schematic view of evaporation test setup for determination of isothermal vapor diffusion properties

3.8. Soil Water Characteristic Curve

Soil water characteristic curve (SWCC) is considered as the basis for the prediction of unsaturated soil parameters like permeability, diffusion, and hydraulic conductivity. The SWCC is defined in three stages as suction increases (Barbour, 1998). At low suction values until the air entry value is reached, the soil remains fully saturated. In the second stage, until the residual water content is reached, there is a decrease in water content with suction. In the third stage, vapor diffusion can only be used to remove the remaining water. Therefore, the third stage is of interest in investigations of water vapor diffusion, whereas, most of the other cases focus on the first two stages of SWCC (Dobchuk et al., 2004). The SWCC for the selected buffer materials were obtained by quantifying the variation of suction corresponding to volumetric moisture content. Suction value of soil over the drying curve was obtained by employing dew point potentiometer (WP4-T, Decagon Devices, USA). The suction range which could be measured using this equipment was 0 to 300 MPa. Figure 3.14 depicts the WP4 apparatus used for the present study. Further, the SWCC for the selected buffer materials was established by plotting suction value against logarithm of volumetric moisture content.

Figure 3.14 Dewpoint potentiometer (WP4)

In order to establish the SWCC, the samples were extracted from the compacted soil mass using stainless steel rings with 34.5 mm diameter and 6.7 mm height. The extracted samples were immersed in water for 5 to 6 h after sealing the exposed sides with filter paper and porous disc arrangement to attain complete saturation. The saturated soil sample was placed in SWCC cup and the same was tested for its suction value using Dewpoint potentiometer. Once the wet weight and corresponding suction value was obtained, the sample along with the ring was kept in humidity controlled desiccator to allow controlled drying of the specimen. The procedure was repeated till the sample get dried completely and the final suction reading was taken by keeping the sample in the oven for 24 h. Using the dry weight of the sample, water content corresponding to each reading was obtained and the SWCC was established by plotting suction value against volumetric moisture content.

Similarly, SWCC was obtained for different sand-bentonite mixtures compacted at different compaction states and the SWCC for each sand-bentonite mixture was taken as the average value of that for different compaction state. The SWCC curves obtained were modeled using Fredlund and Xing (1994) model with the help of a numerical tool called Soil Vision systems.

3.9. Gas Permeability Characteristics

The decay of radionuclides present in the high-level nuclear wastes leads to the generation of sister compounds, which are predominantly gaseous in nature such as radon (Fall et al., 2014). Hence, the gas transport properties of the buffer materials need to be evaluated for its efficient design to contain the radioactive waste canisters. Among the mechanisms of gas transport, advective flow is predominant as these gases are at a moderate pressure under repository conditions (Billiotte et al., 2008). In addition to this, the buffer materials are subjected to elevated temperatures throughout their service life due to the presence of natural geothermal gradient at DGR level as well as radiation and exothermic fission reactions occurring within the waste. Previous researchers have attempted to predict the gas permeability characteristics of various geomaterials under ambient conditions based on their unsaturated characteristics. However, not many efforts were made in the literature to establish the gas permeability properties over a range of elevated temperatures (Brace and Martin, 1968; Alzaydi and Moore, 1978; Calogovic, 1995; Skoczylas and Henry, 1995; Stormont, 1997; Bouazza and Vangpaisal, 2003; Innocentini et al., 2007; Billiotte et al., 2008; Fedor et al., 2008; Gardner et al., 2008). In view of these facts, gas permeation properties of buffer materials were evaluated over a range of temperature. The effect of dry unit weight and placement moisture content of the buffer material on these characteristics was established by considering different compaction states.

For determination of gas permeability, either steady state or transient methods are employed. The steady-state method yields accurate results and is suitable for materials exhibiting gas permeability value larger than 10^{-19} m^2. This method requires a high precision gas flow meter in order to measure the slow flux and a substantial experimental duration for assessing steady state flow at a lower range of permeability.

In addition to this, the steady-state methods require a constant flow rate to be maintained throughout the experiment for efficient determination of gas permeability characteristics. Apart from the fact that the steady state methods are time intensive, Klinkenberg slippage further deteriorates the efficacy of the method to a large extent, particularly for low permeable materials. In view of the above, transient techniques are popularly used to determine the gas permeability of low permeable materials as these methods are less cumbersome and time intensive. Moreover, it is not necessary to have the knowledge of gas flux, since this can be calculated from changes in pressure with time. In the transient technique, the test region is initially filled with a model gas of desired pressure and subsequent pressure decay is measured with time. The pressure decay method is usually deployed when the flow rates become infinitesimally small and difficult to measure it experimentally. In this scenario, the flow rates are quantified precisely in terms of change in pressure which can be easily recorded. In view of these beneficial factors, the present study employed the transient pressure decay method to establish the gas permeability characteristics of the selected buffer materials.

3.9.1. Working principle of transient pressure decay method

The transient pressure decay method is proposed by Brace and Martin (1968), which works based on the principle illustrated in Figure 3.15. In this method, the sample is sandwiched between two reservoirs which are kept at constant and uniform pressure at the beginning of the test. A sudden incremental pressure is then applied to the upstream reservoir and corresponding pressure changes in both the reservoirs are recorded with time. The pressure decay through the sample during the test can be expressed by the following relationship.

$$\frac{\partial\left[K_a \times \frac{\rho}{\mu} \times \frac{\partial P}{\partial x}\right]}{\partial x} = \beta\eta\rho \times \frac{\partial P}{\partial t} \tag{3.8}$$

The rate of permeation of gas from the high-pressure reservoir to low-pressure reservoir varies with time which in turn imposes transient flow conditions. In view of this, the governing equation for gas flow can be modified as follows.

$$\frac{\partial^2 P}{\partial x^2} + \frac{1}{K_a} \times \frac{\partial K_a}{\partial P} \times \left[\frac{\partial P}{\partial x}\right]^2 = \frac{\beta\eta\mu}{K_a} \times \frac{\partial P}{\partial t} \tag{3.9}$$

where P is pressure in kPa; x is linear distance in m; K_a is effective gas permeability in m^2; ρ is density of gas in $kN \cdot m^{-3}$; μ is dynamic viscosity of gas in Pa·s which is a function of temperature and pressure; β is compressibility factor of the gas, its variation with temperature and pressure is obtained as per Green and Perry, 1984, and η is effective porosity of the sample.

Once the pressure variation of both source and receiver reservoirs with time is experimentally obtained, the difference in pressure between the reservoirs with time is normalized with a pressure difference between them at the start of the test. The coefficient of exponential fit of the normalized pressure variation curve indirectly provides the coefficient of gas permeability using the simplified solution of Brace and Martin (1968) as explained in Equations 3.10 and 3.11.

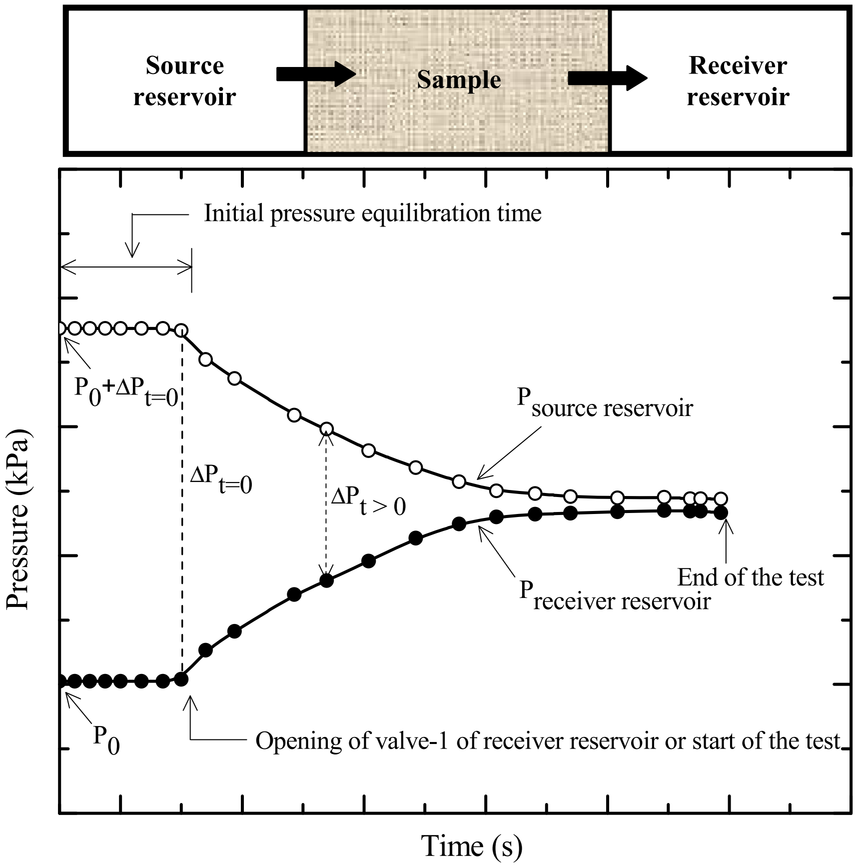

Figure 3.15 Schematic view of the principle of pressure decay method

$$\frac{\Delta P_{t>0}}{\Delta P_{t=0}} = e^{-\alpha t} \tag{3.10}$$

$$\alpha = \frac{K_a A}{\beta \times \mu \times L \times \left(\frac{1}{V_{source}} + \frac{1}{V_{receiver}}\right)} \tag{3.11}$$

where $\Delta P_{t=0}$ is initial pressure difference between source and receiver reservoirs; $\Delta P_{t>0}$ is pressure difference between the reservoirs at a given time; α is coefficient of exponential function; A is cross-sectional area of the sample; L is length of the sample; V_{source} and $V_{receiver}$ are volumes of source and receiver reservoirs.

3.9.2. Gas permeability apparatus

The experimental setup developed to determine the gas permeability characteristics of geomaterials over a range of compaction states and temperature is detailed in Figure 3.16. The test setup comprised of a cylindrical sample holder and two gas reservoirs (source and receiver) on either side of it. The sample holder, receiver, and source reservoirs were of 93 mm diameter and lengths 50 mm, 54 mm, and 190 mm, respectively. All components of the permeability apparatus were connected together by two end plates and two intermediate plates using four tie rods and wing nuts. The chances of leakage through the interface between various components were completely arrested using silicon O-rings. The source and receiver reservoirs were fitted with two gas-tight valves (Swagelok, USA) each. One of the valves (valve 1) was used for filling the model gas into the reservoirs and was set to the initial desired gas pressure. The other valve (valve 2) on both the reservoirs were short-circuited for initial pressure equilibration across the sample during the early phase of testing.

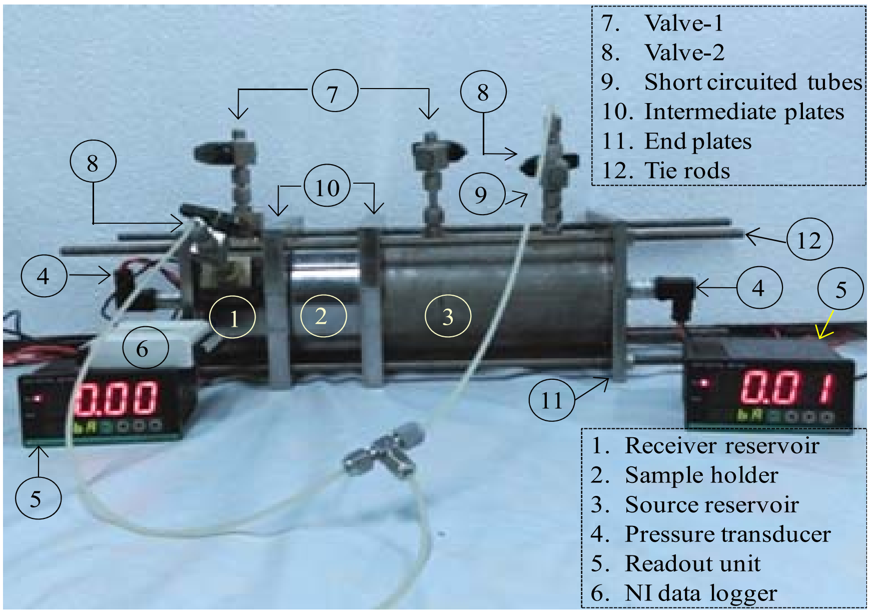

Figure 3.16 Gas permeability apparatus

Both the reservoirs were connected to pressure sensors having 0-6 bar pressure range by which pressure of respective chambers was measured with the help of readout units and data logging system (National Instruments, USA). The soil sample was placed in the sample holder with porous metal discs on either side of it to avoid crumbling and spalling of the soil particles into the reservoirs. Gas pressure was directly supplied by connecting to the inlet valve which was controlled by a pressure regulator to maintain a constant pressure. The preferential flow of the candidate gas through the annular space between the compacted specimen and the inner circumference of the sample holder was arrested by providing a bentonite paste filled groove of 2 mm width and 5 mm depth along the circumference on either side of the specimen. In order to ensure leak-proof, the interfaces between the inlet and outlet chambers were sealed using silicon glue and leak tests were conducted prior to the commencement of the experiment.

Efficacy of pressure decay method in assessing the gas permeability characteristics of various sand-bentonite mixtures was assured by employing high precision gas pressure transducers (Keller, Germany) with an accuracy of ±0.25 % of full scale with maximum total error of 1.5 %, for working temperatures of -10 °C to 80 °C, respectively. The transducers were calibrated using the pressure calibration unit (Toshniwal, USA) over a pressure range of 20-600 kPa. The applied pressure versus voltage output was used to establish the calibration response of the pressure transducer, as depicted in Figure 3.17.

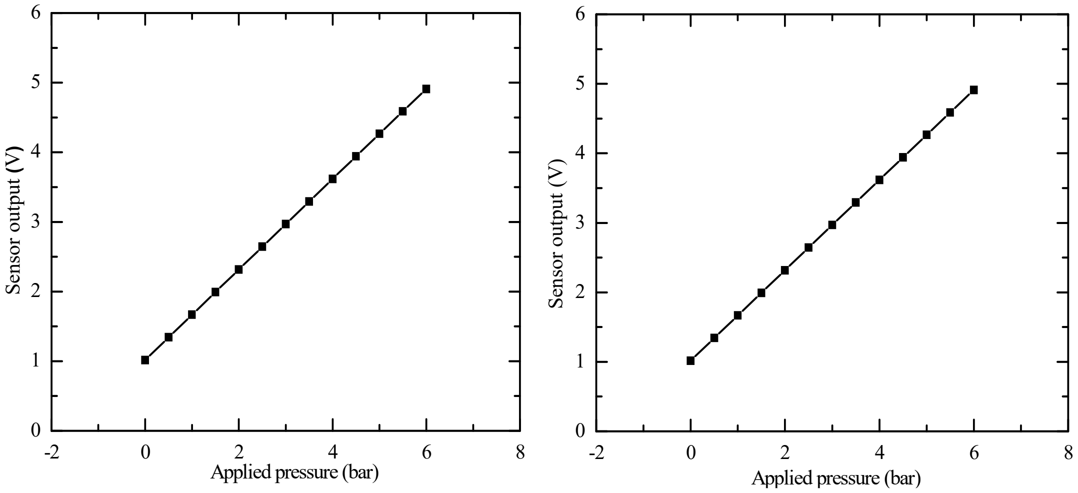

Pressure sensor 1 **Pressure sensor 2**

Figure 3.17 Calibration response of pressure sensors

3.9.3. Gas permeability of buffer materials

The sample for gas permeability test was prepared by mixing the dry weight proportions of sand and bentonite with the desired amount of moisture and stored it in the high humid desiccator for a maturation period of 24 h. After maturation, the sample was compacted to 50 mm thickness and the system was assembled to form the gas permeability cell as depicted in Figure 3.16.

Both the reservoirs were filled with model gas through valve-1 of source reservoir and short-circuited valve-2 of both the reservoirs. This enabled filling of model gas to the desired pressure in both the reservoirs, simultaneously. Once the pressure in both reservoirs attained constant value, it was kept undisturbed until all the pores of the specimen attained the gas pressure as that of the reservoirs by monitoring the variation of applied pressure in both reservoirs. The inert nitrogen gas was chosen as the model permeating gas, and hence, the error incurred due to its sorption on the geomaterial was insignificant. The initial pressure equilibration was essential to minimize the error due to non-uniform pressure distribution within the pores of the specimen. It is also necessary to mitigate the gas pressure loss due to its dissolution in pore water and sorption on available potential sites under testing conditions.

Once the initial pressure equilibration was achieved, the gas pressure in the receiver reservoir was reduced to the desired value by opening valve-1 to impose a known initial pressure gradient across the specimen. It could be noted that valve-2 of both reservoirs were turned off and short-circuiting tube between them was disconnected prior to the application of pressure gradient across the specimen. Thus, a predetermined pressure gradient was applied across the sample and under this gradient, the gas molecules started permeating through it from source (high pressure) reservoir to the receiver (low pressure) reservoir. The variation of pressure with time was monitored and recorded using pressure transducers and data acquisition system (National Instruments, USA), as shown in Figure 3.16. The test was continued till the flow of gas ceased from source reservoir to the receiver reservoir and the pressure gradient across the specimen became insignificant. From the pressure variation with time response of the specimen, its gas permeability coefficient was determined. Similarly, permeability tests were carried out at different compaction states of the geomaterials. Likewise, to study the influence of temperature on the permeability characteristics, the tests were also performed in a temperature controlled chamber by maintaining it at different temperatures such as 10 °C, 27 °C and 50 °C.

The variation of difference in gas pressure between the source and receiver reservoir (ΔP_t) was normalized with initial pressure difference (ΔP_o) and the normalized pressure variation ($\Delta P_t/\Delta P_o$) was obtained with time. From the exponential variation of $\Delta P_t/\Delta P_o$, the exponential coefficient (α) was obtained and the coefficient of gas permeability was determined using the solution suggested by Brace and Martin (1968).

3.10. Gas Diffusion Characteristics

The concentration of HLW contaminants in the surrounding environment is insignificant compared to that in the canister. The concentration gradient imparts flow of contaminants from the canister to the surrounding by means of diffusion. Therefore, the gas transport characteristics of various sand-bentonite buffer materials, in terms of diffusion characteristics were assessed and their ability to contain high-level radioactive waste was evaluated. In addition, the influence of various factors such as dry unit weight and moisture content on their diffusion characteristics was evaluated.

Gas diffusion may be defined as the phenomena of gas transport from higher concentration regions to the lower concentration regions by random motion of gaseous molecules. The motion of a single molecule can be described in terms of the familiar 'random walk' picture. At the same time as it is possible to calculate the mean square distance travelled by a single molecule in a given interval of time, it is not possible to say in what direction a given molecule will move in that time (Crank, 1975). In view of this, Fick (1855) attempted to quantify the diffusion rate by modifying the mathematical equation of heat conduction proposed by Fourier (1822). The theory of diffusion in isotropic substance is based on the hypothesis that the rate of transfer of diffusing substance through unit area of a section is proportional to the concentration gradient measured normal to the section. This can be explained mathematically as,

$$F=-D\frac{\partial C}{\partial x} \tag{3.12}$$

where F is rate of transfer per unit area of the section; C is concentration of the diffusing substance; x is spatial coordinate measured normal to the section, and D is diffusion coefficient. The negative sign of D indicates that the diffusion occurs in the opposite direction of increasing concentration.

Consider a rectangular parallelepiped element with sides parallel to the axes of coordinates as shown in Figure 3.18. The center of the element is considered to be at P (x, y, z) where the concentration of the diffusing substance is C. The rate at which the diffusing substance enters the element through the face ABCD in the plane x-dx is given by,

$$4dydz\,(F_X-\frac{\partial F}{\partial x}dx) \tag{3.13}$$

where F_x is rate of transfer through unit area of the corresponding plane through P.

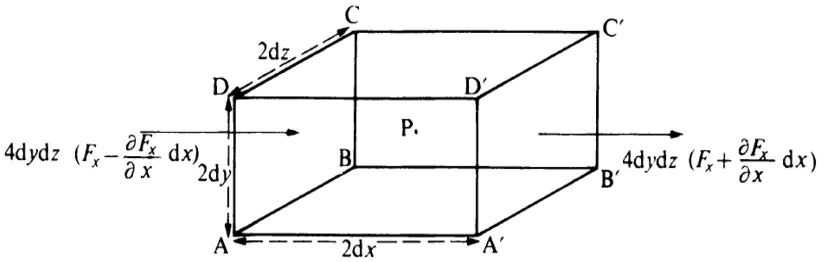

Figure 3.18 Element of volume (modified from Crank 1975)

Similarly, the rate of loss of diffusing substance through the opposite face A'B'C'D' is given by,

$$4dydz\,(F_x+\frac{\partial F_x}{\partial x}dx) \tag{3.14}$$

The rate of increase of diffusing substance in the element from the two faces can be written as,

$$-8dxdydz\frac{\partial F_x}{\partial x} \tag{3.15}$$

and from the other faces, it is

$$-8dxdydz\frac{\partial F_y}{\partial y} \tag{3.16}$$

and

$$-8dxdydz\frac{\partial F_z}{\partial z} \tag{3.17}$$

The rate at which the amount of diffusing substance in the element increase is given by,

$$8dxdydz\frac{\partial C}{\partial t} \tag{3.18}$$

and hence it can be written as,

$$\frac{\partial C}{\partial t}+\frac{\partial F_x}{\partial x}+\frac{\partial F_y}{\partial y}+\frac{\partial F_z}{\partial z}=0 \tag{3.19}$$

F_x, F_y, F_z are given by (3.12) assuming the diffusion coefficient D is constant. Then, (3.19) becomes,

$$\frac{\partial C}{\partial t}=D\left[\frac{\partial^2 C}{\partial x^2}+\frac{\partial^2 C}{\partial y^2}+\frac{\partial^2 C}{\partial z^2}\right] \tag{3.20}$$

which can be reduced as,

$$\frac{\partial C}{\partial t}=D\frac{\partial^2 C}{\partial x^2} \tag{3.21}$$

The Equations (3.12) and (3.21) are referred to as Fick’s first and second laws of diffusion.

When D is not constant and it depends on the concentration of diffusing substance C and also in the case when the medium is not homogeneous so that D varies from point to point, the relation (3.21) can be modified as,

$$\frac{\partial C}{\partial t}=\frac{\partial}{\partial x}\left(D\frac{\partial C}{\partial x}\right)+\frac{\partial}{\partial y}\left(D\frac{\partial C}{\partial y}\right)+\frac{\partial}{\partial z}\left(D\frac{\partial C}{\partial z}\right) \qquad (3.22)$$

where D is a function of x, y, z, and C (Crank, 1975).

The diffusion theory is based on Fick's laws (i.e., Equations 3.12 and 3.21).

3.10.1. Gas diffusion apparatus

The gas diffusion characteristics of buffer materials were assessed by employing carbon dioxide (CO_2) as the model contaminant gas since CO_2 possess similar state and properties as that of the radioactive gases encountered in a typical DGR. CO_2 is also one of the constituents of the gaseous contaminants in the HLW as a result of the emission reactions (Quintessa, 2011). The diffusion apparatus fabricated in the present study was similar to two reservoir diffusion cell developed by Shakelford (1991) to determine the diffusion characteristics of geomaterials for liquid contaminants. The diffusion cell was made of perspex and consisted of three cylindrical chambers such as source reservoir, receiver reservoir and a sample holder (93 mm inner diameter and 100 mm outer diameter) as depicted in Figure 3.19. Each source and receiver reservoirs were provided with 8 mm diameter gas inlet and outlet ports which could be operated with the help of gas-tight quick coupling sockets (Festo, USA). These reservoirs and sample holder were cylindrical in shape, separated with perspex plates of 23 mm thick. Net length of the source, sampling, and receiving chambers was 150 mm, 30 mm and 150 mm, respectively. The separating plates were having dimensions 130×130×23 mm and a groove of 4.5 mm depth and 5 mm width was provided on these plates to fix the cylindrical chambers. The intermediate plates were provided with 70 mm diameter hole for allowing the gas to flow from source reservoir to receiver reservoir through the soil sample and vice versa. In order to ensure gas-tight connection, the joints between the cylinders and intermediate plates were provided with six rubber washers with 93 mm inner diameter and 100 mm outer diameter each. All the chambers and plates were connected together with four stainless steel rods of 500 mm length. In order to keep the soil sample in position, two 93 mm diameter and 10 mm thick acrylic perforated discs were placed on both sides of the sample (which also act as porous discs).

A gas distribution panel as depicted in Figure 3.20 was employed for filling CO_2 in the gas diffusion apparatus. This panel was made of perspex sheets, and SS tubes of one-fourth inch, connected to the CO_2 cylinder with a regulator in between to control the gas flow. End connections were made up of a one-eighth inch stainless steel tubing and ferrule and nut connections.

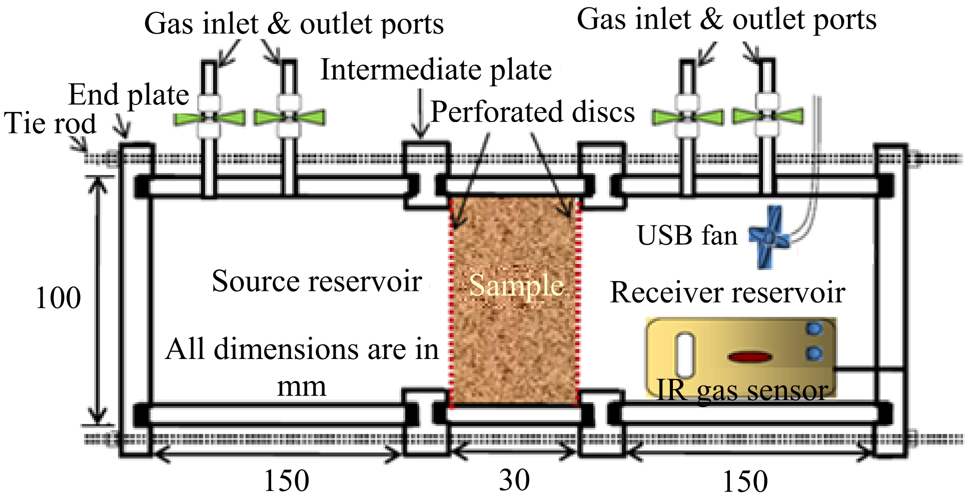

Figure 3.19 Schematic diagram of the gas diffusion apparatus (modified from Aswathy, 2012)

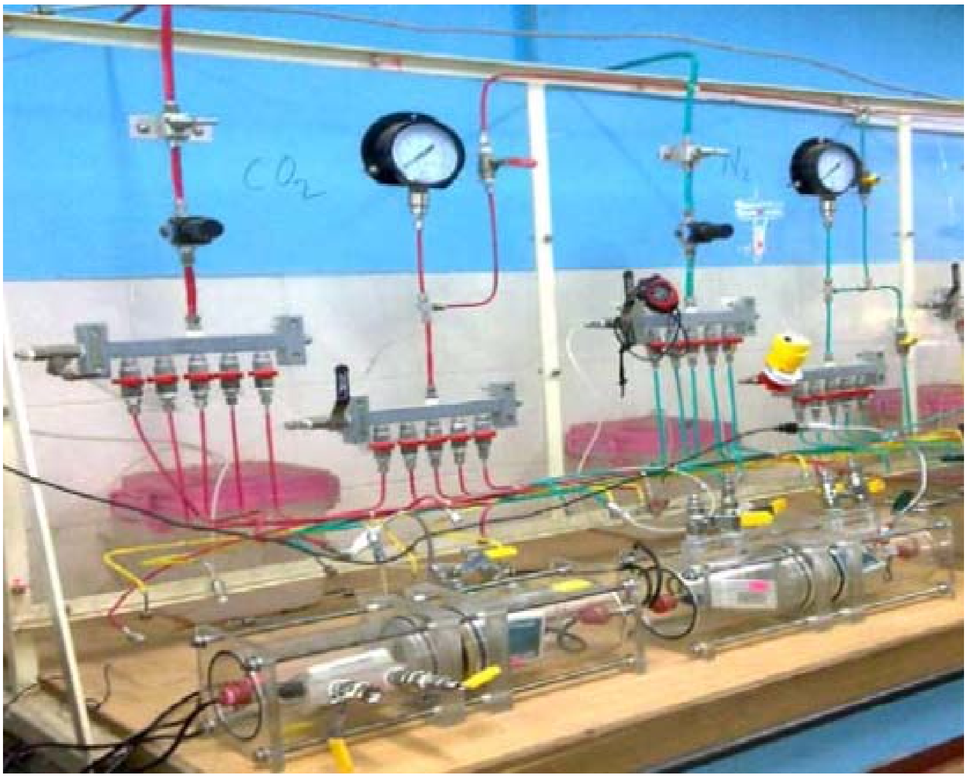

Figure 3.20 Gas distribution and pressure control panel

In order to measure the carbon dioxide concentration, an Infrared (IR) sensor (as shown in Figure 3.21) named 100 % -CO_2 sampling data logger and CO_2 probe

(CO_2 meter, USA) were used. The IR sensor had an inbuilt sampling pump which drew the gas at a particular interval and its concentration was measured. The instrument was provided with a data logger as well as real-time data collection system for data acquisition. Calibration of the sensor was done with the help of calibration gases. The sensor was placed inside the receiver chamber and the CO_2 concentration in the receiver reservoir was measured with respect to time. USB fan was attached to the top of the receiver reservoir to ensure the uniform mixing of the gases inside the reservoir. The fan was programmed with the help of a control box in such a way that the fan was powered a couple of minutes prior to the predetermined sampling time and turned off soon after sampling. This helped in increasing the sensing speed of sensors and also to ensure the accuracy of concentration measurement. Further, to validate the measurements made by the IR sensors, gas samples were collected at specified intervals from the receiving reservoir using a gas-tight syringe (Hamilton, USA) and then analyzed for CO_2 concentration using Agilent make gas chromatograph (GC) equipped with thermal conductivity detector (TCD), as depicted in Figure 3.22.

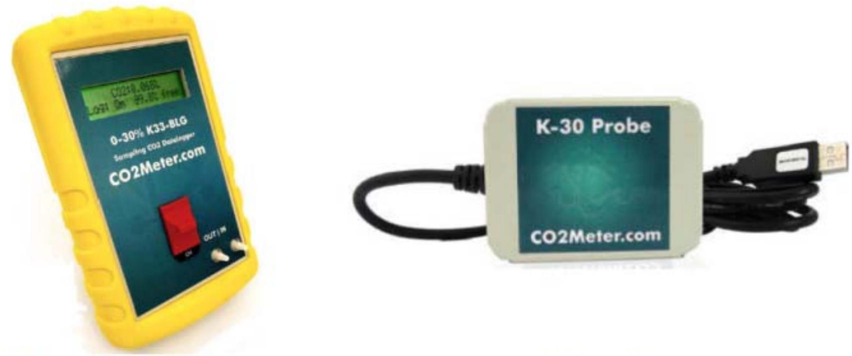

CO_2 Sampling Data Logger ***CO_2 probe***

Figure 3.21 Infrared sensors for measuring CO_2 concentration

3.10.2. Calibration of infrared sensors

Prior to the utilization of infrared sensors for the measurement of carbon dioxide gas concentration during the diffusion test, the IR sensors were calibrated using calibration system developed. The calibration system consisted of an air-tight reservoir, sensor units, and valves for controlling the gas in and out flows, as shown in Figure 3.23. Two gas inlet ports of one-eighth inch size permitted the gas flow into the reservoir. A gas cylinder filled with a calibration gas of known concentration of CO_2 was connected to the reservoir through gas distribution panel. Further, the concentration of carbon dioxide was monitored by the sensors connected to the computer, using data analysis software (DAS). First, the calibration box was flushed with nitrogen gas for displacing the ambient gas and then connected to the calibration gas supply ports. The regulator was adjusted such that the gas flow within the reservoir was maintained constant. Once the flow was set, the carbon dioxide gas was introduced to the system and the pressure development within the reservoir was avoided by opening the outlet valve.

Figure 3.22 Gas chromatograph used for analyzing CO_2 concentration

Further, the system was allowed to stabilize for a few minutes and the measurement was monitored continuously with the help of DAS software. The same procedure was repeated for different known concentrations of calibration gas and the calibration curve was obtained by plotting the known concentrations and the corresponding concentrations displayed by the sensor as shown in Figure 3.24.

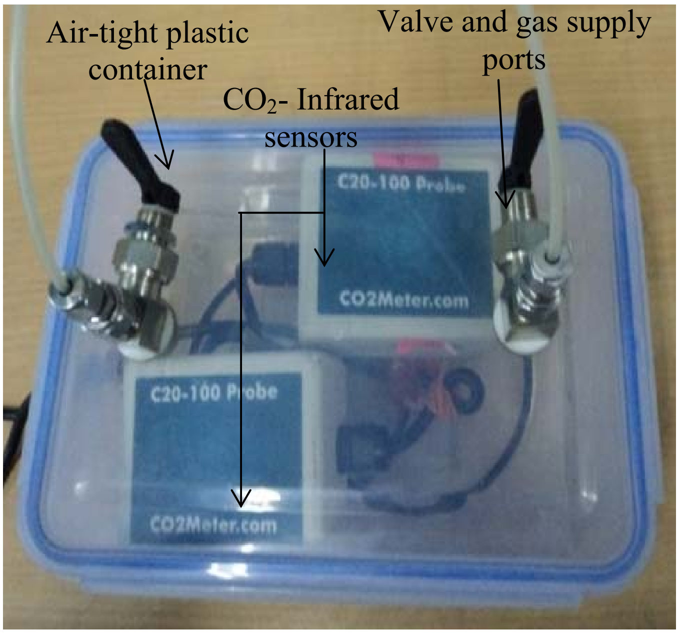

Figure 3.23 Infrared sensor calibration system

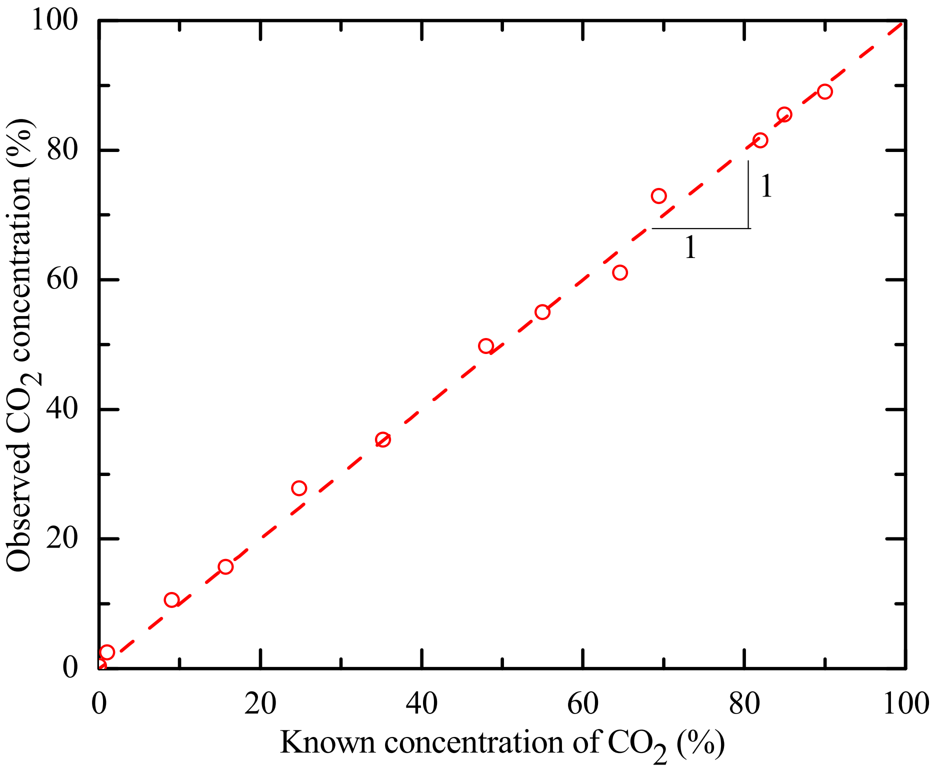

Figure 3.24 Calibration response of infrared sensors

3.10.3. Calibration of gas chromatograph

The calibration of gas chromatograph was achieved by analyzing different concentrations of CO_2 in the gas chromatograph for obtaining the area of eluted peak and corresponding retention time. Gas canisters with standard CO_2 gases of different concentrations such as 0 % (i.e., 100 % nitrogen), 10 %, 30 %, 50 %, and 100 % of CO_2 concentration were injected at the inlet of the GC using gas-tight syringe and the eluted peak area and retention time was noted. The test was repeated for a minimum of 5 times. The average value of eluted peak area was plotted against the known concentration of the standard CO_2 which represented the calibration curve. The standard deviation of each concentration value was obtained and the accuracy of calibration was also established. Calibration results of the gas chromatograph are presented in Figure 3.25.

The soil sample was prepared in the same manner as that prepared for gas permeability test. The sample was compacted to 10 mm thickness in the sample holder at desired compaction state with the help of handheld tamper and spacer discs. In order to avoid boundary leaking effects, a layer of bentonite paste of liquid limit consistency was applied around the interface between the sample holder and sample edge. Porous discs were then placed on both sides of the sample to avoid spalling of the sample towards the source and receiver side. Further, the sample holder containing the sample was placed in between the source and receiver reservoir connected by intermediate plates. In addition to this, the infrared sensor was also placed in the receiver reservoir side for the measurement of diffused gas concentration. The entire system was then assembled to form the diffusion cell as shown in Figure 3.26.

Prior to the experimentation, all the joints of the diffusion cell were made airtight by tightening the threaded rod-nut system connecting the intermediate and end plates. In addition to this, the joints were sealed using silicon glue. Once the gas tightness was ensured, the gas inlets of the source and receiver chambers were connected to the nitrogen gas supply ports of the distribution panels and both the chambers were flushed with nitrogen gas at atmospheric pressures to displace the ambient gas. In order to avoid the development of pressure within the chambers, the outlet valves were kept open to atmosphere while filling as well as flushing the chambers. The chamber was flushed with nitrogen gas for 15 minutes and then left the system for attaining equilibrium for a time span of 5 h. The IR sensor was configured such that the carbon dioxide concentration within the receiver chamber was monitored continuously with the help of the DAS software.

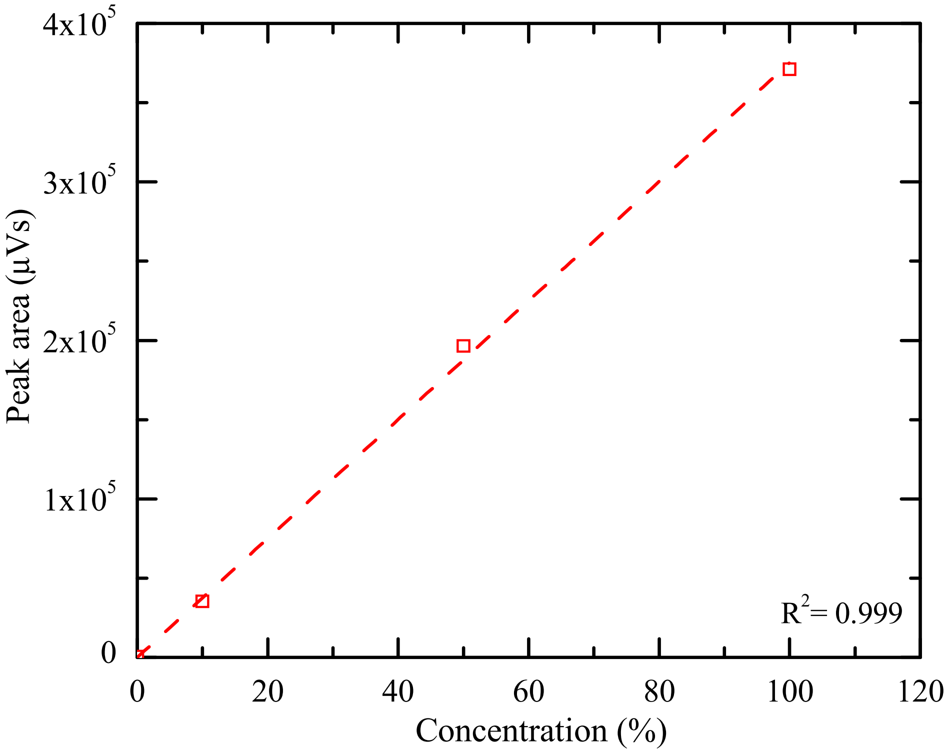

Figure 3.25 Calibration response of gas chromatograph

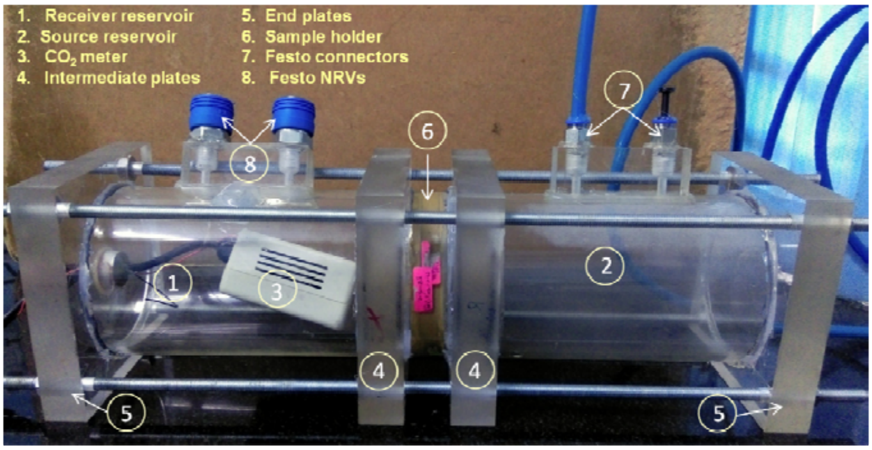

Figure 3.26 Gas diffusion apparatus

Further, carbon dioxide gas was filled into the source reservoir to the desired concentration by connecting the inlet valve to an intermediate gas reservoir with IR sensor for measuring the concentration, which in turn was connected to the carbon dioxide gas supply cylinder through the gas distribution panel. During filling of the model gas into the source reservoir, the pressure within reservoir was maintained close to atmospheric pressure to ensure zero pressure gradient across the sample. After this step, the infrared sensor was configured with the help of DAS software. Soon after connecting the sensor to the computer, the system was monitored for CO_2 gas concentration in the receiver reservoir with respect to time. Further, the source reservoir was connected to a CO_2 reservoir with CO_2 gas of known concentration at ambient pressure which maintained the source reservoir concentration constant.

The variation of effluent gas (CO_2) concentration, C_t, was normalized with the source reservoir gas concentration, C_0, over a period of time. The experiment was continued till the normalized effluent concentration, C_t/C_0 approached close to unity. By employing the methodology presented above, a variation of normalized effluent concentration, C_t/C_0, with time for different buffer materials over a range of moisture contents, in terms of the breakthrough curves (BTCs) was obtained. All the tests were conducted in a temperature controlled room (25 ± 2 °C) where density and viscosity of gas were assumed to be constant.

3.11. Sorption Characteristics

Sorption characteristic studies on buffer materials were conducted to quantify the mass of contaminant sorbed by them. It provided a quick understanding of the geomaterial-contaminant interaction over variable environmental conditions. Sorption characteristics of the geomaterials can be obtained by adopting two methods such as batch sorption and column flow-through experiments. Among the two methods, batch sorption studies are simple and easy to conduct whereas, column flow-through experiments better represent the contaminant-geomaterial interaction. The sorption characteristics of geomaterials predominantly depend on their physico-chemico-mineralogical properties; liquid to solid ratio, L/S; temperature; chemical composition of the contaminant and geomaterial-contaminant interaction time (Harter, 1983; Gray et al., 1988; Yong and Phadungchewit, 1993; Gao et al., 1997). Keeping these parameters in mind, batch sorption experiments were conducted over a wide range of L/S at different temperatures of 10 ºC, 27 ºC, 50 ºC and relative humidity of 50 percent was maintained constant throughout the experiment.

The liquid to solid ratio, L/S, is defined as the ratio of mass (or volume) of the solution to the mass of the dry soil. According to ASTM D4646 (2004) and Roy et al., (1991), it is very difficult to perform batch sorption experiments for L/S values less than 4, as the resulting paste hinders separation of the solid particles from the mixture of contaminant solution and geomaterials. With this in view, in the present study, L/S values of 10, 20, 50, 100, and 200 were adopted to obtain the sorption characteristics of geomaterials.

To achieve different L/S values such as 10, 20, 50, 100 and 200, the sample weighing 10, 5, 2, 1 and 0.5 g, respectively, were mixed with 100 ml of the corresponding contaminant solution with a different initial concentration in air tight polypropylene sample bottles. The samples were weighed according to their dry weight proportions to obtain different sand-bentonite mixtures. Since sorption is a physicochemical phenomenon, the equilibration time (the optimal geomaterial-contaminant interaction time) was obtained by following the recommendations proposed by Roy et al. (1991) and Nithya (2011). To obtain equilibration sorption time, experiments were conducted by allowing buffer materials in different L/S ratios to interact with contaminant solution of initial concentration C_i equal to 100 mg/L. The contaminants selected for the present study were strontium, Sr^{2+} in its nitrate form and cesium, Cs^{2+} in its chloride form and the buffer materials considered were SB30, SB50, SB70, and SB100. The mixture of geomaterial and contaminant was allowed to interact over a wide range of interaction time as minimum as 5 minutes to as long as 10 days. Proper interaction was obtained by shaking the sample bottles in a mechanical wrist shaker for specified interaction time. After the interaction time, the contents of these bottles were centrifuged at 1000 g for 30 minutes to separate the solid particles from the solution. The filtrate thus obtained was analyzed for the contaminant concentration using atomic absorption spectrophotometer, AAS (Thermo scientific, USA). Further, similar experiments on sample bottles filled with a certain concentration of heavy metal solution without the geomaterial (blank samples) as well as that on sample bottles filled with the geomaterials and the distilled water (control samples) were performed to establish the sorption affinity of the sample bottle and the trace level concentrations of the concerned contaminant initially present in various geomaterials (Grolimund et al., 1995; Gao et al., 1997; ASTM D4646, 2004; Nithya, 2011). Using the obtained sorption capacity of the sample bottles and trace level initial concentrations present in different geomaterial, the corrected initial concentration of the solution, C_i and equilibrium solution concentration, C_e were determined. Later, the mass of contaminant sorbed by the geomaterial, C_s was computed using the following relationship.

$$C_s=\left(C_i-C_e\right)\times\left({}^{L}/_{S}\right) \tag{3.27}$$

The equilibrium was considered to be achieved if the change in variation was not more than five percent between two consecutive solution concentration values during 24 h of interaction. From the result, it could be observed that the contaminant concentration decreased gradually from its initial concentration to equilibrium concentration value corresponding to interaction time of 96 h and later remained constant. Similarly, the equilibrium concentration values for other buffer materials with selected contaminant solution were obtained and incidentally, these values were found not to be more than 96 h and hence interaction time of 96 h was considered as equilibrium interaction time. Further, the experiments on different sand-bentonite mixtures with corresponding contaminants at temperatures of 10 °C, 27 °C, and 50 °C were conducted for an equilibration time of 96 h.

The column flow-through sorption experiments represent geomaterial-contaminant interaction in a very realistic way (Jackson et al., 1984). For this purpose, column test setups were fabricated to study the sorption characteristics of the geomaterials as depicted in Figure 3.27 and Figure 3.28. The setup was made up of perspex material and consisted of a cylindrical column of 50 mm diameter and 80 mm height. The bottom 30 mm of the cylindrical portion was filled with geomaterial and compacted in three layers by providing a specified number of blows using a hand-held hammer to achieve compaction state corresponding to maximum dry unit weight. To facilitate the drainage at top and bottom of the specimen, two porous discs were placed at both ends of the sample. The void ratio of the sample was maintained constant throughout the experiment by keeping the height of the sample same with the help of loading ram and tie rod arrangement. Initially, the soil column was saturated by permeating distilled water under constant hydraulic gradient. Once the steady-state flow condition was achieved, the permeant was replaced with the model contaminant of specified concentration. The effluent coming out of the compacted geomaterial was collected at the top of the sample in the sample collection bottle and was withdrawn regularly into glass vials. The effluent in the vials was stored in a refrigerator and analyzed for their metal concentration, C_t, using AAS. This process was repeated until the normalized effluent concentration, C_t/C_0, of the effluent approaches to 0.5 or higher.

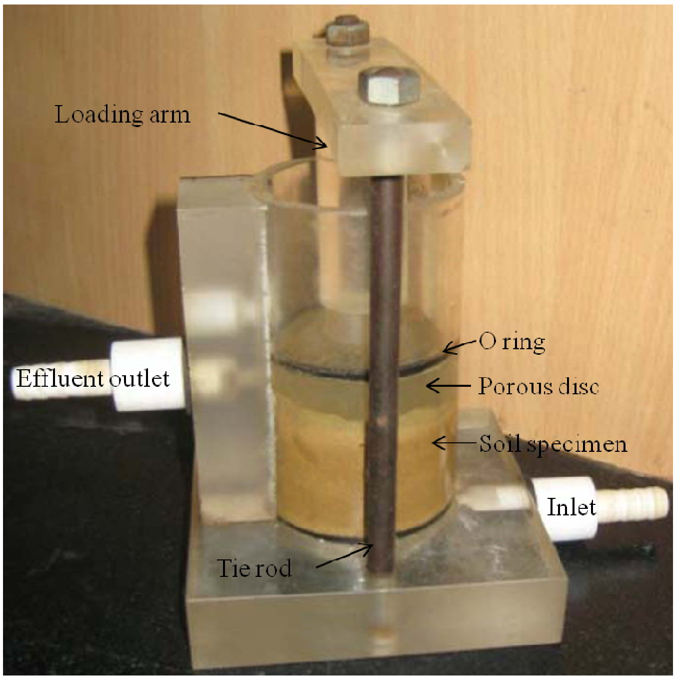

Figure 3.27 The laboratory (1-g) column flow-through the experimental setup

Similarly, column flow-through experiments were conducted in geotechnical centrifuge at 100g. The sorption characteristics corresponding to 1g test was achieved by applying scaling laws (Nithya, 2011). The geotechnical centrifuge and column flow-through experimental setups placed in a swinging bucket of the geotechnical centrifuge are detailed in Figure 3.29 and 3.30.

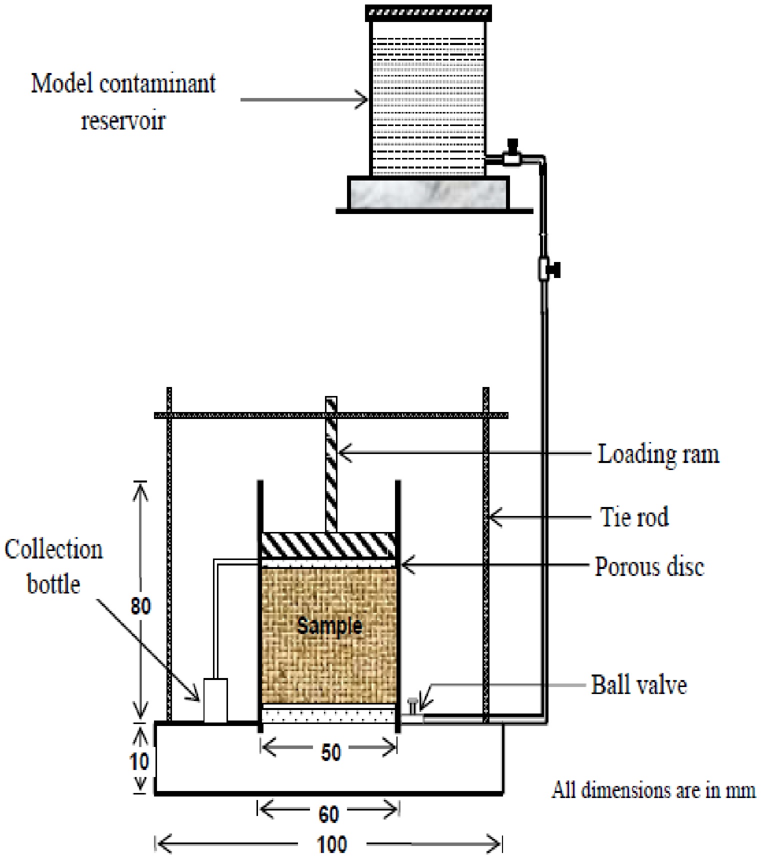

Figure 3.28 The schematic diagram of laboratory (1-g) column flow-through experimental setup (modified from Nithya, 2011)

Figure 3.29 Column flow-through experimental setups placed in a swinging bucket of a geotechnical centrifuge

Figure 3.30 Two-meter diameter balanced beam geotechnical centrifuge

Chapter 4

RESULTS AND DISCUSSIONS

4.1. General

This chapter presents the results of experimental investigations carried out according to the methodologies described in chapter 3. The physico-chemico-mineralogical and geotechnical properties of the selected materials are elaborately discussed. The heat and contaminant migration properties of the synthesized buffer materials are reported. The generalized relationships for estimation of transport properties of buffer materials were developed, and the same is illustrated. Further, the efficacy of the buffer materials was assessed for containing the radioactive waste and the details pertaining to this aspect are described.

4.2. Physical Characteristics

The physical properties and consistency indices of the selected virgin materials were obtained, and the results are reported in Table 4.1 and Figure 4.1. Based on the particle size distribution characteristics and consistency limits, the selected virgin materials were classified as per Unified Soil Classification System, USCS (ASTM D2487, 2011) and the same is reported in Table 4.1.

Table 4.1 Physical properties and consistency indices of the materials

Property	**Value**	
	Sand	**Bentonite**
Specific gravity	2.70	2.72
Particle size	**Percent fraction by weight (%)**	
Gravel size (i.e., > 4.75 mm)	0	0
Coarse sand size (i.e., ≤ 4.75 mm and > 2 mm)	0	0
Medium sand size(i.e., ≤ 2 mm and > 0.425 mm)	0	0
Fine sand size (i.e., ≤ 0.425 mm and > 0.075 mm)	100	1
Silt size (i.e., ≤ 0.075 mm and > 0.002 mm)	0	38
Clay size (i.e., ≤ 0.002 mm)	0	61
Consistency limits	**Percent by weight (%)**	
Liquid limit (w_L)	Non-plastic	364
Plastic limit (w_P)		46
Plasticity index (PI)		318
Shrinkage limit (w_S)		4
Soil classification as per USCS*	SP	CH

*Unified soil classification system (ASTM D2487, 2011)

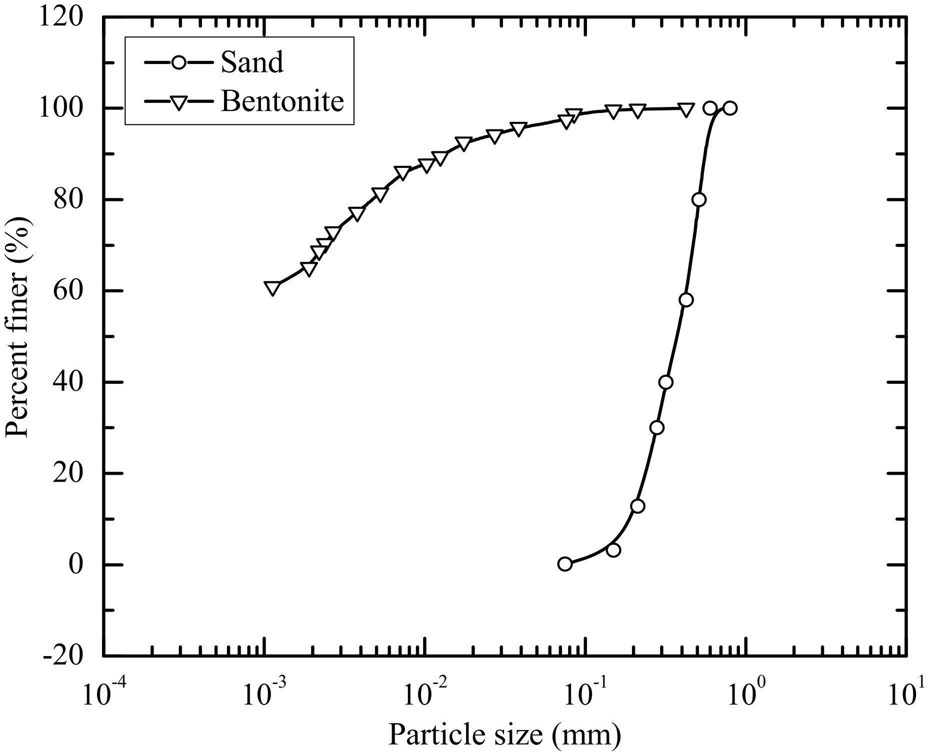

Figure 4.1 Particle size distribution characteristics of the materials

4.3. Chemical and Mineralogical Characteristics

The chemical composition of the selected materials was determined using XRF and the results obtained are presented in Table 4.2 in their major oxide form. It can be observed that the selected geomaterials predominantly constitute oxides of silica, alumina, and iron.

Table 4.2 Chemical composition of the materials

Oxide	**Percent by weight (%)**	
	Sand	**Bentonite**
SiO_2	41.8	59.7
Al_2O_3	10.2	17.6
Fe_2O_3	26.8	10.6
CaO	14.2	0.7
MgO	1.2	1.7
Na_2O	0.1	3.7
K_2O	0.7	1.5
TiO_2	3.0	4.2
P_2O_5	1.6	0.0
MnO	0.4	0.3

The mineralogical properties of the selected materials were examined using powder XRD technique. Figure 4.2 depicts the X-ray diffractograms of the selected materials. The minerals present in the geomaterials were identified with the help of a database of international centre for diffraction data (ICDD, 2010) and the same is listed in Table 4.3.

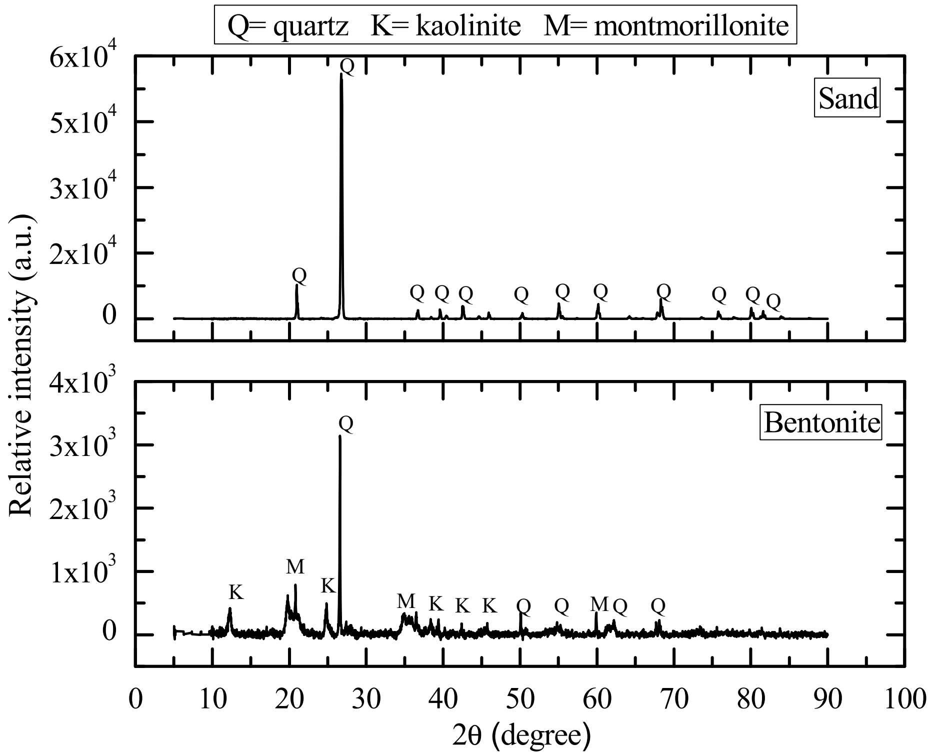

Figure 4.2 X-ray diffractograms of the materials

Table 4.3 Mineralogical characteristics of the materials

Material	Minerals present
Sand	quartz
Bentonite	montmorillonite, quartz, kaolinite

4.4. Geotechnical Characteristics

4.4.1. Compaction characteristics

The engineering behavior of the materials is strongly influenced by their dry unit weight and placement moisture content. In view of this, the compaction characteristics of virgin bentonite, and mixtures of sand and bentonite were established. For the sake of brevity, the compaction characteristic curve of bentonite (referred as SB100) is illustrated in Figure 4.3, along with the corresponding zero air void line. The pivotal compaction characteristics such as maximum dry unit weight (γ_{dmax}) and optimum moisture content (OMC) of the sand-bentonite mixtures were obtained and the same is reported in Table 4.4.

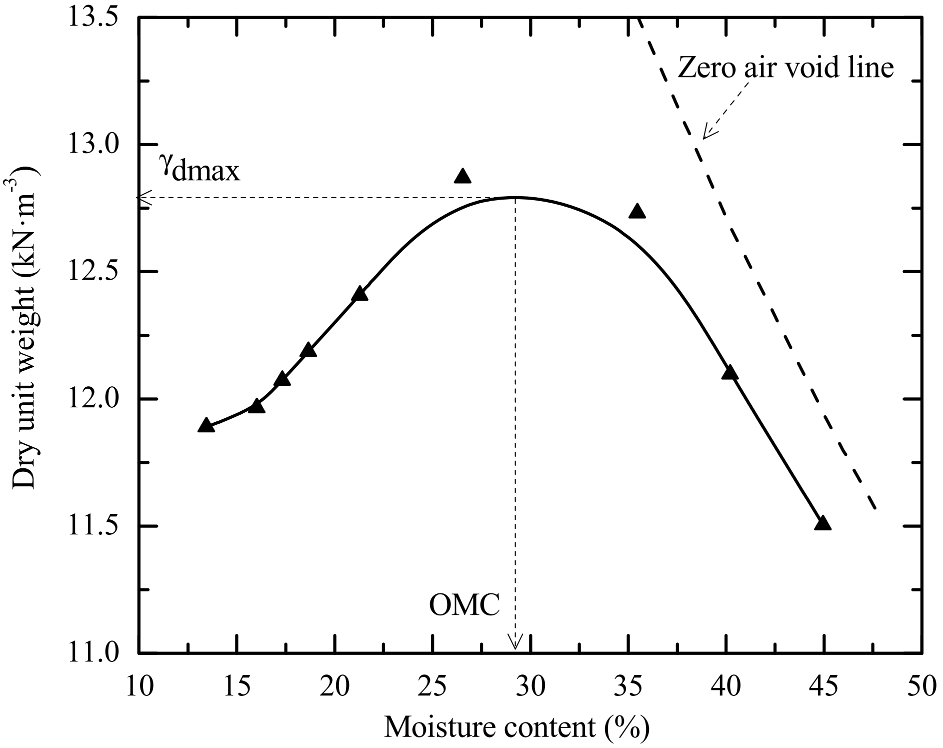

Figure 4.3 Compaction characteristics of bentonite

Table 4.4 Compaction characteristics of sand-bentonite mixtures

Material	γ_{dmax} (kN·m^{-3})	OMC (%)
SB10	19.5	14.6
SB20	20.3	12.0
SB30	17.9	13.5
SB40	20.3	14.2
SB50	18.9	19.6
SB70	19.2	13.8
SB100	12.8	29.3

4.4.2. Hydraulic conductivity

The hydraulic conductivity of the geomaterial determines its suitability as a liner or buffer material (Daniel, 1987 & 1990). Therefore, the hydraulic conductivity of the sand-bentonite mixtures (referred as buffer materials) was determined using flexible wall permeameter. The variation of cumulative volume of the effluent (permeant) with time was obtained under the steady state conditions. Based on the observed cumulative volume of the permeant per unit time through a unit cross section of the buffer material under applied hydraulic gradient, its hydraulic conductivity was determined using the following relationship. The experimentally obtained hydraulic conductivity of various buffer materials is reported in Table 4.5.

$$k=\frac{QL}{Aht} \tag{4.1}$$

where k is hydraulic conductivity in m·s^{-1}, Q is cumulative volume of water collected in m^3, L is length of the soil specimen in m, A is cross-section area of the soil specimen in m^2, h is head difference in m, and t is time elapsed in seconds.

Table 4.5 Hydraulic conductivity of the buffer materials

Material	**Hydraulic conductivity (×10^{-9} m·s^{-1})**
SB10	21.3
SB20	4.20
SB30	0.12
SB40	0.14
SB50	0.19
SB70	0.22
SB100	0.20

It can be noticed that the buffer materials considered in this study exhibited lower hydraulic conductivity than the stipulated value for construction of compacted clay liners of an engineered landfill (1×10^{-9} m·s^{-1} as per USEPA, 1989).

4.5. Thermal Properties

The thermal characteristics of buffer materials in terms of their thermal conductivity were obtained using transient heat technique by employing thermal probe. In order to quantify the influence of soil fabric on thermal conductivity, specimens compacted at different compaction states were selected. For this purpose, three specimens compacted on dry of optimum, one specimen in the proximity to OMC and three more specimens compacted on wet of optimum were considered. The schematic representation of these compaction states is illustrated in Figure 4.4. Upon compaction of the buffer material to the desired compaction state, the thermal probe was inserted and the thermal conductivity of it was determined. Table 4.6 depicts the variation of thermal conductivity values with the compaction state.

Further, the performance of the thermal probe was established by comparing the thermal conductivity of a wide variety of geomaterials vis-à-vis with that of obtained from the widely accepted C-Therm TCi^{TM}. The C-Therm TCi^{TM} thermal analyzer primarily measures thermal effusivity of the bulk material using transient plane heat source which in turn enable the determination of its thermal conductivity precisely (www.ctherm.com). The C-Therm TCi^{TM} thermal analyzer consists of high precision temperature measuring sensor, electronics to precisely impose the heat flux and to control the heat emission from the sensor and the software to measure the thermal properties, as shown in Figure 4.5. The plane heat source of C-Therm TCi^{TM}

comprises of a spiral-shaped primary heating element which in turn is surrounded by the secondary heat source in the form of a guarded heat ring. The heat emanated from the guarded ring ensures the one-dimensional heat flow from the primary heat source into the material under consideration. The electrical potential difference across the primary heat source is monitored precisely and the same is used for determining the thermal effusivity of the material using TCi's patented iterative technique (www.ctherm.com). The thermal effusivity of the material can be defined as the square root of the product of thermal conductivity, K, unit weight, ρ and specific heat capacity, C_p, (i.e., $\sqrt{K \times \rho \times C_p}$) and has units of $W \cdot s^{0.5} \cdot m^{-2} \cdot K^{-1}$. From the measured thermal effusivity, the thermal conductivity of the material was determined by knowing its specific heat capacity. The C-Therm TCi^{TM} has the ability to compensate variations in ambient temperature, which enables its suitability for measuring the thermal conductivity of various materials over a wide range of temperatures. The efficient determination of thermal conductivity of geomaterials using C-Therm TCi^{TM} demands an intimate contact between the material surface and the heat source of the device. For this purpose, the manufacturer recommends applying a very thin layer of non-wettable contact agent such as Anabond 652C between the plane heat source of the thermal analyzer and the material.

Table 4.6 Variation of thermal conductivity of buffer materials with compaction state

Material	w (%)	γ_d (kN·m^{-3})	θ (%)	K (W·m^{-1}·K^{-1})
SB0-A	1.0	14.1	14.1	0.651
SB0-B	2.0	13.9	27.7	0.721
SB0-C	3.0	13.6	40.8	0.759
SB0-D	4.0	13.9	55.8	0.870
SB0-E	5.0	13.9	69.4	0.930
SB0-F	6.0	14.2	85.3	1.053
SB10-A	4.5	16.1	7.4	0.648
SB10-B	6.4	16.5	10.8	0.726
SB10-C	8.5	16.6	14.5	0.786
SB10-D	15.0	16.3	25.0	1.095
SB10-E	20.2	16.1	33.1	1.121
SB10-F	28.1	15.9	45.5	1.384
SB20-A	5.2	15.9	8.5	0.676
SB20-B	7.4	16.3	12.2	0.895
SB20-C	10.9	16.8	18.7	0.966
SB20-D	16.3	17.1	28.4	1.346
SB20-E	19.2	16.7	32.6	1.650
SB20-F	25.4	15.0	38.8	1.772
SB30-A	10.7	14.2	15.5	0.299
SB30-B	12.0	14.7	18.0	0.357
SB30-C	13.7	14.5	20.3	0.476

Material	**w (%)**	**γ_d (kN·m^{-3})**	**θ (%)**	**K (W·m^{-1}·K^{-1})**
SB30-D	18.2	14.2	26.3	0.553
SB30-E	22.0	13.7	30.8	1.231
SB40-A	10.1	16.0	16.5	0.806
SB40-B	17.2	17.1	30.0	1.271
SB40-C	20.1	16.9	34.6	1.466
SB40-D	25.2	15.7	40.2	1.579
SB50-A	12.3	12.7	16.0	0.249
SB50-B	15.2	12.8	19.8	0.490
SB50-C	18.0	13.4	24.6	0.531
SB50-D	19.8	14.5	29.3	0.568
SB50-E	20.9	14.0	29.9	0.572
SB50-F	22.1	13.6	30.6	0.619
SB60-A	5.4	16.2	8.9	0.572
SB60-B	9.7	16.7	16.5	1.516
SB60-C	10.1	16.8	17.3	1.701
SB60-D	15.0	17.0	26.0	1.784
SB60-E	16.8	16.6	28.4	1.850
SB70-A	5.2	16.0	8.5	0.496
SB70-B	10.5	16.4	17.6	1.280
SB70-C	13.2	16.6	22.3	1.53
SB70-D	16.7	16.5	28.1	1.775
SB70-E	18.4	16.2	30.4	1.783
SB80-A	4.9	15.8	7.9	0.420
SB80-B	11.3	16.5	19.1	1.034
SB80-C	16.5	16.6	27.9	1.350
SB80-D	18.9	16.1	31.0	1.784
SB80-E	20.2	15.8	32.5	1.720
SB90-A	10.5	13.4	14.3	0.365
SB90-B	14.5	13.6	20.1	0.851
SB90-C	19.2	14.5	28.4	1.345
SB90-D	22.5	14.5	33.3	1.693
SB90-E	24.1	15.1	37.1	1.557
SB100-A	12.8	11.0	14.4	0.292
SB100-B	17.2	11.4	20.1	0.597
SB100-C	23.9	12.3	29.9	1.439
SB100-D	26.3	12.4	33.1	1.734
SB100-E	28.1	12.3	35.2	1.795
SB100-F	29.4	12.2	36.5	1.840

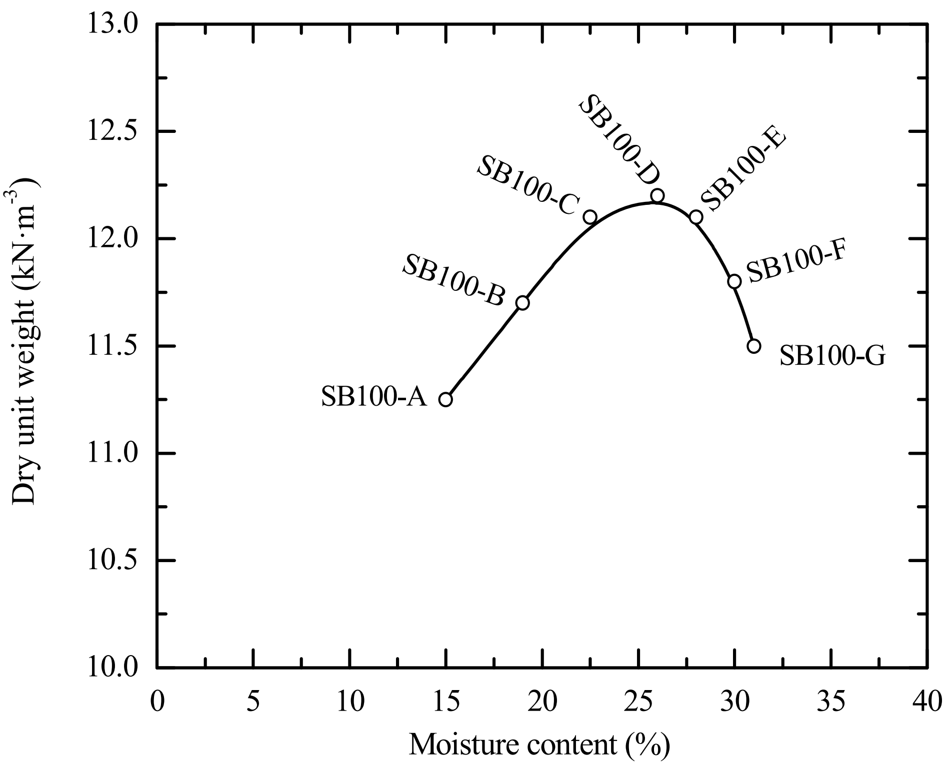

Figure 4.4 Compaction states of the samples used for determination of thermal conductivity of buffer material SB100

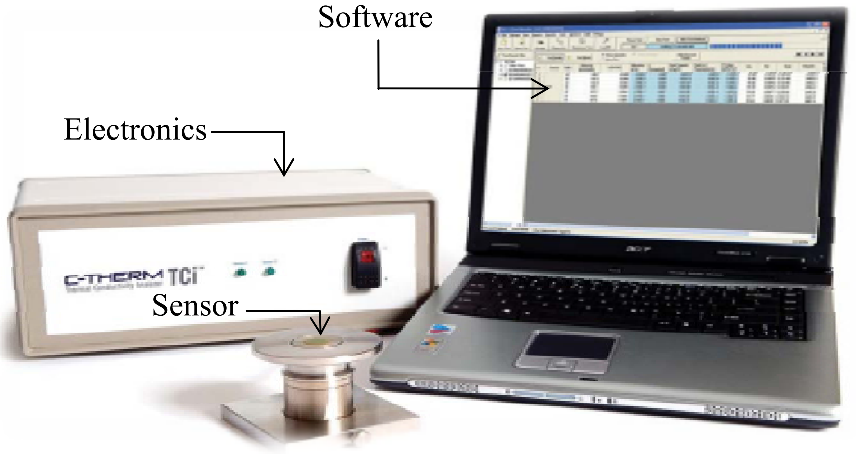

Figure 4.5 C-Therm TCi^{TM} thermal analyzer (www.ctherm.com)

For the determination of thermal conductivity of buffer materials employing C-Therm TCi^{TM}, a disc-shaped soil specimens of 34.5 mm diameter and 6.7 mm height were extracted from the compacted mass of the buffer material using a stainless steel ring. The thermal conductivity of selected buffer materials (viz. SB30, SB50 and SB100) were obtained using the C-Therm TCi^{TM} thermal analyzer and the results are presented in Table 4.7.

Table 4.7 Variation of thermal conductivity of buffer materials obtained from probe and C-Therm TCi^{TM}

Material	**w (%)**	**γ_d (kN·m^{-3})**	**θ (%)**	**K (W·m^{-1}·K^{-1})**		**Percent difference**
				Probe	**C-Therm TCi^{TM}**	
SB30-A	7.17	13.76	10.06	0.226	0.254	11.0
SB30-B	9.53	14.04	13.64	0.271	0.294	7.8
SB30-C	10.7	14.21	15.50	0.299	0.304	1.6
SB30-D	12	14.74	18.04	0.357	0.368	3.0
SB30-E	13.67	14.55	20.27	0.476	0.499	4.6
SB30-F	18.23	14.15	26.31	0.553	0.569	2.8
SB30-G	22.03	13.71	30.80	1.831	1.886	2.9
SB50-A	12.3	12.73	15.97	0.443	0.469	5.54
SB50-B	15.17	12.80	19.8	0.49	0.524	6.49
SB50-C	18.0	13.42	24.62	0.531	0.565	6.02
SB50-D	19.8	14.51	29.28	0.568	0.572	0.70
SB50-E	20.9	14.04	29.91	0.572	0.596	4.03
SB50-F	22.1	13.59	30.61	0.619	0.634	2.37
SB50-G	25.4	13.17	34.11	1.602	1.667	3.90
SB100-A	12.8	11.05	14.41	0.522	0.543	4.02
SB100-B	17.2	11.44	20.06	0.597	0.618	3.40
SB100-C	21.9	12.04	26.87	0.641	0.662	3.17
SB100-D	23.9	12.25	29.85	1.439	1.499	4.00
SB100-E	26.3	12.36	33.14	1.734	1.758	1.37
SB100-F	28.1	12.29	35.21	1.795	1.813	0.99
SB100-G	29.4	12.16	36.46	1.84	1.887	2.49

For establishing the efficacy of the thermal probe, the thermal conductivity of typical buffer materials obtained using it was compared with that obtained using C-Therm TCi^{TM} as illustrated in Figure 4.6. It can be observed that the thermal conductivity of buffer material obtained using the thermal probe is in good agreement with that of obtained using C-Therm TCi^{TM}. Hence, it can be concluded that the thermal probe yields accurate thermal conductivity of various geomaterials including the buffer materials, for all practical purposes. Further, the percent difference between the thermal conductivities arrived using probe and C-Therm is in the order of ten percent in few instances, however, the majority of the measurements are well within five percent.

Figure 4.7 depicts the variation of thermal conductivity with volumetric moisture content, θ for a typical buffer material (SB30). It is evident that the thermal conductivity of the buffer material is increasing with the volumetric moisture content. This increase in thermal conductivity with volumetric moisture content is owing to the enhanced packing density attributed from the higher placement moisture content up to OMC and beyond this threshold moisture content, the increase in thermal conductivity is ascribed to variation in the degree of saturation.

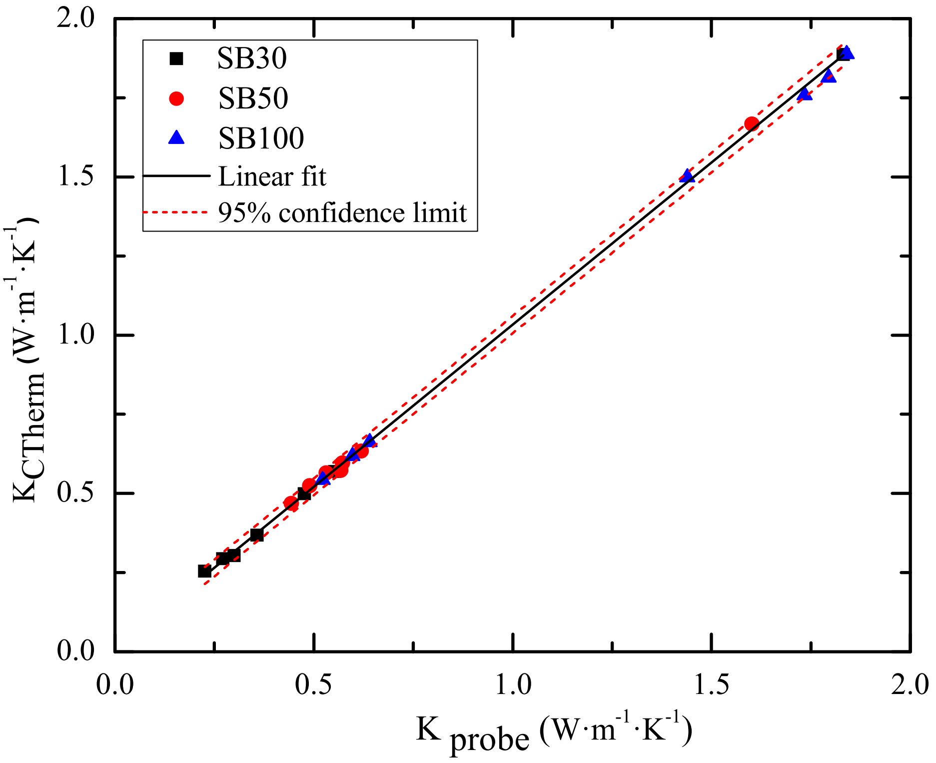

Figure 4.6 Comparison of thermal conductivity of SB30, SB 50 and SB 100 from probe and C-Therm TCi^{TM}

The proportionate increase in thermal conductivity of buffer material with its volumetric moisture content reveals the significance of placement moisture content (Arnepalli and Singh, 2004a; Joseph, 2014). When the moisture is added to the soil, a thin layer of water develops around the soil particles, which bridges the voids between the particles and increases the effective contact area; which in turn is responsible for better heat flow and enhanced thermal conductivity. Similarly, with the increase in dry unit weight more number of particles are packed into a unit bulk volume and thus formation of large number of contact points between the soil particles, which in turn results in higher thermal conductivity (Salomone et al., 1984; Salomone and Kovacs, 1984; Salomone and Marlowe, 1989).

The sand with high quartz content exhibited a greater thermal conductivity compared to the counterpart, comprised of plagioclase, feldspar, and pyroxene (Kersten, 1949; Mitchell and Soga, 2005). Whereas, the soils with high organic content yield lower thermal conductivity (Salomone and Marlowe, 1989). In the present study, it was observed that with a decrease in sand content (primarily made up of quartz) by increasing the bentonite fraction in the sand-bentonite buffer material, the thermal conductivity value has increased. For instance, this observation appears to be contradicting with the findings reported in the literature. This is attribute to the fact that, the increase in bentonite fraction in the buffer material results in improved packing density, which in turn provides an effective contact area for surface heat flow and leads to enhanced thermal conductivity. Moreover, bentonite considered in the synthesis of buffer material is also characterized by moderate amounts of quartz mineral which might be partly responsible for the increased thermal conductivity of the buffer.

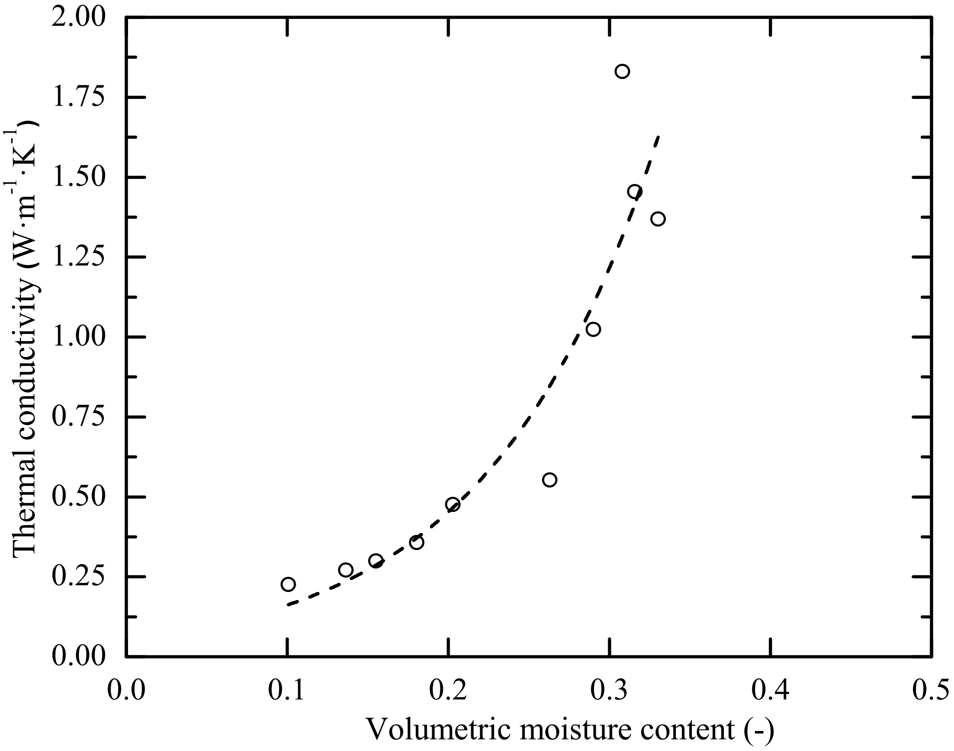

Figure 4.7 Variation of thermal conductivity with volumetric moisture content for SB30

Further, for a given moisture content and dry unit weight the thermal conductivity of coarse-grained angular soils is higher than that of fine-grained soils (Kersten, 1949; Salomone and Marlowe, 1989). In addition, uniformly graded soils generally exhibit lower thermal conductivity when compared to well-graded soils (Salomone and Marlowe, 1989). In the present study, it is observed that the thermal conductivity of compacted SB100 is highest when compared to the other sand-bentonite mixtures. This may be attributed to synergetic contribution from bridging water as well as improved contact between the particles, and hence the improved surface heat transfer.

Incidentally, the variation of thermal conductivity of various buffer materials with the volumetric moisture content corroborated with the findings reported in literature. For the sake of completeness, the obtained results are presented in Table 4.6 and Figure 4.8.

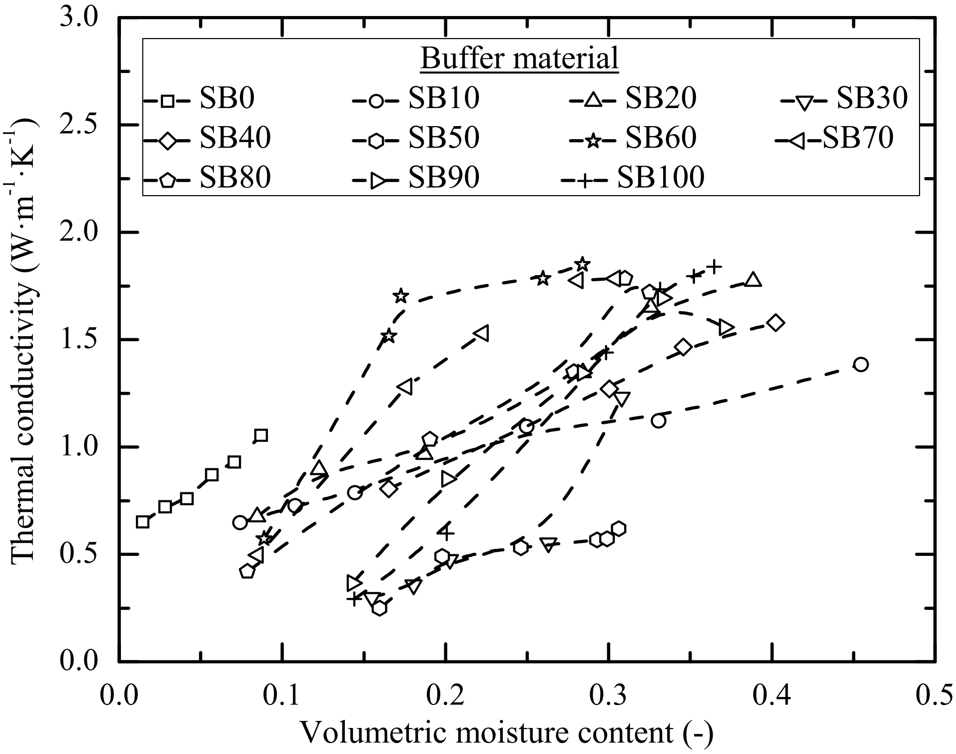

Figure 4.8 Variation of thermal conductivity of buffer materials with volumetric moisture content

4.5.1. Generalized model for predicting thermal conductivity of buffer materials

The buffer materials are subjected to variable environmental conditions including the temperature variation and moisture imbalance, which alter their thermal conductivity. To ensure the long-term performance of buffer material in typical DGR conditions, the comprehensive understanding of variability in its thermal conductivity owing to the above factors is essential. For this purpose, the experimentally obtained thermal conductivity of buffer materials considered in this study was corroborated with various prediction models available in the literature in view of assessing their suitability for predicting the thermal conductivity. This revealed the lacuna of existing models in the precise estimation of thermal conductivity of buffer materials and highlighted the need for the development of a generalized prediction model.

In general, the heat migration phenomenon through the porous materials is determined by three fundamental mechanisms viz. conduction, convection, and radiation. Among these mechanisms, conduction contributes to the heat migration significantly via contact between the particles. In general, a typical engineered buffer material exhibits reasonable contact area among the particles owing to the presence of different sized particles in it. The effective contact area, which is a function of their relative size and packing density, has relevance to conductive heat flow. In addition, among the major minerals occurring in natural geomaterials, quartz, 1:1 kaolinitic clay mineral, and 2:1 smectite-based clay minerals contribute the lion's share. It is interesting to note that the quartz and smectite-based clay mineral exhibit greater thermal conductivity when compared to the other minerals (Mitchell and Soga, 2005; Jobmann and Buntebarth, 2009). Further, literature established the thermal conductivity of quartz, kaolinite and smectite as 7.8, 2.8 and 1.8 $W \cdot m^{-1} \cdot K^{-1}$, respectively (Horai, 1971). In the case of sand-bentonite based buffer materials, quartz along with smectite-based clay minerals are present abundantly. Therefore, it is quite rationale to incorporate the mineralogical nature of buffer materials while predicting their bulk thermal conductivity. The dry unit weight of geomaterial represents the packing density which in turn governs the heat flow, and hence, it is essential to consider the influence of dry unit weight in estimating the thermal conductivity. On the contrary, the heat migration through partially saturated geomaterials is governed by the fraction of voids filled by the pore fluid and their interconnectivity since the thermal conductivity of pore water ($K \approx 0.58$ $W \cdot m^{-1} \cdot K^{-1}$) is higher than the air phase (Fredlund et al., 2012).

From the above discussion it can be realized that, the four inherent properties of the geomaterials viz. mineralogical nature, particle size distribution characteristics (percent fraction of various sized particles), and compaction state (dry unit weight and molding moisture content) predominantly determines its thermal conductivity (Arnepalli and Singh, 2004 a & b; Jobmann and Buntebarth, 2009; Gualtieri et al., 2010; Caridad et al., 2014). In view of this, an effort was made to evaluate the efficacy of various existing prediction models in terms of statistical measures, by considering the input parameters originally proposed by the authors. The present study considered various prediction models for comparison viz. Kersten model (1949), de Vries model (1963), series and parallel heat flow equations (McGaw, 1969; Farouki, 1982), Johansen model (1975) and MDDTherm (Arnepalli et al., 2004b). Table 4.8 presents the experimental results of various buffer materials and predicted thermal conductivity values along with the percent difference between them. It can be observed that the average percent difference between the predicted and measured thermal conductivity values from all the models are more than 50 %. In addition, Table 4.9 enumerates the input variables considered, prediction efficiency in terms of statistical parameters and lacuna of each model mentioned above. Further, Figure 4.9 furnishes a graphical comparison between experimental and predicted thermal conductivities of the geomaterials obtained by employing the empirical relationships listed in Table 4.9.

The correlation coefficient (R^2) and the root mean square error (RMSE) obtained by comparing the thermal conductivity values obtained using the prediction models with the experimental values are also presented in Table 4.9. It can be noted that none of the models predict the experimental thermal conductivity of the buffer materials precisely. The correlation coefficient obtained for all the models are less than 70 percent and most of the models yield even less than 50 percent. Further, the RMSE values are found to be high (more than 50 percent). Hence, the need of proposing a generalized model for prediction of thermal conductivity of sand-bentonite based buffer materials was ascertained.

For the development of a generalized prediction model, a multiple linear regression (MLR) based empirical model, which is in line with the MDDTherm proposed by Arnepalli and Singh (2004b), incorporating the effects of particle size distribution characteristics (in terms of fraction of sand-, silt- and clay-sized particles), and mineralogical composition (in terms of amounts of quartz, kaolinite, and montmorillonite). For comparison purpose, an artificial neural network (ANN) based prediction model was also proposed.

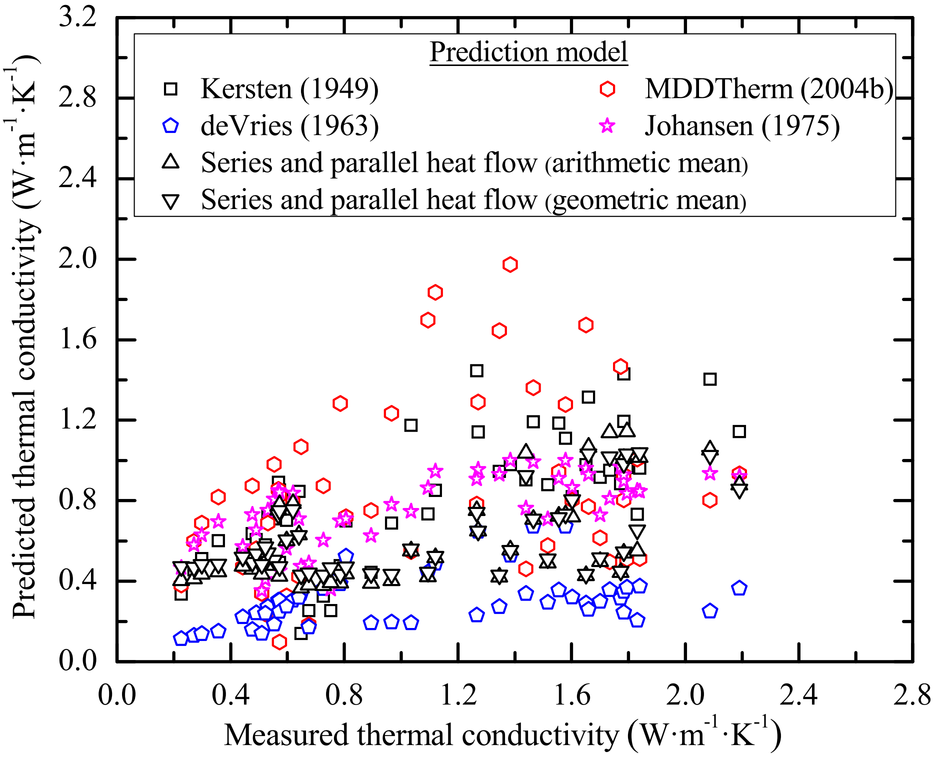

Figure 4.9 Comparison of measured and estimated soil thermal conductivity by existing prediction models

Table 4.8 Efficacy of various empirical models in predicting the thermal conductivity of buffer materials

Material	Measured K ($W \cdot m^{-1} \cdot K^{-1}$)	Predicted K ($W \cdot m^{-1} \cdot K^{-1}$)											
		Kersten model	**Percent difference (%)**	**MDD Therm**	**Percent difference (%)**	**deVries model**	**Percent difference (%)**	**Johansen model**	**Percent difference (%)**	**Flow model (arithmetic mean)**	**Percent difference (%)**	**Flow model (geometric mean)**	**Percent difference (%)**
SB10	0.65	0.14	78.44	1.07	-64.89	0.34	47.98	0.47	26.90	0.37	43.41	0.43	33.58
	0.73	0.33	55.12	0.87	-20.49	0.36	50.07	0.60	16.89	0.38	47.74	0.43	40.69
	0.79	0.48	39.26	1.28	-63.12	0.39	50.86	0.70	10.98	0.39	50.15	0.43	44.96
	1.10	0.73	32.92	1.70	-54.93	0.44	59.54	0.86	21.18	0.42	61.37	0.44	59.49
	1.12	0.85	24.01	1.84	-63.73	0.49	56.43	0.95	15.65	0.52	53.84	0.52	53.38
	1.38	0.98	29.29	1.97	-42.52	0.53	61.86	1.00	27.75	0.56	59.85	0.55	60.06
SB20	0.68	0.25	62.61	0.18	72.84	0.17	74.65	0.49	27.55	0.38	43.62	0.44	34.76
	0.89	0.44	50.31	0.75	16.03	0.19	78.59	0.63	29.98	0.39	56.41	0.44	51.15
	0.97	0.69	28.69	1.23	-27.73	0.20	79.77	0.78	19.16	0.40	58.25	0.43	55.17
	1.35	0.95	29.72	1.64	-22.15	0.27	79.76	0.93	30.96	0.42	68.75	0.43	68.02
	1.65	0.98	40.74	1.67	-1.30	0.29	82.39	0.96	41.80	0.43	74.04	0.43	73.71
	1.77	0.88	50.14	1.47	17.29	0.31	82.28	0.97	45.49	0.44	74.96	0.45	74.66
SB30	0.30	0.51	-71.26	0.69	-130.04	0.14	53.76	0.63	-110.19	0.44	-45.66	0.48	-61.24
	0.36	0.60	-68.28	0.82	-129.33	0.15	57.96	0.70	-94.92	0.45	-25.40	0.48	-35.75
	0.48	0.64	-33.61	0.87	-83.74	0.16	66.50	0.73	-53.39	0.46	3.45	0.49	-3.39
	0.55	0.71	-28.30	0.98	-77.17	0.19	66.47	0.81	-46.14	0.48	13.35	0.50	9.14
SB40	0.81	0.70	13.12	0.72	10.62	0.52	35.18	0.71	11.99	0.44	45.76	0.47	41.64
	1.27	1.14	10.23	1.29	-1.52	0.65	49.18	0.95	24.96	0.65	48.81	0.65	48.95
	1.47	1.19	18.68	1.36	7.14	0.67	54.27	0.99	32.25	0.71	51.69	0.71	51.74
	1.58	1.11	29.73	1.28	19.11	0.67	57.53	1.00	36.67	0.73	53.71	0.73	53.68
SB50	0.53	0.73	-36.65	0.69	-29.80	0.27	48.82	0.75	-41.48	0.52	2.30	0.54	-1.56
	0.57	0.89	-56.90	0.86	-50.74	0.30	46.39	0.85	-49.43	0.75	-32.49	0.73	-28.50
	0.57	0.85	-49.12	0.82	-44.08	0.30	46.83	0.84	-47.15	0.78	-36.36	0.75	-31.19
	0.62	0.82	-32.29	0.80	-28.49	0.30	50.85	0.84	-35.14	0.79	-27.17	0.75	-21.84

Material	Measured K (W·m^{-1}·K^{-1})	Predicted K (W·m^{-1}·K^{-1})											
		Kersten model	Percent difference (%)	MDD Therm	Percent difference (%)	deVries model	Percent difference (%)	Johansen model	Percent difference (%)	Flow model (arithmetic mean)	Percent difference (%)	Flow model (geometric mean)	Percent difference (%)
SB60	0.57	0.49	13.88	0.10	82.93	0.25	56.61	0.45	21.30	0.43	25.69	0.47	17.65
	1.52	0.88	41.99	0.58	61.90	0.29	80.65	0.71	53.28	0.49	67.65	0.51	66.28
	1.70	0.92	46.17	0.61	63.88	0.30	82.47	0.73	57.12	0.50	70.73	0.52	69.65
	1.78	1.19	33.04	0.93	48.01	0.35	80.54	0.90	49.76	0.54	69.70	0.55	69.40
SB80	1.03	1.17	-13.55	0.55	47.08	0.19	81.50	0.75	27.88	0.55	46.83	0.56	45.90
	1.27	1.44	-14.12	0.78	38.16	0.23	81.71	0.91	28.36	0.75	40.62	0.74	41.48
	1.78	1.43	19.91	0.80	54.95	0.24	86.30	0.93	47.96	1.01	43.34	0.98	44.84
SB100	0.60	0.70	-17.74	0.33	45.40	0.27	54.09	0.56	5.63	0.60	-0.73	0.60	-1.31
	0.64	0.85	-32.10	0.42	34.12	0.32	50.31	0.71	-10.70	0.63	1.70	0.63	2.46
	1.44	0.90	37.21	0.46	67.99	0.34	76.54	0.76	47.02	1.04	28.00	0.93	35.70
	1.73	0.95	45.16	0.50	71.42	0.36	79.40	0.81	53.21	1.14	34.39	1.02	41.34
	1.80	0.96	46.29	0.51	71.62	0.37	79.49	0.84	53.46	1.14	36.29	1.03	42.54
	1.84	0.96	47.75	0.51	72.14	0.37	79.70	0.85	54.01	1.02	44.79	1.04	43.58

Table 4.9 Nature of various empirical models in predicting the thermal conductivity of buffer materials and their limitations

Prediction model	**Model nature**	**R^{2*}**	**$RMSE^{\#}$**	**Comment/limitations**
Flow models (arithmetic mean)	$K=\frac{K_{up}+K_{lw}}{2}; \quad K_{up},K_{lw}=f(\chi_s,\chi_f,K_s,K_f)$	0.59	0.66	Primitive model, doesn't represent actual soil geometry
Flow models (geometric mean)	$K=K_s^{1-\eta}\times K_w^{\eta}$	0.58	0.65	Applicable for lower values of χ_s/χ_f
Kersten model	For sandy soils $K_u=0.1442[0.7\log(w)-0.4]\times 10^{0.6243\times\gamma_d}$ $K_f=0.001096\ 10^{0.8116\times\gamma_d}+0.00461w\times 10^{0.9115\times\gamma_d}$ For fine-grained soils $K_u=0.1442[0.9\log(w)-0.2]\times 10^{0.6243\times\gamma_d}$ $K_f=0.001442\ 10^{1.373\times\gamma_d}+0.01226w\times 10^{0.4994\times\gamma_d}$	0.72	0.47	Particle size and mineralogy is not considered
DeVries model	$K=\frac{\chi_f K_{fl}+f_s\chi_s K_s+f_a\chi_a K_a}{\chi_f+f_s\chi_s+f_a\chi_a}$	0.39	0.93	Several important input parameters such as dry density, weight fraction, mineralogy are missing
Johansen model	For sandy soils $K_{ru}=0.7\log(S_r)+1; K_{rf}=S_r$ For fine-grained soils $K_{ru}=\log(S_r)+1; K_{rf}=S_r$ $K=K_r(K_s-K_{dry})+K_{dry}$	0.69	0.55	Degree of saturation can be representative of soil moisture, contribution of clay minerals along with placement density is not given enough due
MDD Therm	$\frac{1}{K}=0.01\times\left[a\times 10^{-3+0.6243\times\gamma_d}\right]$; a=f(w, type of soil)	0.32	0.63	Mineralogy is not considered

K_{up}, K_{lw} are the upper and lower bound for thermal conductivity; χ_s, χ_f are the fraction of solids and fluid respectively in the soil; K_s, K_{fl} are the thermal conductivity of solid and fluid phase respectively; η is the porosity of the geomaterial; K_u, K_{fr} are thermal conductivity for unfrozen and frozen soils respectively; w is the gravimetric moisture content of the soil; γ_d is dry unit weight of the soil; χ_f, χ_s, χ_a are fractions of fluid, solid and air respectively in the soil; K_f, K_s, K_a are thermal conductivities of fluid, solid and air respectively; f_s, f_a are the weighing factors for solid and air phase respectively; K_{ru}, K_{rf} are normalized thermal conductivity for unfrozen and frozen soils respectively; S_r is Degree of saturation; K_r, K_{sr}, K_{dry} are normalized, saturated and dry thermal conductivity of soil; *Correlation coefficient (R) is a measure of nature (positive or negative) and strength of the formulation; # Root mean square error (RMSE) relates to the scatteredness in a data set; it is calculated as the square root of sum of mean squared errors.

Multiple linear regression based prediction model

The proposed MLR based empirical model relies on the experimentally obtained thermal conductivity of various buffer materials such as SB10, SB20, SB30, SB40, SB50, SB60, SB70, SB80, SB90, and SB100 (Mishra et al., 2016). It assumes the following relationship:

$$K = \alpha_T[\log\ (w) + \beta_T] \times 10^{0.06363\times\gamma_d} \tag{4.2}$$

where K is thermal conductivity of buffer materials in $W\cdot m^{-1}\cdot K^{-1}$, w is gravimetric moisture content in percent, γ_d is dry unit weight of the buffer material in $kN\cdot m^{-3}$, α_T and β_T are fitting parameters relied upon particle size- and mineral-fractions of the buffer material, i.e., $\alpha_T=\xi(f_{sa}, f_{si}, f_{sc})$ and $\beta_T=\psi(f_Q, f_K, f_M)$, f_{sa} is fraction of sand-sized particles present in the buffer material, f_{si} is fraction of silt-sized particles present in the buffer material, f_{sc} is fraction of clay-sized particles present in the buffer material, f_Q is fraction of quartz minerals present in the buffer material, f_K is fraction of kaolinite minerals present in the buffer material, and f_M is fraction of smectite based montmorillonite minerals present in the buffer material (refer Figure 4.10).

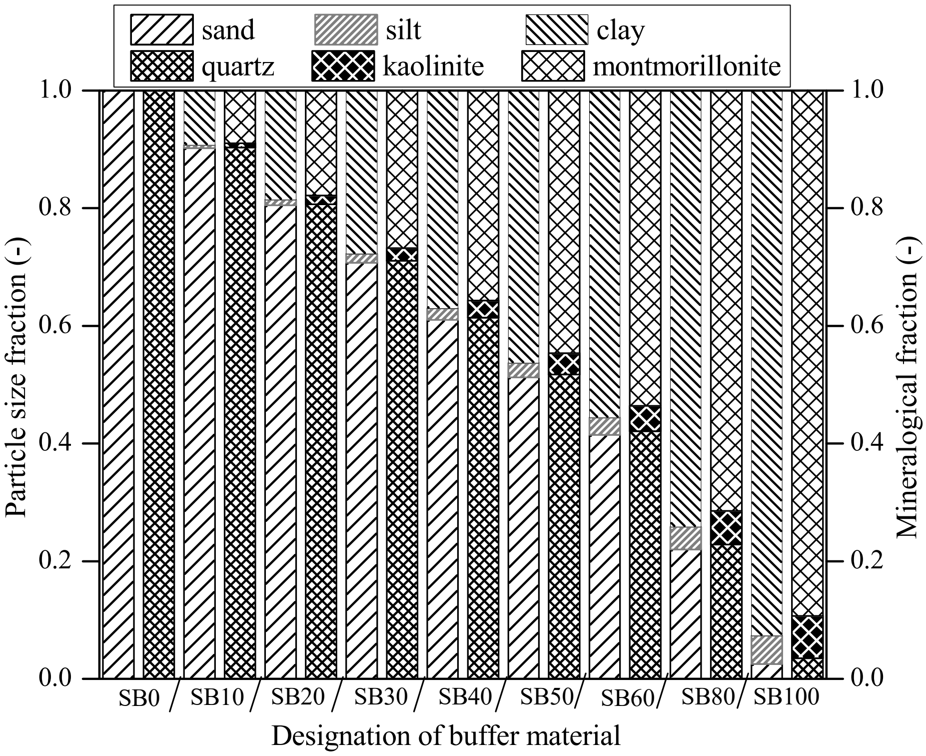

Figure 4.10 Various size (sand-, silt-, clay-size) and mineralogical (quartz, kaolinite, montmorillonite) fractions present in the buffer materials considered in this study

The fitting parameters α_T and β_T obtained based on Equation 4.2 and thermal conductivity along with corresponding compaction state data are presented in Table 4.10. Further, an attempt was made to correlate α and β in terms of several basis functions and linear regression technique as per the Equations 4.3 and 4.4. The nature of the basis functions along with the relevant weights, correlation coefficient (R^2) and standard error (SE) are summarized in Table 4.11.

$$\alpha_T = \sum_{i=sa,\, si,\, sc} W_i B_i \tag{4.3}$$

$$\beta_T = \sum_{i=Q,\, K,\, M} W_i B_i \tag{4.4}$$

where W_i is weight for i'th input variable, B_i is basis function for i'th input variable.

The basis functions enumerated in Table 4.11 seem to deliver similar performance in terms of statistical indices. However, negative exponential basis (NEB) models are in line with the theoretical understanding. This is mainly due to the fact that $K_{sa} > K_{si} > K_{sc}$ and $K_Q > K_K \approx K_M$ is being represented by the absolute weights predicted by NEB.

Table 4.10 Fitting parameters for different buffer materials

Material	α_T	β_T
SB0	0.046	0.080
SB10	0.093	-0.096
SB20	0.159	-0.396
SB30	0.347	-0.895
SB40	0.091	0.051
SB50	0.333	-0.996
SB60	0.211	-0.417
SB70	0.207	-0.465
SB80	0.210	-0.523
SB90	0.485	-0.877
SB100	0.666	-1.032

The comparison of experimentally measured and predicted thermal conductivity of buffer materials using the proposed model is presented in Figure 4.11. It can be perceived that the proposed MLR model performs well in terms of statistical indices with an overall R^2 of 0.95 and RMSE of 0.148.

Artificial neural network based prediction model

An ANN model based on the experimental data was also developed in the present study. The proposed model has incorporated different input parameters (w, γ_d, f_{sa}, f_{si}, f_{sc}, f_Q, f_K, f_M) for estimating the soil thermal conductivity (K). The model was developed as a feed-forward network with the sigmoid basis and trained using Levenberg-Marquardt backpropagation algorithm, which is quite efficient compared to gradient descent backpropagation algorithm (Juang and Elton, 1997; Demuth and Beale, 2000; Goh et al., 2005). Experimental data from Table 4.6 and Figure 4.8 were randomized; 60 % of the data for training, 20 % for validation and 20 % of the data used for testing the proposed ANN network.

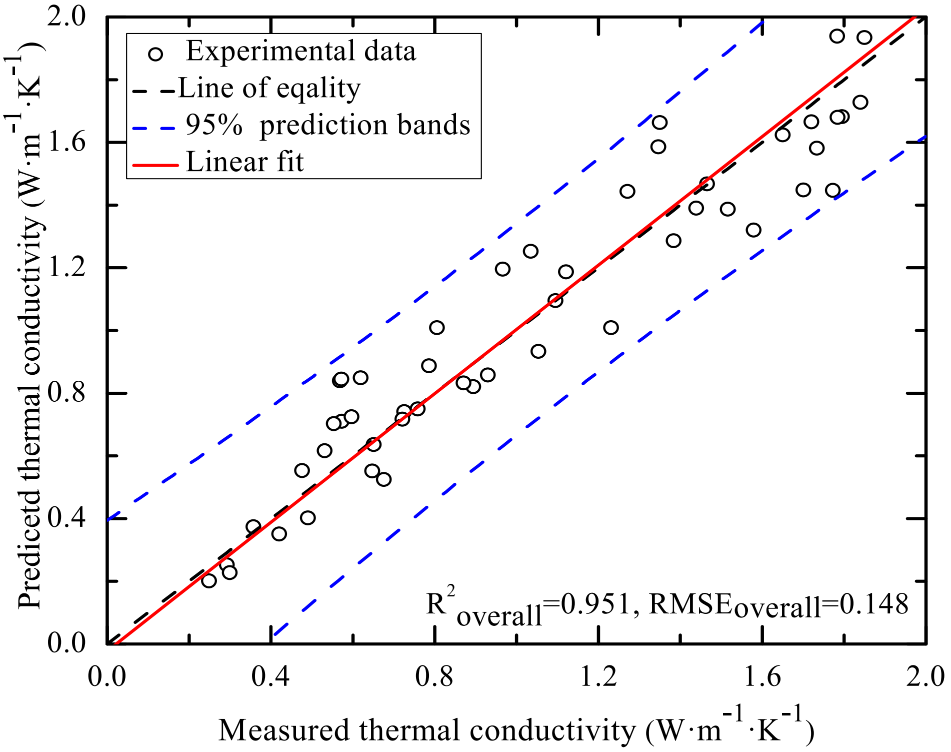

Figure 4.11 Performance of the proposed multiple linear regression model to predict thermal conductivity of buffer materials

The governing equation for the network is presented below:

$$K = f_{sig}\left\{b_o + \sum_{k=1}^{h}\left[w_k \times f_{sig}\left(b_{hk} + \sum_{i=1}^{m} w_{ik} I_i\right)\right]\right\} \tag{4.5}$$

where h is number of neurons in the hidden layer, f_{sig} is sigmoid basis or transfer function, b_o represents bias at the output layer, b_{hk} is bias at the kth neuron of hidden layer, w_k is connection weight between kth neuron of hidden layer and the single output neuron, w_{ik} is connection weight between ith input variable and kth neuron of hidden layer.

The weights and biases for the proposed model are evaluated by following the principles depicted by Das and Basudhar (2006), and the same is summarized in Table 4.12. For sake of validation, the Equation 4.5 is rewritten in terms of the weights and biases for 8-3-1 network architecture and the same is also presented in Table 4.12,

$$K = \frac{e^C - e^{-C}}{e^C + e^{-C}} \tag{4.6}$$

where

$$C = -0.1614 + B_1 + B_2 + B_3 \tag{4.7}$$

$$B_1=0.8355\times\frac{e^{A_1}-e^{-A_1}}{e^{A_1}+e^{-A_1}} \tag{4.8}$$

$$B_2=-1.3940\times\frac{e^{A_2}-e^{-A_2}}{e^{A_2}+e^{-A_2}} \tag{4.9}$$

$$B_3=-1.1897\times\frac{e^{A_3}-e^{-A_3}}{e^{A_3}+e^{-A_3}} \tag{4.10}$$

$$A_1=-1.6249+1.6848w+0.0367\gamma_d-0.1188f_{sa}-0.8634f_{si}-1.4011f_{sc}+0.0750f_Q+0.0417f_K -0.8658f_M \tag{4.11}$$

$$A_2=0.7721+0.2044w-1.19141\gamma_d+0.3715f_{sa}-0.1762f_{si}+0.5484f_{sc}+0.9508f_Q+0.6268f_K -0.9254f_M \tag{4.12}$$

$$A_3=-2.2819-2.2608w+0.3495\gamma_d-0.3251f_{sa}+0.7981f_{si}+0.5577f_{sc}+0.0589f_Q+0.04869f_K +1.3419f_M \tag{4.13}$$

The architecture and the performance of the proposed ANN model in training, validation and testing phase are detailed in Figures 4.12 and 4.13. The proposed ANN scheme detailed in Equation 4.6 has an overall R^2 of 0.951 and RMSE of 0.151. The performance of ANN scheme is comparable to MLR based model.

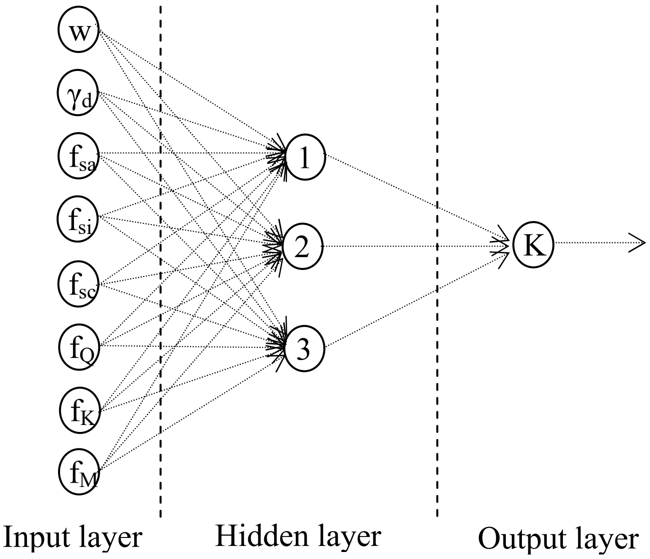

Figure 4.12 Architecture of the proposed artificial neural network

Further, cumulative probability plotted against the ratio of predicted to the measured thermal conductivity of the buffer materials for the proposed MLR and ANN model are superimposed in Figure 4.14. Ideal prediction models free from overprediction and underprediction should have a ratio of predicted to measured output at 50 % cumulative probability (P_{50}) close to 1 (Mishra et al., 2016). The P_{50} for ANN and MLR model was observed to be 0.946 and 0.984, respectively. Hence, the MLR model seems to perform better than the ANN model.

Table 4.11 Basis functions, weights and statistical parameters for estimation of α and β

Type of basis function	**B_i**	**For α_T**					**For β_T**				
		W_{sa}	**W_{si}**	**W_{sc}**	**R^2**	**SE**	**W_Q**	**W_K**	**W_M**	**R^2**	**SE**
Linear	i	0.05	0	0.52	0.92	0.15	-0.21	0	-0.99	0.87	0.38
Exponential	$\exp(i)$	0.32	-1.31	0.64	0.93	0.14	0.13	-0.29	-0.30	0.87	0.41
Negative exponential	$\exp(-i)$	1.49	-1.33	0.98	0.93	0.14	-0.72	-0.43	0.47	0.87	0.41
Sigmoid	$\frac{\exp(i)-\exp(-i)}{\exp(i)+\exp(-i)}$	0.25	56.82	-2.95	0.95	0.14	-0.33	-24.78	1.24	0.87	0.41
Power	10^i	0.02	-0.05	0.07	0.94	0.14	0.03	-0.47	-0.05	0.87	0.41

Table 4.12 Weights and biases for the proposed network

Identification of the neuron	**Weights (w_{ik})**									**Biases**	
	w	**γ_d**	**f_{sa}**	**f_{si}**	**f_{sc}**	**f_Q**	**f_K**	**f_M**	**Output**	**b_{hk}**	**b_o**
Hidden neuron 1 (k=1)	2.08	0.28	1.22	-0.59	-0.40	-0.28	-1.39	-0.66	0.70	-2.30	0.42
Hidden neuron 2 (k=2)	-0.37	-1.19	-0.75	-0.25	-0.49	1.02	-0.34	-0.40	-1.66	1.18	
Hidden neuron 3 (k=3)	-1.63	1.77	-0.84	0.95	0.51	-1.29	0.06	1.52	-1.01	-3.87	

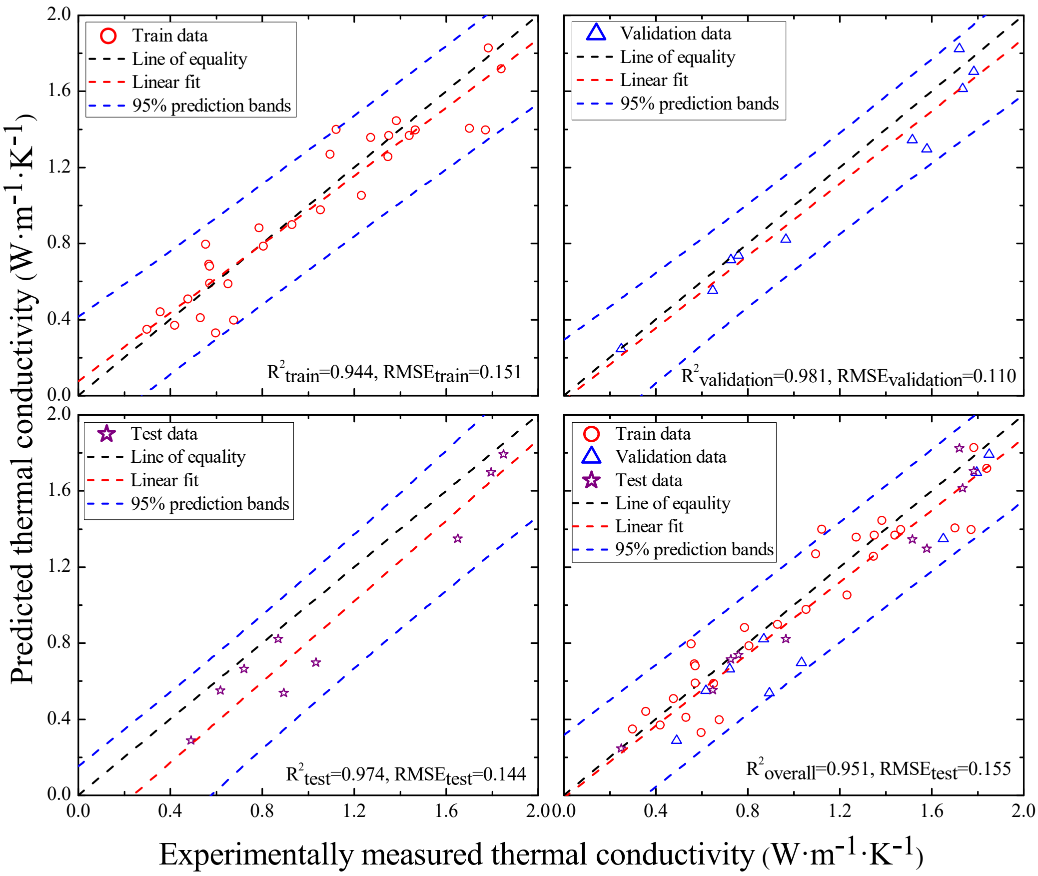

Figure 4.13 Performance of the proposed artificial neural network model to predict thermal conductivity of buffer materials

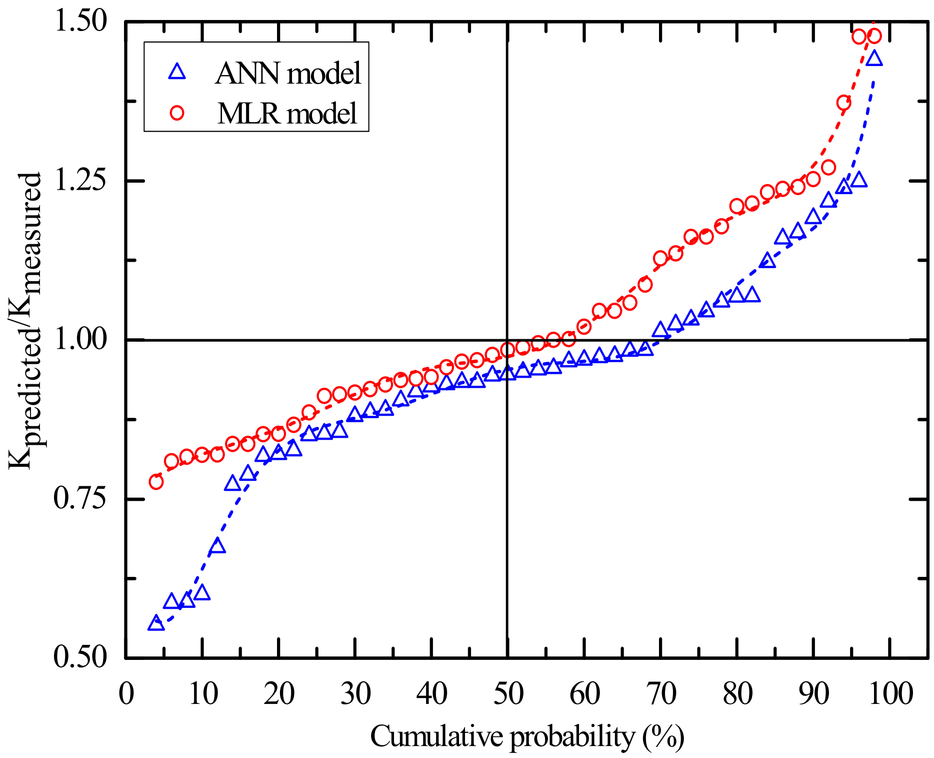

Figure 4.14 Cumulative probability versus ratio of predicted to measured thermal conductivity of buffer materials by multiple linear regression and artificial neural network models

4.6. Coupled Flow Characteristics

When the buffer materials are subjected to temperature, it leads to moisture imbalance due to the coupled flow of heat and moisture. This phenomenon affects the integrity of buffer materials in a long run. In view of this, the coupled flow characteristics of buffer materials were determined by employing the methodology presented earlier. The sand-bentonite mixture was compacted in the PVC mold at its OMC. Thermocouples, RH sensors, and TDR probes were placed at radial distances of 10 mm, 21 mm, and 33 mm from the heater surface and at depths of 10 mm, 100 mm, 190 mm, and 280 mm from the bottom of the mold. The line heat source, representing the canister in the real life in a typical DGR, was placed at the center of the mold and maintained at a constant temperature of 45 °C using temperature control unit. The temporal and spatial variation of temperature, humidity, and volumetric moisture content was recorded using the data logger.

The isothermal water vapor diffusion test was also conducted to measure the variation of moisture loss with respect to time. Though the study has considered a wide variety of buffer materials for assessing their compaction, hydraulic, and thermal properties, sand-bentonite mixtures containing bentonite fraction greater than 30 percent only exhibited favorable engineering properties for DGR application (Dixon et al., 1985; Ada, 2007; Rao et al., 2008). Therefore, sand-bentonite mixtures viz. SB30, SB50, SB70, and SB100 were considered for the vapor diffusion studies. For the sake of brevity, the variation of moisture loss from a sand-bentonite mixture SB30 with time is depicted in Figure 4.15. A typical evaporation (drying) rate curve of a capillary active hygroscopic material can depict the state of the art convective drying model. It has been reported that during the evaporation process free moisture at the material interface with the atmosphere evaporates first, and the water vapor diffusion rate within the material governs the evaporation rate from its surface. Under this steady state evaporation rate the moisture within the bulk matrix is transported towards the evaporating surface via capillary forces. The drying rate remains constant as long as the moisture transport sustains the loss of moisture from the surface (Belleghem et al., 2014). Hence, the rate of evaporation, E, was experimentally obtained from the slope of the straight line portion of the moisture loss versus time response (Evgin and Svec, 1988).

In addition to moisture loss, the variation in volumetric moisture content with distance from the evaporating surface of the specimen was quantified. For the sake of completeness, the variation in volumetric moisture content of a sand-bentonite mixture SB30 with a distance form the evaporating end is reported in Figure 4.16. Using the established relationship between volumetric moisture content and distance, the gradient of volumetric moisture content at the evaporating end of the specimen was obtained and the same was employed for determining the water vapor diffusion coefficient using Equation 4.14.

$$D_v = \frac{E}{A \cdot \rho_l} \times \frac{-1}{(d\theta/dx)_{end}} \tag{4.14}$$

where E is evaporation rate from the specimen, A is cross-sectional area of the specimen, ρ_l is density of the specimen and $(d\theta/dx)_{end}$ is volumetric moisture content gradient across 5 mm of the specimen at its open end. Similarly, the water vapor diffusion coefficients of rest of the sand-bentonite mixtures were determined and the results are presented in Table 4.13.

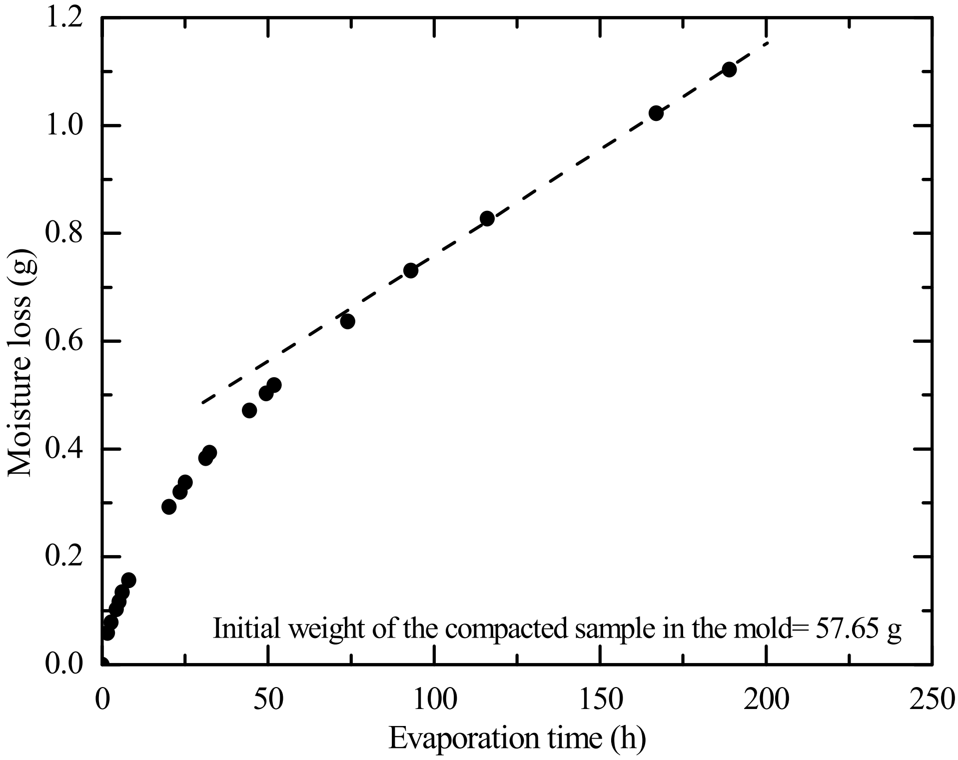

Figure 4.15 Variation of moisture loss with time for SB30

Table 4.13 Water vapor diffusion coefficient of buffer materials

Material	**Isothermal vapor diffusion coefficient ($\times 10^{-9}$ $m^2 \cdot s^{-1}$)**
SB30	1.45
SB50	1.56
SB70	1.62
SB100	0.83

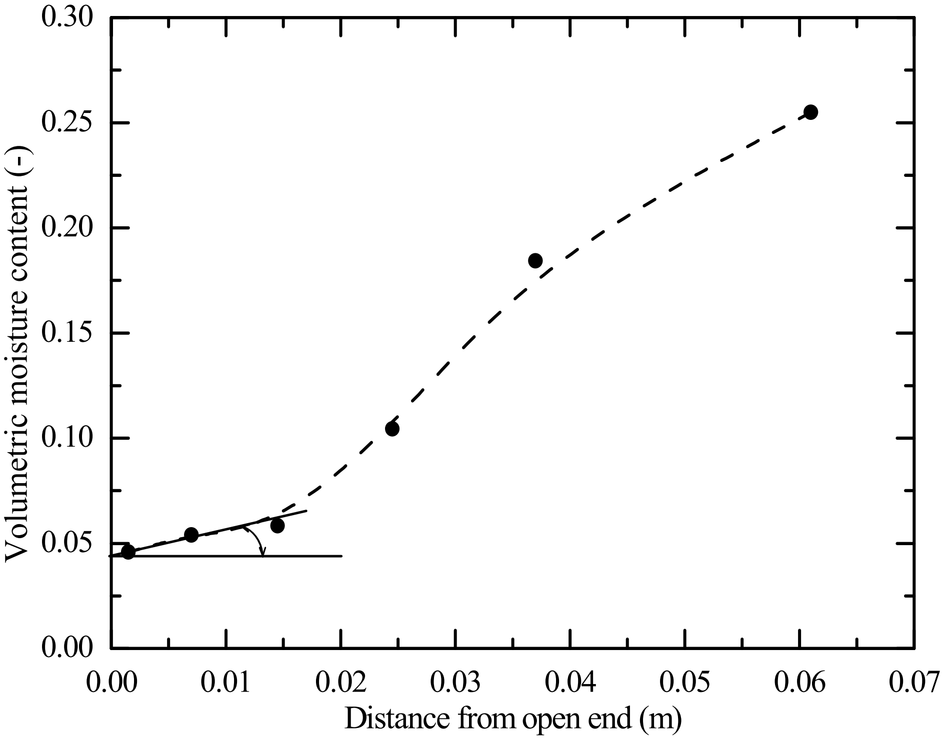

Figure 4.16 Volumetric moisture content distribution along the length of the specimen for SB30

Based on the observed spatial (radial) variation in relative humidity and temperature in coupled heat and moisture migration test setup (refer to Figure 3.12), and the water vapor diffusion coefficient obtained from the isothermal evaporation test, the water vapor flow along the radial distance was quantified using the relation proposed by Bittelli et al., 2008 (Equation 4.15).

$$q_V = q_V^i + q_V^T = -D_V \cdot C_V' \cdot \frac{dh}{dz} - D_V \cdot h_r \cdot s \cdot \frac{dT}{dz} \tag{4.15}$$

where q_v corresponds to rate of vapor flow, q_v^i is isothermal vapor flow rate and q_v^T is non-isothermal (i.e., thermally driven) vapor flow rate, D_v is isothermal vapor diffusivity of the material in $m^2 \cdot s^{-1}$, h_r is fractional relative humidity, C_v' is saturation vapor concentration in $g \cdot m^{-3}$, s is slope of the saturation vapor concentration function, T is temperature in K, and z is linear distance (depth or radial distance).

The variation of vapor flow along the radial distance from the heater surface for sand-bentonite mixture SB30 is detailed in Figure 4.17. From the vapor flow variation along the linear distance, the variation in other parameters of a typical buffer material (viz. thermal conductivity, contaminant transport properties etc.) can be estimated and thereby the real-life behavior of the buffer material can be estimated.

4.7. Gas Permeability Characteristics

The gas permeability characteristics of buffer materials were established using pressure decay method. The pressure decay experiments were conducted in triplicate using various sand-bentonite mixtures compacted at different compaction states. The results pertaining to mean normalized pressure decay variation along with standard deviation of sand-bentonite mixture SB30 is reported in Figure 4.18. The corresponding exponent value (α) is also reported in Figure 4.18. Based on the experimentally obtained exponent value, the coefficient of gas permeability of buffer materials was determined using the specimen geometry and physical properties of the permeant gas. The measured gas permeability values of SB30 prepared at different compaction states (SB30-A to SB30-H) are detailed in Table 4.14. In addition, the effect of temperature on gas permeability was assessed by conducting experiments under controlled temperatures such as 10 °C (283 K), 27 °C (300 K) and 50 °C (323 K). Though the variation of coefficient of gas permeability with volumetric moisture content over a range of temperatures for all sand-bentonite mixtures was established; however, the results pertaining to sand-bentonite mixture SB30 are only presented in Figure 4.19.

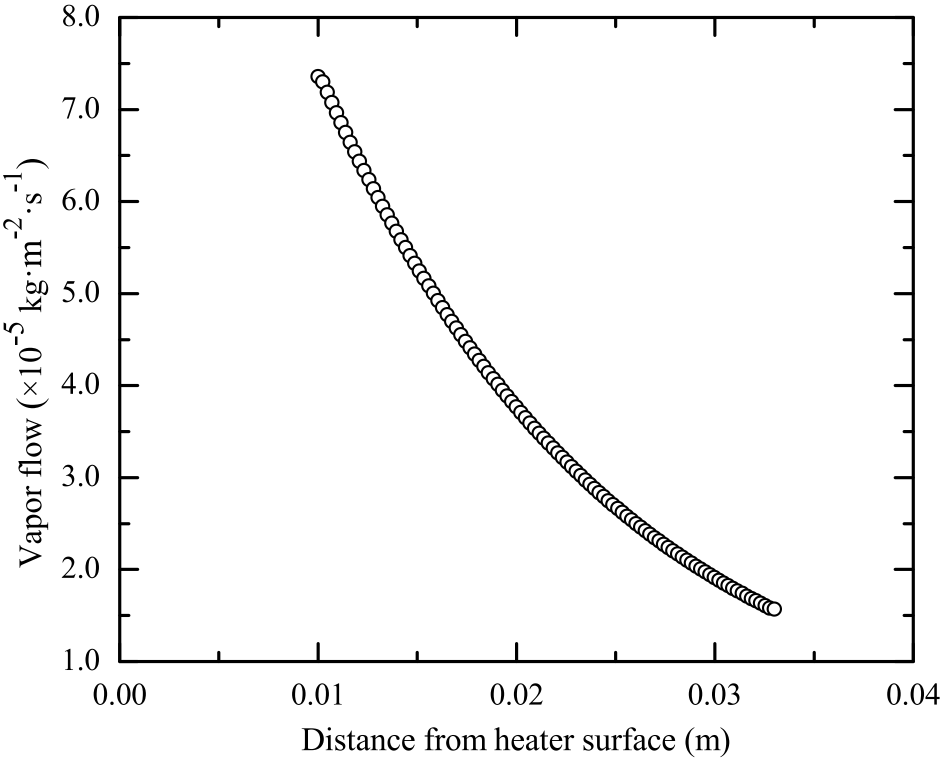

Figure 4.17 Vapor flow along the radial distance from heater surface for SB30

Table 4.14 Variation of gas permeability coefficient with compaction state at 27 °C

Material	**Compaction state of the sample**			**K_a (×10^{-10} m^2)**
	w (%)	**γ_d (kN·m^{-3})**	**θ (%)**	
SB30-A	13.5	15.9	21.9	3.6
SB30-B	14.5	14.9	22.0	2.87
SB30-C	14.9	14.8	22.5	2.52
SB30-D	15.7	16.0	25.6	0.29
SB30-E	16.2	16.8	27.7	0.26
SB30-F	19.5	16.3	32.4	0.29
SB30-G	20.5	15.6	32.6	0.26
SB30-H	22.6	15.6	35.9	0.16

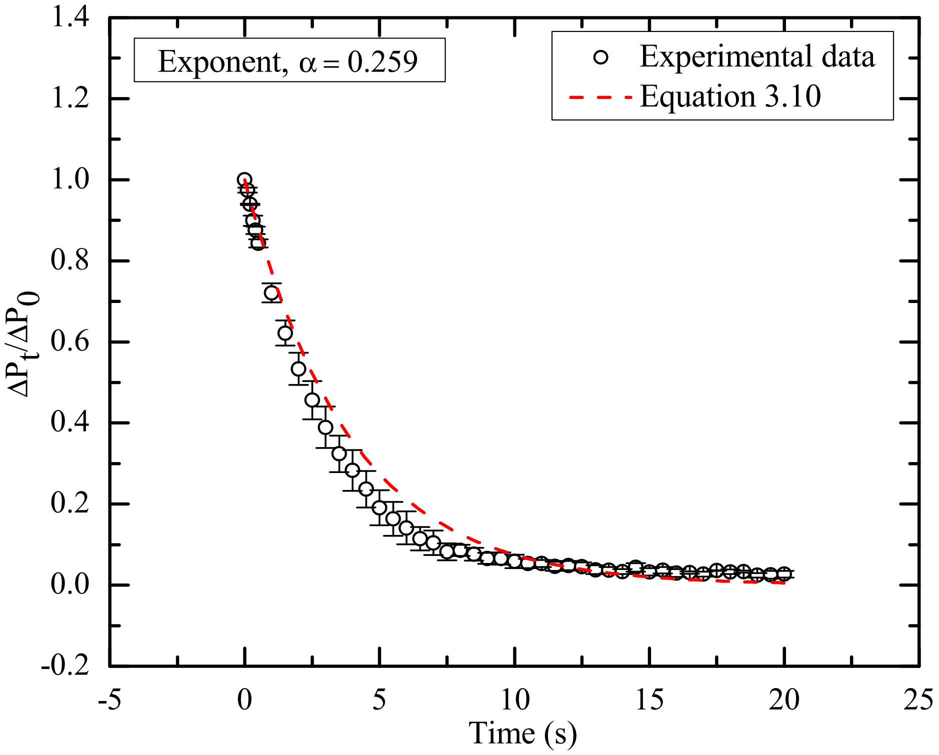

Figure 4.18 Variation of normalized pressure change with time for SB30 at 27 °C, compacted to dry unit weight of 16.3 kN·m^{-3} and moisture content of 19.5 percent

The observed reduction in permeability value with increase in temperature can be explained as per particle theory. According to this theory, when the temperature raises, the collision between gas molecules gets enhanced and thereby the viscosity increases. When the viscosity of the gas increases, a constraint is imposed on permeation of gas through the pores present in the buffer material; therefore, the gas permeability decreases. However, the influence of gas viscosity will be minimal when the soil is compacted on the wet side of optimum (Ye et al., 2012). Hence, the effect of temperature is mainly due to change in viscosity of the gas when the specimens are compacted in moderately dry state and the corresponding matric suction is in the range of 60 MPa. Whereas, at low suction (ψ<60 MPa), the effect of both viscosity and pore closing phenomena are predominant (Ye et al., 2012).

In addition, the water retention capacity of soil decreases with increase in temperature. Therefore, the pores are filled with more free water at elevated temperatures. This causes reduction of the transport porosity available for the gas to permeate, which in turn decreases the gas permeability. Moreover, the water entrapped in isolated pores may form continuously interconnected water-filled pores with the increase in temperature. This may be attributed to the reduction of attractive forces between water and solid surfaces with an increase in temperature. Further, the increase in temperature also leads to reduction in the residual moisture content of the soil (Hopmans and Dane, 1986). According to diffused double layer (DDL) theory, the repulsion between double layers increases as the temperature increases, resulting in an increase in swelling capacity. This causes a reduction in transport porosity and tortuosity, and thus the reduction in gas permeability (Hopmans and Dane, 1986).

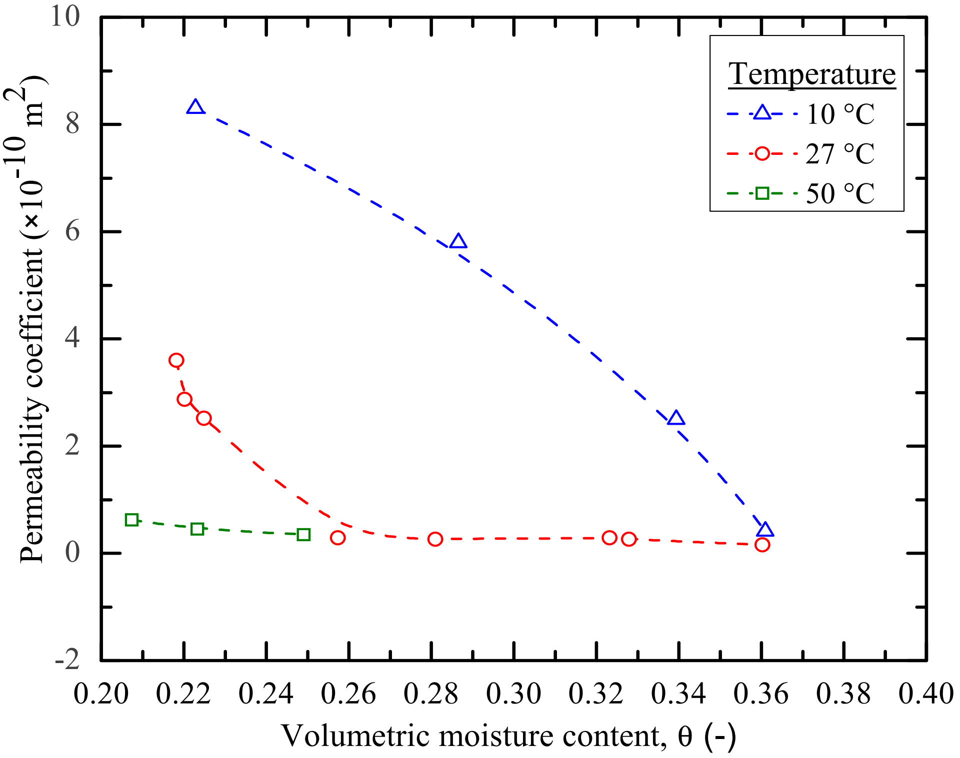

Figure 4.19 Variation of gas permeability with temperature and volumetric moisture content for SB30

The coefficient of permeability was observed to be decreasing with increase in volumetric moisture content (as depicted in Figure 4.19). This is attributed to the fact that at higher moisture contents more number of pores are filled with water which will reduce the gas-filled porosity or air content of the soil thus finding it difficult for the gas to permeate through the geomaterial. Also, the montmorillonite mineral present in the bentonite exhibits significant swelling in the presence of high moisture content, which results in a reduction of effective transport porosity and hence the permeability reduces (Komine, 2006). In view of the above-mentioned facts, the effect of bentonite content on gas permeability was examined and the variation of gas permeability coefficient with bentonite content is depicted in Figure 4.20. The obtained results showed decrease in gas permeability with increasing bentonite content, owing to the fact that the dry unit weight increases with increase in bentonite content. The increase in dry unit weight results in a reduction of porosity and inter connected pores, thereby reducing the gas permeability (Burak et al., 2004; Chen and Huang, 2013).

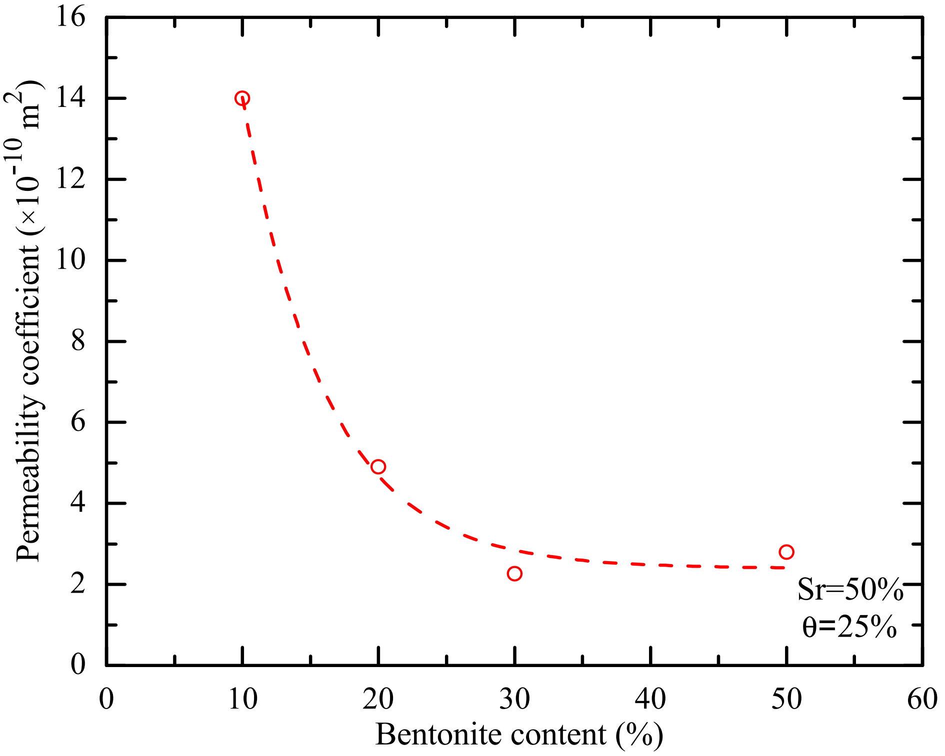

Figure 4.20 Variation of permeability with bentonite content at 27°C

Experimental results revealed that the gas permeability of geomaterials was significantly influenced by the placement moisture content, temperature, nature of the permeating fluid and unsaturated properties of the geomaterials. Few attempts were made by the previous researchers to develop a prediction model based on the basic characteristics of geomaterials for prediction of gas permeability under ambient conditions. However, none of the prediction models could incorporate the effect of temperature which is one of the major parameters influencing the gas permeability property when the geomaterial is exposed to different temperatures as in the case of buffer materials of DGR. In view of this, it was intended to develop a prediction model for gas permeability of geomaterials by considering the influence of temperature on it. In order to achieve this, the experimentally obtained gas permeability coefficients were compared with the existing models available in the literature for the prediction of gas permeability and necessary modifications were done to the existing models by considering the temperature effect, as explained in the following section.

4.7.1. A generalized model for estimation of gas permeability of buffer materials

The sound knowledge of gas permeability characteristics of the material is essential to understand the mechanism of radon gas escape from a DGR, greenhouse gas mitigation and soil vapor extraction for hydrocarbon contaminated site remediation. Among the various governing parameters, the gas permeability plays a vital role in assessing the performance of remediation techniques. Hence, a renewed interest has been created towards the development of an accurate gas permeability prediction model (Moldrup et al., 2003). The SWCC has been effectively considered for quantifying the gas permeability characteristics (Fredlund et al., 2012).

The SWCC relates volumetric moisture content of the material and corresponding suction value. The experimental results of suction measurement using dewpoint potentiometer were represented with Fredlund and Xing (1994) fit using a numerical tool called Soil Vision. The obtained SWCC of sand-bentonite mixtures SB30, SB50, and SB100 are presented in Figures 4.21, 4.22, and 4.23. From the established SWCC, it was observed that the residual moisture content of all the sand-bentonite mixtures considered (viz. SB30, SB50, and SB100) were observed to be around 1.08 %. However, the air entry value was increasing with increase in finer particles (bentonite content), attributed to their lower permeability and finer pores.

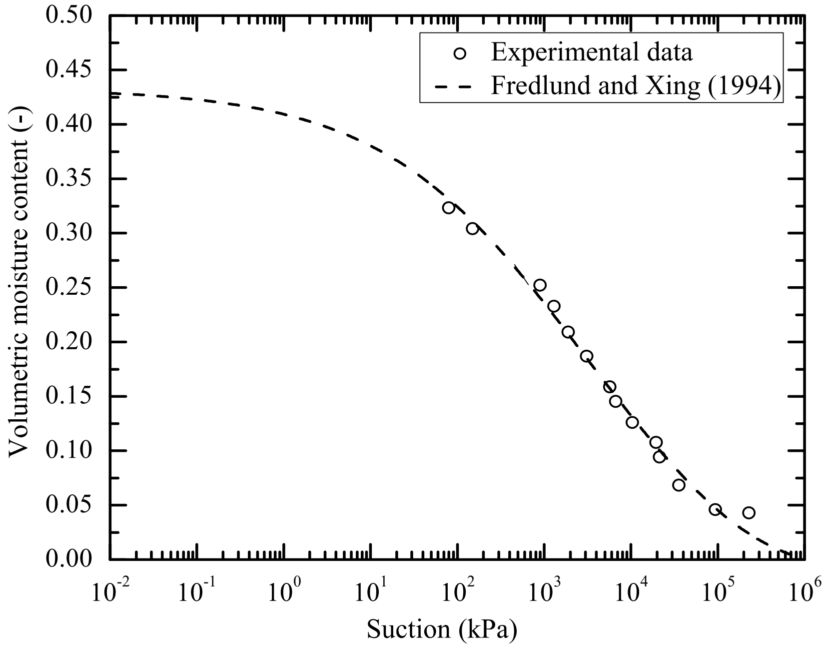

Figure 4.21 Soil water characteristic curve for SB30

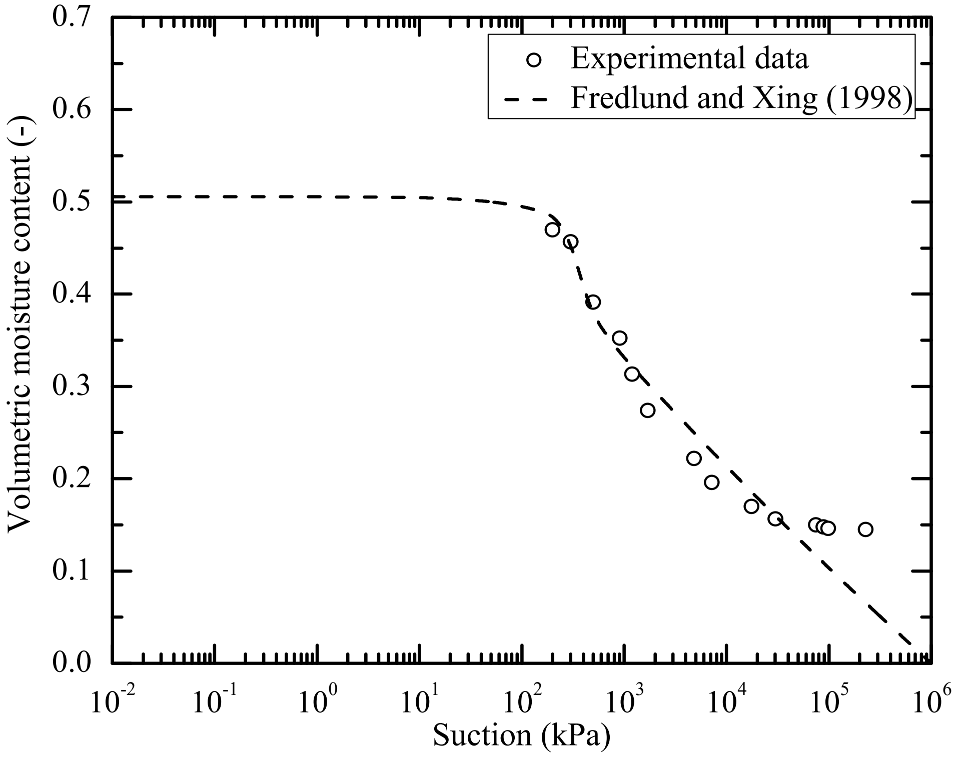

Figure 4.22 Soil water characteristic curve for SB50

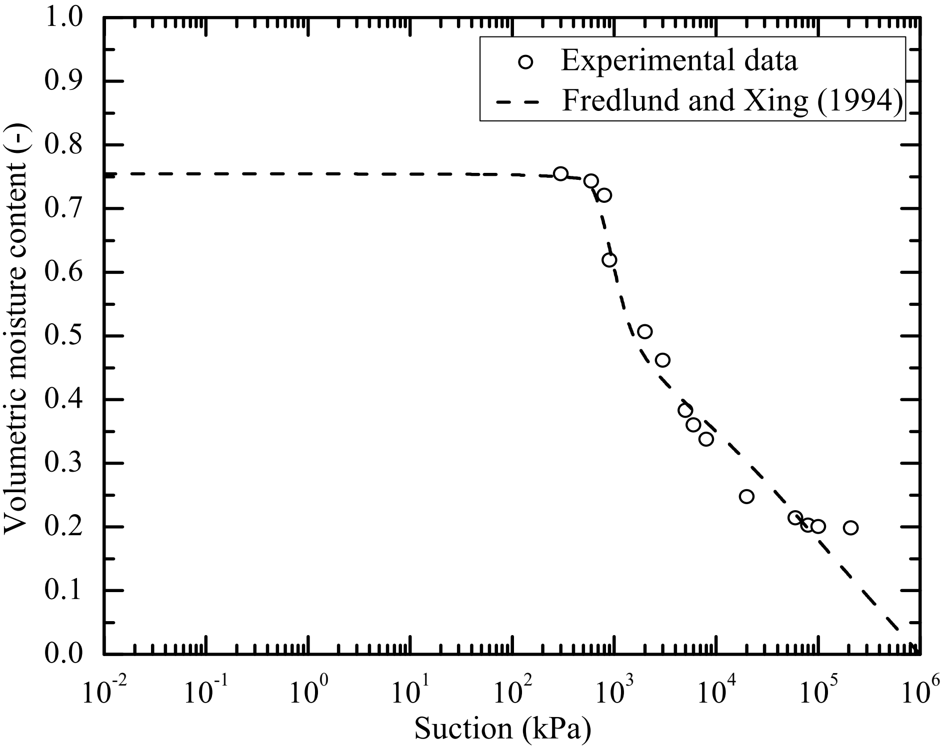

Figure 4.23 Soil water characteristic curve for SB100

It has been observed that rather than SWCC, the prediction of gas permeability will be precise when soil air characteristic curve (SACC) is considered. The SACC can be derived from the SWCC and correlates the volumetric air content and soil suction value.

In view of estimating the gas permeability of undisturbed soils as a function of soil air content (ε), a mathematical correlation has been developed in the past and the same is shown below (Moldrup et al., 1998).

$$\frac{K_a}{K_a^*}=\left(\frac{\varepsilon}{\varepsilon^*}\right)^{\eta} \tag{4.16}$$

where ε is volumetric soil air content, K_a^* and ε^* are benchmark gas permeability value and corresponding soil air content at a specified soil suction (ψ), and η is tortuosity or pore connectivity parameter (η=2 represents the gas permeability of sandy and loamy soils), K_a is coefficient of gas permeability. Further, it has been observed that the pore connectivity value is analogous to the tortuosity of fluid permeability (Millington and Quirk, 1960) and gas diffusivity (Buckingham, 1904).

However, this model overestimates the gas permeability of clay-loam soils; this is due to the selection of benchmark gas permeability and corresponding volumetric air content. The benchmark gas permeability considered in this model is in correspondence to the dry state of the soil. To overcome this limitation, a gas diffusivity models have been proposed (Moldrup et al., 2000, 2001 and 2003). In gas diffusivity model, the benchmark gas permeability value corresponding to the suction value of -100 cm water has been considered. The suction value of -100 cm water is close to the natural field capacity of agricultural soils. By considering the suction value of -100 cm water, it is convenient, rapid and non-invasive to alter the moisture content of an undisturbed soil specimen and measuring its respective benchmark gas permeability, K_a^* (Inversion et al., 2001). The value of K_a at the suction of -100 cm of water is closely linked to soil saturated hydraulic conductivity (Loll et al., 1999). Hence, by considering the same benchmark point, the model can effectively predict both air and water permeability.

Moldrup et al. (2001) suggested η value as a function of pore size distribution index, b_i. The pore size distribution index proposed by Campbell (1974) represents the slope of the soil water characteristic curve (SWCC). Moldrup et al. (1998 & 2001) found that the originally proposed expression for η (i.e., $1+0.25\times b_i$) failed to represent the measured K_a value of wide varieties of geomaterials (Moldrup et al., 2003). Subsequently, Moldrup et al. (2001) suggested an alternative expression for η (i.e., $1+0.05\times b_i$), which precisely predicted the gas permeability of undisturbed soils representing a broad soil texture having clay-size fraction of 11 to 46 %.

In view of the above, the efficacy of existing prediction models was evaluated by comparing the quality controlled experimental results of the present study. For this purpose, the ε^* was obtained from the established SWCC corresponding to matric suction of -100 cm water, the corresponding K_a^* was determined experimentally and the same is detailed in Table 4.15. It can be noted that all the prediction models failed to estimate the gas permeability values of buffer materials considered in this study, as the deviation of predicted value from the experimental value is close to 100 percent. Further, to evaluate the efficacy of various prediction models, the variation of experimentally obtained and predicted gas permeability coefficients of buffer materials were estimated. For the sake of brevity, the comparison of results pertaining to sand-bentonite mixture SB30 is presented in Figure 4.24. Based on the data presented in Table 4.15 and Figure 4.24, it can be noted that the existing models underestimated the gas permeability of buffer material.

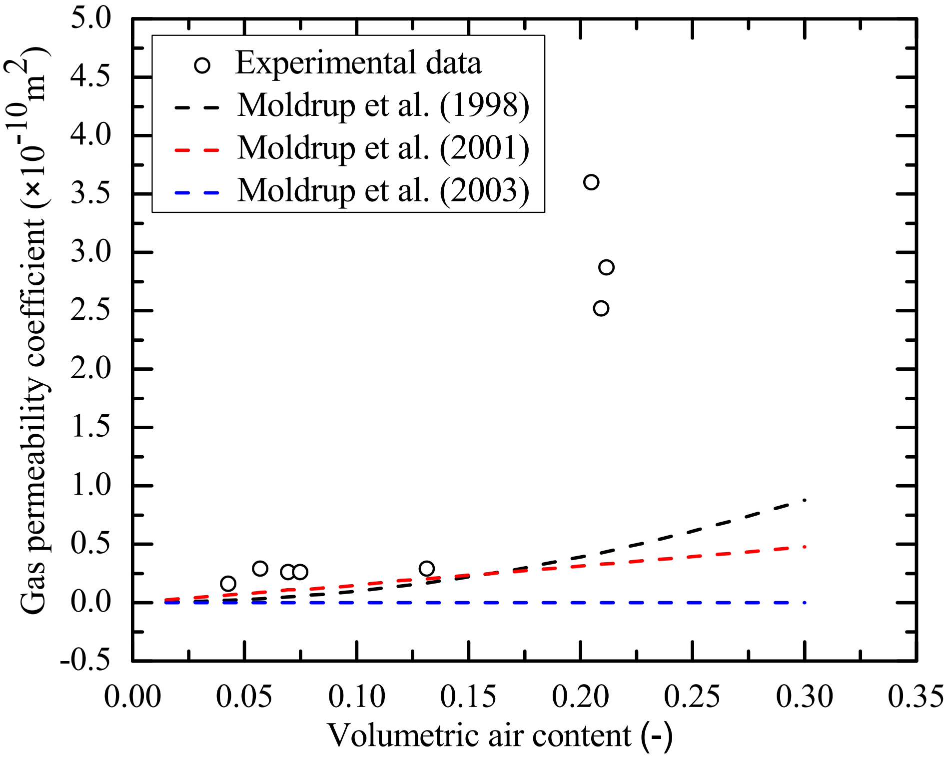

Figure 4.24 Experimentally obtained coefficient of gas permeability versus predicted using models available in literature for SB30 under ambient condition

The observed variation in gas permeability of buffer material is due to the effect of fabric arrangement. In Moldrup model (2001), the gas permeability characteristics have been evaluated by considering coarse-textured silty soil at a temperature of 20 °C (293 K). To account the fine-grained nature of the buffer materials, the model has been further modified with $\eta=1+4\times b_i$. This can be substantiated due to the fact that, the selected buffer materials are expected to exhibit distinct SWCC as well as pore size distribution characteristics when compared to that of coarse-textured silty soils considered by previous researchers.

The proposed model needs to be further modified to consider the influence of temperature on gas permeability characteristics, as the air content present in the geomaterials might be altered with temperature. Hence, it is quite reasonable to extend similar rationality as earlier in choosing the benchmark air content (ε^*) and corresponding permeability (K_a^*) values, since the variation in temperature, is not expected to alter the SWCC significantly (Zhang et al., 2013). In view of these facts, the proposed prediction model for estimation of gas permeability of wide range of geomaterials including the buffer material may be of the following form.

$$\frac{K_a}{K_a^*}=\left[\frac{\varepsilon\times e^{0.005\times(\frac{300}{\Delta T})}}{\varepsilon^*}\right]^{\eta} \tag{4.17}$$

where ΔT is difference in temperature in Kelvin with respect to a reference temperature of 300 K. When the temperature is around 300 K, the value of ΔT is taken as unity, and when the temperature is less than or greater than the reference temperature (300 K), ΔT is taken as the absolute difference between the temperatures.

Table 4.15 Comparison of experimentally obtained coefficient of gas permeability with predicted values using models available in the literature for SB30 at 27 °C

Reference	**Benchmark values**	**ε (-)**	**K_a ($\times10^{-10}$m^2)**		**Percent error (%)**	**RMSE**
			Predicted (Eq. 4.16)	**Present study**		
Moldrup et al. (1998)	$K_a^*=2.5\times10^{-11}$ m^2 $\varepsilon^*=0.16$ $\eta=2$	0.20	0.41	3.60	-88.6	**4.3×10^{-10}**
		0.21	0.44	2.87	-84.7	
		0.21	0.43	2.52	-82.9	
		0.13	0.17	0.29	-41.3	
		0.07	0.05	0.26	-80.8	
		0.06	0.03	0.29	-89.7	
		0.04	0.02	0.16	-87.5	
					R^2	**0.90**
Moldrup et al. (2001)	$K_a^*=2.5\times10^{-11}$ m^2 $\varepsilon^*=0.16$ $\eta=(1+0.25b_i)$ $b_i=0.0947$	0.20	0.32	3.60	-91.1	**4.3×10^{-10}**
		0.21	0.33	2.87	-88.5	
		0.21	0.33	2.52	-86.9	
		0.13	0.20	0.29	-31.0	
		0.07	0.11	0.26	-57.7	
		0.06	0.09	0.29	-69.0	
		0.07	0.11	0.26	-57.7	
		0.04	0.06	0.16	-62.5	
					R^2	**0.85**
Moldrup et al. (2003)	$K_a^*=2.5\times10^{-11}$ m^2 $\varepsilon^*=0.16$ $\eta=(1+0.05b_i)$ $b_i=0.0947$	0.20	0.32	3.60	-91.1	**4.3×10^{-10}**
		0.21	0.33	2.87	-88.5	
		0.21	0.33	2.52	-86.9	
		0.13	0.21	0.29	-27.6	
		0.07	0.11	0.26	-57.7	
		0.06	0.09	0.29	-69.0	
		0.07	0.12	0.26	-53.8	
		0.04	0.07	0.16	-59.4	
					R^2	**0.85**

The efficacy of the proposed model was evaluated by comparing the experimental results obtained for different sand-bentonite mixtures with that of values estimated using the proposed model (Equation 4.17), and the same is illustrated in Table 4.16. The accuracy of the proposed model was evaluated by measuring the regression coefficient, root mean square error (RMSE) and percent error between the measured and predicted values, and the obtained results are reported in Table 4.16. It can be observed that the proposed model predicts the gas permeability values satisfactorily over a range of temperature considered in this study. Further, the percent error between the predicted and measured values is minimal at lower temperature and volumetric air content values. As indicated in the Table 4.16, the proposed model is effective in predicting the gas permeability characteristics of typical sand-bentonite mixtures with moderate clay content as well as silt-based geomaterials. However, the proposed model is recommended for further improvement to precisely estimate the gas permeability behavior of pure clayey type soils.

Table 4.16 Comparison of experimentally obtained coefficient of gas permeability with the predicted values using proposed model for SB30 at different temperatures

Reference	**Benchmark values**	**T (K)**	**ε (-)**	**K_a ($\times 10^{-10} m^2$)**		
				Predicted (Eq. 4.17)	**Present study**	**RMSE**
SB 30 from present study	K_a*=5.2×10^{-10} m^2 ε*=0.16 η= (1+4b_i)=1.38 b_i=0.0947	283	0.21	8.40	7.90	**4.5 ×10^{-11}**
			0.14	4.69	5.60	
			0.10	2.79	2.40	
			0.05	1.26	0.39	
					R^2	**0.95**
	K_a*=2.5×10^{-11} m^2 ε*=0.16 η= (1+4b)=1.38 b=0.0947	300	0.20	2.78	3.60	**3.0×10^{-11}**
			0.21	2.91	2.87	
			0.07	0.63	0.26	
			0.06	0.48	0.29	
			0.04	0.32	0.16	
					R^2	**0.90**
	K_a*=5.2×10^{-10} m^2 ε*=0.16 η= (1+4b_i)=1.38 b_i=0.0947	323	0.18	0.32	0.66	**4.5×10^{-11}**
			0.08	0.14	0.47	
			0.05	0.05	0.37	
					R^2	**0.98**
Silty soils (Moldrup et al., 2003)	K_a*= 6.1×10^{-9} m^2 ε*=0.39 η= (1+4b_i)=1.4 b_i=0.1	293	0.41	88.80	63.57	**1.5×10^{-9}**
			0.39	81.89	61.93	
			0.19	31.19	45.72	
					R^2	**0.99**
Singapore residual soils (Samingan et al., 2003)	K_a*=8.8×10^{-11} m^2 ε*=0.25 η= (1+4b_i)=1.61 b_i=0.15	293	0.05	0.001	0.09	**8.6×10^{-12}**
			0.18	0.66	0.74	
					R^2	**1.00**

In order to enhance the confidence in the application of the proposed model, the predicted gas permeability values were compared vis-à-vis experimentally measured gas permeability values for different sand-bentonite mixtures over a range of temperature and compaction states, and the same is reported in Figure 4.25. Further, to demonstrate the generalized nature of the proposed prediction model, the results pertaining to silt-based materials reported in literature were superimposed (Moldrup et al., 2003, Samingan et al., 2003), as depicted in Figure 4.25. It is realized that the proposed model effectively estimates gas permeability values of a variety of geomaterials over a range of temperature and compaction states, with 95 percent precision. Further, it can be noted that the difference between predicted and measured values at elevated temperature and at higher moisture content becomes prominent; hence, proper caution must be exercised while implementing the proposed model in these situations.

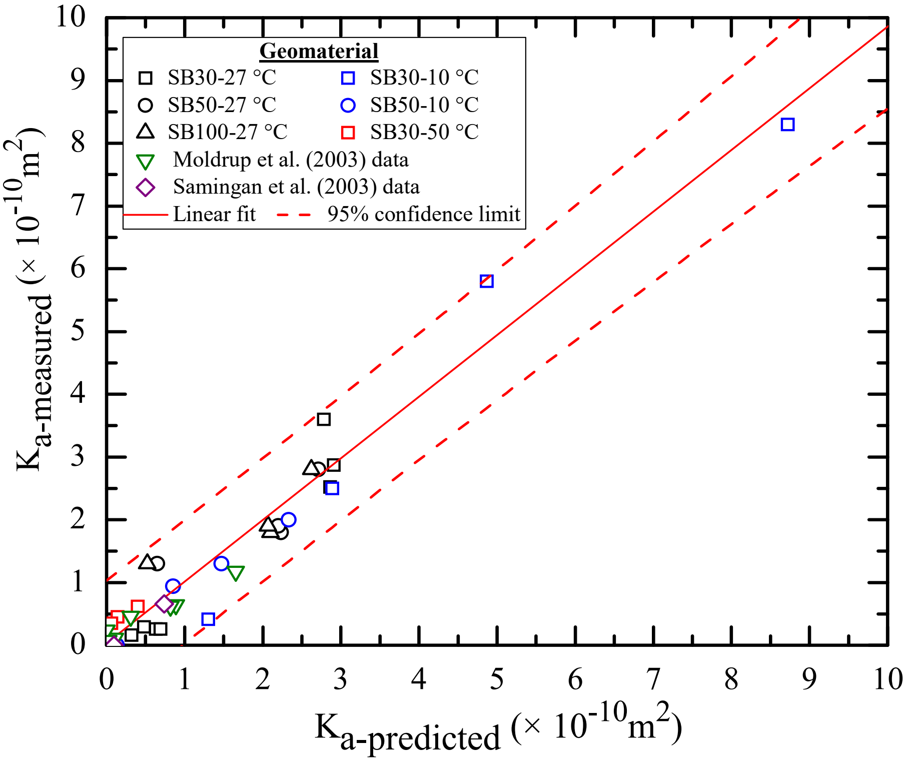

Figure 4.25 Comparison of experimentally obtained coefficient of gas permeability with predicted values using proposed generalized model for different geomaterials

4.8. Gas Diffusion Characteristics

The gas diffusion experiments were conducted on different sand-bentonite mixtures and BTCs were obtained. From the BTCs and inverse solution to the one-dimensional advective dispersion equation (1D-ADE) presented by STudio of ANalytical MODels, STANMOD, the gas diffusion characteristics were determined in terms of gas diffusion coefficient (Toride et al., 1999). The input parameters, as well as initial and boundary conditions pertaining to the proposed diffusion apparatus, were considered for the analysis. The mathematical models available in STANMOD provide an analytical solution to the 1D-ADE (Equation 4.18) proposed by Freeze and Cherry (1979).

$$\frac{\partial C}{\partial t} = \frac{D_h}{R}\left(\frac{\partial^2 C}{\partial x^2}\right) - \frac{v_f}{R}\left(\frac{\partial C}{\partial x}\right) \tag{4.18}$$

where C is concentration of the contaminant, t is time, D_h is longitudinal hydrodynamic dispersion coefficient, R is retardation coefficient, v_f is seepage velocity and x is spatial distance.

Among the various mathematical models available in STANMOD, CXTFIT model was used for the determination of transport parameters with the help of inverse problem method. The inverse problem works by fitting analytical solution of the above governing partial differential equation to the observed experimental data, and the diffusion and sorption parameters were obtained. In this method, the parameter estimation was done by minimizing the objective function that consists of the sum of squared differences between the concentrations of experimentally observed and analytical values. As mentioned above, the BTCs obtained numerically using STANMOD was superimposed on experimental BTCs. For the sake of brevity, the results pertaining to the sand-bentonite mixture, SB30 is presented in Figure 4.26 with the estimated gas diffusion coefficient.

The measured variation of gas diffusion coefficient over volumetric moisture content of SB30 is detailed in Figure 4.27. It is observed that similar to the gas permeation, gas diffusion also decreases as the moisture content increases. This is attributed to the fact that as the moisture increases, the available gas-filled pores decreases and therefore the gas diffusion as well as permeation decreases.

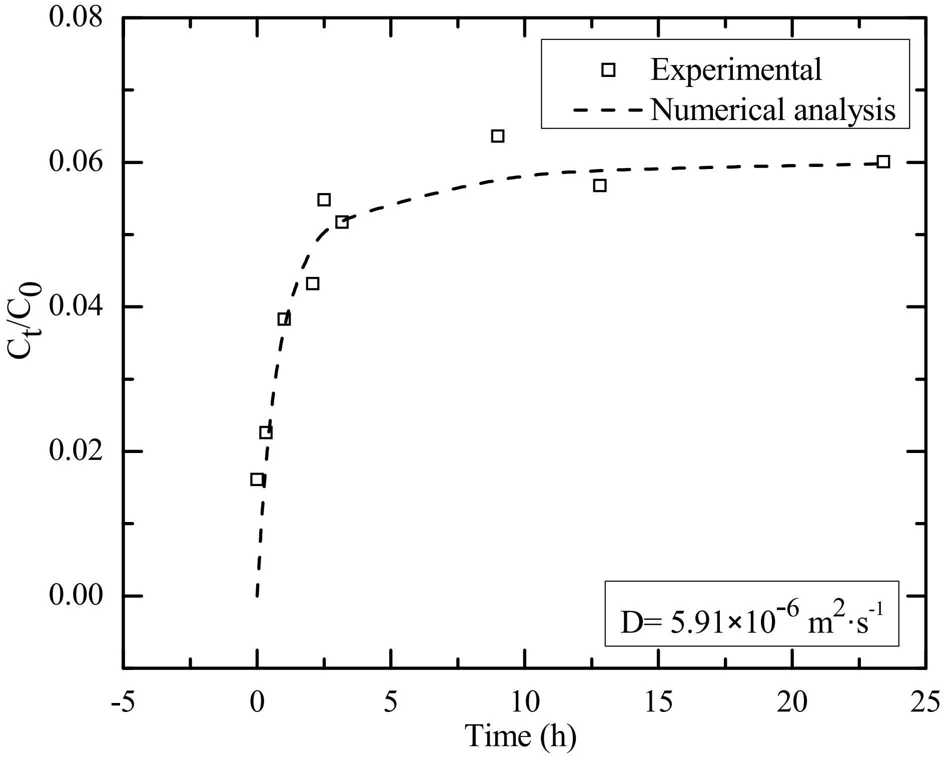

Figure 4.26 Break through curve at 12 % moisture content for SB30

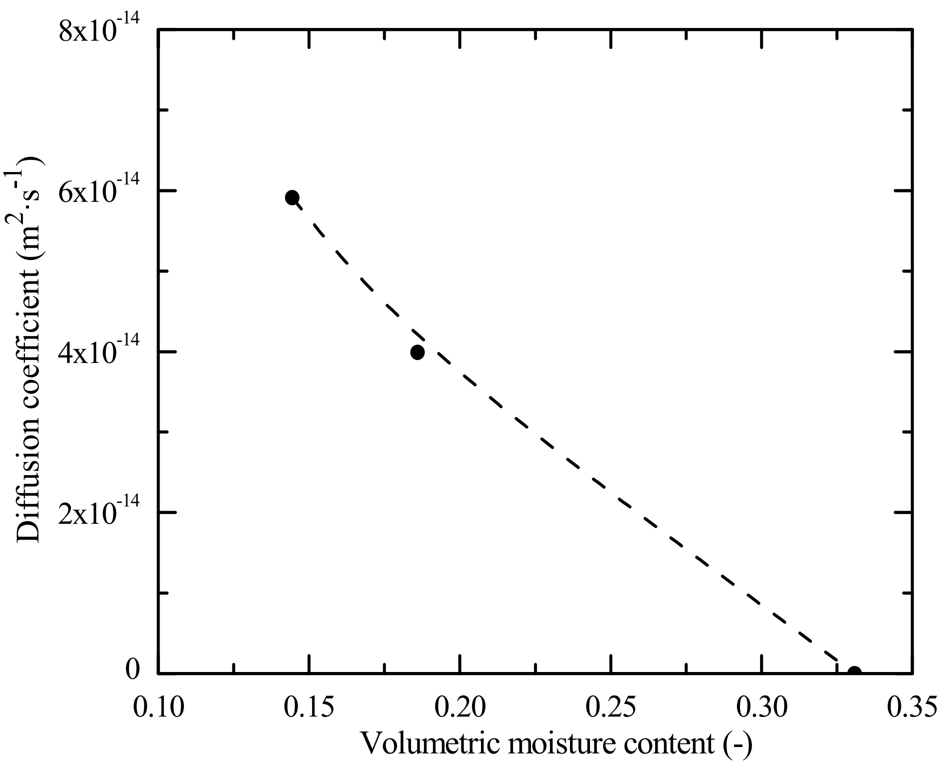

Figure 4.27 Variation of gas diffusivity with volumetric moisture content for SB30

4.9. Sorption Characteristics

4.9.1. Batch sorption experiments

The batch sorption experiments are commonly employed to quantify the mass of contaminant that can be sorbed by the geomaterial when the liquid contaminant comes in contact with it. In addition to this, these experiments also provide a quick understanding of the geomaterial-contaminant interaction over a range of environmental conditions (Holzlohner et al., 1997; Jessberger et al., 1997).

Suitability of sorption isotherm

The results of batch sorption experiments were modeled using various theoretical sorption isotherms such as Linear, Langmuir, and Freundlich isotherms available in the literature (Spark, 2003). For this purpose, the amount of contaminant sorbed by the geomaterial, C_s and the equilibrium concentration of the solute, C_e were used as model parameters.

If the variation of the C_s is linear with C_e over a wide range of concentration values, the geomaterial-contaminant interaction can be modeled effectively using the theoretical linear sorption isotherm, designated as LR and represented mathematically by Equation 4.19 (Sposito, 1989).

$$C_s = K_l \times C_e \tag{4.19}$$

where K_l is partition coefficient. Previous researchers have classified the linear sorption isotherm as C-type sorption isotherm that represents the constant partitioning of various contaminants between the solute and geomaterial over a range of solute concentrations (McBride, 2000; Nithya, 2011).

Further, if the relation between C_s and C_e is non-linear in nature, it can be modeled by Freundlich sorption isotherm, designated as FH and is represented in Equation 4.20 (Freundlich, 1926).

$$C_s=K_f\sqrt[n]{C_e} \tag{4.20}$$

where K_f is Freundlich sorption constant which is a measure of sorption capacity of the geomaterial and n is constant.

It can be noted that linear isotherm is a special case of Freundlich isotherm when n value equals to one. When n value is less than one, it indicates unfavorable sorption scenario, as the mass of the contaminant present in the solution is quite higher than that sorbed by the geomaterial. Likewise, if the value of n is greater than one, it is considered to be favorable for sorption phenomena. In that case, the Freundlich sorption isotherm with higher n value is classified as L-type sorption isotherm that reflects the affinity of geomaterial by chemisorption (Giles et al., 1960; Nithya, 2011). For better analysis, Equation 4.20 can be modified as follows.

$$\log(C_s)=\log(K_f)+n^{-1}\times\log(C_e) \tag{4.21}$$

Langmuir sorption isotherm is based on the assumption that solid surface have finite amount of active sorption sites for sorption to take place i.e., if all the active sorption sites are occupied with the contaminants, the solid surface will no longer be able to exhibit the affinity towards the contaminant present in the solution (Langmuir, 1918). Hence, this isotherm offers an advantage over the other two by limiting the amount of contaminant sorbed by the geomaterial (Giles et al., 1960; Nithya, 2011). Langmuir isotherm can be represented as follows.

$$C_s=\left(\frac{K_L C_e b}{1+K_L C_e}\right) \tag{4.22}$$

or

$$\frac{C_e}{C_s}=\frac{1}{K_L b}+\frac{C_e}{b} \tag{4.23}$$

where K_L is Langmuir sorption coefficient and b is the maximum amount of solute that can be sorbed by the geomaterial (Veith and Sposito, 1977; Nithya, 2011).

With the results obtained from batch sorption experiments, the suitability of various theoretical sorption isotherms to represent the geomaterial-contaminant interaction in terms of sorption characteristics was assessed. For this purpose, variation of normalized mass of contaminant sorbed on the geomaterial (C_s) to the equivalent concentration of the solution (C_e) called as sorption isotherm corresponding to the equilibrium interaction time of 96 hours (Nithya, 2011) over wide range of liquid to solid (L/S) ratios were developed for contaminants cesium (Cs) and strontium (Sr). Further, the experimental results were modeled using theoretical linear, Freundlich and Langmuir sorption isotherms and the sorption parameters obtained for different isotherms are presented in Tables 4.17 and 4.18. Though, the present study evaluated sorption isotherms to represent the geomaterial-contaminant interaction between the selected geomaterials (SB30, SB50, SB70, and SB100) and the contaminants considered (Cs and Sr); for the sake of brevity, the sorption isotherms of SB30 is only presented in Figures 4.28 and 4.29. It can be observed that the sorption behavior of buffer material is nonlinear in nature and hence the geomaterial-contaminant interaction can be represented effectively using Freundlich/Langmuir sorption isotherms. It is reported that the Langmuir sorption isotherm assumes monolayer sorption and uniform surface energy distribution within the geomaterial (Chen et al., 1999). However, the majority of the geomaterials are heterogeneous in nature and exhibits nonuniform surface energy distribution which results in multilayer sorption of contaminants. Freundlich sorption isotherm yields higher regression coefficient compared to the counterparts and is considered to be appropriate to model multilayer mechanism of heterogeneous geomaterials considered in the present study (Ho et al., 2002; Arnepalli et al., 2010; Nithya, 2011). Therefore, Freundlich isotherm is considered to be the best suitable sorption isotherm to represent the geomaterial-contaminant interaction of the selected geomaterials.

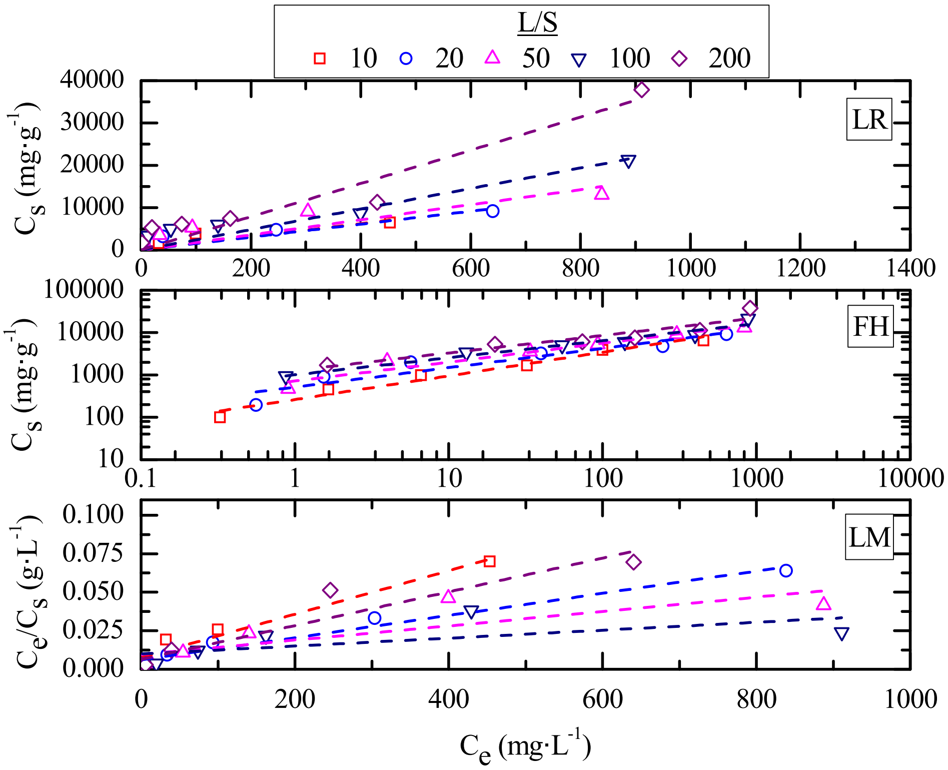

Figure 4.28 Sorption isotherms of SB30 for strontium

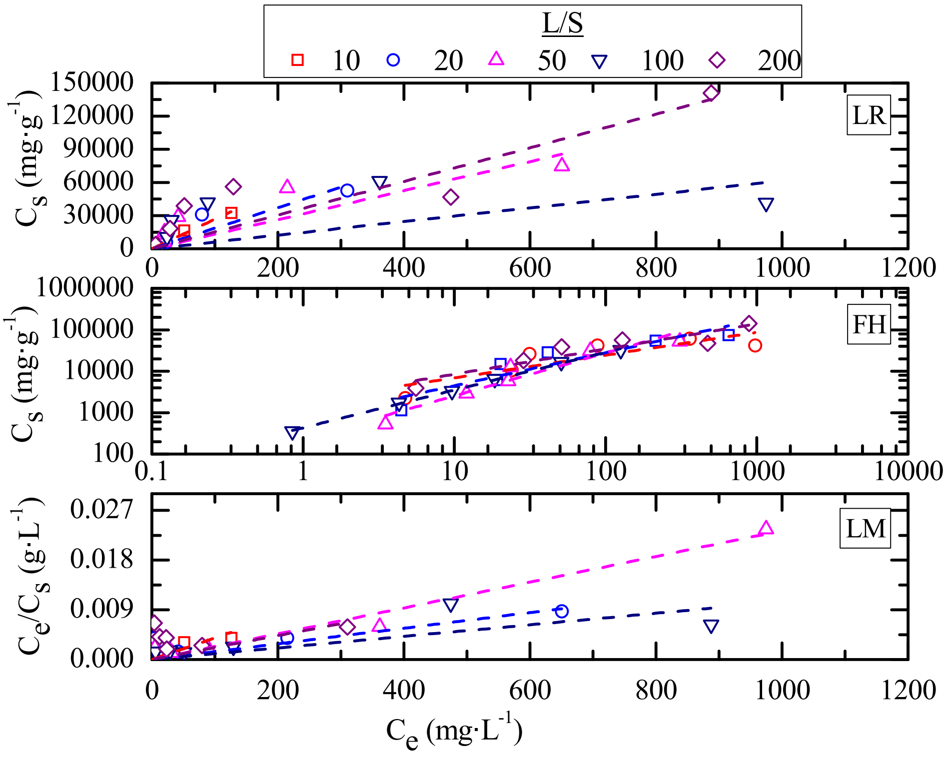

Figure 4.29 Sorption isotherms of SB30 for cesium

Table 4.17 Sorption characteristics of buffer materials for strontium

Material		**K_l**	**K_f**		**b**	**K_L**	**R^2**		
	L/S	**(L·g^{-1})**	**(L·g^{-1})**	**n**	**(×10^3 mg·g^{-1})**	**(L·mg^{-1})**	**Linear**	**Freundlich**	**Langmuir**
SB100	10	94.54	712.85	1.77	10.04	0.06	0.96	0.97	0.80
	20	138.93	544.39	1.39	28.69	0.01	0.96	0.90	0.47
	50	55.83	1325.35	1.79	10.04	0.06	0.67	0.75	0.80
	100	69.28	1556.04	1.85	29.72	0.03	0.82	0.91	0.99
	200	39.34	2774.73	2.54	45.25	0.01	0.62	0.91	0.94
SB70	10	4.78	231.49	2.32	2.23	0.02	0.62	0.76	0.87
	20	8.32	314.85	2.56	2.25	0.01	0.65	0.52	0.10
	50	150.13	267.45	1.36	-117.40	0.00	0.77	0.67	-0.33
	100	4.84	948.37	1.93	2.77	0.03	0.54	0.61	0.99
	200	14.88	893.06	4.61	7.67	0.05	0.24	0.46	0.96
SB50	10	7.84	189.27	2.61	4.86	0.01	0.80	0.69	0.61
	20	6.60	339.49	3.46	4.16	0.01	0.45	0.57	0.42
	50	66.61	300.10	1.99	58.97	0.00	0.95	0.65	-0.27
	100	57.39	466.02	4.09	14.27	0.00	0.79	-0.31	-0.48
	200	210.10	1371.80	2.39	47.92	0.01	0.82	0.10	-0.16
SB30	10	15.61	262.82	1.79	7.09	0.02	0.84	0.97	0.96
	20	15.27	515.78	2.19	13.86	0.01	0.88	0.86	0.96
	50	17.84	715.98	2.24	21.52	0.00	0.83	0.93	0.61
	100	24.20	1007.28	2.49	38.88	0.00	0.94	0.94	0.28
	200	39.26	1276.50	2.42	9.13	0.02	0.95	0.84	0.88

Table 4.18 Sorption characteristics of buffer materials for cesium

Material	**L/S**	**K_l**	**K_f**	**n**	**b**	**K_L**	**R^2**		
		($L \cdot g^{-1}$)	**($L \cdot g^{-1}$)**		**($\times 10^3$ $mg \cdot g^{-1}$)**	**($\times 10^{-3}$ $L \cdot mg^{-1}$)**	**Linear**	**Freundlich**	**Langmuir**
SB100	10	16.03	147.09	1.26	11.25	10.58	0.72	0.94	0.98
	20	16.03	342.77	1.73	9.62	20.80	0.72	0.85	0.99
	50	9.75	786.32	2.62	7.58	44.00	0.56	0.72	0.99
	100	4.97	1309.18	3.89	4.03	62.00	0.04	0.27	0.99
	200	52.00	1131.36	2.41	7.04	275.19	0.52	0.69	0.97
SB70	10	22.19	234.42	1.49	166.67	62.57	0.80	0.89	0.99
	20	13.30	457.09	1.96	200.00	46.30	0.69	0.83	0.99
	50	9.58	933.25	2.94	166.67	46.88	0.55	0.70	0.92
	100	26.45	870.96	2.00	166.67	162.60	0.88	0.90	0.82
	200	2.65	5495.41	1.22	22.73	55.14	0.18	0.28	0.98
SB50	10	206.79	275.42	1.05	78.74	3.43	0.99	0.99	0.95
	20	284.57	239.88	0.92	1040.58	0.275	0.99	0.98	0.25
	50	145.90	363.08	1.09	116.14	2.69	0.85	0.86	0.41
	100	122.13	724.44	1.30	104.06	4.00	0.86	0.87	0.89
	200	118.26	1348.96	1.49	106.38	5.53	0.83	0.86	0.95
SB30	10	268.16	1949.84	1.82	94.34	4.08	0.99	0.68	0.91
	20	185.49	724.44	1.22	103.09	4.41	0.89	0.82	0.8
	50	131.39	229.09	0.96	44.64	34.04	0.81	0.90	0.96
	100	61.57	436.52	1.10	130.38	4.26	0.42	0.99	0.45
	200	152.16	2089.30	1.64	194.55	1.35	0.86	0.83	0.11

Effect of liquid to solid ratio (L/S)

The effect of liquid to solid (L/S) ratio on sorption was demonstrated by plotting the variation of C_s with L/S for the geomaterials and contaminants considered in the study. For the sake of brevity, the variation of the mass of contaminant sorbed by the sand-bentonite mixture SB30 is presented in Figures 4.30 and 4.31. Further, percentage removal (PR) of the contaminant from 100 ml solution of the contaminants over a range of concentrations and L/S were obtained as per Equation 4.24.

$$PR=\frac{(C_i-C_e)}{C_i}\times 100 \tag{4.24}$$

where C_i is initial concentration of the contaminant in $mg\cdot L^{-1}$ and C_e is equilibrium concentration of the contaminant in $mg\cdot L^{-1}$.

Figures 4.30 and 4.31 demonstrate the non-linear variation of the amount of contaminant sorbed by the buffer material SB30 with L/S and its variation becomes insignificant at high L/S values. This indicates that the mass of the contaminant present in the solution is significantly high at large L/S values as compared to the affinity of the potential sorption sites available (Shackelford and Daniel, 1991; Roy et al., 1991; Vengris et al., 2001; Nithya, 2011). At the same time, the potential active sites available for sorption to take place are quite higher at low L/S values compared to that at high L/S values. This is more visible from the data presented in Tables 4.19 and 4.20.

Effect of initial concentration (C_i)

Effect of initial concentration of the contaminant present in the solution on sorption characteristics of buffer materials was evaluated by conducting batch sorption experiments with different initial contaminant concentrations. Figure 4.32 presents the results obtained for sand-bentonite mixture, SB30 in the form of variation of C_s with C_i as well as variation of PR of contaminants with C_i for L/S of 50 for all buffer materials and contaminants considered in the study. It can be observed that the increase in contaminant concentration in the solution results in an increase in the amount of contaminant uptake per unit weight of the sorbent and decrease in percent removal rate of the contaminant. This may be due to the fact that, at high initial concentration the number of moles of the contaminant available for the sorption sites is high as compared to that at low initial concentration. Further, the difference in percent removal rate of the contaminant at same initial concentration (as observed in

Figure 4.32) is attributed to the difference in their chemical affinity and cation exchange capacity. It can also be observed from Table 4.19 and 4.20 that the contaminant removal efficiency of SB100 is high compared to the other mixes considered in the study. Therefore, it can be concluded that the effect of initial concentration of contaminants depends on the nature of the geomaterial and contaminant (Ayala et al., 2008; Shu-li et al., 2009; Nithya, 2011).

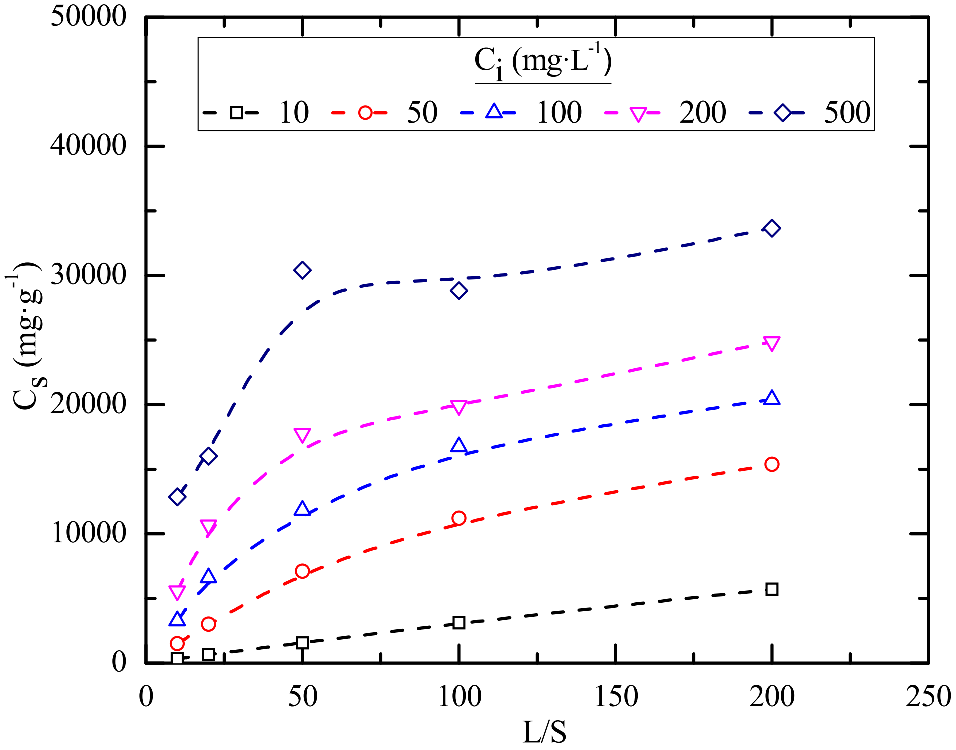

Figure 4.30 Variation of the mass of strontium sorbed by SB30 with liquid to solid ratio

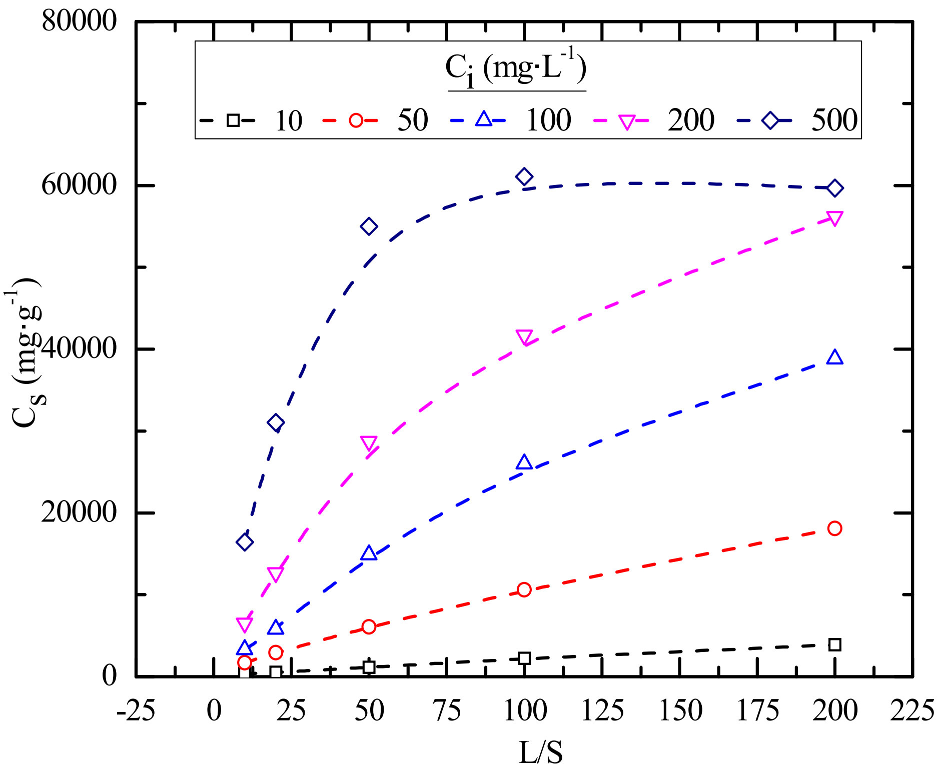

Figure 4.31 Variation of the mass of cesium sorbed by SB30 with liquid to solid ratio

Effect of sorbent

The influence of sorbent or the buffer material nature was demonstrated by the variation of mass of contaminants sorbed by buffer materials with initial concentration. For the sake of brevity, the results pertaining to L/S value of 50 is presented in Figure 4.33. It is observed that the buffer material SB30 exhibits higher sorption affinity towards both the contaminants considered in the study. Generally, the high reactive geomaterial like bentonite exhibits higher affinity towards all the contaminants including heavy metals because of their high cation exchange capacity, specific surface area, pH, and a high percent of organic and carbonate content (Buchter et al., 1989; Nithya, 2011). But, the results obtained from the present study are quite contrary to the previous findings. This may be due to the fact that, even though the total L/S considered is same, actual liquid to bentonite ratio is different depending on the sand-bentonite mixture. However, it is clear that SB30 also exhibits considerable sorption characteristics. It can be noted that the pH of the solution was maintained constant around 8.0 during all the batch sorption experiments.

Table 4.19 Percent removal of strontium by SB30 over a wide range of L/S values

Material	**L/S**	**Initial concentration (mg·L^{-1})**					
		10	**50**	**100**	**200**	**500**	**1000**
SB100	10	99.53	98.88	99.00	98.06	91.31	90.22
	20	97.47	89.66	94.28	97.41	89.95	86.94
	50	94.68	88.93	93.10	97.69	82.93	50.58
	100	92.82	87.85	76.98	88.71	52.46	38.75
	200	91.78	82.20	67.86	55.89	25.85	13.99
SB70	10	87.16	84.93	87.15	70.79	26.31	23.23
	20	87.21	67.22	54.97	55.25	6.86	25.37
	50	84.00	45.93	37.98	39.05	-5.52	73.68
	100	73.72	15.71	24.65	-527.97	5.09	2.61
	200	31.56	-0.77	21.81	23.75	-6.14	3.63
SB50	10	90.67	78.16	94.52	52.31	22.21	28.35
	20	94.55	81.16	53.33	55.14	8.12	13.77
	50	88.50	34.98	28.03	33.07	43.21	-1.78
	100	76.29	14.00	3.49	25.64	-9.89	-2.03
	200	48.88	87.26	21.91	36.15	-18.02	-13.29
SB30	10	96.75	96.43	93.69	83.81	79.46	58.80
	20	94.42	96.68	94.57	80.06	49.35	41.78
	50	90.96	91.44	67.63	53.27	37.49	23.77
	100	91.29	71.97	47.84	29.83	17.76	19.31
	200	83.86	56.99	29.16	18.62	11.58	17.19

Effect of temperature

The sorption tests were conducted on various sand-bentonite mixtures (SB30, SB50, SB70 and SB100) with corresponding contaminants at different temperatures of 10 °C, 27 °C, and 50 °C. The obtained results are explained by plotting the variation of sorption coefficient with L/S value for three different temperatures considered in this study as depicted in Figure 4.34 for the contaminant strontium. It is observed that the sorption coefficient decreases with increase in temperature. This is attributed to the fact that with increasing temperature the attractive forces between buffer material surface and contaminant ions are weakened and the sorption decreases (Horsfall and Spiff, 2005). Moreover, at high temperature, the thickness of the boundary layer decreases due to an increased tendency of the contaminant ion to escape from the buffer material surface to the solution phase which results in a decrease in adsorption (Aksu and Kutsal, 1991). Also, the 1/n values were found to be more than unity at higher temperatures, signifying that desorption occurs, especially at lower L/S values.

This implies that at low-temperature significant amount of adsorption takes place and it becomes insignificant at higher temperatures (Horsfall and Spiff, 2005).

Table 4.20 Percent removal of cesium by SB30 over a wide range of L/S values

Material	**L/S**	**Initial concentration (mg·L^{-1})**					
		10	**50**	**100**	**200**	**500**	**1000**
SB100	10	90.94	90.73	91.78	93.10	87.53	75.50
	20	88.47	89.97	90.44	89.69	66.15	41.03
	50	83.70	86.54	81.56	55.54	24.71	13.55
	100	74.06	69.99	56.70	33.14	-0.17	3.66
	200	67.32	52.38	39.88	15.60	-1.53	-2.10
SB70	10	89.34	91.46	58.26	92.53	78.59	58.26
	20	86.77	89.21	28.40	83.13	46.67	28.40
	50	81.94	79.37	10.42	45.31	13.27	10.42
	100	75.49	65.71	15.08	23.62	-4.38	15.08
	200	62.92	43.98	0.39	7.52	-3.27	0.39
SB50	10	92.24	92.23	91.12	91.31	90.62	88.51
	20	67.91	78.19	79.15	88.97	85.41	71.76
	50	59.25	65.24	81.47	80.60	60.56	40.76
	100	56.68	56.62	71.14	58.50	33.58	11.25
	200	49.21	48.19	52.95	39.31	12.84	19.21
SB30	10	92.44	93.04	93.06	92.84	92.11	90.91
	20	82.36	87.39	89.61	90.91	89.66	87.17
	50	64.38	67.64	80.32	85.72	75.92	56.61
	100	59.93	59.47	69.17	76.46	46.67	35.40
	200	51.60	53.12	65.95	52.77	28.40	20.64

The effect of temperature on sorption behavior is generally explained in terms of thermodynamic parameters such as enthalpy, $\Delta H°$; entropy, $\Delta S°$; and Gibb's free energy, $\Delta G°$.

4.9.2. Column flow-through experiments

The column sorption experiments were also conducted as part of the present study to simulate the actual geomaterial-contaminant interaction. With this in view, effluent was collected at regular intervals and the concentration of the effluent was analyzed using atomic absorption spectrophotometer (AAS). Further, a variation of the normalized effluent concentration, C_t/C_0 with time was established in terms of BTCs. The observed BTC for SB30 for the contaminant Sr is presented in Figure 4.35.

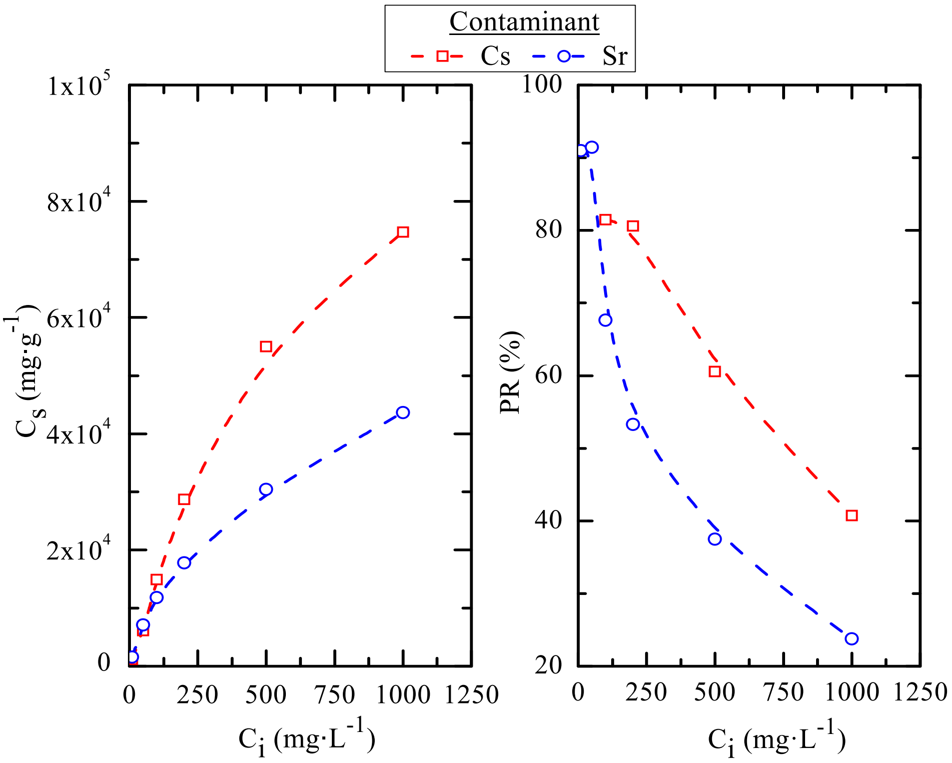

Figure 4.32 Effect of initial concentration on the mass of contaminant sorbed and percent removal by SB30

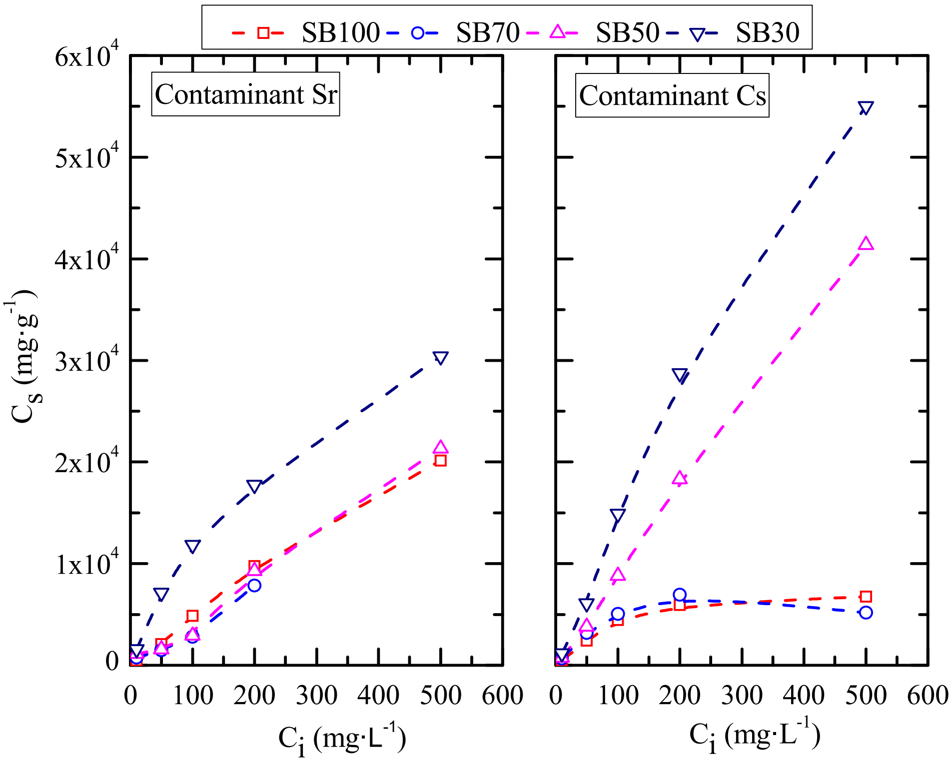

Figure 4.33 Effect of sorbent on sorption behavior of strontium and cesium

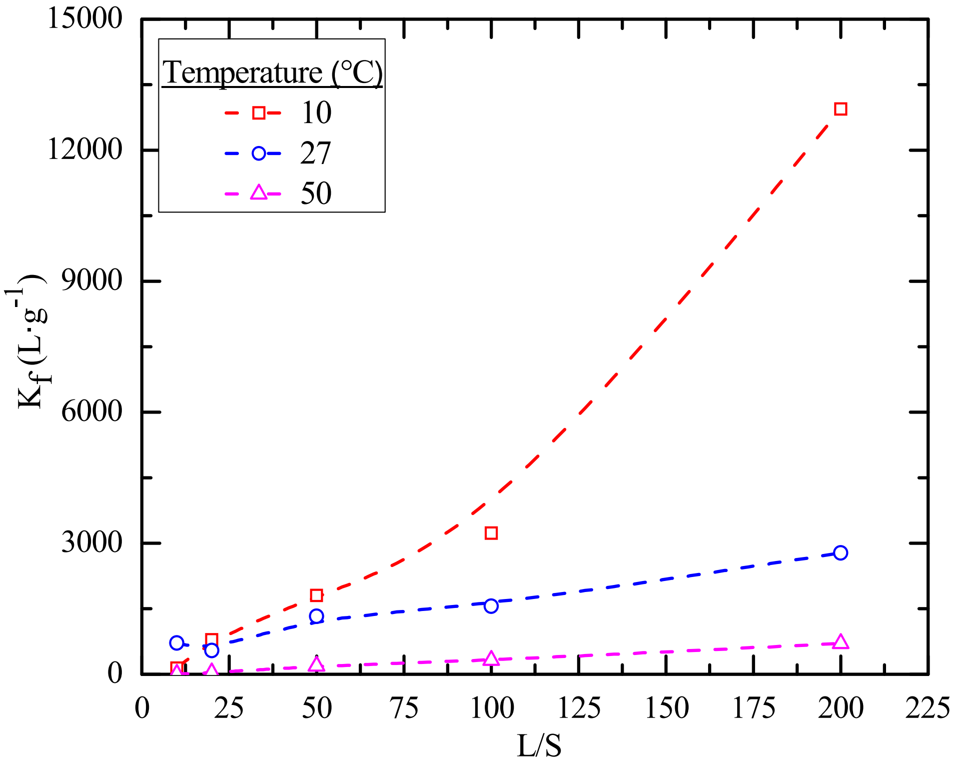

Figure 4.34 Effect of temperature on sorption behavior of strontium for SB100

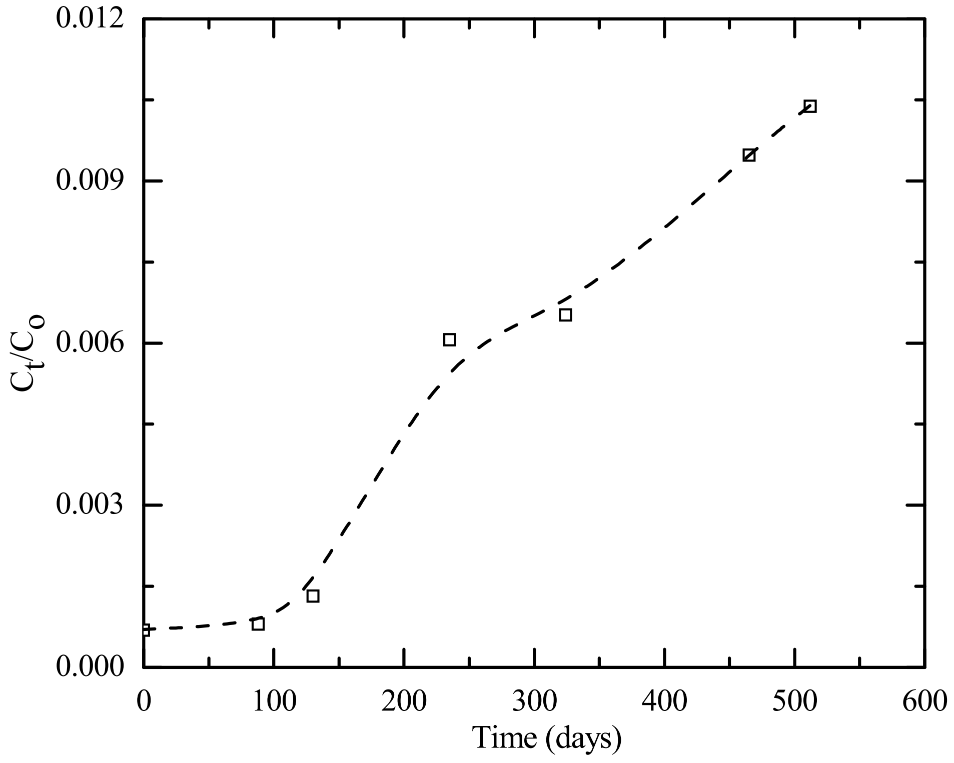

Figure 4.35 Breakthrough curves obtained from laboratory (1-g) column flow-through experiments for SB30 for the contaminant strontium

It can be observed that the selected buffer material attained a maximum C_t/C_o of 0.01 over the interaction period of 512 days. Using the BTC and mathematical models available with STANMOD the sorption characteristics of buffer materials were determined in terms of retardation factor, R and hydrodynamic dispersion coefficient D (Toride et al., 1999). As explained in section 4.8, the mathematical models available in STANMOD provides an analytical solution to the 1D-ADE contaminant transport equation (Equation 4.18) proposed by Freeze and Cherry, 1979. In Equation 4.18, the retardation coefficient R can be defined by Equation 4.25.

$$R=1+\frac{K_d \times \rho}{\eta} \tag{4.25}$$

where K_d is distribution coefficient, ρ is density of the sample and η is porosity.

To solve the one dimensional advection-dispersion equation for the column flow-through experiments, the initial and boundary conditions are considered as: Initial condition: $C(x, 0) = 0$; top boundary condition of the sample in the column test: $C(0,t) = C_0$ and assumed to be constant throughout the experiment; the bottom boundary condition of the sample in the column test: $\frac{\partial C}{\partial X}(\infty,t)=0$. (Shakelford, 1991). For comparison, the calculated effluent concentration based on the predicted fitting parameters at the bottom of the sample was obtained and superimposed with the experimental data as depicted in Figure 4.35. Using the retardation value obtained from STANMOD the sorption parameter i.e., distribution coefficient K_d in $L \cdot kg^{-1}$ is found to be 192.98 $L \cdot kg^{-1}$ for Sr.

4.9.3. Prediction of equivalent column distribution coefficient

Even though the batch sorption experiments are easy and simple to conduct, they fail to simulate the buffer material-contaminant interaction (Jackson et al., 1984; Arnepalli et al., 2010; Nithya, 2011). To overcome this, an elaborate comparison study between column flow-through experiments and batch sorption experiments were conducted and a generalized relation was developed to predict the equivalent column distribution coefficient $K_{d\text{-equivalent}}$ based on the measured batch sorption results (Nithya, 2011). The generalized relationship for predicting the equivalent column distribution coefficient by knowing the distribution coefficient K_d from the batch sorption experiment and corresponding L/S is presented in the form of Equation 4.26.

$$\text{average } K_{d\text{-ratio}}=A_1 \exp\left[\frac{-L/S}{B_1}\right]+C_1 \tag{4.26}$$

where average $K_{d\text{-ratio}}$ is the ratio of distribution coefficient obtained from batch sorption experiments and equivalent column distribution coefficient; L/S is liquid to solid ratio; A_1, B_1, and C_1 are constant parameters for the respective contaminants. In the above equation the values of the constants A_1, B_1 and C_1 are considered as 2.29, 29.7, and 1.00 for Sr and 3.28, 8.97, and 1.01 for Cs (Nithya, 2011).

The variation of average $K_{d\text{-ratio}}$ estimated for the contaminants Sr and Cs are presented in Figure 4.36 and the predicted K_d values obtained for the buffer materials for the contaminants Sr and Cs are presented in Table 4.21. It can be observed that the estimated K_d values of column sorption are lower than that of batch sorption owing to the realistic buffer material-contaminant interaction. In batch sorption experiments greater part of the sorption sites within the buffer material interact with the contaminants and results in high sorption coefficient (Celorie et al., 1989).

Table 4.21 Equivalent column K_d of the buffer materials for strontium and cesium

Material	L/S	Contaminant Sr		Contaminant Cs	
		K_f ($L\cdot g^{-1}$)	Column K_d ($L\cdot g^{-1}$)	K_f ($L\cdot g^{-1}$)	Column K_d ($L\cdot g^{-1}$)
SB100	10	712.85	270.50	147.09	70.52
	20	544.39	251.12	342.77	251.52
	50	1325.35	929.87	786.32	769.06
	100	1556.04	1442.13	1309.18	1296.16
	200	2774.73	2767.19	1131.36	1120.16
SB70	10	231.49	87.84	234.42	112.39
	20	314.85	145.24	457.09	335.40
	50	267.45	187.64	933.25	912.76
	100	948.37	878.94	870.96	862.30
	200	893.06	890.63	5495.41	5441.00
SB50	10	189.27	71.82	275.42	132.05
	20	339.49	156.60	239.88	176.02
	50	300.1	210.55	363.08	355.11
	100	466.02	431.90	724.44	717.23
	200	1371.8	1368.07	1348.96	1335.60
SB30	10	262.82	99.73	1949.84	934.84
	20	515.78	237.92	724.44	531.58
	50	715.98	502.33	229.09	224.06
	100	1007.28	933.54	436.52	432.18
	200	1276.5	1273.03	2089.3	2068.61

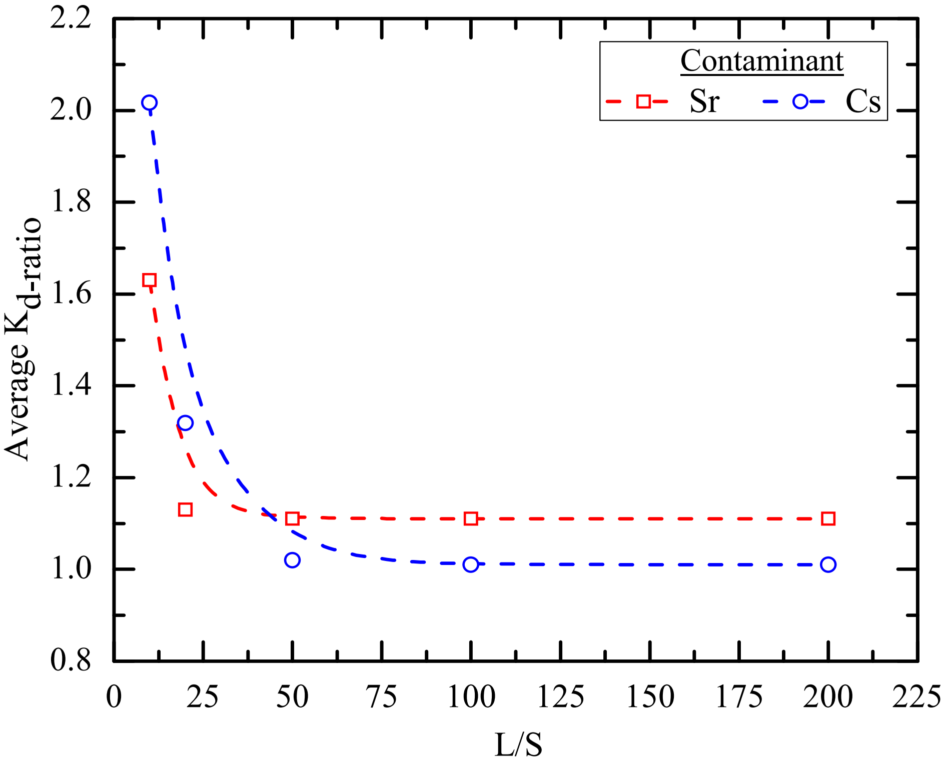

Figure 4.36 Variation of average $K_{d\text{-ratio}}$ with liquid to solid ratio for contaminants strontium and cesium

Chapter 5

NUMERICAL ANALYSIS FOR ASSESSING LONG-TERM PERFORMANCE OF BUFFER MATERIALS

5.1. General

The efficacy of buffer material to contain hazardous waste depends on its long-term performance under the synergetic influence of physical, chemical and thermal loadings. In view of this, the present chapter demonstrates the long-term performance of buffer materials in terms of thermal and contaminant transport properties using numerical tools SVHeat™ and POLLUTE. For this purpose, heat migration in a typical DGR was investigated by considering the single canister and multiple canisters scenarios. The importance of safe placement distance between the canisters in case of multiple canisters was also established. Further, the contaminant transport through the buffer material was demonstrated for 200 years using POLLUTE.

5.2. Two-dimensional Modeling of Heat Migration through Buffer Material

As the radioactive waste is associated with moderate temperature, the thermal properties of buffer materials and the rate of loss of moisture from them for a given exposure condition determine their performance without losing integrity, in terms of engineering properties. These properties need to be evaluated over the service life of DGR to assess its long-term performance. With this in view, heat migration through the buffer material of a typical DGR was modeled and analyzed using a commercially available finite element based numerical tool called SVHeat™.

SVHeat™ is commonly employed for understanding the heat migration through saturated as well as partially saturated porous media, by both conductive and convective heat transport phenomena. SVHeat™ has the ability to model natural thermosyphons of heat exchange mechanism. The numerical tool has the capability to incorporate atmospheric weather data to predict its influence while modeling the heat and moisture migration mechanisms through barriers. Further, SVHeat™ allows analyzing steady-state or transient thermal models.

The numerical model considered in the present study is aimed to obtain the spatial and temporal variation of temperature in a buffer material as well as in host rock of a DGR, for 200 years so as to establish the long-term performance of the DGR. Figure 5.1

depicts the schematic of a typical DGR used in the model with horizontal tunnel whose geometry and the parameters adopted for modeling are discussed in the following.

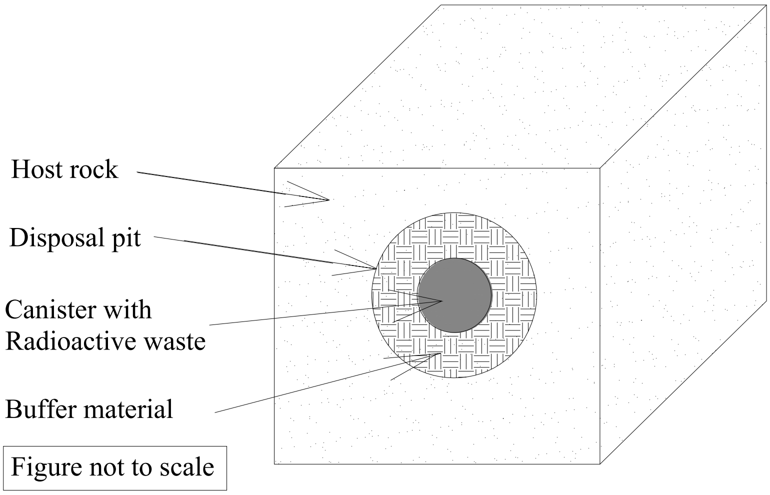

Figure 5.1 Schematic of the deep geological repository used in the model

5.2.1. Model geometry

The model DGR in the present study consisted of a horizontal tunnel with the canister surrounded by the buffer material. Figure 5.2 depicts the schematic representation of the model DGR. The modeled DGR was situated at a depth of 500 m from the ground surface and the extent of the host rock was considered to be infinite in the radial direction. The canister was of 1.25 m diameter, situated at a depth of 500 m from the ground surface. It was surrounded by a candidate buffer material (viz. SB30) to an extent of 2.5 m diameter. Since the spatial variation of temperature is confined to the finite region of the host rock adjacent to the buffer material, the present study considered the model dimension as 100 m×100 m. This also helped to minimize the computational efforts to model the heat and contaminant transport in a typical DGR.

5.2.2. Material property

As indicated in Figure 5.2, the model comprised of host rock, buffer material, and canister. The lithology of the continental crust of the planet earth at shallow depths predominantly consist of alkaline sedimentary formations as evident in Canadian prototype DGR (Mitchell and Soga, 2005). Therefore, the present study considered limestone as the host rock with a thermal conductivity value of 2.3 $W \cdot m^{-1} \cdot K^{-1}$ and dry unit weight of 25.5 $kN \cdot m^{-3}$ (Wolfaardt and Korber, 2012). The thermal conductivity of the steel component of the canister was taken as 300 W·m^{-1}·K^{-1} with a dry unit weight of 76.52 kN·m^{-3} (Wolfaardt and Korber, 2012). The buffer material considered to be a sand-bentonite mixture with 30 percent bentonite in it (SB30). The dry unit weight, moisture content and thermal conductivity of the candidate buffer material were established and the details were presented in Table 4.7.

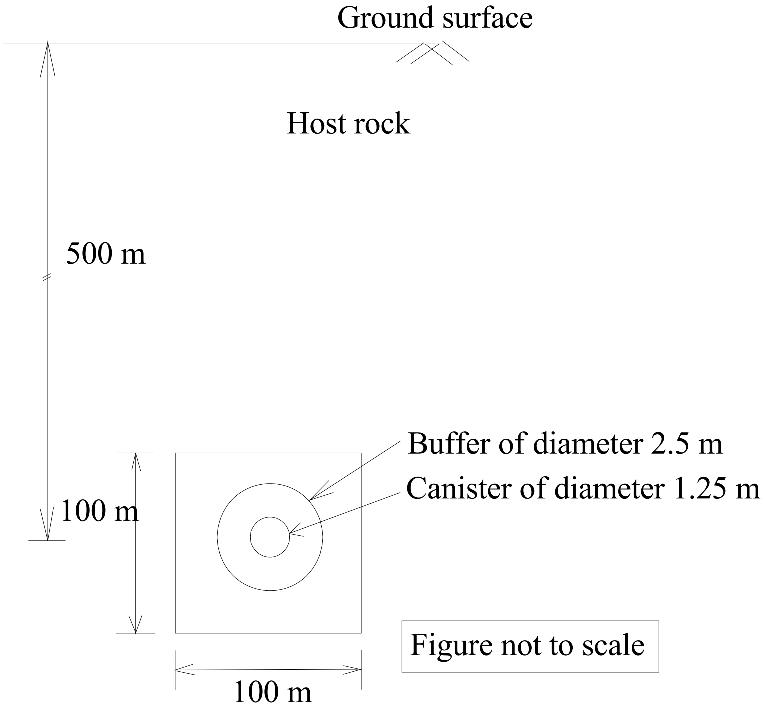

Figure 5.2 Geometry of the model deep geological repository

5.2.3. Initial and boundary conditions

After defining the geometry of the model, material properties were assigned and the initial and boundary conditions of the model were specified. The model was divided into several finite elements with the specified material properties and initial and boundary conditions. For this purpose mesh generation algorithm was used, by defining the corresponding material properties.

The numerical model considered the temperature of 30 ºC at the ground surface and a geothermal gradient of +0.016 ºC·m^{-1}. Therefore, the temperature of the geological formation where the typical DGR is located (the canister level i.e., 500 m from the ground surface) was ascertained using the relationship: $T=30+0.016z$, where z is the depth in meters from ground surface. The surface temperature of the canister is expected to vary with time owing to the decay of radionuclides present in it and hence the temperature at the interface between canister and buffer material is subjected to a temporal variation of temperature. With this in view, majority of the prototype studies approximated this variation of temperature using a step function. Wolfaardt and Korber (2012) proposed the variation in temperature of the canister as reported in Table 5.1.

Table 5.1 Variation of temperature of the canister with time

Time (years)	**Temperature (°C)**
0-10	120
10-20	115
20-30	110
30-50	100
50-100	80
100-200	60

5.2.4. Properties of mesh

The DGR was modeled as two-dimensional and analyzed under transient heat conditions for 200 years. Since the temporal and spatial variation in temperature of the buffer is expected to change its engineering behavior significantly compared to the host rock, the buffer material was discretized using a fine mesh size of 0.05 m. The variation in temperature within the canister is not of primary interest, its discretization was restricted to 0.1 m in view of avoiding computational efforts and for all the regions in the host rock, the coarser mesh size of 1 m was used. Figure 5.3 presents the model with generated mesh. After defining the input parameters and mesh size, the model was analyzed for temporal and spatial variation of temperature.

5.2.5. Results and discussion

The DGR was modeled and analyzed for the performance evaluation of buffer material over its service life. The variation of temperature with time at the interface of the canister-buffer and buffer-host rock is given in Figures 5.4 and 5.5, respectively. It can be observed that the variation of temperature at the canister (i.e., at a distance of 0 m from the canister surface) is following a stepped decay. The temperature variation in the buffer and host rock also followed a similar trend as above. Further, it can be observed that the magnitude of the temperature at any given time is governed by the molding moisture content.

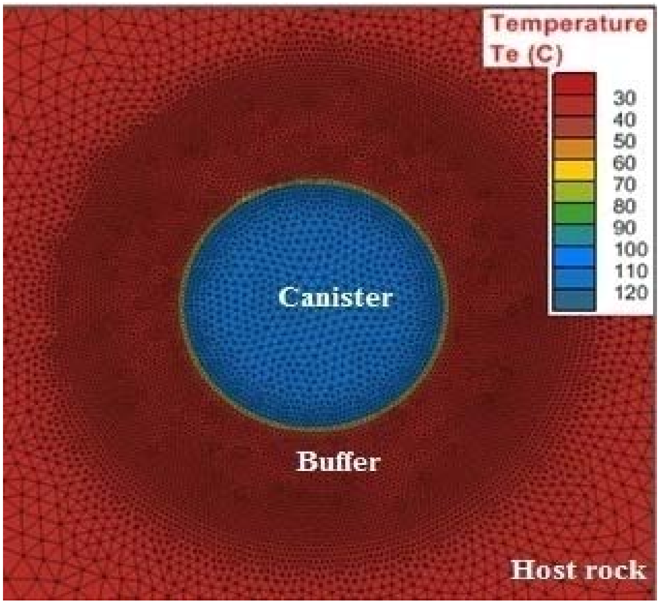

Figure 5.3 Schematic of the mesh generated for SB30

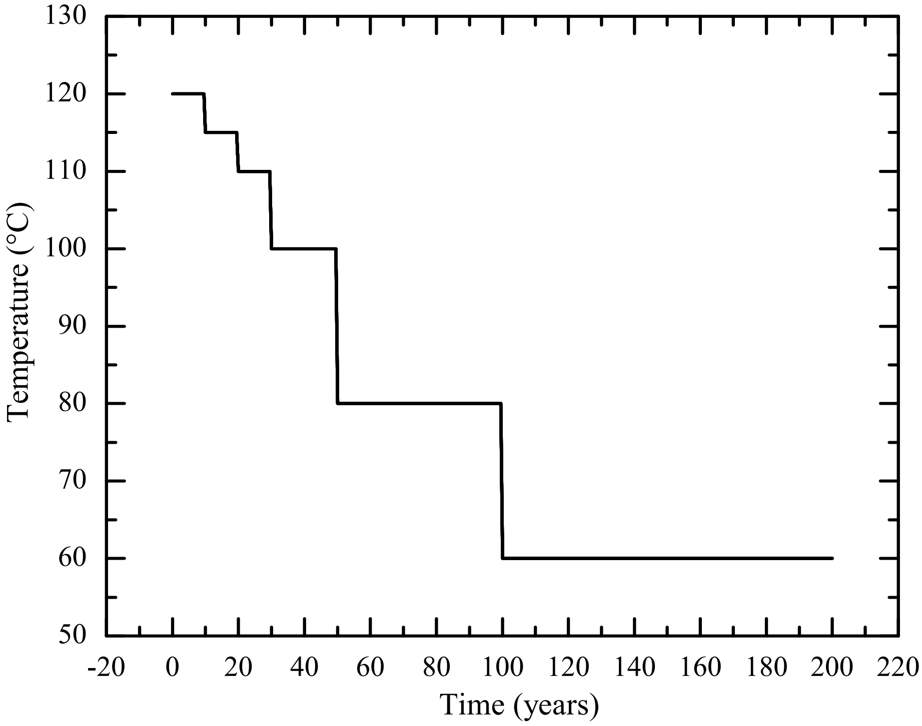

Figure 5.4 Variation of temperature with time at the interface of the canister and buffer for SB30

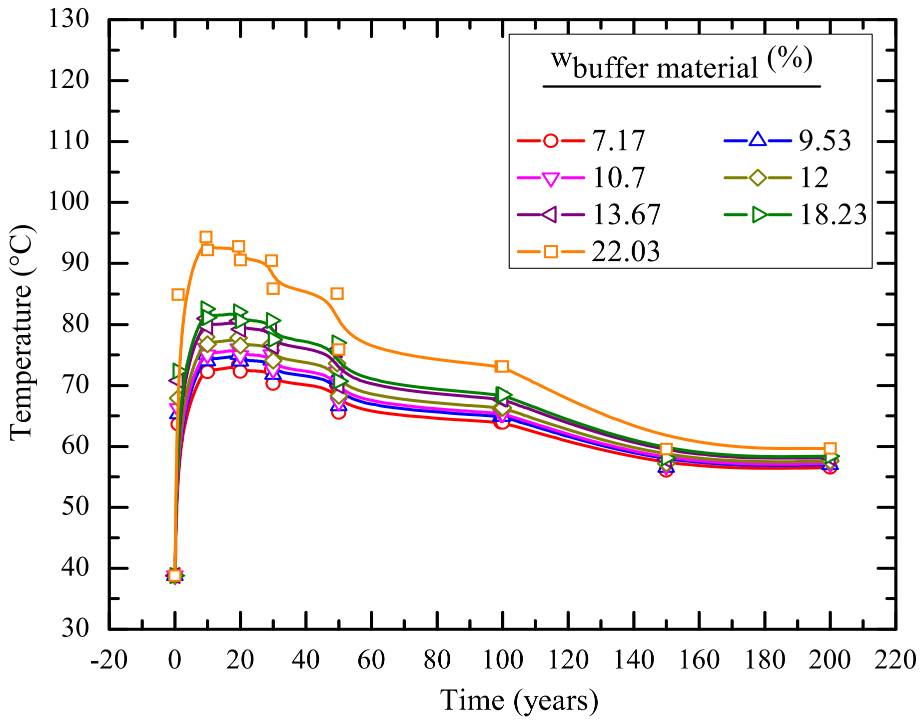

Figure 5.5 Variation of temperature with time at the buffer-host rock interface for SB30 having different placement moisture

Figure 5.6 presents the temperature variation with time at the mid-depth of the buffer material. At the middle of the buffer, the temperature rose to a maximum extent of 105 °C and then decreased. Beyond 100 years, the temperature dropped to 60 °C. Whereas at 10 m distance from the canister surface the temperature rose for the first 50 years and then remained almost constant as shown in Figure 5.7. Therefore, it can be concluded that after 10 m from the canister surface the higher temperature of the canister has no significant effect.

From the Figures, it can be concluded that when the placement moisture content is on dry of optimum, the heat migration towards the host rock is very slow and as the moisture content of the buffer increases the temperature within the host rock also increases. This can be attributed to the fact that, buffer material compacted on wet of optimum exhibits high thermal conductivity than that of compacted on dry of optimum, and hence, transport more heat towards the host rock. The time of arrival of peak temperature at buffer-host rock interface is about 9.5 years and thereafter the temperature receded. Further, beyond 100 years the temperature variation is found to be negligible.

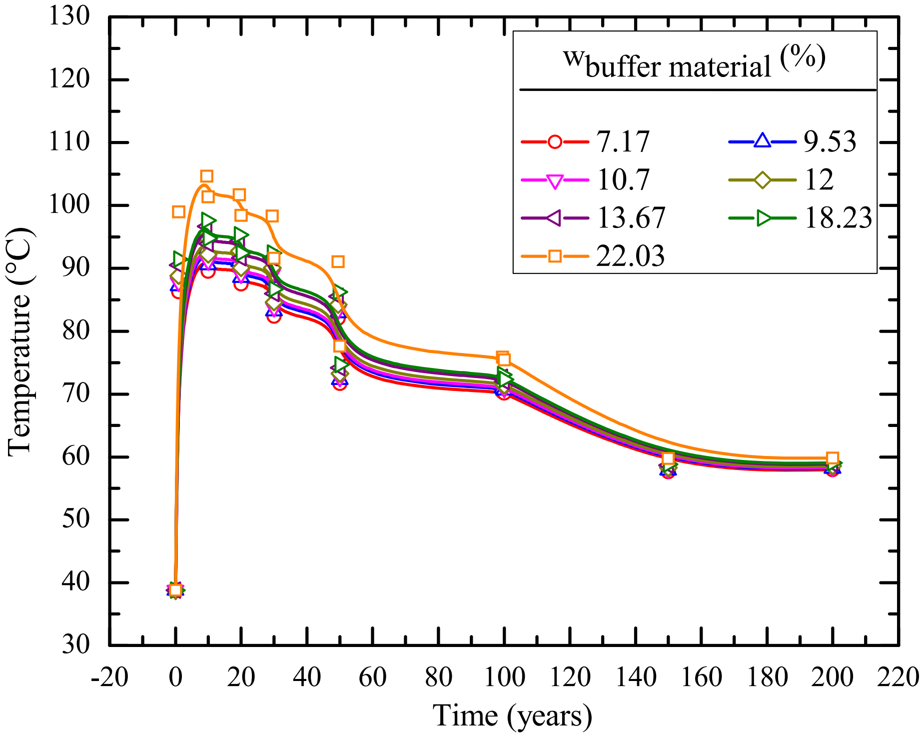

Figure 5.6 Variation of temperature with time at the middle of the buffer for SB30

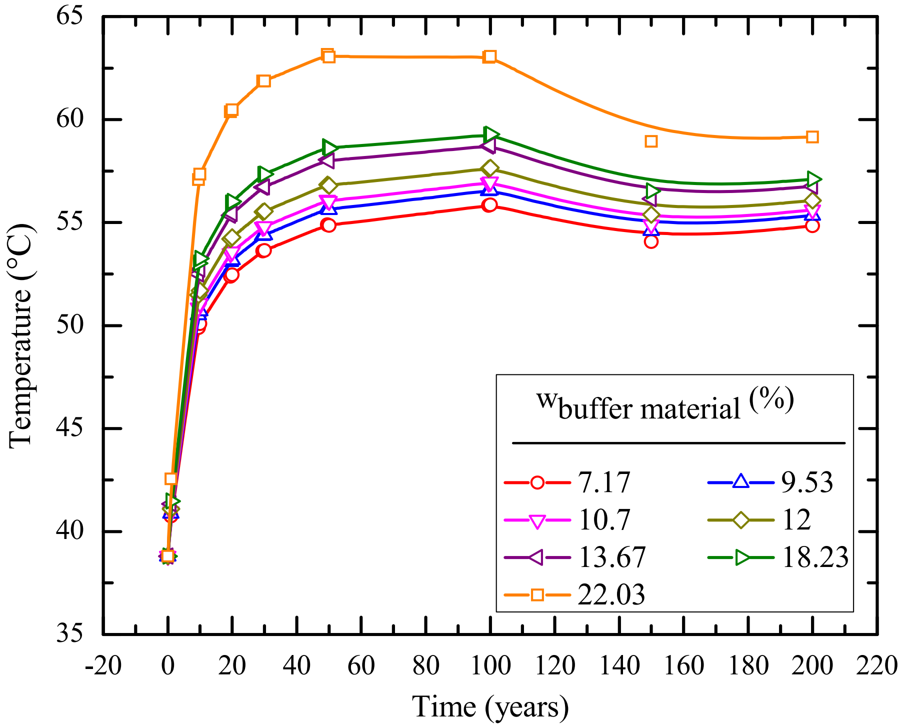

Figure 5.7 Variation of temperature with time at a distance of 10 m from canister surface with SB30 as buffer material

Figure 5.8 depicts the variation of temperature along the radial distance corresponding to the peak temperature arrival time of 9.5 years. It can be observed that the maximum temperature occurs at the canister surface and reduces with radial distance. Beyond 20 m radial distance (i.e., 19.375 m within the host rock) the temperature is more or less equal to ambient. Figure 5.9 presents the variation of temperature with radial distance at the end of the analysis period (i.e., t = 200 years). At the end of 200 years the variation in temperature with radial distance is negligible which indicates that buffer material and host rock attains steady state thermal equilibrium with the canister.

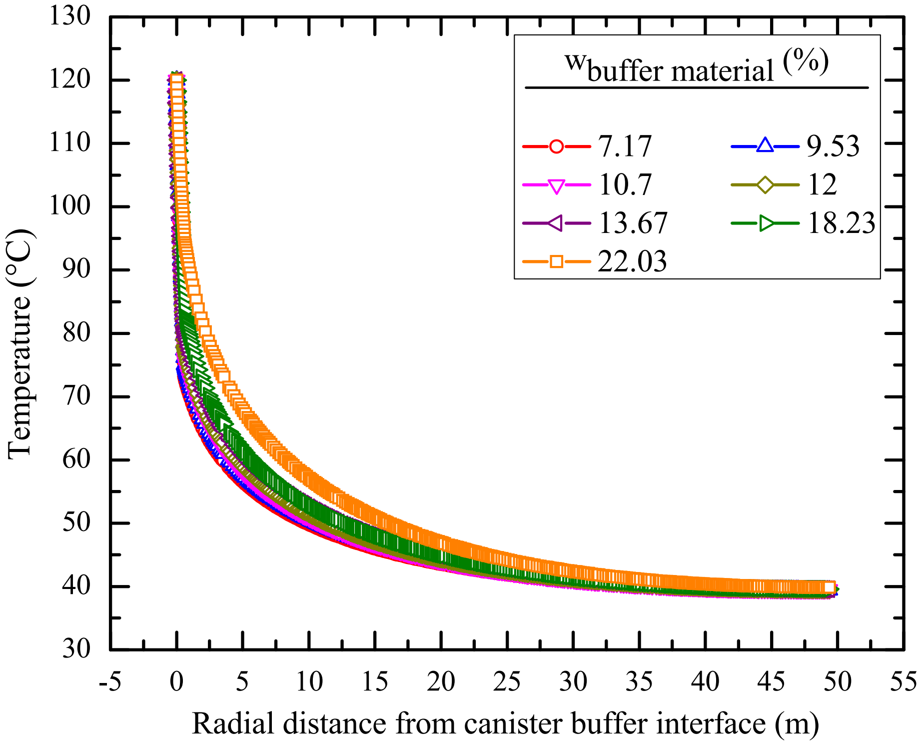

Figure 5.8 Variation of temperature with radial distance for SB30 corresponding to peak temperature time of 9.5 years

Figure 5.10 depicts the variation of temperature with radial distance for SB30 corresponding to the time intervals at which stepped temperature decay happens at the canister and buffer material interface for the buffer material compacted at optimum moisture content. It can be observed that at t=100 years when the canister temperature dropped to 60 °C, the buffer is still at a higher temperature and slowly dissipating heat to the host rock; however, it attains 60 °C within a six months time. From the above discussion, when the temperature of the canister decrease, the temperature at the buffer-host rock interface increased to a maximum of 95 °C corresponding to 9.5 years and eventually dropped to 60 °C only at the end of 200 years.

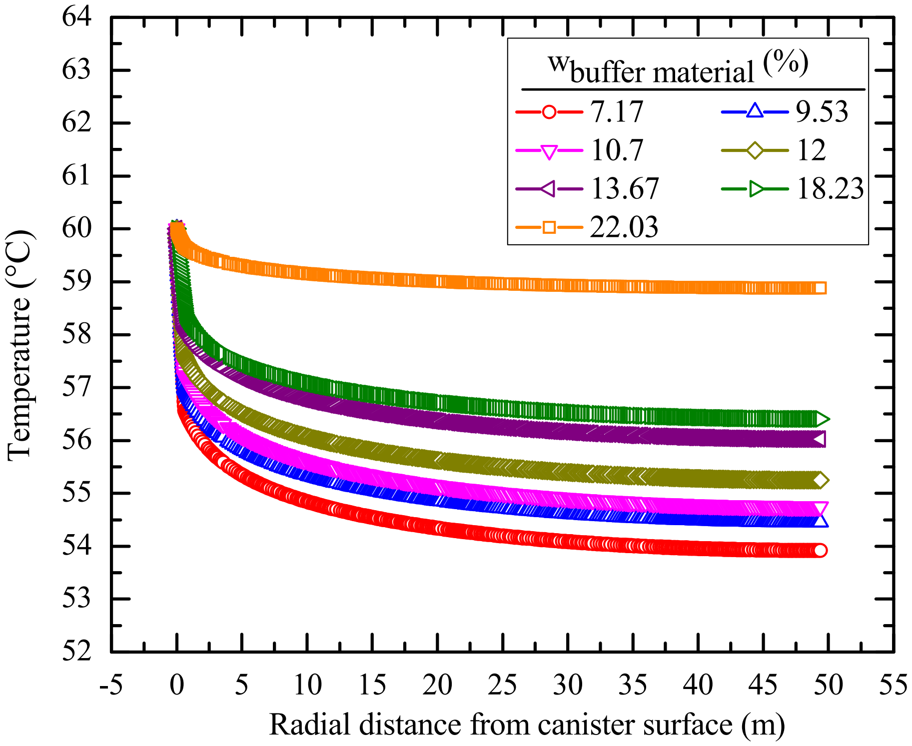

Figure 5.9 Variation of temperature with radial distance for SB30 at the end of the analysis period

In order to evaluate the effect of stepped variation of temperature, an additional model was considered and analyzed with 120 °C constant elevated temperature at the canister-buffer interface. Based on the analysis carried out, a maximum temperature within the buffer material was observed to rise to 113 °C at the end of 200 years and increases continuously. Therefore, if a DGR is modeled with the assumption that the canister is subjected to constant elevated temperature, the result shows a continuous heating up of buffer material and host rock, which is not desirable. This scenario may result in complete drying of the buffer material, which in turn leads to severe desiccation cracking of the buffer as well as host rock. Therefore, modeling the canister temperature variation with time represents the real-life scenario since majority of radionuclides present in the waste have half-life in the order of few decades and mostly less than a century.

When the molding moisture content of the buffer material was on dry of optimum, the temperature increased slowly as the thermal conductivity of the buffer material on dry side of optimum was low. Therefore, it can be concluded that for the effective heat transfer from the canister to the host rock, the buffer material shall have high molding moisture content and it should be compacted using modified proctor energy. It can be inferred from the above discussion that higher the bentonite content in the buffer material higher will be the heat migration through it, as the pores of the coarser fraction of buffer material are filled with the bentonite and water resulting in superior thermal conductivity. However, in arriving at the optimal bentonite content in the buffer material; the thermal properties, volume change and strength characteristics of the buffer material are to be considered. Needless to mention, the economics of the design as well as construction require special attention while finalizing the optimal design mixture of the buffer material of a DGR.

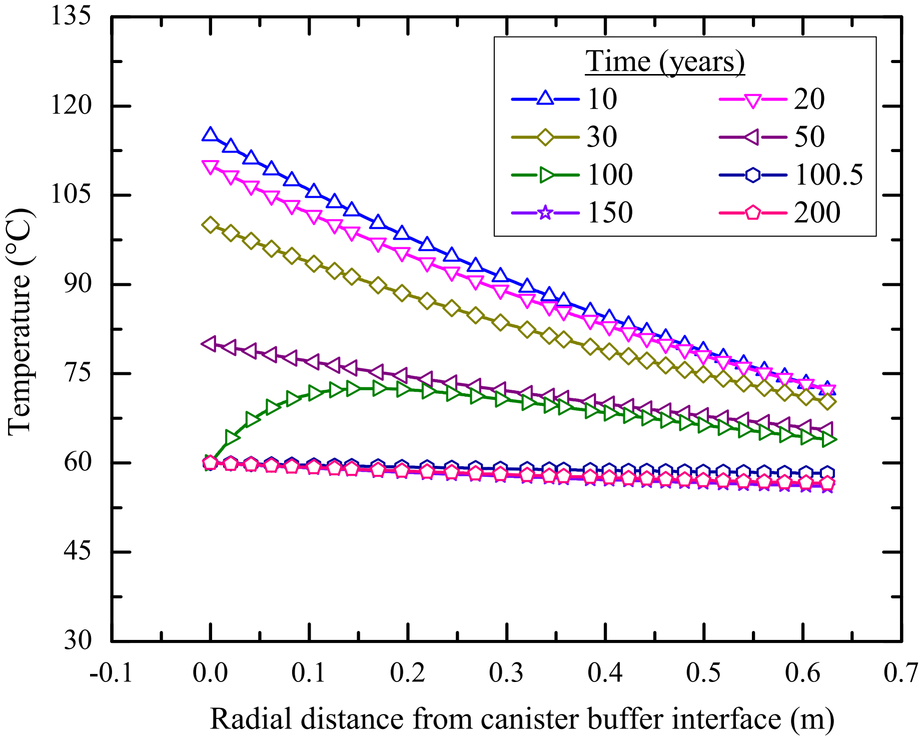

Figure 5.10 Variation of temperature with radial distance for SB30 corresponding to the time intervals at which stepped temperature decay happens at canister

5.3. Appraisal of Safe Placement Distance between Canisters in a DGR

5.3.1. Two-dimensional analysis

Prior to the placement of canisters in a DGR, a safe horizontal placement distance between them has to be maintained to ensure the effective heat migration to the surrounding host rock and hence to the geoenvironment without rising the temperature in the buffer material beyond the threshold value. Considering this fact, numerical analysis using SVHeat™ was extended to the analysis of heat migration with time for various modes of placement distances. Two DGRs with horizontal tunnels were considered for this purpose. The boundary conditions and properties of the materials are maintained identical to the previous section and the analysis was conducted for different placement distances of 2 m, 4 m, 6 m, and 8 m centre to centre. For the sake of brevity, a schematic of the model DGR with 2 m placement distance is depicted in Figure 5.11. From the thermal conductivity results, it can be noted that the water content of 22 % in the case of SB30 sample furnished the highest value of thermal conductivity i.e. 1.831 $W \cdot m^{-1} \cdot K^{-1}$. Giving regards to preciseness and conciseness, the further analyses were carried out considering this water content. It was observed that as the placement distance between the canisters increases, the maximum observed temperature at the interface reduces. Figure 5.12 depicts the variation of temperature with time at the interface of buffer and host rock for various placement modes of the canister.

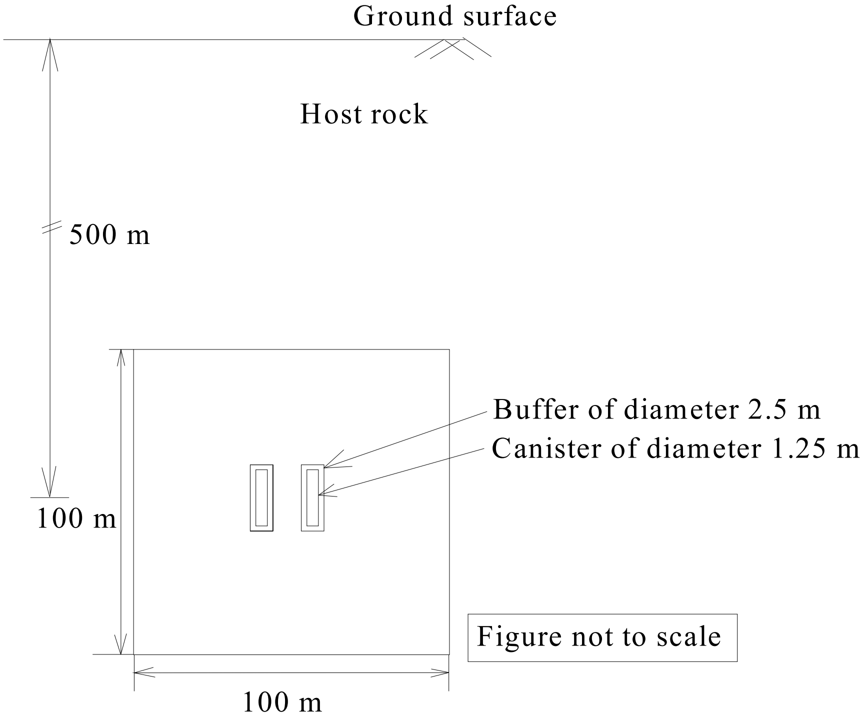

Figure 5.11 Schematic of the model deep geological repository with 6 m placement distance

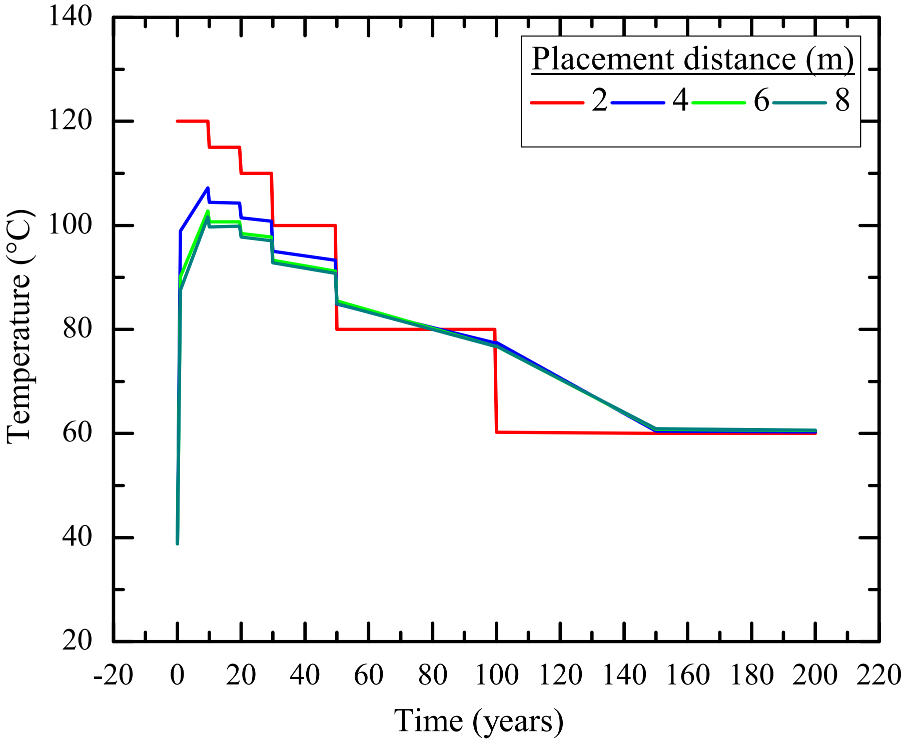

Figure 5.12 Temperature variation with time at buffer-host rock interface

The analysis explained in the previous section demonstrated a maximum rise of temperature up to 95 °C at the end of 9.5 years near the buffer host rock interface. The present model also endorsed the fact that maximum rise of temperature at the buffer host rock interface occurred after 9.5 years. However, as the distance between canisters increases, the highest temperature observed at the interface reduced. The temperatures observed at the interface of buffer and host rock when the thermal migration to the host rock was at its peak were 120 °C, 107 °C, 102 °C and 101 °C for placement distances of 2 m (radial coordinates of 49 and 51 at the centers of the canisters), 4 m (radial coordinates of 48 and 52 at the centers of the canisters), 6 m (radial coordinates of 47 and 53 at the centers of the canisters), and 8 m (radial coordinates of 46 and 54 at the centers of the canisters), respectively. For all the placement distances considered, an ambient temperature of 60 °C was noticed after 150 years. A stepped decay in temperature was also noticed irrespective of the placement distance. Figure 5.13 emphasizes the temperature variation along the radial distance when maximum heat migration to the host rock occurs. It can be observed that heat is getting more dispersed as the placement distance increases. The temperature reduced to more than 10 °C when the placement distance changed from 2 m to 4 m. At 8 m spacing, the temperature observed at the buffer interface is more or less independent of each other. After that, for every 2 m increase in placement distance, the maximum observed temperature is reduced 5 °C. As the disposal area is limited, placement distance between adjacent canisters of 4 m distance is preferable. The caution must be exercised while extending this conclusion to the conditions other than the one considered in this study. Figure 5.14 exhibits the variation of temperature with distance at the end of analysis period of 200 years for the second canister. An ambient temperature range of 60 °C to 63 °C is observed.

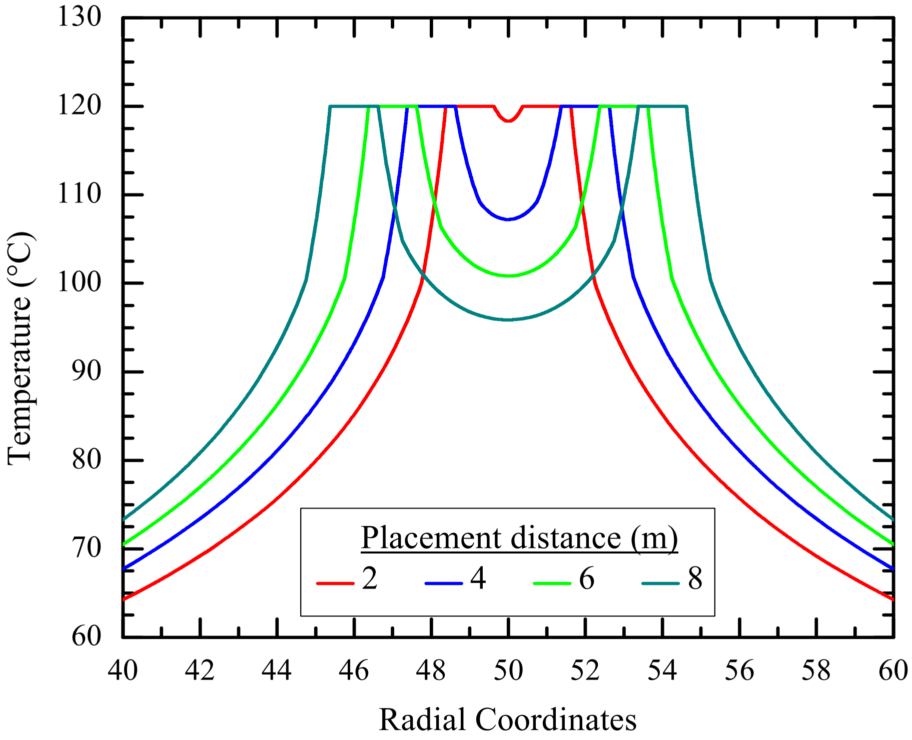

Figure 5.13 Temperature along the radial coordinates when maximum heat migration to host- rock occurs

5.3.2. Three-dimensional analysis

Heat migration studies using SVHeat™ were further extended to three dimensional (3D) analyses using the identical material properties and other parameters and the results were compared with that obtained from two dimensional (2D) analyses. It was observed that the 2D analyses results are overestimating the temperature variation when compared to 3D analysis. Figure 5.15 shows the variation of temperature with time for SB30 at different moisture contents obtained from both 2D as well as 3D analyses. It can be observed from the Figure that the 2D analyses are overestimating the temperature values in the order of 20 °C and therefore 3D analysis is preferred over 2D analyses for precise estimation of temperature variation with time.

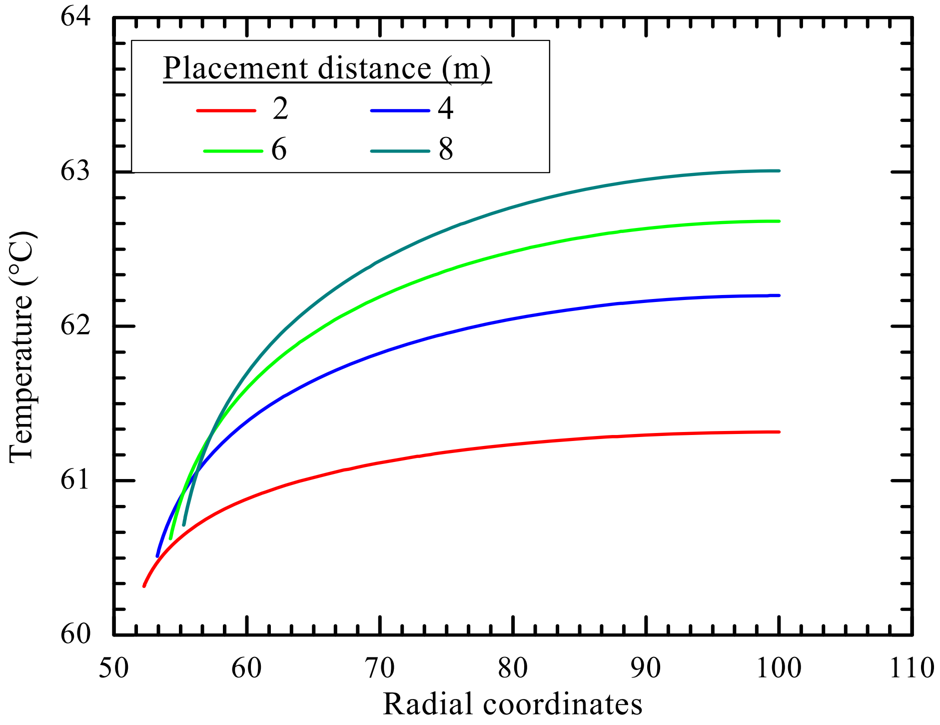

Figure 5.14 Temperature along radial coordinates at the end of analysis period

Further, the analysis of heat migration with time for various modes of placement distances was extended to a three-dimensional analysis using SVHeat™. Two DGRs with vertical tunnels were considered for this purpose. The identical properties and placement distances as in the previous section were considered for the analysis and the results were compared with that obtained from two-diemnsional analysis. The variation of temperature with time at the buffer host rock interface is presented in Figure 5.16 and the variation of temperature with time at the interface in between the canister is depicted in Figure 5.17.

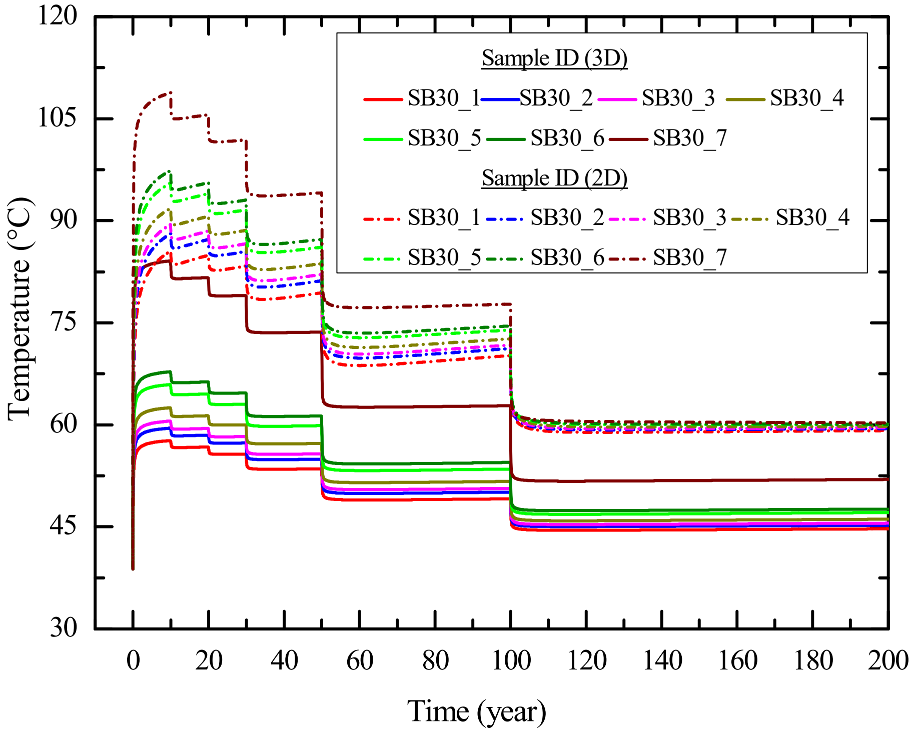

Figure 5. 15 Variation of temperature with time at buffer host rock interface

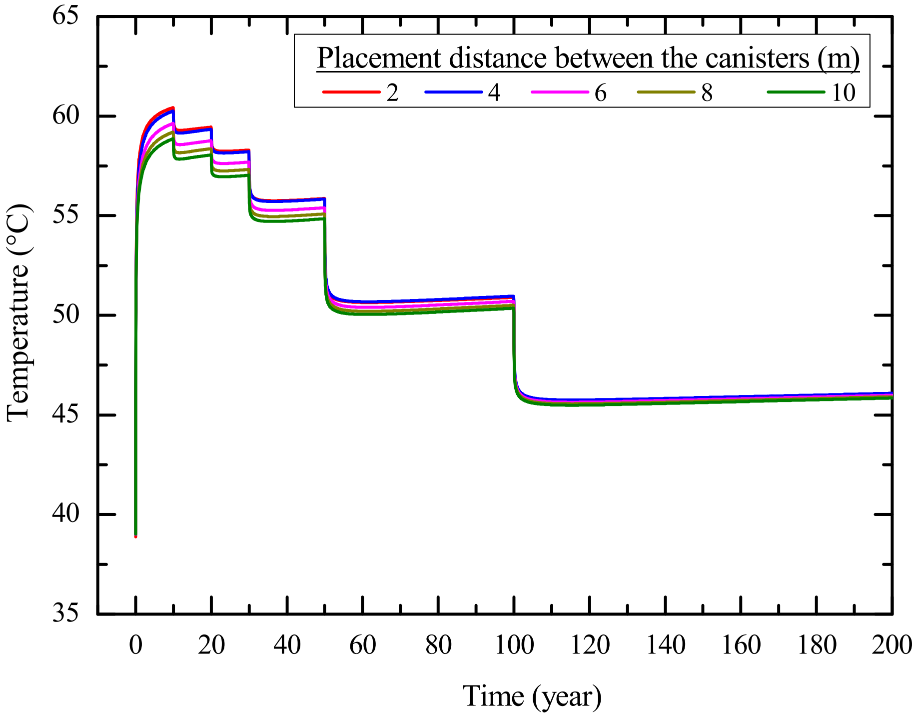

Figure 5.16 Temperature variation at buffer host rock interface outside the second canister

From Figure 5.16 it is observed that the maximum temperature reached up to 62 °C after 10 years at the buffer host rock interface outside the canister and at the buffer host rock interface in between the canisters (Figure 5.17), a maximum temperature of 115 °C is observed for a placement distance of 2 m. Further, as the placement distance increases, the maximum temperature at the buffer host rock in between the canister reduces and reached up to 65 °C for 4 m placement distance and it is further reducing with the increase in placement distance. Therefore, from the 3D analysis also 4 m placement distance is considered as the safest.

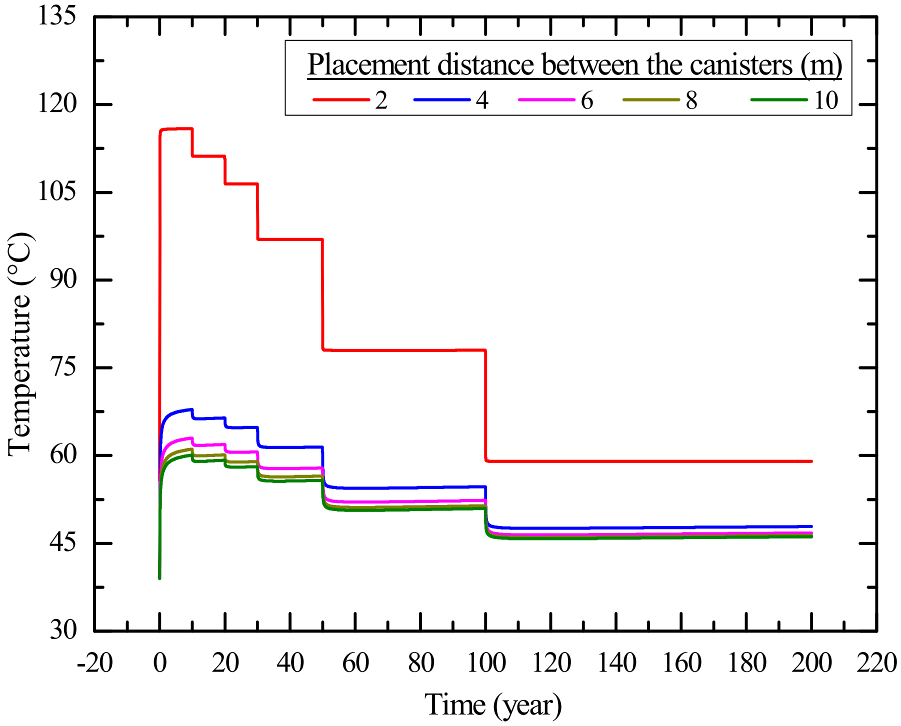

Figure 5.17 Temperature variation at buffer host rock interface in between the canisters

5.4. Modeling of Contaminant Migration through Buffer Material in a DGR

The contaminant migration through the buffer material involves different transport mechanisms like advection, diffusion, and sorption as explained in the preceding chapters. Freeze and Cherry (1979) reported that the contaminant transport through a highly porous media is governed by the dispersion mechanism, whereas, for compacted geomaterials with low hydraulic conductivity the contaminant migrate in response to the concentration gradient which is also called diffusion. Further, if the porous material is rich in reactive clay minerals, it results in attenuation of contaminants by sorption phenomena.

Among the existing the numerical tools to model contaminant transport through waste containment and disposal facilities, the tool developed by Rowe and Booker (1987) is considered to be efficient and popular. The present study considered the finite layer technique POLLUTE proposed by Rowe and Booker (1985, 1994) to demonstrate the contaminant transport phenomenon through buffer material in a DGR. The POLLUTE solves the advection-dispersion equation for layered deposits of finite thickness and infinite extent. This technique predicts the concentration profiles in spatial and temporal domains for the predefined initial and boundary conditions. The real-life contaminant transport scenarios can be modeled and this method is widely used for evaluating the long-term performance of engineered landfill liners (Rowe, 1989).

The governing differential equation for the possible phenomena taking place in a DGR is presented as follows.

$$\eta\frac{\partial C}{\partial t}=\eta D(\frac{\partial^2 C}{\partial z^2})-\nu\frac{\partial C}{\partial z}-\rho K_d\frac{\partial C}{\partial t}-\eta\lambda C \tag{5.1}$$

where η is porosity; C is concentration of the contaminant in $mg\cdot L^{-1}$; D is diffusion coefficient in $m^2\cdot s^{-1}$; ν is permeability coefficient in $m\cdot s^{-1}$; ρ is density of the buffer material in $kN\cdot m^{-3}$; K_d is distribution coefficient or the sorption coefficient in $mg\cdot L^{-1}$; λ is decay constant.

A typical DGR considered for the heat migration analysis was considered for the contaminant transport analysis. The contaminant transport parameters such as diffusion coefficient, permeation coefficient, and sorption coefficient were obtained experimentally at corresponding compaction state. Decay constant was taken as 30 years (US Nuclear Waste Technical Review Board). After inputting the parameters, initial and boundary conditions were defined. A concentration of 1000 $mg\cdot L^{-1}$ as initial concentration was imposed at the surface of the canister and buffer material, and zero flux boundary condition at the buffer host rock interface was also considered. Further, the analysis was carried out with contaminant transport parameters at different temperatures. Figures 5.18, 5.19, and 5.20 show the variation of contaminant concentration over the thickness of the buffer material at different temperatures of 10 °C, 27 °C, and 50 °C respectively.

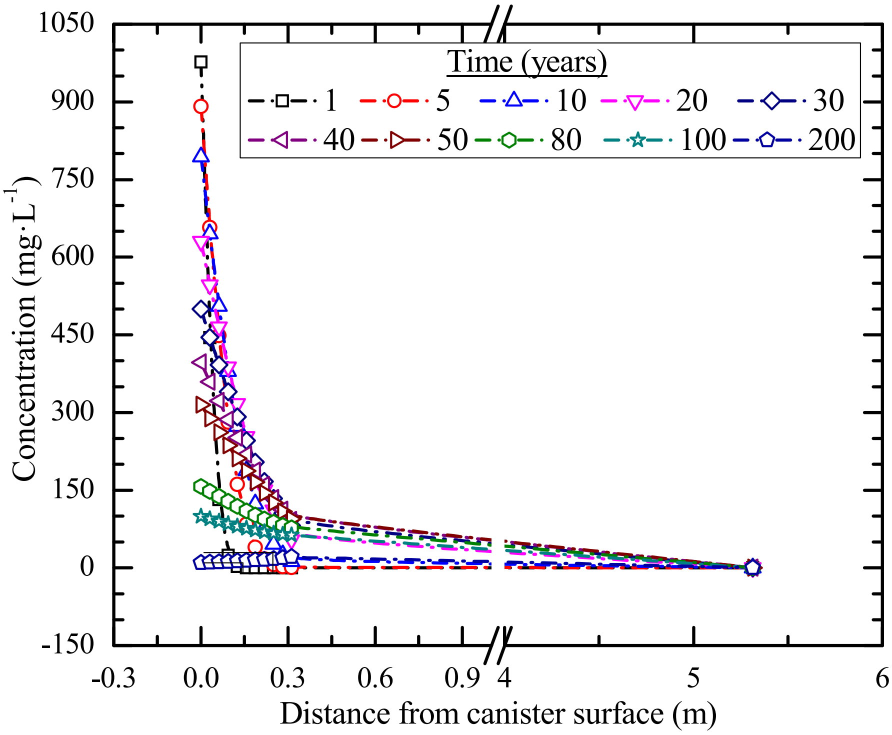

Figure 5.18 Variation of concentration with distance from the canister surface at 10 °C

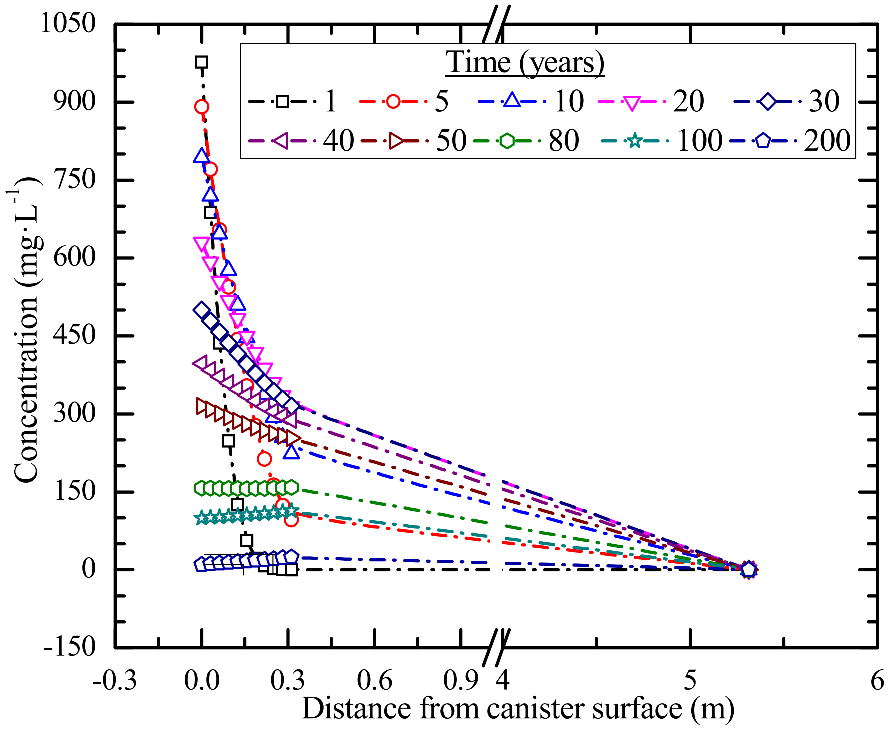

Figure 5.19 Variation of concentration with distance from the canister surface at 27 °C

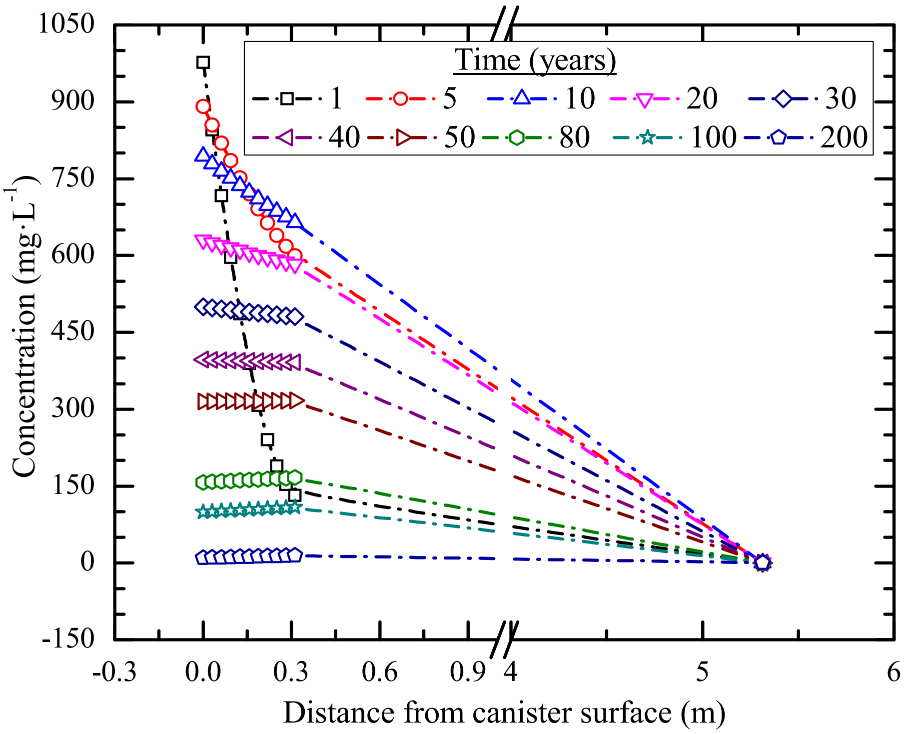

Figure 5.20 Variation of concentration with distance from the canister surface at 50 °C

It is can be observed from the Figures that, as the temperature of the buffer material increases the distribution coefficient decreases and therefore the concentration range is on the higher side as depicted in Figure 5.20 when compared to companion results presented in Figure 5.19 and 5.18. It can also be seen that there is a drastic decrease in the concentration of the contaminant after 30 years and the concentration reaches almost zero at 200 years. Further, if we consider the variation of concentration with time at a radial distance from the canister surface as shown in Figure 5.21, at the middle portion of the buffer material (0.3125 m from the canister surface) there is an increase in concentration at around 25 years and after 30 years it starts decreasing. Whereas at the interface of buffer and host rock (0.625 m) there is a slight increase in concentration and as an average, the concentration is close to 50 mg/L. Therefore, from the above discussion, it can be inferred that the DGR modeled in the study is safe in terms of contaminant transport properties at a temperature of 10 °C.

Figures 5.22 and 5.23 depict the variation of concentration with time at a different radial distance from the canister surface at temperatures of 27 °C and 50 °C. It can be observed from the figures that, at an elevated temperature since the sorption coefficient is less, more concentrated contaminant comes out at the buffer host rock interface (almost half of the initial concentration) when the temperature of the buffer material is 50 °C. Therefore, at elevated temperatures, thicker buffer material should be provided.

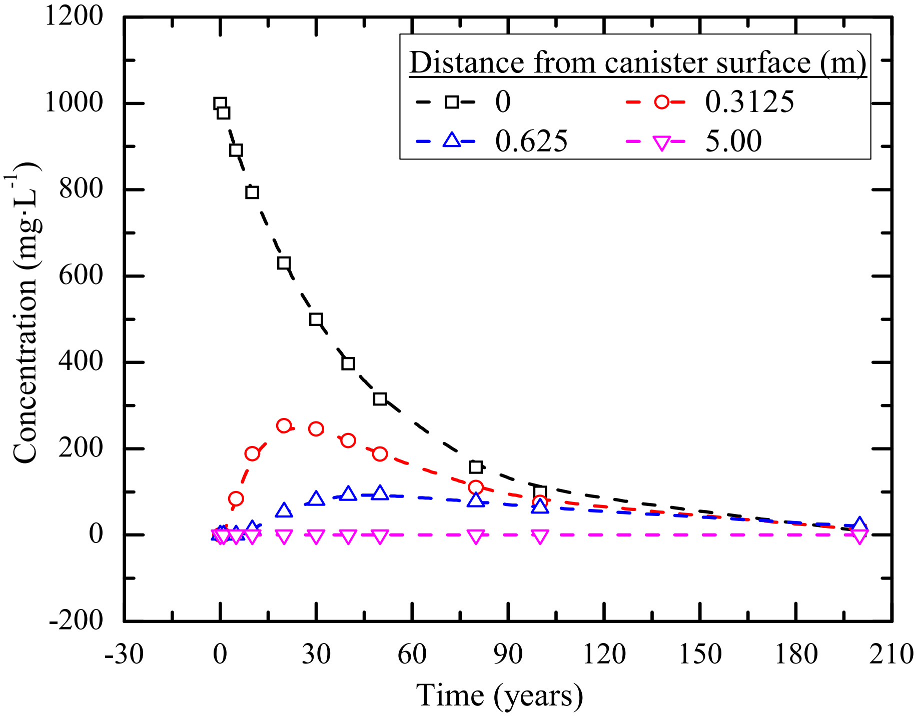

Figure 5.21 Variation of concentration with time at different radial distance from canister surface at temperature of 10 °C

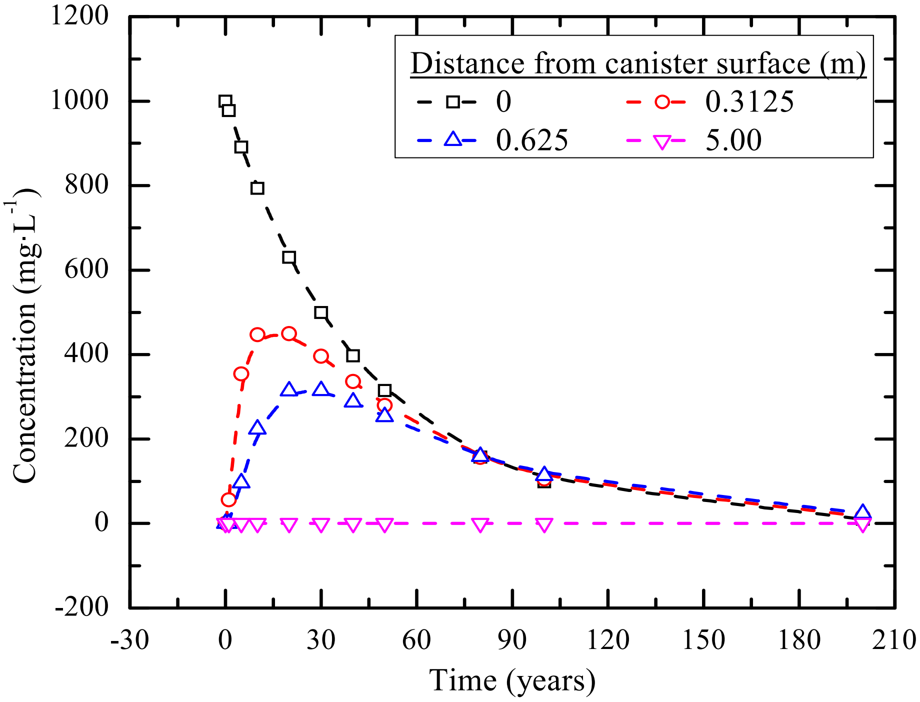

Figure 5.22 Variation of concentration with time at different radial distance from canister surface at temperature of 27 °C

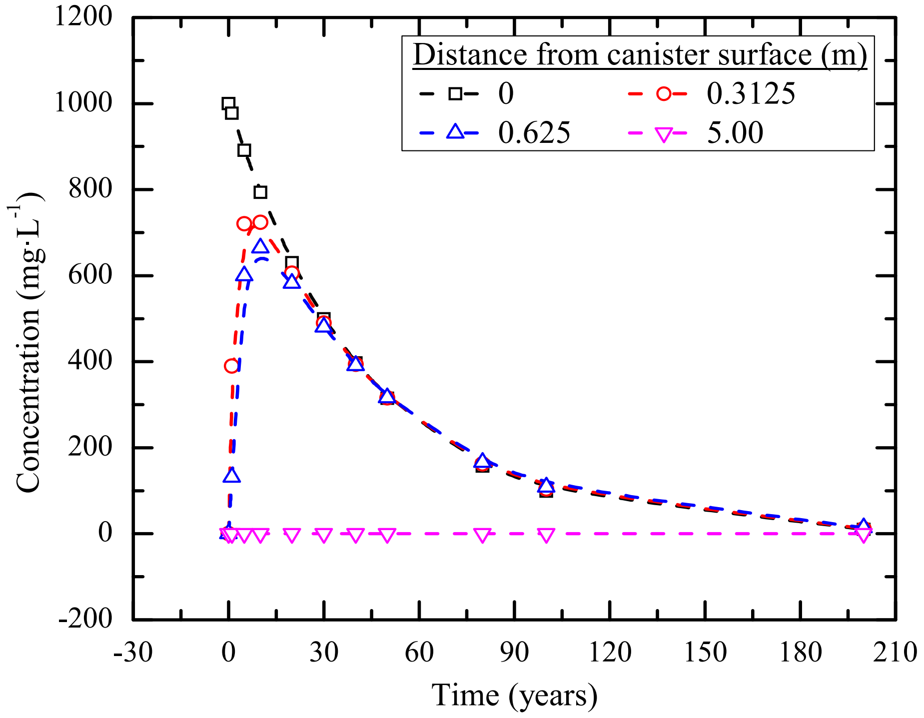

Figure 5.23 Variation of concentration with time at different radial distance from canister surface at temperature of 50 °C

Chapter 6

SUMMARY AND CONCLUSIONS

The application of sand-bentonite mixtures as an engineered buffer material of deep geological repositories (DGR) to ensure long-term confinement and isolation of radioactive waste contained canisters is a common practice. The efficacy of DGR to contain the radioactive waste primarily depends on the long-term performance of the buffer materials under the combined influence of physical, chemical and thermal loadings. In view of this, the sand-bentonite buffer material is expected to facilitate heat transfer from the canister surface to the host rock and hence, to the surrounding geoenvironment, effectively. The essential properties of a buffer material are low hydraulic conductivity, low diffusion characteristics, low gas permeability characteristics and high sorption affinity towards radionuclides and heavy metals. In addition, the buffer material must maintain its physical and engineering integrity at elevated temperatures for a prolonged period. Keeping in view of the quite demanding requisites, it is essential to understand the fundamental behavior of buffer material over a wide range of environmental conditions to ascertain its long-term performance.

With this in mind, experimental investigations were carried out to characterize the buffer materials. The selected virgin geomaterials such as sand and bentonite were characterized for their physico-chemico-mineralogical and geotechnical properties. The performance of synthesized sand-bentonite buffer materials was assessed in terms of their thermal properties, the rate of loss of moisture from them for a given exposure condition, and contaminant migration mechanisms, viz. diffusion, permeation, and sorption. Further, the long-term performance of buffer materials upon the application of physical, chemical and thermal loadings was assessed using numerical techniques. Based on the experimental findings and numerical analyses the following conclusions can be drawn.

- In terms of thermal and contaminant transport properties, the buffer material with 30 % bentonite was found to be optimal for its efficacious long-term performance.
- The generalized prediction model developed in this study showed that thermal conductivity of buffer material increases with the increase in volumetric moisture content and amount of quartz mineral present in it.
- With the experimental methodology proposed in this study, for assessing the coupled flow of heat and moisture through a buffer material upon application of

thermal flux, an exponential decrease in vapor flow along the radial distance was obtained.

- The prediction model proposed for estimating the gas permeability coefficient of buffer materials by considering the effect of temperature on it was efficacious in estimating the gas permeability characteristics of wide varieties of geomaterial with a precision of 95 %.
- The coefficient of gas permeability of compacted buffer material decreased with increase in temperature, placement moisture content, and bentonite mass fraction. However, the addition of bentonite content higher than 30 % by weight failed to bring further noticeable change in its gas permeability.
- It was reaffirmed that the geomaterial-contaminant interaction can be represented by a nonlinear Freundlich sorption isotherm. The sorption affinity of the buffer material decreased with increase in temperature.
- As a whole, the present study described an integrated approach for evaluating the long-term performance of buffer materials by considering the combined influence of physical, chemical, and thermal loadings which prevail in a typical DGR.

Future Scope of Research

The present study made an attempt to characterize the buffer materials to contain HLW canisters based on their physico-chemical, geotechnical, thermal and contaminant transport properties under the combined influence of physical, chemical and thermal loadings. The coupled flow of heat and moisture under the given thermal flux in terms of water vapor diffusion characteristics were quantified for SB 30 as it was exhibiting favorable engineering properties for DGR application. The study needs to be extended to other sand-bentonite mixtures in future including SB10, SB20, SB50, SB70, and SB100. Even though, it is given in literature that the temperature variation does not affect the SWCC, proper quantification of this is required to support the fact.

The efficacy of the generalized gas permeability model needs to be validated with more experimental data. Gas diffusion studies need to be extended to study the effect of temperature on diffusion characteristics. Column flow through experiments and centrifuge tests need to be performed for more samples and the generalized model need to be validated to predict the equivalent column distribution coefficient from batch sorption data.

Numerical analysis for the long-term performance of buffer materials in DGR should be upgraded by incorporating other parameters.

List of References

1. **Abaci, S., Edwards, J. S. and Whittaker, B. N.** (1992). Relative permeability measurements for two phase flow in unconsolidated sands. *Mine, Water and the Environment*, **11 (2)**, 11-26.
2. **Ada, M.** (2007). *Performance Assessment of Compacted Bentonite/ Sand Mixtures Utilized as Isolation Material in Underground Waste Disposal Repositories*. Masters dissertation, The Graduate School of Natural and Applied Sciences of Middle East Technical University.
3. **AERB, Atomic Energy Regulatory Board, India report** (2001). *Liquid and Solid Radioactive Waste Management in Pressurized Heavy Water Reactors*. AERB Safety Guide No. AERB/SG/D-13.
4. **Agus, S. S.** (2005). *An Experimental Study on Hydro-mechanical Characteristics of Compacted Bentonite-sand Mixtures*. Doctoral dissertation, Bauhaus University Weimar.
5. **Aksu, Z. and Kutsal, T. A.** (1991). A bioseperation process for removing Pb (II) ions from waste water by using C. vulgaris. *Journal of Chemical Technology and Biotechnology*, **52(1)**, 108-118.
6. **Alba, M. D., Chain, P. and Orta, M. M.** (2009). Rare earth disilicate formation under deep geological repository approach conditions. *Applied Clay Science,* **46**, 63-68.
7. **Allaire, S. E., Lafond, J. A., Cabral, A. R. and Lange, S. F.** (2008). Measurement of gas diffusion through soils: comparison of laboratory methods. *Journal of Environmental Monitoring*, **10**, 1326-1336.
8. **Altena, F. W., Knoef, H. A. M., Heskamp, H., Bargeman, D. and Smolders, C. A.** (1983). Applicability of gas permeability methods to characterize porous membranes based on improved experimental accuracy and data handling. *Journal of Membrane Science*, **12**, 313-322.
9. **Alzaydi, A. A. and Moore, C. A.** (1978). Combined pressure and diffusional transition region flow of gases in porous media. *American Institute of Chemical Engineers Journal*, **24 (1)**, 35-43.
10. **Arnepalli, D. N. and Singh, D. N.** (2004a). A generalized procedure for determining thermal resistivity of soils. *International Journal of Thermal Sciences*, **43(1)**, 43-51.
11. **Arnepalli, D. N. and Singh, D. N.** (2004b). Field probe for measuring thermal resistivity of soils. *Journal of Geotechnical and Geoenvironmental Engineering*, **130(2)**, 213-216.
12. **Arnepalli, D. N., Hanumantharao, B., Shanthakumar, S. and Singh, D. N.** (2010). Determination of distribution coefficient of geomaterials and immobilizing agents. *Canadian Geotechnical Journal*, **47**, 1139-1148.
13. **ASTM D 2487** (2011). Standard practice for classification of soils for engineering purposes (Unified soil classification system). *ASTM International*, West Conshohocken, Pennsylvania, USA.
14. **ASTM D 422** (2007). Standard test method for particle size analysis of soils. *ASTM International*, West Conshohocken, Pennsylvania, USA.

15. **ASTM D 427** (2008). Standard test method for shrinkage factors of soils by mercury method. *ASTM International*, West Conshohocken, Pennsylvania, USA.

16. **ASTM D 5550** (2006). Standard test method for specific gravity of soil solids by gas pycnometer. *ASTM International*, West Conshohocken, PA, USA.

17. **ASTM D 6913** (2009). Standard test methods for particle size distribution (gradation) of soils using sieve analysis. *ASTM International*, West Conshohocken, Pennsylvania, USA.

18. **ASTM D 698** (2012). Laboratory compaction characteristics of soil using standard effort (12 400 ft-lbf/ft3 (600 kN-m/m3)). *ASTM International*, West Conshohocken, Pennsylvania, USA.

19. **ASTM D4318** (2002). Standard test method for liquid limit, plastic limit and plasticity index of soils. *ASTM International*, West Conshohocken, Pennsylvania, USA.

20. **ASTM D4646** (2004). Standard test method for 24-h batch-type measurement of contaminant sorption by soils and sediments. *ASTM International*, West Conshohocken, Pennsylvania, USA.

21. **ASTM D5084** (2010). Standard test methods for measurement of hydraulic conductivity of saturated porous materials using a flexible wall permeameter. *ASTM International*, West Conshohocken, Pennsylvania, USA.

22. **Aswathy K.** (2012). *Geosequestration of Carbon Dioxide: Material-gas Interaction*. Masters dissertation, Indian Institute of Technology Madras, Chennai, India.

23. **Ayala, A., Vega, J. L., Alvarez, R. and Loredo, J.** (2008). Retention of heavy metal ions in bentonites from Grau region. *Environmental Geology*, **53**, 1323-1330.

24. **Barbour, S. L.** (1998). The soil-water characteristic curve: a historical perspective. *Canadian Geotechnical Journal*, **35**, 873-894.

25. **Belleghem, M. V., Steeman, M., Janssens, A. and Paepe, M. D.** (2014). Drying behavior of calcium silicate. *Journal of Construction and Building Materials*, **65**, 507-517.

26. **Bellir, K., Lehocine, M. B. and Meniai, A. H.** (2005). Study of the retention of heavy metals by natural material used as liners in landfills. *Desalination*, **185**, 111-119.

27. **Bhardwaj, S. A.** (2013). Indian nuclear power programme- past, present and future. *Sadhana*, Indian Academy of Sciences, **38 (5)**, 775-794.

28. **Billiotte, J., Yang, D. and Su, K.** (2008). Experimental study on gas permeability of mudstones. *Physics and Chemistry of the Earth*, **33**, S231-S236.

29. **Bittelli, M., Ventura, F., Campbell, G. S., Snyder, R. L., Gallegati, F. and Pisa, P. R.** (2008). Coupling of heat, water vapor, and liquid water fluxes to compute evaporation in bare soils. *Journal of Hydrology*, **362**, 191-205.

30. **Bouazza, A. and Vangpaisal, T.** (2003). An apparatus to measure gas permeability of geosynthetic clay liners. *Geotextiles and Geomembranes*, **21**, 85-101.

31. **Brace, W. F. and Martin, R. J.** (1968). A test of the law of effective stress for crystalline rocks of low porosity. *International Journal of Rock Mechanics and Mining Sciences*, **5**, 415-426.

32. **Buchter, B., Davidoff, B., Amacher, M. C., Hinz, C., Iskandar, I. K. and Selim, H. M.** (1989). Correlation of Freundlich K_d and n retention parameters with soils and elements. *Soil Science*, **148 (5)**, 370-379.

33. **Buckingham, E.** (1904). *Contributions to our Knowledge of the Aeration of Soils*. USDA bureau of soil bulletin, **25**. U. S. Government print office, Washington, DC.

34. **Burak, S.** (2004). *Lateral versus Vertical Swell Pressures in Expansive Soils*. Masters dissertation, The Graduate School of Natural and Applied Sciences of Middle East technical University.

35. **Calogovic, V.** (1995). Gas permeability measurement of porous materials (concrete) by time- variable pressure difference method. *Cement and Concrete Research*, **25(5)**, 1054-1062.

36. **Calvet, R.** (1989). Adsorption of organic chemicals in soils. *Environmental Health Perspectives*, **83**, 145-177.

37. **Campbell, G. S.** (1974). A simple method for determining unsaturated conductivity from moisture retention data. *Soil Science*, **117**, 311-314.

38. **Caridad, V., de Zarate, J. M. O., Khayet, M. and Legido, J. L.** (2014). Thermal conductivity and density of clay pastes at various water contents for pelotherapy use. *Applied Clay Science*, **93-94**, 23-27.

39. **Cary, J. W.** (1979). Soil heat transducers and water vapor flow. *Soil Science Society of America Journal*, **43(5)**, 835-839.

40. **Celorie, J. A., Vinson, T. S., Woods, S. L. and Istok, J. D.** (1989). Modeling solute transport by centrifugation. *Journal of Environmental Engineering*, **115,** 513-526.

41. **Chen, W. C. and Huang, W. H.** (2013). Effect of ground water chemistry on the swelling behavior of a Ca-bentonite for deep geological repository. *Physics and Chemistry of the Earth*, **65**, 42-49.

42. **Chen, Z., Xing, B. and McGrill, W. B.** (1999). A unified sorption variable for environmental applications of the Frendlich isotherm. *Journal of Environmental Quality*, **28**, 1422-1428.

43. **Cho, G. C., Dodds, J. and Santamarina, J. C.** (2006). Particle shape effects on packing density, stiffness and strength: natural and crushed sands. *Journal of Geotechnical and Geoenvironmental Engineering*, **132**, 591-602.

44. **Cho, W. J., Oscarson, D. W. and Hahn, P. S.** (1993). The measurement of apparent diffusion coefficients in compacted clays: an assessment of methods. *Applied Clay Science*, **8**, 283-294.

45. **Cho, W. J., Lee, J. O. and Kang, C. H.** (2001). A compilation and evaluation of thermal and mechanical properties of bentonite- based buffer material for a high level waste repository. *Journal of Korean Nuclear Society*, **34(1)**, 90-103.

46. **Cleall, P. J., Singh, R. M. and Thomas, H. R.** (2011). Non-isothermal moisture movement in unsaturated kaolin: an experimental and theoretical investigation. *Geotechnical Testing Journal*, **34(5)**, 1-11.

47. **Cleall, P. J., Singh, R. M. and Thomas, H. R.** (2013). Vapor transfer in unsaturated compacted bentonite. *Geotechnique*, **63 (11)**, 957-964.

48. **Crank, J.** (1975). *The Mathematics of Diffusion*. Brunel University Uxbridge, Second edition, Clarendon press, Oxford.

49. **Cuevas, B. and Leguey, S.** (2009). Behaviour of kaolinite and illite based clays as landfill barriers. *Applied Clay Science*, **42**, 497-509.

50. **Cui, Y. J. and Tang, A. M.** (2013). On the thermo-hydro-mechanical behavior of geological and engineered barriers. *Journal of Rock Mechanics and Geotechnical Engineering*, **5**, 169-178.

51. **Daniel, D. E.** (1987). *Geotechnical Practice for Waste Disposal*, Springer, USA.

52. **Daniel, D. E.** (1990). A note on falling head water and rising tail water permeability tests. *Geotechnical Testing Journal*, **12(4)**, 308-310.

53. **Das, S. K. and Basudhar, P. K.** (2006). Undrained lateral load capacity of piles in clay using artificial neural network. *Computers and Geotechnics*, **33**, 454–459.

54. **de Vries, D. A.** (1963). *Thermal Properties of Soils*. W. R. van Wijk (Ed.), The physics of plant environment, North-Holland Publishing Company, Netherlands.

55. **Demuth, H. and Beale, M.** (2000). *Neural Network Toolbox*. The math works, Inc.

56. **Devulapalli, S. S. N. and Reddy, K. R.** (1996). Effect of non linear adsorption on contaminant transport through landfill clay liners. *Environmental Geotechnics*, 473- 478.

57. **Dixon D. A., Gray M. N. and Thomas A. W.** (1985). A study of the compaction properties of potential clay-sand buffer mixtures for use in nuclear fuel waste disposal. *Engineering Geology*, **21**, 247-255.

58. **Dobchuk, B. S., Barbour, S. L. and Zhou, J.** (2004). Prediction of water vapor movement through waste rock. *Journal of Geotechnical and Geoenvironmental Engineering*, **130**, 293-302.

59. **Evgin, E. and Svec, O. J.** (1988). Heat and moisture transfer characteristics of compacted mackenzie silt. *Geotechnical Testing Journal*, **11(2)**, 92-99.

60. **Fall, M., Nasir, O. and Nguyen, T. S.** (2014). Coupled hydro-mechanical model for simulation of gas migration in host sedimentary rocks for nuclear waste repositories. *Engineering Geology*, **176**, 24-44.

61. **Farouki, O. T.** (1982). *Thermal Properties of Soils*. CRREL Monograph No. 81-1, U.S. Army Cold Regions Research and Engineering Laboratory.

62. **Fedor, F., Hamos, G., Jobbik, A., Mathe, Z., Somodi, G. and Szucs, I.** (2008). Laboratory pressure pulse decay permeability measurements of Boda clay stone. *Physics and Chemistry of the Earth*, **33**, S45-S53.

63. **Feng, M., Fredlund, D. G. and Shuai, F.** (2002). A laboratory study of the hysteresis of a thermal conductivity soil suction sensor. *Journal of Geotechnical Testing*, **25 (3)**.

64. **Fick, A.** (1855). On liquid diffusion. *Journal of Membrane Science*, **100**, 33-38.

65. **Fourier, J. B.** (1822). *Théorie Analytique de la Chaleur: English Translation by Freeman, A.*, Dover publications, New York.

66. **Franz, T. and Rowe, R. K.** (1993). Simulation of groundwater flow and contaminant transport at a landfill site using models. *International Journal for Numerical and Analytical Methods in Geomechanics*, **17**, 435-455.

67. **Fredlund, D. G. and Xing, A.** (1994). Equations for the soil water characteristic curve, *Canadian Geotechnical Journal*, **31**, 521-532.

68. **Fredlund, D. G., Rahardjo, H. and Fredlund, M. D.** (2012). *Unsaturated Soil Mechanics In Engineering Practice*. John wiley & sons, inc., 487-516.

69. **Freeze, R. A. and Cherry, J. A.** (1979). *Groundwater*. Prentice-hall, Eagle wood cliffs, New Jersey.

70. **Freundlich, H. (**1926). *Colloid and Capillary Chemistry*, Methuen, London.

71. **Galbraith, G, H., McLean, R, C., Gillespie, I., Guo, J. and Kelly, D.** (1998). Non-isothermal moisture diffusion in porous building materials. *Building Research & Information*, **26(6)**, 330-339.

72. **Galunin, E., Alba, M. D. and Vidal, M.** (2011). Stability of rare- earth disilicates: ionic radius effect. *Journal of the American Ceramic Society*, **94 (5)**, 1568- 1574.

73. **Gao, S., Walker, W. J., Dahlgren, R. A. and Bold, J.** (1997). Simultaneous sorption of Cd, Cu, Ni, Pb and Cr on soil treatment with sewage sludge supernatant. *Water Air and Soil Pollution*, **93**, 331-345.

74. **Gardner, D. R., Jefferson, A. D. and Lark, R. J.** (2008). An experimental, numerical and analytical investigation of gas flow characteristics in concrete. *Cement and Concrete Research*, **33**, 360-367.

75. **Gens, A., Guimaraes, N., Olivella, S. and Sanchez, M.** (2010). Modeling thermo- hydro- machano- chemical interactions for nuclear waste disposal. *Journal of Rock Mechanics and Geotechnical Engineering*, **2(2)**, 97-102.

76. **Giles, C. H., Mac Ewan, T. H. and Smith, D.** (1960). Studies in adsorption, part XI. *Journal of Chemical Society*, **10**, 3973-3993.

77. **Goh, A. T. C., Kulhawy, F. H. and Chua, C. G.** (2005). Bayesian neural network analysis of undrained side resistance of drilled shafts. *Journal of Geotechnical and Geoenvironmental Engineering*, **131(1)**, 84–93.

78. **Gray, M. N., Rock, C. A. and Pepin, R. G.** (1988). Pretreating landfill leachate with biomass boiler ash. *Journal of Environmental Engineering*, **114(2)**, 465-470.

79. **Green, D. W. and Perry, R. H.** (1984). *Perry's Chemical Engineers Handbook (6th edition)*, MC Graw Hill.

80. **Grolimund, D., Bokkovec, M., Federer, P. and Sticher, H.** (1995). Batch experiments for sorption capacity of porous media. *Environmental Science and Technology*, **29**, 2317-2321.

81. **Gualtieri, M. L., Gualteiri, A. F., Gagliardi, S., Ruffini, P., Ferrari, R. and Hanuskova, M.** (2010). Thermal conductivity of fired clays: Effects of

mineralogical and physical properties of raw materials. *Applied Clay Science*, **49**, 269-275.

82. **Guven, N.** (1990). Longevity of bentonite as buffer material in a nuclear-waste repository. *Engineering Geology*, **28**, 233-247.
83. **Harter, R.D.** (1983). Effect of soil pH on adsorption of Lead, Copper, Zinc, and Nickel. *Soil Science Society of America Journal*, **47**, 47-51.
84. **Higashihara, T., Ostuka, T., Sato, S. and Ohashi, H.** (2001). Diffusion of helium and estimated diffusion coefficients of hydrogen dissolved in water saturated, compacted Ca- montmorillonite. *Japan-China Workshop on Nuclear Waste Management and Reprocessing*, **7(1)**.
85. **Ho, Y. S., Porter, J. F. and McKay, G.** (2002). Equilibrium isotherm studies for the sorption of divalent metal ions onto peat: copper, nickel and lead single component systems. *Water, Air, and Soil Pollution*, **141**, 1-33.
86. **Holzlohner, U., August, H. and Meggyes, T.** (1997). Advanced Landfill Liner Systems, Thomas Telford, London. 31-37.
87. **Hopmans, J. W. and Dane, J. H.** (1986). Temperature dependence of soil hydraulic properties. *Soil Science Society of America Journal*, **50**, 4-9.
88. **Horai K.** (1971). Thermal conductivity of rock-forming minerals. *Journal of Geophysical Research*, **76**, 1278-1308.
89. **Horsfall, M. and Spiff, A. I.** (2005). Effects of temperature on the sorption of Pb2+ and Cd2+ fromaqueous solution by Caladium bicolor (wild Cocoyam) biomass. *Electronic Journal of Biotechnology*, **8(2)**, 162-169.
90. **IAEA** (1994). *Classification of Radioactive Wast*e. IAEA Safety Series No.111-G-1.1. (STI/PUB/950) International atomic energy agency, Vienna.
91. **Ikonen, K**. (2003). *Thermal Analysis of Spent Nuclear Fuel Repository*. Posiva report.
92. **Innocentini, M. D. M., Mullens, S., Colombo, P. and Biasetto, L.** (2007). Gas permeability of microcellular ceramic foams. *Industrial & Engineering Chemistry Research*, **46**, 3366-3372.
93. **Inversion, B. V., Moldrup, P., Schjonning, P. and Loll, P.** (2001). Air and water permeability in differently textured soils at two measurement scales. *Soil Science*, **166**, 643-659.
94. **Issa, S.** (1996). *Performance of Unsaturated Clay Based Barrier under Opposing Thermal and Hydraulic Gradients*. Doctoral dissertation. McGrill University, Montreal, Canada.
95. **Itakura, T., Airey, D, W. and Leo, C, J.** (2003). The diffusion and sorption of volatile organic compounds through kaolinitic clayey soils. *Journal of Contaminant Hydrology*, **65**, 219- 243.
96. **Jabro, J. D.** (2009). Water vapor diffusion through soil as affected by temperature and aggregate size. *Transport through Porous Media*, **77**, 417-428.
97. **Jackson, D. R., Garrett, B. C. and Bishop, T. A.** (1984). Comparison of batch and column methods for assessing leachability of hazardous waste. *Environmental Science and Technology*, **18**, 668-673.

98. **Janssen, H.** (2011). Thermal diffusion of water vapor in porous materials: fact or fiction? *International Journal of Heat and Mass Transfer*, **54**. 1548-1562.

99. **Jessberger, H. L., Onnich, K., Finsterwalder, K. and Beyer, S.** (1997). *Experimental and Numerical Studies of Contaminant Transport through Mineral Liners and Resulting Improvements in Liner Materials*. Advanced landfill liner system, Thomas Telford, London.

100. **Jobmann, M. and Buntebarth, G.** (2009). Influence of graphite and quartz addition on the thermo-physical properties of bentonite for sealing heat-generating radioactive waste. *Applied Clay Science*, **44**, 206-210.

101. **Johansen O.** (1975). *Thermal Conductivity of Soils*. Technical report, Trondheim, group for thermal analysis of frost in the ground, Institute for Kjoleteknikk.

102. **Joseph, R. A.** (2014). *Modeling and Analysis of Heat Migration through Buffer Materials*. Masters dissertation, Indian Institute of Technology Madras, India.

103. **Juang, C. H. and Elton, D. J.** (1997). *Prediction of Collapse Potential of Soil with Neural Networks*. Transportation research record, **1582**, 22–8.

104. **Kanno, T., Kato, K. and Yamagata, J.** (1994). Moisture movement under a temperature gradient in highly compacted bentonite. *Engineering Geology*, **41**, 287- 300.

105. **Kersten, M. S.** (1949). *Laboratory Research for the Determination of the Thermal Properties of Soils*. ACFEL technical report 23, University of Minnesota, MN.

106. **King, S. Y. and Halfter, N. A.** (1982). *Underground Power Cables*. London, U. K: Longman.

107. **Knop, A. and Gulok, J. V.** (2008). Compacted artificially cemented soil- acid leachate contaminant interactions: breakthrough curves and transport parameters. *Journal of Hazardous Materials*, **155**, 269-276.

108. **Komine, H.** (2006). Designing method of bentonite based buffer materials for HLW-disposal from the viewpoint of self-sealing. *5th ICEG-Environmental Geotechnics: Opportunities, Challenges and Responsibilities for Environmental Geotechnics*, **2**, 741-748.

109. **Komine, H. and Ogata, N.** (2004). Predicting swelling characteristics of bentonites. *Journal of Geotechnical and Geoenvironmental Engineering*, **130 (8)**, 818- 829.

110. **Kraus , J. F., Benson, C. H., Erickson, A. E. and Chamberlain, E. J.** (1997). Freeze-thaw cycling and hydraulic conductivity of bentonite barriers. *Journal of Geotechnical Engineering*, **123**, 229-238.

111. **Lahoucine, C. O., Sakashita, H. and Kumada, T.** (2002). Measurement of thermal conductivity of buffer materials and evaluation of existing correlations predicting it. *Nuclear Engineering and Design*, **216**, 1-11.

112. **Lai, T. M. and Mortland, M. M.** (1962). Self diffusion of exchangeable cations in bentonite. *Clays and Clay Minerals: Proceedings 9th Conference*, Pergamon press, New York, 229-247.

113. **Lambert, T. L. and Renken, K. J.** (1999). Experiments on industrial by product utilization as a concrete admixture to reduce radon gas transport properties. *International Radon Symposium*, 13.00-13.24.

114. **Langmuir, I.** (1918). The adsorption of gases on plane surfaces of glass, mica and platinum. *Journal of American Chemical Society*, **40**, 1361–1382.

115. **Load Generation Balance Report 2016-17** (2016). Central electricity authority, Ministry of power, Government of India.

116. **Loiseau, C., Cui, Y. J. and Delage, P.** (2002). The gradient effect on water flow through a compacted swelling soil. *Proceedings: 3rd International Conference on Unsaturated Soils*, Recife, Brazil, **1**, 395-400.

117. **Loll, P., Moldrup, P., Schjonning, P. and Riley, H.** (1999). Predicted saturated hydraulic conductivity from air permeability: application in stochastic water infiltration modeling. *Water Resource Research*, **35**, 2387-2400.

118. **Madsen, F. T.** (1998). Clay mineralogical investigations related to nuclear waste disposal. *Clay Minerals*, **33**, 109-129.

119. **Mathur, R. K., Narayan, P. K., Joshi, M. R. and Rakesh, R. R.** (1998). *In Situ Multi Heater Thermomechanical Experiments in Mysore Mines, Kolar Gold Fields*, Bhabha atomic research centre, Mumbai, India.

120. **Mazzeiri, F., Emidio, G. D. and Peter, O. V. I.** (2010). Diffusion of calcium chloride in a modified bentonite: Impact on osmotic efficiency and hydraulic conductivity. *Clays and Clay Minerals*, **58(3)**, 351- 363.

121. **McBride, M. B.** (2000). *Chemisorption and Precipitation Reactions*. Handbook of soil science, CRC press, Boca Raton, B265–B302.

122. **McGaw, R.** (1969). *Heat Conduction in Saturated Granular Materials: Effects of Temperature and Heat on Engineering Behavior of Soils*. Highway research board special report, **103**,114-131.

123. **Millington, R. J. and Quirk, J. M.** (1960). Transport in porous media. *Transactions of International Congress of Soil Science*, **7 (1)**, 14-24.

124. **Mishra, P. N., Suman, S. and Das, S. K.** (2016). Experimental investigation and prediction models for thermal conductivity of biomodified buffer materials for hazardous waste disposal. *Journal of Hazardous, Toxic and Radioactive Waste*, **21(2)**.

125. **Mitchell, J. K. and Soga, K.** (2005). *Fundamentals of Soil Behavior*. 3rd edition, John Wiley & sons, Hoboken, New York.

126. **Moldrup, P., Olesen, T., Komastsu, T., Schjonning, P. and Rolston, D. E.** (2001). Tortuosity, diffusivity, and permeability in the soil liquid and gaseous phases. *Soil Science Society of America Journal*, **65**, 613-623.

127. **Moldrup, P., Olesen, T., Schjonning, P., Yamaguchi, T. and Rolston, D. E.** (2000). Predicting the gas diffusion coefficient in undisturbed soil from soil water characteristics. *Soil Science Society of America Journal*, **64**, 94-100.

128. **Moldrup, P., Poulsen, T. G., Schjonning, P., Olesen, T. and Yamaguchi, T.** (1998). Gas permeability in undisturbed soils: measurements and predictive models. *Soil Science,* **163**, 180-189.

129. **Moldrup, P., Yoshikawa, S., Olesen, T., Komastsu, T. and Rolston, D. E.** (2003). Air permeability in undisturbed volcanic ash soils: predictive model test and soil structure fingerprint. *Soil Science Society of America Journal*, **67**, 32-40.

130. **Montes, G. H., Marty, N., Fritz, B., Clement, A. and Michau, N.** (2005). Modelling of long term diffusion reaction in a bentonite barrier for radioactive waste confinement. *Applied Clay Science*, **30**, 181-198.

131. **Nakayama, S., Sakamoto, Y., Yamguchi, T., Akai, M., Tanaka, T., Sato, T. and Iida, Y.** (2004). Dissolution of montmorillonite in compacted bentonite by highly alkaline aqueous solutions and diffusivity of hydroxide ions. *Applied Clay Science*, **27**, 53-65.

132. **Nichol, C., Smith, L. and Beckie, R.** (2003). Long-term measurement of matric suction using thermal conductivity sensors. *Canadian Geotechnical Journal*, **40**, 587-597.

133. **Nithya, K. M.** (2011). *Accelerated Physical Modeling of Sorption and Desorption Characteristics*. Doctoral dissertation, Indian Institute of Technology Madras, Chennai, India.

134. **Pachepsky, Y. Timlin, D. and Rawls, W.** (2003). Generalized Richard's equation to simulate water transport in unsaturated soils. *Journal of Hydrology*, **272**, 3-13.

135. **Poltze, M., Kahr, G., Dohrmann, R. and Weber, H.** (2007). Hydro-mechanical, geochemical and mineralogical characteristics of the bentonite buffer in a heater experiment: The HE-B project at the Mont Terri rock laboratory. *Physics and Chemistry of the Earth*, **32**, 730-740.

136. **Quintessa** (2011). *Postclosure Safety Assessment: System and its Evolution*. Report for nuclear waste management organization, Quintessa Ltd., Toronto, Canada.

137. **Raj, K., Prasad, K. K. and Bansal, N. K.** (2006). Radioactive waste management practices in India. *Nuclear Engineering and Design*, **236**, 914-930.

138. **Rao, M. V. B. B. G. and Singh, D. N.** (1999). A generalized relationship to estimate thermal resistivity of soils. *Canadian Geotechnical Journal*, **36**, 767-773.

139. **Rao, S. M. and Ravi, K.** (2013). Hydro-mechanical characterization of Barmer 1 bentonite from Rajasthan, India. *Nuclear Engineering and Design*, **265**, 330-340.

140. **Rao, S. M., Kachroo, T. A. and Allam, M. M.** (2008). Geotechnical Characterization of some Indian bentonites for their uses as buffer materials in geological repository. *The 12th International Conference of International Association for Computer Methods and Advances in Geomechanics*, Goa, India.

141. **Rochais, D., Le Meur, G., Basini, V. and Domingues, G.** (2008). Microscopic thermal characterization of HTR particle layers. *Nuclear Engineering and Design*, **238**, 3047- 3059.

142. **Rowe, R. K.** (1989). Movement of pollutants through clayey soil. *Proceedings of 37th Annual Geotechnical Conference*, Minnesota section ASCE, USA, 1-37.

143. **Rowe, R. K.** (1990). *Background Documentation for Programs POLLUTE and MIGRATE*. Geotechnical research centre, The university of Western Ontario, London.

144. **Rowe, R. K. and Booker, J. R.** (1985). 2D pollutant migration in soils of finite depth. *Canadian Geotechnical Journal*, **22(4)**, 429-436.

145. **Rowe, R. K. and Booker, J. R.** (1987). *An Efficient Analysis of Pollutant Migration through Soil.* Numerical methods in transient and coupled systems, John Wiley & Sons, 13-42.

146. **Rowe, R. K. and Booker, J. R.** (1994). *Program POLLUTE.* Geotechnical research centre, University of Western Ontario report, GAEA environmental engineering Ltd., Ontario, Canada.

147. **Roy, W. R., Krapac, I. G., Chou, S. F. G. and Griffith, R.A.** (1991). *Batch Type Procedures for Estimating Soil Adsorption of Chemicals*. EPA/530/SW-87/006-F, USEPA, Washington, DC.

148. **Salomone, L. A. and Kovacs, W. D.** (1984). Thermal resistivity of soils. *Journal of Geotechnical Engineering*, **110 (2)**, 375-389.

149. **Salomone, L. A. and Marlowe, J. I.** (1989). *Soil Rock Classification according to Thermal Conductivity*. EPRI CU-6482, Palo Alto: Electric Power Research Institute.

150. **Salomone, L. A., Kovacs, W. D. and Kusuda, T.** (1984). Thermal performance of fine-grained soils. *Journal of Geotechnical Engineering*, **110 (2)**, 359-389.

151. **Samingan, A. S., Leong, E. C. and Rahardjo, H.** (2003). A flexible wall permeameter for measurements of water and air coefficients of permeability of residual soils. *Canadian Geotechnical Journal*, **40**, 559-574.

152. **Selvadurai, A. P. S.** (1996). Heat induced moisture movement in a clay barrier II: computational modeling and comparison with experimental results. *Engineering Geology*, **41**, 219-238.

153. **Sengupta, P., Kaushik, C. P. and Dey, G. K.** (2013). Immobilization of high level nuclear wastes: the Indian scenario. *Earth System Sciences*, **2**, 25-52.

154. **Sezer, G. A. and Turkmenoglu, A. G.** (2003). Mineralogical and sorption characteristics of Ankara clay as a landfill liner. *Applied Geochemistry*, **18**, 711-717.

155. **Shackelford, C. D.** (1991). Laboratory diffusion testing for waste disposal-a review. *Journal of Contaminant Hydrology*, **7**, 177-217.

156. **Shackelford, C. D. and Daniel, D. E.** (1991). Diffusion in saturated soil: II. Results for compacted clay. *Journal of Geotechnical Engineering*, **117(3)**, 485–506.

157. **Shuai, F., Clements, C., Ryland, L. and Fredlund, D. G.** (2002). Some factors that influence soil suction measurements using a thermal conductivity sensor. *Proceedings: 3rd International Conference on Unsaturated Soils*, Recife, Brazil.

158. **Shu-li, D., Yu-Zhuang, S., Cui-na, Y. and Bo-hui, X.** (2009). Removal of copper from aqueous solution by bentonites and the factors affecting it. *Mining Science and Technology*, **19**, 489-492.

159. **Sivachidambaram, S. and Rao, S. M.** (2012). Iodide retention by modified kaolinite in the context of safe disposal of high level nuclear waste. *Journal of Hazardous, Toxic and Radioactive Waste*, 192-200.

160. **Skoczylas, F. and Henry, J. P.** (1995). A study of the intrinsic permeability of granite to gas. *International Journal of Rock Mechanics and Mining Sciences & Geomechanics*, **32(2)**, 171-179.

161. **Snoddy, R.** (2005). *Laboratory Assesment of the Permeability and Diffusion Characteristics of Florida Concretes: Phase II. Field Samples and Analysis*. Project summary, United States environmental protection agency.

162. **Spark, D. L.** (2003). *Environmental Soil Chemistry*, Academic press, Netherlands.

163. **Sposito, G.** (1989). *The Chemistry of Soils*, Oxford University press, New York.

164. **Sridharan, A. and Sivapullaiah, P. V.** (2005). Mini compaction test apparatus for fine grained soils. *Geotechnical Testing Journal*, **28(3)**, 1-7.

165. **Stewart, D. I., Studds, P. G. and Counsens, T. W.** (2003). The factors controlling the engineering properties of bentonite enhanced sand. *Applied Clay Science*, **23 (1-4)**, 97-110.

166. **Stormont, J. C.** (1997). Conduct and interpretation of gas permeability measurements in rock salt. *International Journal of Rock Mechanics and Mining Sciences*, **34 (3-4)**.

167. **Studds, P. G., Stewart, D. I. and Cousens, T. W.** (1998). The effects of salt solutions on the properties of bentonite- sand mixtures. *Clay Minerals*, **33**, 651-660.

168. **Tang, A. M., Cui, Y. J. and Le, T. T.** (2008). A study on thermal conductivity of compacted bentonites. *Applied Clay Science*, **41**, 181-189.

169. **Tarnawski, V. R. and Leong, W. H.** (2000). Thermal conductivity of soils at very low moisture content and moderate temperatures. *Transport in Porous Media*, **41**, 137-147.

170. **Thomas, H. R.** (1985). Modeling two-dimensional heat and moisture transfer oin unsaturated soils, including gravity effects. *International Journal of Numerical and Analytical Methods in Geomechanics*, **9**, 573-588.

171. **Tien, Y. M., Chu, C. A. and Chuang, W. S.** (2005). The prediction model of thermal conductivity of sand bentonite based buffer material. *International Meeting: Clays in Natural and Engineered Barriers for Radioactive Waste Confinement*, 657-659.

172. **Toride, N., Leij, F. J. and Van Genuchten, M. T.** (1999). *The CXTFIT Code for Estimating the Transport Parameters from Laboratory or Field Tracer Experiments*. Research report No. 137, United States salinity laboratory, Agricultural research service, California.

173. **Tsai, S. C., Ouyang, S. and Hsu, C. N.** (2001). Sorption and diffusion behavior of Cs and Sr on Jih- Hsing bentonite. *Applied Radiation and Isotopes*, **54**, 209-215.

174. **USEPA** (1989). *Guide to Technical Resources for the Design of Landfill Facilities*. Risk reduction engineering laboratory and centre for environmental research information, Cincinnati, Ohio.

175. **Unatrakarn. D., Asghari. K. and Condor. J.** (2011). Experimental studies of CO2 and CH4 diffusion coefficient in bulk oil and porous media. *Energy Procedia*, 2170-2177.

176. **Vardon, P. J., Cleall, P. J., Thomas, H. R., Philip, R. N. and Banicescu, I.** (2011). Three-dimensional field scale coupled therrmo-hydro-mechanicaal modeling: parallel computing implementation. *International Journal of Geomechanics*, **11**, 90-98.

177. **Veith, J. A. and Sposito, G.** (1977). On the use of the Langmuir equation in the interpretation of adsorption phenomena. *Journal of American Soil Science Society*, **41**, 697–702.

178. **Vejsada, J. and Vokal, A.** (2006). Study of Cesium sorption on Na and Ca-Mg bentonite using batch and diffusion experiments. *Czechoslovak Journal of Physics*, **56**, D73-D79.

179. **Vengris, T., Binkiene, R. and Sveikauskite, A.** (2001). Nickel, copper and zinc removal from waste water by a modified clay sorbent. *Applied Clay Science*, **18**, 183-190.

180. **Villar, M. V., Iglesias, R. J., Alvarez, C. G. and Carbonell, B.** (2018). Hydraulic and mechanical properties of compacted bentonite after 18 years in barrier conditions. *Applied Clay Science*, doi.org/10.1016/j.clay.2017.12.045.

181. **Vinsova, H., Adamcova, J. and Prikryl, R**. (2008). The influence of temperature and hydration on the sorption properties of bentonite. *Journal of Environmental Radioactivity,* **99(2)**, 415-425.

182. **Wattal, P. K.** (2013). Indian program on radioactive waste management. *Sadhana*, Indian Academy of Sciences, **38(5)**, 849-857.

183. **Werner, D., Karapanagioti, H. K. and Sabatini, D. A.** (2011). Assessing the effect of grain- scale sorption rate limitations on the fate of hydrophobic organic ground water pollutants. *Journal of Contaminant Hydrology*, **129- 130**, 70- 79.

184. **Wersin, P. Johnson, L. H. and McKinley, I. G.** (2007). Performance of the bentonite barrier at temperatures beyond 100^0C: a critical review. *Physics and Chemistry of Earth*, **32**, 780-788.

185. **Wilson, J., Savage, D., Bond, A., Watson, S., Pusch, R. and Bennett, D** (2011). *Bentonite- A Review of Key Properties, Processes and Issues for Consideration in UK Context.* Quintessa Ltd. United Kingdom.

186. **Wolfaardt, G. M. and Korber, D. R.** (2012). *Near Field Microbiological Considerations Relevent to A Deep Geological Repository for Used Nuclear Fuel- State of Science Review*. Nuclear waste management organization, Toronto, Ontario, Canada.

187. www.ctherm.com accessed on 19-06-2013

188. www.icdd.com accessed on 07-11-2013

189. www.indiaonlinepages.com accessed on 09-03-2018

190. www.wikipedia.org/wiki/Tirumalapalle_Uranium_mine accessed on 01-06-2015

191. www. nei.org accessed on 28-12-2017

192. **Xie, M., Miehe, R., Kasbohm, J., Herbert, H. J., Meyer, L. and Ziesche, U** (2012). *Bentonite Barriers- New Experiments and State of the Art*. Final report, GRS- 300, ISBN 978-3-939355-79-3.

193. **Ye, W., Wan, M., Chen, B., Chen, Y., Cui, Y. and Wang, J.** (2009). Effect of temperature on soil water characteristics and hysteresis of compacted Gaomiaozi bentonite. *Journal of Central South University of Technology*, **16**, 0821-0826.

194. **Ye, W.M., Wan, M., Chen, B., Chen, Y. G., Cui, Y. J. and Wang, J.** (2012). Temperature effect on the unsaturated permeability of the densely compacted GMZ 01 bentonite under confined conditions. *Engineering Geology*, **126**, 1-7.

195. **Yong, R. N.** (1999). Overview of modeling of clay microstructure and interactions for prediction of waste isolation barrier performance. *Engineering Geology*, **54**, 83-91.

196. **Yong, R. N., Ouhadi, V. R. and Goodarzi, A. R.** (2009). Effect of Cu^{2+} Ions and buffering capacity on smectite microstructure and performance. *Journal of Geotechnical and Geoenvironmental Engineering*, **135 (12)**, 1981-1985.

197. **Yong, R.N. and Phadungchewit, Y.** (1993). pH influence on selectivity and retention of heavy metals in some clay soils. *Canadian Geotechnical Journal*, **30**, 821-833.

198. **Yong, R.N., Mohamed, A.M.O., Shooshpasha, I. and Onofrei, C.** (1997). Hydro-thermal performance of unsaturated bentonite- sand buffer material. *Engineering Geology*, 351-365.

199. **Zhang, M., Zhang, H., Zhou, L. and Jia, L.** (2013). Temperature effects of unsaturated hydraulic property of bentonite-sand buffer backfilling mixtures. *Journal of Wuhan University of Technology- Material Science Edition*, **28 (3),** 487-493.

Publications from the Thesis

In Refereed Journals

1. **Mishra, P. N., Surya, S. S., Gadi, V. K., Joseph, R. A. and Arnepalli, D.N.** (2017). A generalized approach towards determination of thermal conductivity of sand-bentonite based buffer materials. *Journal of Hazardous, Toxic and Radioactive waste*, ASCE, DOI: 10.1061/(ASCE) HZ.2153-5515.0000357.
2. **Surya, S. S. and Arnepalli, D.N.** (2018). A generalized model for estimation of soil gas permeability. *Environmental Geotechnics*, ICE Publication (In press).

To be communicated

3. **Surya, S. S., Joseph, R. A. and Arnepalli, D.N.** (2018). Reappraisal of thermal needle probe for evaluation of thermal conductivity of buffer materials (to be communicated).
4. **Surya, S. S., Mishra, P. N., and Arnepalli, D.N.** (2018). An investigation on significance of temperature on the placement of hazardous waste containing canisters (to be communicated).
5. **Krishnan, A., Surya, S. S., and Arnepalli, D.N.** (2018). Gas diffusion characteristics of geomaterials (to be communicated).
6. **Surya, S. S. and Arnepalli, D.N.** (2018). Effect of temperature on sorption characteristics of buffer materials (paper under preperation).
7. **Nithya, K. M., Surya, S. S. and Arnepalli, D.N.** (2018). Prediction of equivalent column distribution coefficient from batch sorption tests results (paper under preperation)

In Peer-reviewed Conferences

1. **Surya, S. S., Joseph, R. A. and Arnepalli, D.N.** (2014). Modeling and analysis of heat migration through buffer material. *Indian Geotechnical Conference*, IGC-2014, Kakinada, India.
2. **Mishra, P. N., Gadi, V. K., Surya, S. S., Arnepalli, D.N.** (2014). Appraisal of safe placement distance between canisters in a typical deep geological repository. *National conference on Geo-Environmental Issues and Sustainable Urban Development*, GEN-2014, Allahabad, India (Best Paper Award).

3. **Surya, S. S. and Arnepalli, D. N.** (2016). Effect of sample thickness on laboratory determination of gas permeability of buffer materials. *Indian Geotechnical Conference*, IGC-2016, Chennai, India.
4. **Surya, S. S., Arsha, L. K. R., Nikhil, J. K. and Arnepalli, D. N.** (2017). Coupled flow of heat and moisture through compacted geomaterials. *Geotechnical Frontiers-2017*, Florida, USA.

Curriculum Vitae

1. Name : Surya, S. S.
2. Date of Birth : 06 May 1989

3. Educational Qualifications

2010 : Bachelor of Technology (B. Tech)
Institute : Mar Athanasius College of Engineering, Kerala
Specialization : Civil Engineering

2012 : Master of Technology (M. Tech)
Institute : National Institute of Technology Calicut, Kerala
Specialization : Environmental Geotechnology

2018 : Doctor of Philosophy (Thesis submitted)
Institute : Indian Institute of Technology Madras, Chennai, Tamilnadu
Registration Date : 16 July 2012

Doctoral Committee

Chairperson : **Dr. K. Ramamurthy**
Professor and Head
Department of Civil Engineering
Indian Institute of Technology Madras
Chennai-600 036, India

Supervisor : **Dr. D. N. Arnepalli**
Associate Professor
Department of Civil Engineering
Indian Institute of Technology Madras
Chennai-600 036, India

Members : **Dr. G.Appa Rao**
Professor
Department of Civil Engineering
Indian Institute of Technology Madras
Chennai-600 036, India

Dr. Ligy Phillip
Professor
Department of Civil Engineering
Indian Institute of Technology Madras
Chennai-600 036, India

Dr. K. Srinivasa Reddy
Professor
Department of Mechanical Engineering
Indian Institute of Technology Madras
Chennai-600 036, India

Dr. Abhijith Choudhury
Associate Professor
Department of Applied Mechanics
Indian Institute of Technology Madras
Chennai-600 036, India